The Coking Properties of Coal at Elevated Pressures

Michael S. Lancet
Frank A. Sim
George P. Curran

Conoco Coal Development Company
Research Division
Library, PA 15129

INTRODUCTION

Conoco's experience with the gasification of Pittsburgh No. 8 and Ohio No. 9 coals in Westfield, Scotland has suggested that the coking properties of these coals, and other Eastern U.S. coals by inference, under increased pressure are different from those normally measured at one atmosphere.

Convinced that the initial coal-based commercial synfuels plants in the U.S. will be gasification plants, Conoco has invested in the equipment necessary to carry out this study.

The work reported herein involves the operation of a pressurized coker, a pressurized Gieseler Plastometer and a device for measuring the Pressurized Swelling Index (PSI). The results of testing various coals by these methods are particularly useful in the evaluation of said coals for use in both dry and wet bottomed Lurgi gasifiers.

Seven coals, covering a fairly wide range of ranks and characteristics, were included in this work. These included three Eastern U.S. bituminous coals, EPRI-Champion and Westland from the Pittsburgh No. 8 seam and Noble County from the Ohio No. 9 seam. Also included were an Illinois No. 6 bituminous coal, Burning Star, a Western U.S. subbituminous coal, Upper Hiawatha, from Utah, and two bituminous coals, Frances and Rossington from the U.K. Four of these coals, EPRI-Champion, Noble County, Frances and Rossington were actually run in the BGC/Lurgi slagging gasifier during various programs in Westfield, Scotland.

EXPERIMENTAL

Drum sized samples of each coal were prepared for testing by the flow sheet shown in Figure 1. All samples were stored in sealed plastic bags until ground finer than 1/4" after which time they were saved in a CO_2 atmosphere in a dry ice chest.

The parting material or gob from each coal sample was saved and sized as needed for each test where gob addition was called for. Several of the samples, as received, contained no gob, hence waste material from another mine in the same seam or, if that was not available, parting material from a similar coal sample was used. The following gob was used with each coal as listed below:

Coal	Gob
EPRI	Westland
Westland	Westland
Noble County	Egypt Valley - Ohio No. 9
Burning Star	Hillsboro - Illinois No. 6
Frances	None
Rossington	Hillsboro
Upper Hiawatha	Upper Hiawatha

The proximate and ultimate analyses of these coals are given in Table 1. Also shown in this table are the heating values, ASTM Gieseler fluidity and Free Swelling Index (FSI), the Hardgrove grindability and a strength index for each coal. These represent the normally measured physical and chemical properties of coal.

The Gieseler fluidity in DDPM and the Free Swelling Index (FSI) reported in Table 1 are the standard ASTM test values for each coal.

The relative strength of each coal was determined by the CCDC mini drum method which consists of tumbling a 10 g sample in a specially designed 8" diameter tumbler with two 180° opposed internal vanes. A composite mini drum index was calculated for each coal which can be used to compare the relative strengths of coals and/or cokes. The higher the number the stronger the material. The same test was used to measure the strengths of all cokes produced in the pressure coker runs described later.

The coal strengths, ranging from a low of 0.81 for the Noble County coal to 0.94 for the Frances, are quite high. In almost every case the strength of each coal is greater than that of the cokes derived from them.

The grindability numbers are consistent with the strength indices with Frances at 38.6 being the hardest to grind and the strongest from a strength index standpoint. Based on the grindability all the coals are physically rugged and should pose no problems upon feeding to a Lurgi gasifier.

Pressurized Coal Fluidity Studies

The measurement of the fluidity of coals as they are heated through 350 to 500°C has been of significant benefit to the steel industry in predicting the performance of various coals in slot ovens. The standard method of determining coal fluidity is via the Gieseler plastometer. This test, normally carried out at 1 atm total pressure in air, consists of applying a constant torque to a rabble arm stirrer, packed in a sample of finely ground coal, and measuring the rate of rotation of the stirrer as the sample is heated at a constant rate (usually 3°C/min) through the plastic zone.

In general, coals of higher rank (except anthracite) are found to be more fluid by this test than those of lower rank. Little is known, however, about the fluidity of coals at elevated pressures and in gas atmospheres other than air.[1,2] This becomes of particular interest for moving bed coal gasifiers where raw coal is introduced at rather high temperatures and at elevated pressures of reducing gas. Hence, the work described herein was aimed at determining the effect of these variables, as well as higher heating rates, on the fluidities of different coals. Table 2 lists the parameters tested in this work.

Apparatus:

The basic equipment used in this work has been described previously.[2] Both the heating rate and the torque are continuously variable on this machine between the values of 0 and 6°C/minute and 0 and 720 g.cm, respectively. The variable heating rate permits examination of the effect of this parameter on coal fluidity whereas normal Gieseler operation is at a fixed heating rate of 3°C/minute. The capability of lowering the torque below the standard value of 100 g·cm permits measurement of fluidities far in excess of the normal 30,000 DDPM maximum.

Procedure:

Hand picked lumps of coal were ground in air to -35 mesh and either tested immediately or stored in a CO_2 atmosphere in a dry-ice chest. Coal samples of this kind are identified in this report as "clean coal". When specified by the program, "clean" coal samples were doped with gob ground to -35 mesh. Frances coal was not doped due to the clean nature of this seam. Tar was added to the coal and gob mixture as a solution in toluene. The coal-gob-tar slurry was then placed in a vacuum oven and the toluene was evaporated at about 50°C.

A modified ASTM D-2639-71 "Standard Method of Test for Plastic Properties of Coal by the Constant-Torque Gieseler Plastometer" was employed. As opposed to the ASTM standard method, the majority of the runs in this study were done at a heating rate of 6°C/minute and only one for each coal was made at the standard rate of 3°C/minute. Also, the standard torque of 1.40 oz-in (100 gm-cm) was used only when the maximum fluidity of the coal in question was within the range of the apparatus, i.e., 0-28,000 DDPM. In the cases where the coal fluidity exceeded the operating range of the instrument, "low" torques, i.e., 0.45 oz-inch (32.4 g-cm) or 0.26 oz-inch (18.7 g-cm), were employed and the results were corrected by factors of 3.1 or 5.4, which are the ratios of the standard torque and the lower torques, (1.4/0.45 and 1.4/0.26), respectively. A considerable degree of uncertainty may be associated with the numerical value of the high torque/low torque correction factor. The actual ratio of the torques is theoretically correct for Newtonian fluids. However, since each coal in its plastic state may deviate from Newtonian behavior to a different degree, the values of 3.1 or 5.4 may only be considered to be approximations to the true values.

When the test was to be performed in a gas mixture containing 18 or 31.5 vol % H_2 at a total pressure of 350 psig, the pressure vessel containing the plastometer was evacuated and then pressurized with hydrogen to 51 psig and 100 psig, respectively. The hydrogen was then diluted to the desired degree by pressurizing the vessel up to 350 psig with prepurified nitrogen. The remainder of the runs were carried out in a prepurified nitrogen atmosphere or in air.

Results and Discussion:

Tables 3 through 6 show the effects of the studied variables, i.e., of the heating rate, gas composition, gob content, tar content, and nitrogen pressure, on the fluidity of the coals studied. Figures 2 through 6 are graphical representations of the data obtained on the fluidities of the seven coals in this program.

The following conclusions may be drawn from these data:

1. In all cases, an increase in the heating rate resulted in substantially increased fluidity (Figures 2 and 3). This effect is directly comparable to and in complete agreement with that observed by Van Krevelen, et.al.[3]

2. In all cases, except that of Frances and Upper Hiawatha coals, the fluidity of the coal is moderately sensitive to hydrogen partial

pressure at 350 psig total pressure (Figure 4). The effects of all the variables - except the heating rate - on the fluidity of Frances and Upper Hiawatha coal is so small that these coals may be considered non-fluid.

3. The observed effect of an increase in fluidity with an increase in total, or nitrogen pressure, Table 6, is consistent with work done previously on other coals[1,2] in this pressure range.

4. Increasing the gob content in all coals reduced the fluidity in all cases. Frances coal was not subject to this type of test.

5. The addition of 4 wt % of Pittsburgh No. 8 derived tar significantly increased the fluidity of all coals except the Frances and Upper Hiawatha.

The results of this work on the effect of both total pressure and hydrogen partial pressure, qualitatively support the conclusion of Lewellen,[4] however, the available data are insufficient to quantitatively test this model. To fully test this model would require a much wider range of both pressures (10^{-2}-10^{+3} atm) and heating rates (up to 10^{4}°C/min) than is currently possible.

The qualitative correlations of the fluidity with the experimental parameters, as discussed above, suggest that with additional data, especially from work on other coals, a meaningful predictive correlation of these data may eventually be possible. Initial attempts to correlate the observed fluidity data with various physical and chemical properties have been encouraging. There is strong evidence which suggests that with data from several additional coals a correlation of fluidity with various petrographic features may be obtained.

Pressurized Swelling Index

The free swelling index, FSI, of coal as defined by the ASTM[5] is another valuable tool of the steel industry. This test consists of rapidly heating a finely ground coal sample to about 800°C and observing the degree to which the coal cakes and swells. This test, as in the case of standard Gieseler work, is carried out at one atmosphere in air. The values for the ASTM FSI's for each coal are given in Table 1. For the present work it was believed that a similar test under simulated gasifier conditions might be of value in predicting the behavior of coals as fed to a moving bed gasifier.

While the pressurized swelling tests carried out in this work are as close to the ASTM standard method as possible, one major difference was unavoidable. Due to the use of elevated pressures the heating rate of this test is not the same as that prescribed by the ASTM standard method.[5] Furthermore, the heating rate at each test condition was slightly different due to the difference in pressure and thermal conductivity of the gases used. The heating rate was, however, the same for each coal at the same test condition and conclusions drawn from such comparisons should be valid. In general the coke buttons produced in the CCDC pressurized swelling index (PSI) test are significantly less voluminous than those of the ASTM test.

Apparatus:

The equipment for this test, as shown schematically in Figure 7, consists of an electrically heated steel core enclosed in a pressure shell. A sample crucible holder assembly is attached to a 1/4" lifting rod which passes through a packing gland at the top of the vessel. Strategically located thermocouples permit continuous monitoring of the core and crucible temperature.

Procedure:

A 1.00 gm sample of coal, ground to -60 mesh, was placed in the test crucible, covered with a lid and positioned in the holder. The vessel was then closed, sealed and evacuated in order to displace air and then flooded or pressurized with the desired gas. After the required pressure was attained, the lifting rod with the holder and the crucible was pushed down onto the core surface which had previously been equilibrated at 1500° ± 5°F. Temperatures of the core were recorded every 20 seconds beginning with the time when the crucible reached the core. The crucible was lifted after 5 minutes, the apparatus was depressurized, purged with nitrogen and the crucible was removed. The coke button was carefully taken from the crucible and weighed. The pores in the button were plugged by dipping in molten paraffin and the volume was measured by water displacement. The swelling index was defined as the button volume in milliliters. For comparison purposes, the ASTM FSI profile number is very nearly the button volume in ml. Each experiment was repeated 4 to 5 times due to the variability in the button volume, and the value reported for each is the average of all runs. Normally the standard deviation of this average was less than ± 10%.

Temperature profiles were measured in order to ascertain that the samples were subject to comparable heating rates. The initial heating rates are quite high (1000-1200°F/min) and the temperature stabilizes after 3 minutes. The heating rate in both hydrogen and nitrogen is nearly the same.

Experimental Results:

Each of the seven coals in the program was tested by this method. Tar obtained during operation of the Westfield gasifier with Pittsburgh No. 8 coal was used for the tar addition experiments with all tested coals.

The coals and their mixtures with gob and tar were tested at the conditions shown in Table 7.

Table 8 shows the effects of the sample composition on the swelling of different coals at 365 psia total and 115 psia hydrogen partial pressure. Figure 8 is a graphical representation of these results.

The experimental results lead to the following conclusions:

1. There is little difference between the swelling properties of the Noble County, Ohio No. 9 coal and the two Pittsburgh seam coals, EPRI-Champion and Westland, at the test conditions, i.e., at 1500° ± 5°F, 350 psig total pressure and 115 psia hydrogen partial pressure. This is in marked contrast to the 1 atm ASTM FSI data (Table 1) where the two Pittsburgh seam coals have FSI values of 7

while the Ohio No. 9 has an FSI of only 4! The Burning Star-Illinois No. 6 coke buttons and those made of Rossington coal were considerably less voluminous than those of the EPRI coal. Frances and Upper Hiawatha coals are virtually non swelling.

With the exception of the Noble County coal, the order of the pressurized swelling index values is the same as that of the ASTM FSI values. The apparent greater effect of gasifier conditions on the Ohio No. 9 coal than on the Pittsburgh No. 8 coals may help explain some of the unexpected operating difficulties which occurred when the Noble County coal was fed to the BGC/Lurgi slagging gasifier in the DOE sponsored Westfield trials. The observed differences in the caking and swelling of the Ohio No. 9 coal at Westfield versus those predicted by standard ASTM tests was one key factor which eventually led to the present CCDC feedstock evaluation program.

It is interesting that increased hydrogen pressure and total pressure has a larger relative effect on the swelling of the Noble County coal than on its fluidity. The increase in the fluidity of this coal is increased by gasifier conditions by about the same factor as are the two Pittsburgh seam coals.

2. Doping with gob significantly reduces the swelling of all the coals tested except the inactive Upper Hiawatha coal where the gob addition had no effect. This observed effect is essentially that expected from the diluent effect of the inert gob.

3. The addition of tar to the bituminous coals when they have been doped with 10 wt % gob, considerably increases the volume of coke buttons made of these coals (Table 9). Tar addition to the Utah subbituminous coal does not have any effect, while the same tar addition to Frances coal increases its very low swelling activity by about 10%.

   The addition of even 4% tar has little effect on the Noble County coal (Table 9). This, coupled with the much larger observed effect of operating at gasifier conditions discussed above, suggests that the coal-derived tar content of this coal may be significantly higher than that of the other coals. This, however, is not confirmed by the coker yield data to be discussed later. It is possible that such differences in the yield structure would be masked by reactions between the coal-derived tar and added hydrogen or even pyrolysis-derived gases. More coal-derived tar from the Noble County coal could also explain the observation that this coal has the highest ASTM Gieseler fluidity of any coal tested (Table 1).

4. The effect of hydrogen partial pressure on the swelling of all the coals tested, doped with 10% gob, is negligible. There was little difference between the buttons produced in 100% N_2 at 350 psig and those made in 31.5% H_2-68.5% N_2 at 350 psig total pressure. The use of a gas containing 18 vol % H_2 also did not affect the volumes of the coke buttons of EPRI coal containing 10% gob. The effect of

the total pressure on the swelling properties was studied only with EPRI coal doped with 10% gob. Prepurified nitrogen was used and the results suggest there is little or no effect of the total pressure on the swelling properties of this coal.

While the effect of both hydrogen pressure and total pressure on the button volume is small they have a marked effect on the shape of the coke buttons. Coking a highly caking Eastern U.S. coal in the pressurized FSI apparatus produces, at low pressure, a button with a smooth rounded top surface. At pressures above about 150 psig, however, one or more appendages which resemble stalagmites begin to appear on the top surface of the button.

This effect is not observed when lower rank coals are processed in the device. Figure 9 shows a comparison of the effect of pressure on the shape of the buttons produced from a typical Pittsburgh No. 8 seam coal with those produced from a less active, Illinois Basin, coal.

Apparently the pressure tends to prevent the whole top surface from rising as seems to be the case at atmospheric pressure, but internal pressures are built up which are eventually released through the observed stalagmite growth.

As discussed earlier, there is encouraging evidence that more data on these properties, to be obtained by running more coals through the program, will lead to a predictive correlation of the swelling properties based upon petrographic parameters.

Pressurized Coker Studies

The CCDC pressurized coker is a useful tool for testing several parameters which are associated with coke formation in the upper part of a Lurgi gasifier. Especially important in this respect is the friability which may be a key to successful stirrer design in future plants. This property is studied via the mini drum tumbler test described earlier. Other coking properties which are studied are the effect of washing, i.e., the effect of non-coal impurities, on the coke formed under pressure and the effect of recycle tar addition on coke formation. An understanding of these effects will be important for gasifier and coal preparation facilities design requirements.

All coals included in this program were subjected to testing in the pressurized coker system to ascertain the effects of the total operating pressure, the hydrogen partial pressure, gob addition and tar addition on the coke strength and coke density. Product yields were determined for the runs made with clean coal. Also, chemical analysis of gases, tars and cokes were obtained for the clean coal runs and the effects of the above mentioned independent variables on the methane, carbon monoxide and hydrogen contents of the product gas was investigated.

Apparatus:

The pressurized coker is a 48" long, 2" diameter, double x wall pipe made of Alonized 316 SS. The coker tube is capable of being rotated about an axis located at the tube center as shown in Figure 10. The outlet half of the

coker tube is electrically heated with 6, 520 watt, resistance heaters. Skin and internal temperatures are continuously monitored and recorded on a strip chart. The tar trap is a small water-cooled pressure vessel. A dip tube connected to the detachable lid reaches to the bottom of a teflon bottle tightly fitted into the tar trap body. Glass wool, placed in the annular space between the dip tube and the bottle neck acts as a demister. An opening is provided in the tar trap lid for gas withdrawal.

A pressure control valve is located downstream of the tar trap and is operated by a recording pressure controller and a pressure transmitter which is connected to the gas inlet piping of the coker.

A dry ice temperature cold trap is located downstream of the pressure control valve. Gas sampling bags and gas meters are provided on the tail end of the system.

Procedure:

A 100 gram sample of sized coal or of a coal and gob mixture is inserted into the cool inlet side of the coker while the body is kept in the horizontal position. When tar was to be added to the sample a solution of the desired weight of tar in 5 ml of toluene was prepared. The solids were immersed in this solution, the toluene was evaporated in a vacuum oven at 50°C and the sample was chilled in an ice chest prior to loading into the coker.

After the sample was charged into the coker, the inlet flange was attached and the whole system purged with nitrogen at atmospheric pressure. Heat-up was begun and when the coker thermowell temperature approached 1300°F, the nitrogen purge was switched to the desired gas mixture and the gas flow rate and operating pressures were set as specified for the desired run.

When the coker bed temperature reached 1472°F (800°C) an inlet gas sample was taken by opening and closing previously evacuated gas sample bomb. A split stream of the off gas was diverted into a gas sample bag and the coker body was tilted into the vertical position. The sample dropped into the hot zone of the coker and the coking process was begun. This shock heating under pressure attempts to simulate coal falling into the top of a moving bed gasifier.

The power was turned off after 15 minutes running time and the off gas sample was collected for a total of one hour. The system was then depressurized, the cold trap closed, and the coker was vented and kept under a small nitrogen purge until the apparatus cooled down. The tar trap was then disconnected and the tar removed, separated from the water phase and weighed. The coke was removed and weighed after the coker internal temperature had dropped below 200°F.

Results and Discussion:

A total of ten different tests were devised to investigate the effects of the total operating pressure, the hydrogen partial pressure and of the sample composition on coke strength, coke density, coking yields and on the composition of the products. Table 9 is a list of test conditions. All the tests were made on coal sized 3/4" x 1/4" except test 10. Experiments were performed in atmospheres of either 100% prepurified nitrogen or mixtures of prepurified nitrogen with hydrogen. It should be mentioned that the tests identified as No. 2 and No. 7 were done for EPRI-Champion coal only.

A comparison of the results obtained from tests Nos. 3, 4 and 5 shows the effect of total pressure, namely, atmospheric, 215 psig and 365 psig on coke strength and mercury density of the coke. Similarly, a comparison of tests Nos. 2, 3 and 6 shows the effects of 0, 65 and 115 psia hydrogen partial pressure (the balance being nitrogen) on the same variables. Tests Nos. 1, 6 and 9 compare the effects of gob addition to the coal, with test No. 1 investigating "clean" coal, No. 6, coal doped with 10% gob and No. 9, coal doped with 20% gob. Tests Nos. 7 and 8 study the effect on the above mentioned properties of adding 5 and 10 wt % tar to a coal sample doped with 10% gob. Test No. 10 was run on a "clean coal" sample sized 1/4" x 12 mesh at 365 psia total pressure and 115 psia of hydrogen partial pressure. The finer size of the feed coal for this test allowed for a more homogeneous sample than was possible when 3/4" x 1/4" coal was used which, in turn, permitted better data on yield and coke composition to be obtained.

The inherent variability of the coal and particularly that of the gob samples used rendered any yield calculations based on these feed mixtures useless. Hence, only those runs made with undoped clean coal were used for yield determinations.

Figure 11 is a plot of the effect of various parameters on the coke strength. The plotted data are averages of all runs made at each set of conditions. The following conclusions may be drawn from this figure:

1. The strength of the coke made from the low fluidity coals (Frances and Upper Hiawatha) and from the medium fluidity coals (Rossington and Burning Star) is inversely proportional to total pressure.

   The effect of increasing pressure on the strength of coke made from the high fluidity coals (EPRI, Westland and Noble County) is negligible.

2. The effect of hydrogen partial pressure on the coke strength is small and variable (Figure 11).

3. The results related to the effect on the coke strength of doping clean coal with 10% and 20% gob are inconclusive. The coke strength decreases or remains basically unchanged in six of seven cases, the exception being the Burning Star coal.

4. The addition of 10 wt % tar to coal previously doped with 10 wt % gob caused a slight increase in the strength of the coke produced in most cases with the exception of the Upper Hiawatha and Burning Star coals.

Figure 12 is a plot of the effects of pressure, gas composition and gob and tar addition on the coke density. These are particle densities as determined by mercury displacement at one atmosphere. The data shown in this figure suggest that:

1. The coke density remains the same or decreases very slightly when the total pressure is increased from atmospheric to 350 psig.

2. The density of the coke produced from the studied coals depends little on the hydrogen partial pressure. However, a slight increase in density with increased hydrogen pressure is seen for the high fluidity coals.

3. As expected increased gob contents lead to increased particle densities.

4. The addition of 10 wt % tar to low fluidity coals did not have any effect on the density of the coke. However, the same addition to medium fluidity coals doped with 10% gob caused the coke density to increase significantly. A slight increase is observed for two of the three high fluidity coals (EPRI and Westland) while a decrease was found for the Noble County coal.

Interestingly, this rather complex picture of coke strength and density may, as appears to be the case for the fluidity and swelling data, be explainable in terms of a few petrographic parameters. More data on different coals will show just how good a correlation can be obtained.

Yield data were collected for each of the over 100 coker runs in this program, however, as mentioned earlier the majority of these data are of little value. Only the data obtained with clean coal samples give useful yield data. A summary of the yield data from the runs made at simulated gasifier conditions (i.e., 365 psia total pressure and 115 psia hydrogen pressure) on 1/4" x 12 mesh coal is given in Table 10. These data are based on the average measured coke, tar and liquid yields for all runs at these conditions for each coal (on a moisture and ash free basis), with the gas yield calculated by difference.

In all cases the coke yield at simulated gasifier conditions of 365 psia total pressure and 115 psia hydrogen partial pressure is greater than the fixed carbon content determined for each coal at 1 atm (Table 1). This is not surprising since at elevated pressure the release of volatile components is retarded.[1,2,3] The slowing of volatile release allows more of this material to be converted to coke at the expense of liquid and/or gas yield.

The yield data for Frances coal, Table 11, where only clean coal was used, shows that both coke and gas yields are increased at the expense of the liquid yield in going from 1 atm N_2 pressure to 365 psia of N_2. Here the coke yield increases from ~ 65% to ~ 67.5% and the gas yield increases from ~ 25% to 29% while the liquid yield decreases from ~ 10% to ~ 4%. Possibly liquid evolution repression can account for both the increased coke and gas yields. If the liquid is held in the coal matrix some of it is coked and some is further converted to gas by the longer residence time at elevated temperatures thus reducing the overall liquid yield and increasing the coke and gas yields. At elevated hydrogen pressures (115 psia and 365 psia total pressure) the coke yield is about the same as when 365 psia of nitrogen is used, however, the liquid yield is greatly enhanced at the expense of the gas yield. Undoubtedly reaction between the added hydrogen and the coal are responsible for the higher liquid yield.

Figure 13 shows a comparison of produced gas composition with respect to CH_4, CO and H_2 at various conditions. Since most of these data were obtained with coal doped with gob the results may not be as reliable as if only clean coal

was used, however, general trends are not expected to differ from those observed here. The methane content of the product gas is 50-100% higher than for the case with no added hydrogen while the hydrogen content of the product is considerably lower.

Qualitatively this suggests that hydrogen evolved from the coal escapes before it has time to react further with the remaining coal matrix. The CO content of the product appears virtually unaffected by pressure and the addition of gob and/or tar has little or no effect on the gas composition.

CONCLUSIONS

The experimental data presented herein should provide a start on the required data base which will ultimately permit the prediction of the coking properties of coals being considered as potential gasifier feedstocks. The limited data obtained pertaining to pyrolysis yields and gas composition are encouraging and suggest that accurate gas yield predictions may also be possible at the conclusion of this program. The effects of process variables on coal swelling and fluidity has been fairly well established, but more work is needed to get predictive mathematical correlations of these as well as coking and pyrolysis properties of coals.

Acknowledgement

This work was supported in part by the Electric Power Research Institute (EPRI), Contract No. RP 1267-7.

REFERENCES

1. Kaiho, M. and Toda, Y., Changes in Thermoplastic Properties of Coal Under Pressure of Various Gases. Fuel 58, 397 (May, 1979).

2. Lancet, M. S. and Sim, F. A., The Effect of Pressure and Gas Composition on the Fluidity of Pittsburgh No. 8 Coal, Preprints of Fuel Chemistry Div. ACS, Vol 26, No. 3 (August, 1981).

3. Van Krevelen, D. W., Huntjens, F. S. and Dormans, H. N. M., Chemical Structures and Properties of Coal XVI - - Plastic Behavior on Heating, Fuel 35, 462 (1955).

4. Lewellen, P. C., Product Decomposition Effects in Coal Pyrolysis, Masters Thesis, Department of Chemical Engineering, MIT, (1975).

5. ASTM Standard Method D720-67, Free Swelling Index of Coal (1977).

Table 1

Composition of Feed Coals

Coal	EPRI Champion	Westland	Noble County	Burning Star	Frances	Rossington	Upper Hiawatha
Origin	Pgh. No. 8 Seam	Pgh. No. 8 Seam	Ohio No. 9 Seam	Ill. No. 6 Seam	Scotland	England	Utah
Moisture							
% As Analyzed	2.28	2.02	2.68	9.99	6.62	5.81	7.39
Proximate, Dry							
Volatile Matter, %	37.93	36.28	44.36	42.94	38.84	38.01	41.74
Fixed Carbon	49.94	52.21	46.10	43.52	56.93	59.04	50.36
Ash	12.13	11.51	9.54	13.54	4.23	2.95	7.90
Ultimate, Dry							
Hydrogen, %	4.93	4.84	5.16	4.65	5.07	5.06	4.94
Carbon	72.52	73.13	72.70	68.00	78.73	79.13	72.08
Nitrogen	1.45	1.51	1.05	1.31	1.60	1.66	1.25
Oxygen (Diff.)	6.80	7.16	8.12	9.26	9.93	9.68	13.35
Sulfur	2.17	1.85	3.43	3.24	0.44	1.52	0.48
Ash	12.13	11.51	9.54	13.54	4.23	2.95	7.90
HHV, Dry							
Btu/lb	12,955	12,990	13,370	12,165	13,790	14,195	12,688
Ultimate, MAF							
Hydrogen, %	5.61	5.47	5.70	5.38	5.29	5.21	5.36
Carbon	82.53	82.64	80.37	78.65	82.21	81.54	78.26
Nitrogen	1.65	1.71	1.16	1.52	1.67	1.71	1.36
Oxygen (Diff.)	7.74	8.09	8.98	10.71	10.37	9.97	14.50
Sulfur	2.47	2.09	3.79	3.75	0.46	1.57	0.52
Gieseler Fluidity, (DDPM)	5,300	15,800	27,000	4.7	1.0	5.3	0
Free Swelling Index (FSI)	7	7	4	3.5	1.5	3.5	1
Hardgrove Grindability	52.9	62.9	49.7	48.7	38.6	48.3	45.6
Strength Index	0.849	0.886	0.806	0.831	0.942	0.847	0.884

Table 2

List of Testing Conditions
for Pressurized Coal Fluidity Studies

Test No.	Sample Composition	Testing Pressure, psig	Gas Composition	Heating Rate, °C/Min
0	Clean Coal	0	Air	6
1	Clean Coal	350	31.5% H_2, Bal. N_2	3
2	Clean Coal	350	31.5% H_2, Bal. N_2	6
3	90 Wt % Coal + 10 Wt % Gob	350	100% N_2	6
4(1)	90 Wt % Coal + 10 Wt % Gob	350	18% H_2, Bal. N_2	6
5	90 Wt % Coal + 10 Wt % Gob	350	31.5% H_2, Bal. N_2	6
6(1)	89 Wt % Coal + 10 Wt % Gob + 1 Wt % Tar	350	31.5% H_2, Bal. N_2	6
7	86 Wt % Coal + 10 Wt % Gob + 4 Wt % Tar	350	31.5% H_2, Bal. N_2	6
8(1)	90 Wt % Coal + 10 Wt % Gob	200	100% N_2	6
9	80 Wt % Coal + 20 Wt % Gob	350	31.5% H_2, Bal. N_2	6

(1) Test performed on EPRI-Champion, Pittsburgh No. 8 Seam coal only.

Table 3

The Effect of the Heating Rate
on the Fluidity of Various Coals

Heating Rate	EPRI-Champion Pittsburgh No. 8 Seam DDPM	Westland Pittsburgh No. 8 Seam DDPM	Noble County Ohio No. 9 Seam DDPM	Burning Star Illinois No. 6 Seam DDPM	Frances Scotland DDPM	Rossington England DDPM	Upper Hiawatha Utah DDPM
3°C/Min	25,500	6,300	56,200(1)	50	3	520	2
6°C/Min	61,700(1)	19,900	155,000(1)	230	7	2,600	5

Test Conditions: Total Pressure = 365 Psia
Hydrogen Partial Pressure = 115 Psia
Sample Composition = Clean Coal

Reported values are averages of two duplicate runs.

(1) Torque correction factors used for fluidities higher than 30,000 DDPM at 100 g cm torque.

Table 4

The Effect of the Gas Composition on the Fluidity of Various Coals

	EPRI-Champion Pittsburgh No. 8 Seam DDPM	Westland Pittsburgh No. 8 Seam DDPM	Noble County Ohio No. 9 Seam DDPM	Burning Star Illinois No. 6 Seam DDPM	Frances Scotland DDPM	Rossington England DDPM	Upper Hiawatha Utah DDPM
Gas Composition							
100% Nitrogen	36,900(1)	12,600	73,700(1)	30	6	1,400	3
18% H_2, Bal. N_2	48,300(1)	--	--	--	--	--	--
31.5% H_2, Bal. N_2	53,600(1)	14,500	81,200(1)	80	7	1,800	3

Test Conditions: Total Pressure = 365 Psia
Heating Rate = 6°C/min
Sample Composition = 90 wt % coal + 10 wt % gob (except Frances coal)

Reported values are averages of two duplicate runs.

(1) Torque conversion factors used for fluidities higher than 30,000 DDPM at 100 g cm torque.

Table 5

The Effect of Gob and Tar Addition on the Fluidity of Various Coals

	EPRI-Champion Pittsburgh No. 8 Seam DDPM	Westland Pittsburgh No. 8 Seam DDPM	Noble County Ohio No. 9 Seam DDPM	Burning Star Illinois No. 6 Seam DDPM	Frances Scotland(1) DDPM	Rossington England DDPM	Upper Hiawatha Utah DDPM
Sample Composition							
Clean Coal	64,700(2)	19,800	155,000(2)	230	7	2,600	5
90 Wt % Coal + 10 Wt % Gob	53,600(2)	14,500	81,200(2)	80	--	1,800	3
80 Wt % Coal + 20 Wt % Gob	41,200(2)	11,900	56,900(2)	30	--	1,400	3
89 Wt % Coal + 10 Wt % Gob + 1 Wt % Tar	57,300(2)	--	--	--	--	--	--
86 Wt % Coal + 10 Wt % Gob + 4 Wt % Tar	96,200(2)	34,500(2)	+161,500(2)	540	11	5,500	4

Test Conditions: Total Pressure = 365 Psia
Hydrogen Partial Pressure = 115 Psia
Heating Rate = 6°C/min

Reported values are averages of two duplicate runs.

1) No gob added to Frances coal.
2) Torque conversion factors used for fluidities higher than 30,000 DDPM at 100 g cm torque.

Table 6

The Effect of the Nitrogen Pressure on the Fluidity of EPRI-Pittsburgh No. 8 Seam Coal

Pressure, psig	Fluidity, DDPM
200	37,600
350	36,900

Test Conditions: Sample Type = "clean" coal
Torque = 32.4 g cm
Heating Rate = 6°C/min

Remarks: Reported values are averages of duplicate runs. Torque converston factor equal to 3.11 used to obtain fluidity values as shown.

Table 7

List of Testing Conditions for the Pressurized Swelling Index Determination

Test	Sample	P_{Total} Psia	P_{H_2} Psia
1	Clean Coal	365	115
2	90 Wt % Coal + 10 Wt % Gob	365	0
3(1)	90 Wt % Coal + 10 Wt % Gob	365	65
4	90 Wt % Coal + 10 Wt % Gob	365	115
5(1)	89 Wt % Coal + 10 Wt % Gob + 1 Wt % Tar	365	115
6	86 Wt % Coal + 10 Wt % Gob + 1 Wt % Tar	365	115
7(1)	90 Wt % Coal + 10 Wt % Gob	215	0
8	80 Wt % Coal + 20 Wt % Gob	365	115

(1) These were run only for one coal (EPRI-Champion, Pittsburgh No. 8 Seam coal).

Table 8

Effect of Feed Composition
on the Swelling of Different Coals

Sample Composition	Coal: EPRI Champion Pittsburgh No. 8	Westland Pittsburgh No. 8	Noble County Ohio No. 9	Burning Star Illinois No. 6	Frances Scotland	Rossington England	Upper Hiawatha Utah
Clean Coal	3.0	2.8	3.0	2.0	1.0	1.8	0.9
90 Wt % Coal + 10 Wt % Gob	2.4	1.9	2.3	1.8	--	1.8	0.9
80 Wt % Coal + 20 Wt % Gob	2.2	2.1	2.4	1.6	--	1.7	0.9
89 Wt % Coal + 10 Wt % Gob + 1 Wt % Tar	2.6	--	--	--	--	--	--
86 Wt % Coal + 10 Wt % Gob + 4 Wt % Tar	2.9	3.8	2.3	1.9	1.1	2.0	0.9

Swelling index is expressed as the average volume in ml of all coke buttons produced at given test conditions.

P_{tot}: 365 psia

P_{H_2} : 115 psia

T : 1500 ± 5°F

Table 9

List of Pressurized Coker Testing Conditions

Test No.	Total Testing Pressure, psia	Hydrogen Partial Pressure, psia	Sample Composition
1	365	115	Clean Coal
2(1)	365	65	90 Wt % Coal + 10 Wt % Gob
3	365	0	90 Wt % Coal + 10 Wt % Gob
4(1)	215	0	90 Wt % Coal + 10 Wt % Gob
5	15	0	90 Wt % Coal + 10 Wt % Gob
6	365	115	90 Wt % Coal + 10 Wt % Gob
7(1)	365	115	85 Wt % Coal + 10 Wt % Gob + 5 Wt % Tar
8	365	115	80 Wt % Coal + 10 Wt % Gob + 10 Wt % Tar
9	365	115	80 Wt % Coal + 20 Wt % Gob
10(2)	365	115	Clean Coal

(1) Tests performed on EPRI-Champion, Pittsburgh No. 8 Seam coal only.
(2) Test No. 10 performed on 1/4" x 12 mesh sized coals, all other tests on 3/4" x 1/4" sized materials.

Table 10

Coker Yield Data

Feed Coal	Coke Yield (MAF Wt %)	Liquid Yield (MAF Wt %)	Gas Yield+ (MAF Wt %)
EPRI-Champion	64.9	14.0	21.1
Westland	65.5	12.4	23.0
Noble County	60.1	13.3	26.6
Burning Star	62.9	11.8	25.3
Frances	65.7	11.2	23.1
Rossington	62.1	15.4	22.5
Upper Hiawatha	57.8	12.3	29.9

T : 800°C

P_{tot}: 365 psia

P_{H_2} : 115 psia

1/4" x 12 mesh clean coal

+ Gas yield is difference of coke and liquid from 100%.

Table 11

Effect of Pressure and Gas Composition on the Coking Yields from Frances Coal

Hydrogen Partial Pressure (psia)	Total Pressure (psia)	Tar Content in Feed (wt %)	Coke Yield (MAF Basis) (wt %)	Liquid Yield (MAF Basis) (wt %)	Gas Yield (MAF Basis) (wt %)
115	365	0	65.6	10.0	24.4
115	365	0	65.7	12.3	22.0
115	365	0	67.0	--	--
115	365	0	67.8	9.5	22.7
115	365	0	67.9	11.3	20.8
0	365	0	67.5	3.7	28.8
0	15	0	65.0	9.8	25.2
0	15	0	65.0	--	--
0	15	0	65.4	--	--

Figure 1

Sample Preparation Scheme

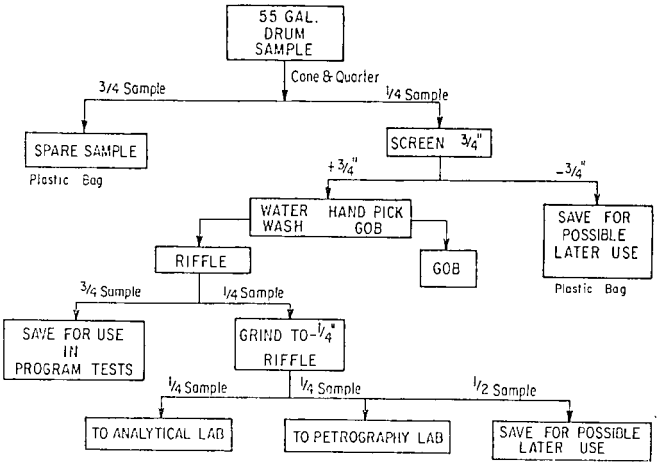

Figure 2

EFFECT OF HEATING RATE ON THE FLUIDITY OF PITTSBURGH NO.8 AND OHIO NO.9 SEAM COALS

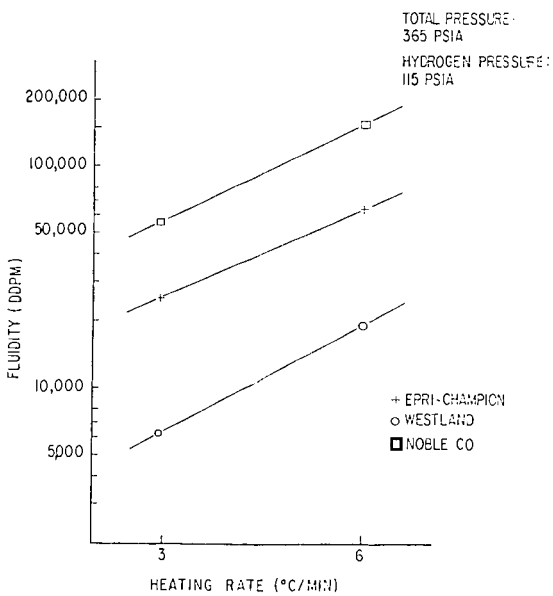

Figure 3
EFFECT OF HEATING RATE ON THE FLUIDITY OF BURNING STAR AND ROSSINGTON COALS

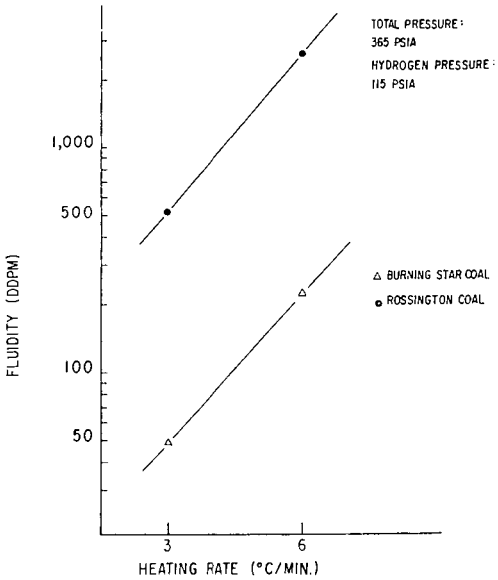

Figure 4
EFFECT OF GAS COMPOSITION ON THE FLUIDITY OF VARIOUS COALS

TOTAL PRESSURE : 350 PSIG
HEATING RATE: 6°C MIN
SAMPLE : 90 WT %- 35 M COAL + 10 WT %- 100 M GOB

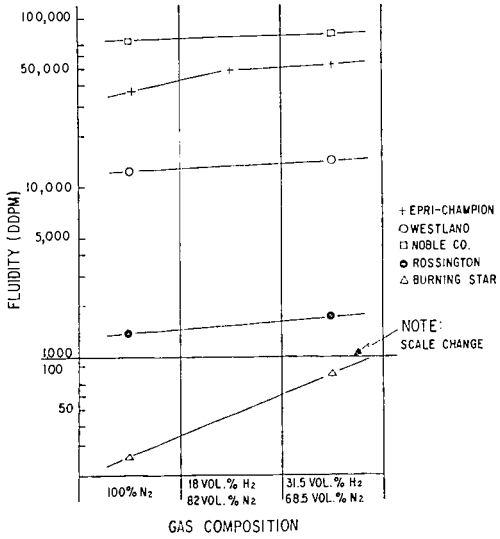

Figure 5
EFFECT OF GOB ADDITION ON THE FLUIDITY OF VARIOUS COALS

TOTAL PRESSURE: 365 PSIA
HYDROGEN PRESSURE: 115 PSIA
HEATING RATE: 6°C/MIN

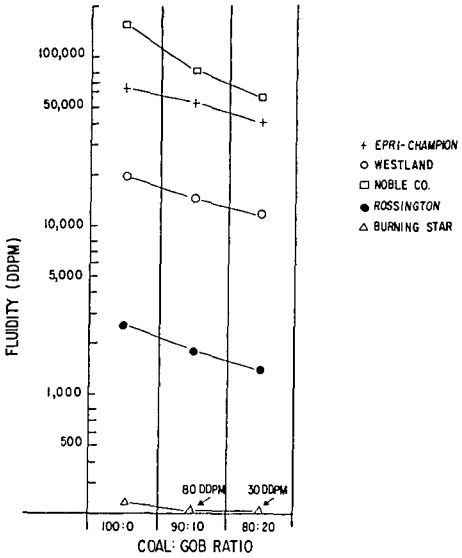

Figure 6
EFFECT OF TAR ADDITION ON THE FLUIDITY OF VARIOUS COALS DOPED WITH 10% GOB.

TOTAL PRESSURE: 365 PSIA
HYDROGEN PRESSURE: 115 PSIA
HEATING RATE: 6° C/MIN

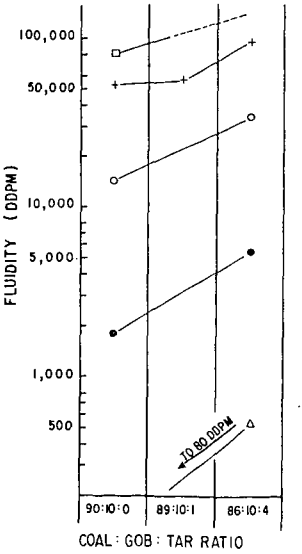

Figure 7

Pressurized Swelling Index Apparatus

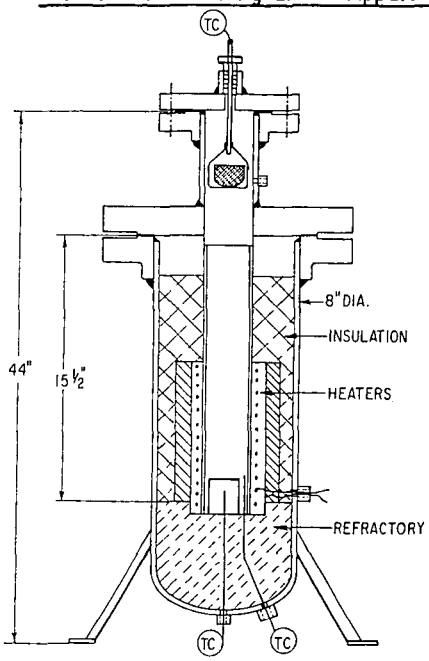

Figure 8

EFFECT OF SAMPLE COMPOSITION ON THE SWELLING OF VARIOUS COALS

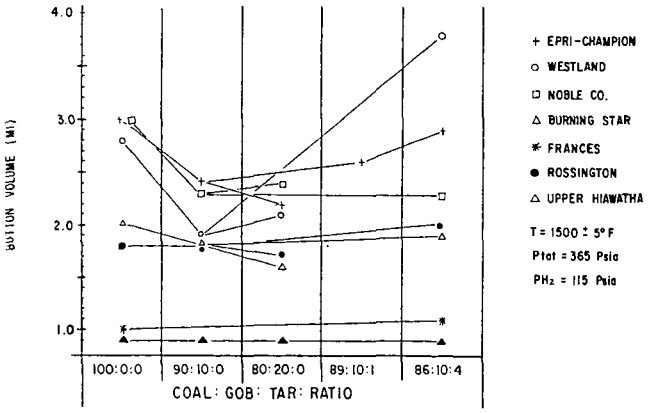

Figure 9

SWELLING PROPERTIES OF PITTSBURGH NO. 8 & ILLINOIS NO. 6 COALS

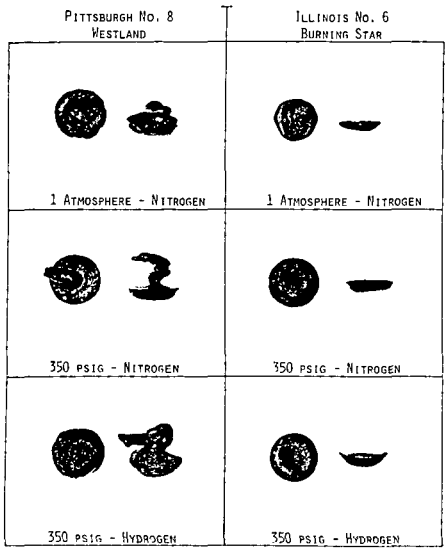

Figure 10

Pressurized Coker

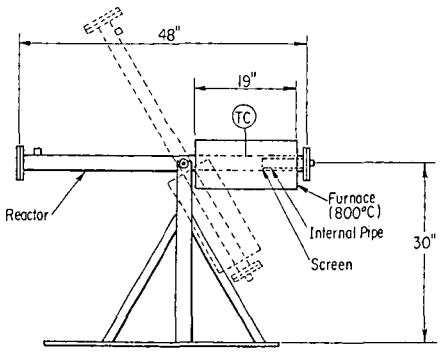

Figure 11
EFFECT OF SAMPLE COMPOSITION, TOTAL PRESSURE AND HYDROGEN PRESSURE ON THE COKE STRENGTH

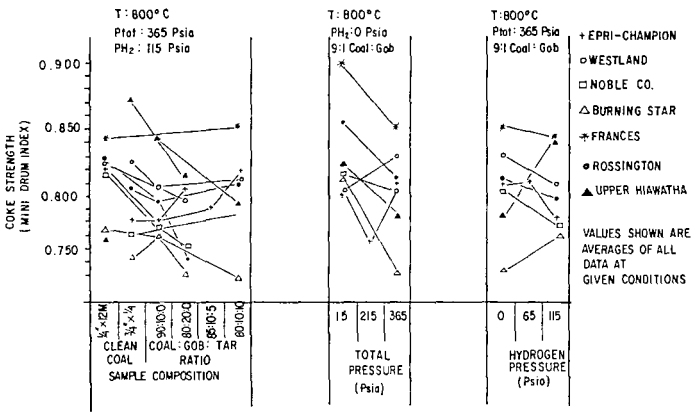

Figure 12
EFFECT OF SAMPLE COMPOSITION, TOTAL PRESSURE AND HYDROGEN PRESSURE ON COKE DENSITY

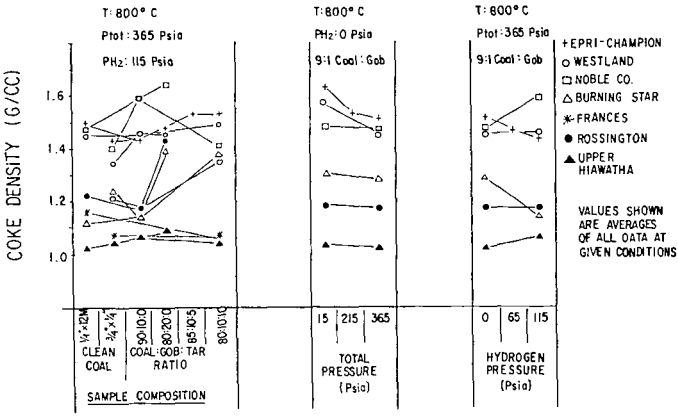

Figure 13

EFFECT OF TOTAL PRESSURE, HYDROGEN PRESSURE AND SAMPLE COMPOSITION ON H_2, CO AND CH_4 CONTENT IN PRODUCT GAS

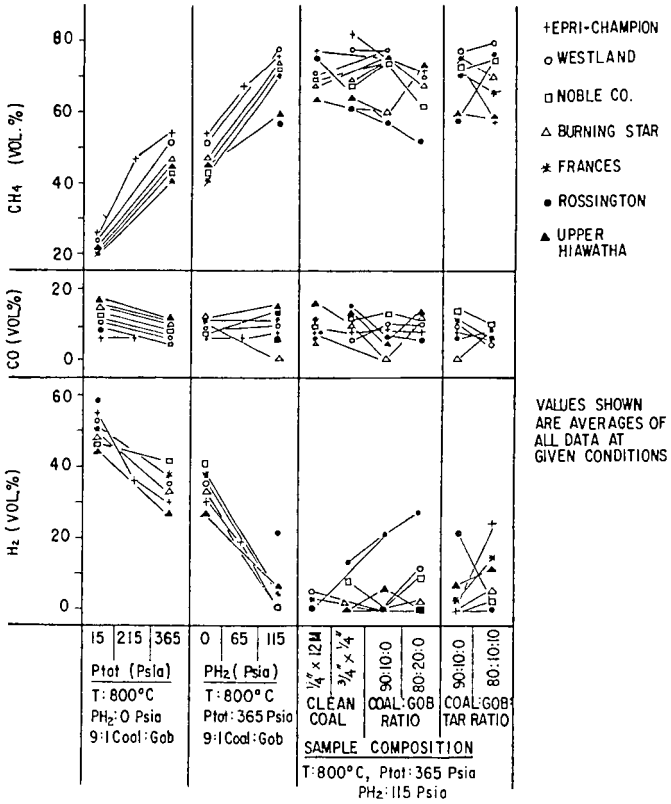

EFFECTS OF PREOXIDATION ON PYROLYSIS BEHAVIOR AND RESULTANT CHAR STRUCTURE OF CAKING COALS

D. J. Maloney and R. G. Jenkins

The Fuels and Combustion Laboratory
The Pennsylvania State University, University Park, PA 16802

INTRODUCTION

Coal gasification processes may be divided into two stages. They are, the initial rapid release of volatile matter and the relatively slow gasification of the residual char. These two processes are not, however, totally independent because the heat treatment conditions under which coal pyrolysis occurs determine, to a large extent, the structure and reactivity of the remaining char (1). The importance of understanding devolatilization kinetics has long been recognized (2-6). However, it is surprising to note that very little information is available in the literature regarding the structure and reactivity of the chars produced in these studies.

The work described here is concerned with the utilization of bituminous (caking) coals in dilute phase, rapid heating gasification and combustion systems. Two highly caking coals were pyrolyzed in an entrained flow tube furnace system and devolatilization kinetics determined for each coal at temperatures of 900 and 1000°C. Structural properties of the chars collected in this work were then analyzed. In addition, the effects of mild preoxidation of these coals upon their subsequent pyrolysis behavior were examined. Samples of each coal were oxidized to various levels prior to heat treatment. Devolatilization kinetics and structural properties of the chars produced were then analyzed. Results reported here follow the development of char structure with varying heat treatment conditions and examine changes in char morphology which occur on preoxidation of these coals. This work is of practical importance in future design considerations for dilute phase gasifiers and of particular interest in gasification schemes where agglomeration of caking coals can cause serious problems.

EXPERIMENTAL

Pyrolysis experiments were conducted in an entrained flow tube furnace somewhat similar to that described by Scaroni et al. (7,8) and Nsakala and coworkers (9). Briefly, a dilute-phase coal stream is entrained in a primary carrier gas, passed through a water cooled probe and then injected into the center of a preheated secondary gas stream. The secondary gas stream enters the reaction zone at a temperature slightly above the furnace wall temperature so that upon mixing the combined gas stream attains the desired reaction temperature (± 10°C). The primary modes of coal particle heating are conduction from the gas and radiation from the furnace walls. Heating rates in excess of 10,000°C/s are estimated. Coal particles travel in a pencil stream down the axis of the furnace tube. Samples are collected and rapidly quenched (> 10,000°C/s quench rate) using a water cooled probe which is inserted up the axis of the furnace. Reaction times are varied by changing the position of the sampling probe relative to the injector. The operating conditions at each temperature studied are given in Table 1. Helium is used as the primary carrier gas and is adjusted to maintain isokinetic sample injection. The secondary gas is nitrogen.

Weight loss due to pyrolysis was determined using ash as a tracer. The proximate analyses of the samples used in this work are presented in Table 2. The coals examined were PSOC-1133 a LV coal from the Lower Kittaning seam in Pennsylvania

TABLE 1. OPERATING CONDITIONS

Operating Temperature °C	900	1000
Coal Feed Rate g/min	0.5	0.5
Mean Gas Velocity cm/s	97	105
Secondary N_2/Primary He (Mole Basis)	26.4	24.2

TABLE 2. PROXIMATE ANALYSES OF SAMPLES (200x270 mesh fractions)

Sample	Moisture, %	Ash, %	Volatile Matter, %	Fixed Carbon, %
PSOC-1099 (Raw Coal)	1.6	9.0	33.7	56.7
PSOC-1099 (1% O_2 added)	0.9	12.6	32.5	64.0
PSOC-1133 (Raw Coal)	0.4	16.4	18.5	64.7
PSOC-1133 (o.5% O_2 added)	1.1	19.3	17.6	62.0
PSOC-1133 (1% O_2 added)	1.1	19.5	18.2	62.2

and PSOC-1099 a HVA coal from the Pittsburgh seam in Pennsylvania. All work was conducted on 200x270 mesh size fractions with mean particle diameter of 63 μm.

Preoxidized samples were prepared in a fluidized bed furnace. Samples of sized coal (200x270 mesh) were fluidized in nitrogen and brought to reaction temperature (175°C). The fluidizing gas was then switched to air and the samples were oxidized for various predetermined times. Oxidation times were determined based upon thermogravimetric studies of the air oxidation of each coal. It is assumed that oxidation rates in the thermobalance and fluidized bed systems are equivalent. This assumption is valid if one insures that the O_2 partial pressure in each system is the same and that there are no bed diffusion effects in the thermobalance system. Operating conditions were selected to meet these requirements. Oxidation levels reported here are given as % weight gain on oxidation (dry coal basis).

RESULTS AND DISCUSSION

Typical weight loss versus time curves for devolatilization of PSOC-1133 (LV coal) are presented in Figure 1. This plot shows weight loss is essentially complete within the first 100 msec of residence time. The same behavior was observed for the HVA coal examined in this study. These results are in good agreement with that of Badzioch and Hawksley (10). In similar experimental systems it is often assumed that pyrolysis occurs isothermally (7-10), however, this assumption cannot be made for the coals analyzed here.

Figure 1 also shows the maximum weight loss for devolatilization at 900°C is greater than at 1000°C. Similar observations have been reported by Menster et al. (11,12). These authors suggest a possible explanation for this behavior which involves a competition between bond breaking reactions (which result in volatile formation) and secondary recombination or polymerization (char forming) reactions,

Figures 2 and 3 demonstrate the effects of preoxidation on devolatilization behavior. Oxidation appears to have little effect on the rate of pyrolysis, however, devolatilization occurs so rapidly that the time resolution of this system may be inadequate to distinguish such effects. Preoxidation reduces the yield of volatile material in all cases examined. This corresponds with a sharp decrease

in the amount of condensible products (tars) collected.* Increases in the level of oxidation prior to pyrolysis result in a progressive reduction in the yield of volatile material. Devolatilization curves for preoxidized coals all have the same characteristic shape. Weight loss passes through a shallow minimum with residence time. Further study of this behavior is in progress.

Figure 4 shows an electron micrograph of PSOC-1133 char collected after 330 msec residence time at 1000°C. Coal structure has undergone extensive physical changes during the pyrolysis process. These chars are thin walled transparent structures commonly called cenospheres (13), the average diameter of which is three times that of the starting coal. This represents a > 20 fold increase in volume. Similar results are obtained at 900°C and for PSOC-1099 at each temperature studied. Under the pyrolysis conditions employed in this work cenospheres are fully developed during the early stages of pyrolysis (< 40 msec) after which no detectable changes in macroscopic properties are observed.

Figure 5 is a micrograph of a preoxidized coal char (PSOC-1133, 1% oxygen added) collected after 330 msec residence time at 1000°C. These chars do not form the cenosphere structures exhibited by the unoxidized coals. Char particles are rounded in shape indicating that the coal passes through a plastic transition during carbonization but no significant swelling is observed.

SUMMARY

The sharp contrast in macroscopic properties of the chars collected in this study give rise to several important questions regarding char gasification. Varying heat treatment conditions and coal feed stocks give rise to chars of widely varying structure. In order to understand the behavior of these materials in subsequent gasification steps a more detailed analysis of char structure is required. At present microstructural properties (surface areas, porosities) of the chars generated in this study are being examined in an effort to better understand the relationship between char structure and heat treatment conditions. Results of this work will be available shortly.

ACKNOWLEDGEMENTS

Financial support for this work was provided by the Cooperative Program in Coal Research at The Pennsylvania State University. Coal samples were obtained from the Penn State/DOE coal sample bank.

*Tar yields were not measured quantitatively in this work, however, the differences in the amounts of condensible materials collected in the filtering systems were substantial enough to warrant the above comment.

REFERENCES

1. Mahajan, O. P. and Walker, P. L., Jr., "Analytical Methods for Coal and Coal Products," Vol. 2, (C. Karr, Editor), Academic Press, New York, 1978, pp. 465-494.

2. Badzioch, S., B.C.U.R.A. Monthly Bull., 25, 285, 1961.

3. Jones, W. Idris, J. Inst. Ful., 37, 3, 1964.

4. Yellow, P. C., B.C.U.R.A. Monthly Bull., 29, 285, 1965.

5. Badzioch, S., Field, M. A., Gill, D. W., Morgan, B. B., and Hawksley, P. G. W., B.C.U.R.A. Monthly Bull., 31, 193, 1967.

6. Anthony, D. B. and Howard, J. B., A.I.Ch.E. Journal, 22, 625, 1976.

7. Scaroni, A. W., Walker, P. L., Jr., and Essenhigh, R. H., ACS Div. Fuel Chem., Preprints, 24, No. 2, 123, Sept. 1979.

8. Scaroni, A. W., Walker, P. L., Jr., and Essenhigh, R. H., Fuel, 60, 71, 1981.

9. Nsakala, N., Essenhigh, R. H., and Walker, P. L., Jr., Comb. Sci. and Tech., 16, 153, 1977.

10. Badzioch, S. and Hawksley, P. G. W., Ind. Eng. Chem. Process Des. Develop., 9, 521, 1970.

11. Menster, M., O'Donnell, H. J., Ergun, S., and Friedel, R. A., "Coal Gasification," Advances in Chemistry Series 131, Am. Chem. Soc., Washington, D. C., 1974.

12. Menster, M., O'Donnell, H. J., and Ergun, S., ACS Div. Fuel Chem., Preprints, 14, No. 5, 94, 1970.

13. Newall, H. E. and Sinnatt, F. S., Fuel, 3, 424, 1924.

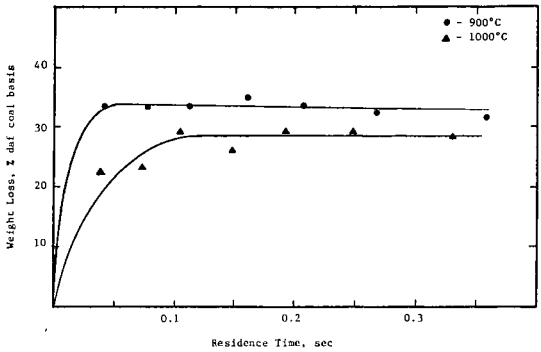

Figure 1. WEIGHT LOSS AS A FUNCTION OF RESIDENCE TIME FOR PSOC-1133

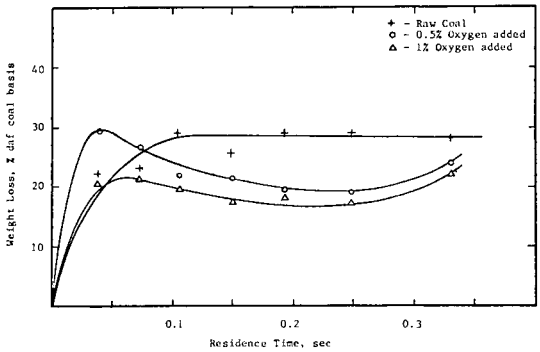

Figure 2. WEIGHT LOSS VERSUS RESIDENCE TIME AS A FUNCTION OF PREOXIDATION LEVEL FOR PSOC-1133

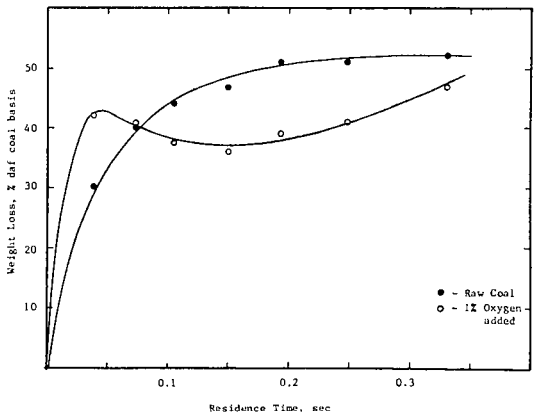

Figure 3. WEIGHT LOSS VERSUS RESIDENCE TIME AS A FUNCTION OF PREOXIDATION LEVEL FOR PSOC-1099

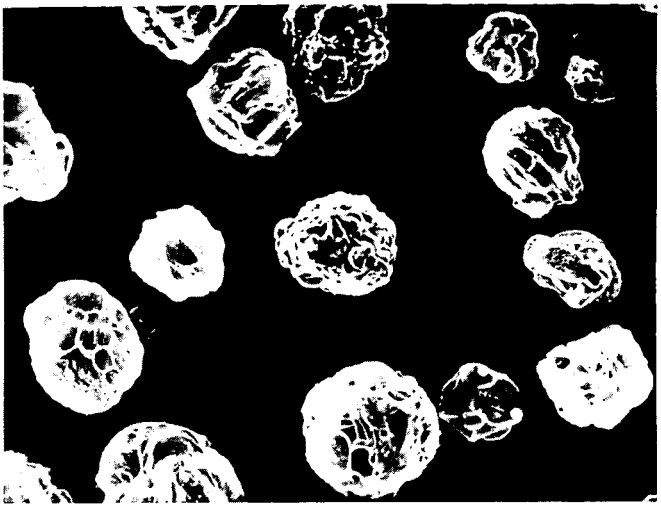

Figure 4. SCANNING ELECTRON MICROGRAPH OF PSOC-1133 CHAR 330 msec Residence Time at 1000°C

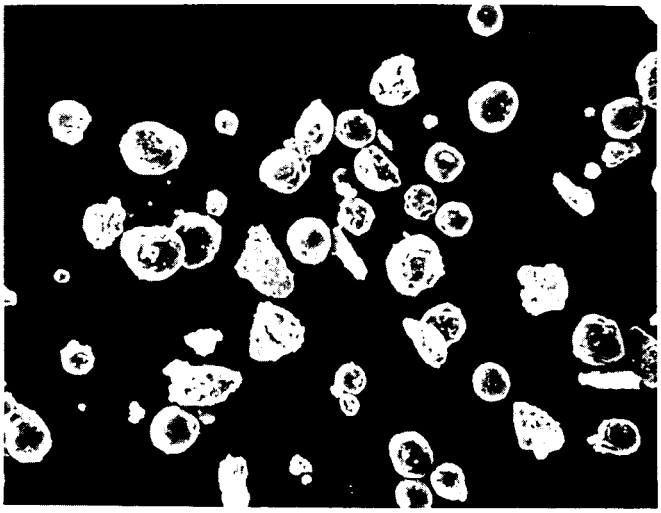

Figure 5. SCANNING ELECTRON MICROGRAPH OF A PREOXIDIZED COAL CHAR (PSOC-1133 1% Oxygen Added) 330 msec Residence Time at 1000°C

INFLUENCE OF PARTICLE STRUCTURE CHANGES ON THE RATE OF COAL CHAR REACTION WITH CO_2

K. A. Debelak, M. A. Clark and J. T. Malito

Department of Chemical Engineering
Vanderbilt University
Nashville, TN 37235

Introduction

A common feature of gas-solid reactions is that the overall process involves several steps: (1) mass transfer of reactants and products from bulk gas phase to the internal surface of the reacting solid particle; (2) diffusion of gaseous reactants or products through the pores of a solid reactant; (3) adsorption of gaseous reactants on solid reactant sites and desorption of reaction products from solid surfaces; (4) the actual chemical reaction between the adsorbed gas and solid.

In studying gas-solid reactants, we are concerned with these four phenomena and other phenomena which affect the overall rate of reaction and performance of industrial equipment in which these gas-solid reactions are carried out. These other phenomena include: heat transfer, flow of gases and solids through reactors, and changes in the solid structure, all of which affect the rate of diffusion and surface area available for reaction. The reaction to be studied is the reaction between carbon and carbon dioxide to form carbon monoxide. This reaction is of importance for it is one of the prime reactions occurring in coal gasifiers, and also it is a reaction on which there is data from other investigations (1-17). Considerable discrepancy has been found for activation energies which ranges from 48-86 kcal/mol and for reaction rate constants. This can be explained by the somewhat oversimplified view of the mechanism which was thought to be rate-controlling, and the simplification made in the corresponding reaction rate models.

Gulbransen and Andrew (2) showed that the internal surface area of graphite increased during reaction with carbon dioxide and oxygen. Walker et al. (3) studied graphite rods for the possible correlations existing between reaction rates and changes in surface area during reaction. They concluded that the reaction develops new surface, to some extent, by enlarging the micropores of the solid but principally by opening up pore volume not previously available to reactant gas either because the capillaries were too small or because existing pores were unconnected. Surface area increased up to a point where rate of production of new surface equalled the destruction of old surface, after which surface area then continued to decrease. For the graphite-carbon dioxide reaction, Petersen (4) found that observed rates were not simple functions of the total available surface area as determined by low-temperature adsorptions prior to reaction, as might be expected if the reaction was chemical-reaction controlled.

Turkgodan et al. (18) studied the pore characteristics of several carbons, graphite, coke and charcoal. They concluded that about 1/2 of the volume is located in micropores and therefore not available for reaction. Most of the internal surface area was located in pores in the micropore range. The pore volume, pore surface area, and effective diffusivity increased with conversion during internal oxidation.

Dutta and Wen (16, 17) studied the reactivities of several raw coals and chars. They noted a change in the actual pore structures of a few samples at different conversions from scanning electron micrographs. A rate equation was proposed that incorporated the change of the relative available surface area during reaction. No measurements of this change were made. A rate expression, which includes the influence of a chemical and diffusion reaction controlling mechanisms, is expressed

$$\frac{dX_c}{dt} = \eta\, S\, k\, C_{CO_2} (1-X_c) \qquad 1)$$

where:

X_c is the conversion of the solid
S is the surface area available for reaction
k is the reaction rate constant
η is the effectiveness factor
C_{CO_2} is the concentration of CO_2 in gas phase
t is time

The effectiveness factor η is equal to the ratio of the reaction rate under diffusion-controlled conditions to that which would occur if the concentration of reactants were equal to the surface concentration. For a first order diffusion-controlled reaction the influence of pore-diffusion is given by equation 2)

$$\eta = \frac{1}{\phi}\left[\frac{1}{\tanh 3\phi} - \frac{1}{3\phi}\right] \qquad 2)$$

$$\phi = \frac{1}{3}\, r_c \left(S\, k/D_e\right)^{1/2} \qquad 3)$$

where:

S is the specific surface
k is the reaction rate constant
r_c is the radius of the particle
D_e is the effective diffusivity

The effectiveness factor η is a function of the effective modulus, ϕ, which is dependent upon the effective diffusivity, D_e. The effective diffusivity and the surface area available for reaction change during the reaction.

This may be expressed as

$$S = S_o f(X_c) \quad 4)$$

$$D_e = D_{e_o} h(X_c) \quad 5)$$

where S_o and D_{e_o} are the available surface area and effective diffusivity at zero conversion, and $f(X_c)$ and $h(X_c)$ are functions of conversion, X_c. The determination of these changing parameters and their influence on the overall reaction rate is the objective of this research.

Effective Diffusivity

I. Theoretical Development of Model

Experimental determination of the effective diffusivity in coal is performed in a packed bed of coal particles with a carrier gas flowing through the bed. A pulse in the concentration of the adsorbate gas is introduced at the inlet of the packed bed. The mass transfer characteristics of the bed change the shape of the pulse as it passes through the bed. A theoretical model describing the mass transfer in the bed is used to relate the unsteady state concentration response in the bed effluent to the original pulse input. By applying the model to the experimental data, the parameters of the model are determined. The model describing the mass transfer in the packed bed consists of unsteady state material balances in the packed bed and the coal particles. Equations (6-14) describe the mass transfer in the packed bed of particles and the boundary conditions.

Material balance on coal particle

$$D_c \frac{\partial^2 q}{\partial r^2} + \frac{2}{r}\frac{\partial q}{\partial r} = \frac{\partial q}{\partial t} \quad 6)$$

Relation between adsorbed concentration and concentration of surface

$$q(r_c, t) = K_c C(r_c, t) \quad 7)$$

Boundary conditions

$$\frac{\partial q}{\partial r}(0, t) = 0 \quad 8)$$

$$\frac{3k}{r_c}\left[C(z, t) - C(r_c, t)\right] = \frac{\partial q}{\partial t} \quad 9)$$

$$\bar{q} = \frac{3}{r_c^3}\int_0^{r_c} r^2 q\,dr \quad 10)$$

Material balance on packed bed

$$\frac{D_L \partial^2 C}{\partial z^2} - v \frac{\partial C}{\partial z} - \frac{1 - \varepsilon}{\varepsilon} \frac{\partial \bar{q}}{\partial t} = \frac{\partial C}{\partial t} \qquad 11)$$

Boundary conditions

$$C(z, 0) = C(r_c, 0) = q(r_c, 0) = 0 \qquad 12)$$

$$C(0, t) = C_o \, \delta(t) \qquad 13)$$

$$C(\infty, t) = 0 \qquad 14)$$

II. Solution of the Model

Three alternative techniques for solution and subsequent parameter estimation from the model are curve fitting in the time domain, curve fitting in the Laplace or Fourier domain, and the method of moments. Moments of the response curve resulting from a pulse input can be solved analytically for the solution to the model in the Laplace domain. Parameter estimation is achieved by matching the measured moments with the analytical expression for the moments. The method of moments was used in this work because it does not require a numerical solution to the model and because parameters estimation can be performed in the time domain. The Laplace transform is applied to the time variable in the equations and boundary conditions of the model. A system of coupled ordinary differential equations is obtained after applying this transform. A theorem relating the transformed solution to the absolute and central moments of time domain solution is

$$M_n = (-1)^n \lim_{s \to o} \frac{d^n}{ds^n} \bar{C}(s, z) \qquad 15)$$

The nth absolute moment is defined as:

$$\mu_1' = \frac{M_n}{M_o} \qquad 16)$$

$$M_n = \int_0^\infty t^n C(z, t) e^{-st} \, dt \qquad 17)$$

The nth central moment is defined by:

$$\mu_n = \frac{1}{M_o} \int_0^\infty (t - \mu_1')^n C(z, t) \, dt, \qquad 18)$$

Applying equation 15) to the transformed solution of the model results in the following equations for the first absolute and second central moments:

$$\mu_1' = \frac{L}{v}\left[1 + \frac{(1-\varepsilon)}{\varepsilon} K_p\right] \qquad 19)$$

$$\mu_2 = \left[\frac{2D_L L}{v^3} + \frac{2L}{v}\,\frac{\varepsilon}{(1-\varepsilon)}\left(\frac{r_c}{3k}\,\frac{r_c^2}{15D_c K_p}\right)\right]\left[1 + K_p\,\frac{(1-\varepsilon)}{\varepsilon}\right] \qquad 20)$$

These two equations relate the model parameters to the moments which can be calculated from experimental data.

Experimental

WYODAK subbituminous coal, particle size 35 x 60, was used in the experimental study. The experimental system consisted of a pulse reactor, Figure 1, a flow type BET apparatus, Figure 2, and the chromatographic apparatus, Figure 3. This allowed determinations of surface area and effective diffusivity to be made in conjunction with reaction studies without removing the sample.

Measurements of surface area and effective diffusivity were made on raw coals. Surface area measurements were made by adsorbing carbon dioxide at 195 K for 30 minutes. The single point BET method was used for evaluation of the surface area. The raw coals were devolatilized by heating at $5^{o}C$/min to a temperature of $800^{o}C$ to produce a coal char. Changes in surface area and effective diffusivity were again determined. The coal char was then partially reacted at a temperature of $800^{o}C$ by injecting a known volume of carbon dioxide. Changes in surface area and effective diffusivity were again determined. This procedure was repeated until the conversion of the carbon in the coal approached 1.0.

Results and Discussion

The devolatilization caused structural changes which are reflected in an average weight loss of 41% of the initial weight, a decrease in the diffusion coefficient, and an increase in total surface area. Table 1 gives these changes for three WYODAK samples. The increase in surface area represents the opening of pores which were not accessible before devolatilization. Walls closing off pores are devolatilized and small pores inaccessible to the initial CO_2 adsorption are enlarged because of the evolution of volatile material during the heating. This new pore structure has a greater resistance to diffusion, seen as a decrease in the diffusion coefficient. The small pores and enlarged pore form a more complex network of voids within the particles. The production of char by devolatilization causes an increase in total available surface area and a decrease in the diffusion coefficient.

The heterogeneous chemical reaction causes continuous changes in the pore structure due to the consumption of carbon. Pore walls are being gasified slowly as the reaction continues toward completion. The continually changing internal structure affects the diffusion of gaseous reactants and products to and from the active carbon sites within the particle.

These phenomena may be described by examining Figure 4 which is a plot of the diffusion coefficient data for the three WYODAK samples measured at various carbon conversions. The diffusion coefficient increases slowly at low conversion and is somewhat stable during the mid-range of conversion, but increases very quickly as the reaction nears completion. Overall the diffusion coefficient increases as carbon conversion inreases. These data can be correlated by

$$\frac{D_c}{r_c^2} = (0.06) \exp (1.7 \cdot X_c) \qquad 21)$$

which gave an index of determination of 0.88. Physically, the pore structure after devolatilization consists of a small amount of void, characteristic of the low diffusion coefficient which means that the resistance to diffusion is substantial. During reaction these pores gradually enlarge due to gasification of the carbon. Therefore as conversion increases the pore volume or void increases resulting in less resistance to diffusion, which is reflected by the increase in the diffusion coefficient.

The CO_2-char reaction occurs at active carbon sites upon the coal char surface. Thus the consumption of the reactant carbon will affect the total surface area. The total surface area decreases for these WYODAK samples as the carbon conversion increases, Figure 5. As conversion goes toward completion, pore walls which are measured as surface area are gasified or consumed by the reaction causing a decrease in total surface area.

Figure 5 shows the specific surface area versus the carbon conversion. The specific surface area first goes through a minimum at low carbon conversions and then a maximum as carbon conversion goes toward completion. Mahajan and Walker (19) predicted the maximum in their qualitative description of the reaction process. Dutta and Wen (16) found that the reaction rate reaches a maximum at a carbon conversion of approximately 0.2 for reactions carried out at low temperatures. In an attempt to correlate this data they assumed a reaction rate model, Equation 1), for the chemical controlled regime. They incorporated into the model a proposed function of conversion which describes changes in surface area.

$$a = 1 \pm 100\, X_c^{\nu\beta} \exp (-\beta X_c) \qquad 22)$$

where a equals the specific surface area divided by the initial specific surface area. Fitting the model to the reaction rate versus conversion data the parameters of the proposed function were estimated by Dutta and Wen (16). This function describing changes in specific surface area exhibits a maximum at approximately the same conversion as our data. At low temperatures where reaction rate is predominantly chemically controlled, the maximum in the reaction rate vs. conversion data can be

explained by the fact that the specific surface for chemical reaction also goes through a maximum and this behavior of the specific area has been experimentally confirmed. The problem with equation 22) is that it predicts either a maximum or minimum for the value of a, but not both. In a recent paper Bhatia and Perlmuter (20), using a random pore model, have derived an expression for surface area as a function of conversion

$$a = \frac{1 - X}{\left(1 - \frac{r_c}{kCt}\right)^3} \sqrt{1 - \frac{4\pi L_o (1-\varepsilon_o)}{s_o^2} \ln \frac{1 - X}{\left(1 - \frac{r_c}{kCt}\right)^3}} \qquad 23)$$

where L_o, S_o and ε_o are the initial total pore length, surface area to volume ratio, and porosity respectively. This equation correlates our data predicting both a minimum and maximum in values of specific surface area, Figure 6.

Acknowledgements

This work was supported by a National Science Foundation Research Institution Grant, Eng. 7907988.

References

(1) Gadsby, J., Long, F. J., Sleighthom, P., and Sykes, K. W., "The Mechanism of the Carbon Dioxide Reaction," Proc. Roy. Soc. London, Ser. A, 193, 377 (1948).

(2) Gulbransen, E. A., and Andrew, K. F., "Reaction of Carbon Dioxide with Pure Artificial Graphite at Temperatures of 500°C," Ind. Eng. Chem., 44, 1039 (1952).

(3) Walker, P. L., Foresti, R. J. and Wright, C. C., "Surface Area Studies of Carbon-Carbon Dioxide Reaction," Ind. Eng. Chem., 45, 8, 1703 (1953).

(4) Petersen, E. E., Walker, P. L. and Wright, C. C., "Surface Area Development Within Artificial Graphite Rods Reacted with Carbon Dioxide from 900°C to 1300°C," Ind. Eng. Chem., 47, 1629 (1955).

(5) Wicke, E., "Fifth Symposium on Combustion," p. 245, Reinhold, New York, New York (1955).

(6) Rossberg, V. M., and Wicke, E., "Transportvogage and Oberflachem-reaktionen bei der Verbrennung Graphitischen Kohlenstoff," Chem. Ing. Tech., 28, 191 (1956).

(7) Ergun, S., "Kinetics of the Reaction of Carbon Dioxide with Carbon," J. Phys. Chem., 60, 480 (1956).

(8) Walker, P. L., Rusinko, F., and Austin, L. G., "Gas Reactions Carbon," Advances in Catalysis, Vol. XI, 133-221 (1959).

(9) Austin, L. G. and Walker, P. L., "Effect of Carbon Monoxide in Causing Nonuniform Gasification of Graphite by Carbon Dioxide," AIChE Journal, 9, 303 (1963).

(10) Turkdogan, E. T., Kaoump, V., Vinters, J. V., "Rate of Oxidation of Graphite in Carbon Dioxide," Carbon, 6, 467 (1968).

(11) Turkdogan, E. T., Vinters, J. V., "Kinetics of Oxidation of Graphite and Charcoal in CO_2," Carbon, 7, 101 (1969).

(12) Yoshida, K., and Kinii, D., "Gasification of Porous Carbon by Carbon Dioxides," J. Chem. Engr., Japan, 2, 170 (1969).

(13) Wen, C. Y., and Wy, N. T., "An Analysis of Slow Reactions in a Porous Particle," AIChE Journal, 20, 5, 833-840 (1974).

(14) Walker, P. L, and Hippo, E., "Reactivity of Heat-Treated Coals in Carbon Dioxide at 900°C," Fuel, 54, 245 (1975).

(15) Fuchs, W., Yavarsky, P. M., "Am. Chem. Soc., Div. Fuel Chem.," 20 (3), 115, (1975).

(16) Dutta, S., Wen, C. Y., "Reactivity of Coal and Char. 2. In Oxygen-Nitrogen Atmosphere," Ind. Eng. Chem., Process Des. Dev., 16, No. 1, 20 (1977).

(17) Dutta, S., Wen, C. Y., "Reactivity of Coal and Char. 2. In Oxygen-Nitrogen Atmosphere," Ind. Eng. Chem., Process Des. Dev., 16, No. 1, 31 (1977).

(18) Turkdogan, E. T., Olsson, R. G., and Vinters, J. V., "Pore Characteristics of Carbon," Carbon, 8, 545-564 (1970).

(19) Mahajan, A. P., Yarzab, R., and Walker, P. L., Jr., "Unification of Coal-Char Gasification Reaction Mechanisms," Fuel, Vol. 57, pp. 643-646, October 1978.

(20) Bhatia, S. K. and Perlmutter, D. D., "A Random Pore Model for Fluid Solid Reactions: I. Isothernal, Kinetic Control", AIChE J., 26, No. 3, 379-385 (1980).

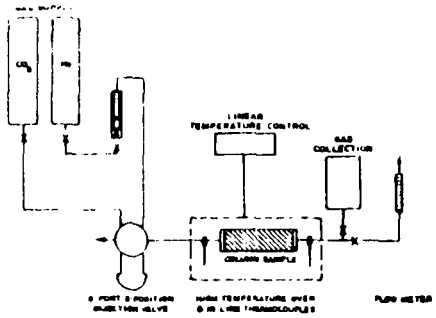

Figure 1 Schematic Diagram of the Apparatus for Reaction of Coal and CO_2 at High Temperatures

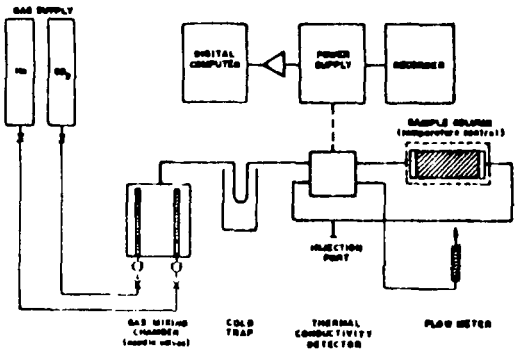

Figure 2 Schematic Diagram of the Experimental Apparatus for Determination of B.E.T. Surface Area

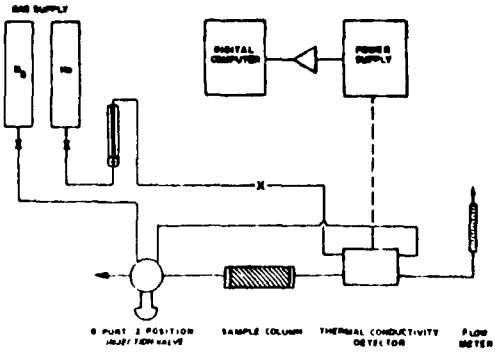

Figure 3 Schematic Diagram of Experimental Apparatus for Determination of Effective Diffusivity

TABLE 1

EFFECTS OF DEVOLATILIZATION

WYODAK	Weight (g) (coal)/(char)	Total Surface (m^2) (coal)/(char)	Specific Surface Area (m^2/g) (coal)/(char)	Diff. Co. (s^{-1}) (coal)/(char)
Sample 1	1.0094/0.6172	80.9/128.0	80.15/207.4	0.216/0.0630
Sample 2	0.9719/0.5712	70.9/104.5	72.9/182.9	1.150/0.0644
Sample 3	1.0169/0.5930	74.7/102.8	71.6/173.0	1.476/0.0719

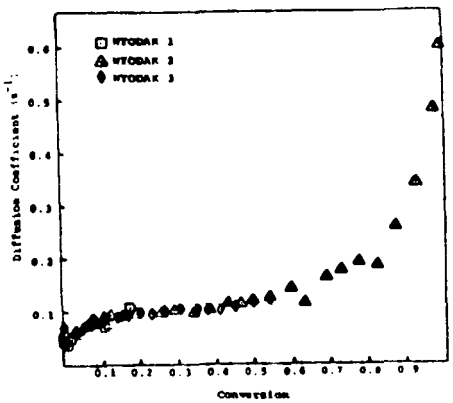

Figure 4 Diffusion Coefficient versus Conversion

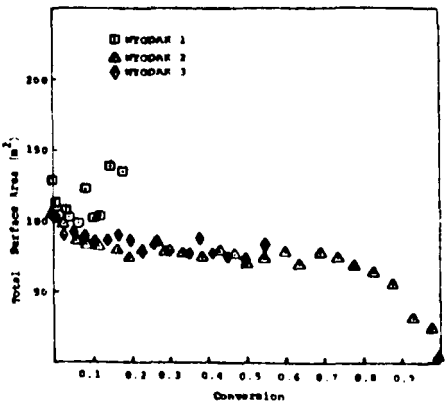

Figure 5 Total Surface Area Versus Conversion

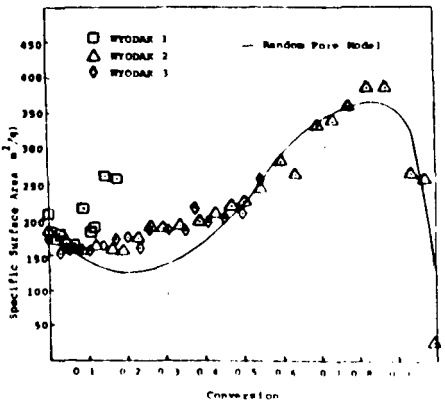

Figure 6 Comparison Between Experimental Specific Surface Area and Prediction of Random Pore Model

AN ENTRAINED FLOW REACTOR WITH IN SITU FTIR ANALYSIS*

Peter R. Solomon and David G. Hamblen

Advanced Fuel Research, Inc. 87 Church St., East Hartford, CT 06108

INTRODUCTION

A key element in predicting coal gasification behavior is pyrolysis. This is the initial step in gasification, the step which controls the amount and physical structure of the char and the step which is most dependent on the properties of the coal. Recent reviews of coal pyrolysis (1,2,3) conclude that the pyrolysis product distribution and apparent kinetic rates vary widely with the experimental measurement. It is clear that to establish a true predictive capability additional work is needed to understand pyrolysis reactions and define usable rates.

Among the experiments which have been useful in investigating pyrolysis have been the captive sample heated grid devices which have achieved good mass and elemental balances and have provided data on individual species evolution (4-16). However, the heating of the coal is slower than in practical devices so that the kinetic data is of limited value.

Entrained flow reactors which provide more realistic particle heating have been employed to study pyrolysis weight loss but have not provided much species evolution data (17-23). New visual data on pyrolysis behavior have been obtained in reactors with optical access (24, 25). These reactors employ flat flame burners into which coal may be injected.

This paper reports on a new apparatus which has been designed to combine the advantages of the reactors described above. The new reactor: 1) injects coal into a preheated gas stream in a hot furnace to provide rapid particle heating, 2) provides for optical access, 3) employs an FTIR for species concentration measurements, both in-situ and in an external cell and 4) has provisions for obtaining mass balances. The reactor will be used in a program to study pyrolysis and secondary reactions of interest in gasification. The results will be used to test the conclusions of a previously developed pyrolysis model (11-15, 26-29) and fill in needed kinetic data. The paper describes the reactor, reports preliminary results obtained with four coals at furnace temperatures from 700°C to 1200°C and assesses how these results compare to data obtained in other experiments.

EXPERIMENTAL

The reactor has been designed to study coal behavior under conditions of temperature and heating rate encountered in an entrained flow gasifier. The schematic of the experiment is presented in Fig. 1. A gas stream of predetermined composition is heated during transit through a bed of alumina chips maintained at furnace temperature. (Prior to heating, the gas composition can be analyzed by routing the stream through an infrared cell). The gas stream then enters a test section, maintained at the furnace temperature, where coal is introduced through a water cooled injector. The coal is fed using a modification of a MIT entrainment system (30). In the modified system, the feeder tube, which extends up through the coal bed, is slowly lowered as the entrainment gas (injected above the bed) exits through the tube. When the tube feeder entrance is at the level of the bed, coal is entrained in the gas and enters the tube. The rate for coal feeding is controlled by the rate at which the tube is lowered.

* This program was initiated under EPRI contract #RP 1654-8. The program scope is currently being expanded under contract #DE AC01-81FE05122 from the US Department of Energy.

After a variable residence time, the reacting stream passes optical access ports and immediately downstream is quenched in a water cooled collector. There are five optical access ports, two of which are presently employed for the FTIR beam. The other three ports are available for additional diagnostics. The quenched stream of char, tar and gases enters a cyclone designed to separate particles larger than 4 microns (31) and then enters a series of filters to remove and sample the tar and soot. The clean gas stream then enters the room temperature FTIR cell which provides a longer path length for higher sensitivity analysis. The particle residence time can be varied from 0 to 700 msec and the furnace has been designed to operate up to 1650°C.

The FTIR can quantitatively determine many gas species observed in coal pyrolysis including CO, CO_2, H_2O, CH_4, C_2H_2, C_2H_4, C_2H_6, C_3H_6, C_3H_8, C_4H_8, C_6H_6, NH_3, HCN, SO_2, COS, CS_2 and heavy paraffins and olefins. The instrument can take spectra every 80 msec to follow rapid changes in the reactor or co-add spectra for long periods of steady state flow to increase signal to noise. FTIR is well suited to in-situ furnace experiments since the FTIR system operates by coding the infrared source with an amplitude modulation which is unique to each infrared frequency. The detector is sensitive to the modulated radiation so that unmodulated stray radiation is eliminated from the experiment.

In the work described below, experiments were run for the four coals listed in Table I. The coals were sieved to produce a -200, +325 mesh size cut. The coal was fed at 2.4 grams/min. Helium was used for both the preheated gas and the entrainment gas. The preheated gas was fed at rates between 40 and 25 l/min depending on temperature to provide a gas velocity of 1 m/sec within the furnace. The entrainment gas was fed at 1.2 l/min. Infrared spectra were obtained with a Nicolet model 7199 FTIR using a globar source and a mercury-cadmium telluride detector. For obtaining the spectra within the furnace and within the cell, 100 scans at 0.5 wavenumber resolutions were accumulated in 140 seconds and transformed in under 2 minutes.

TABLE I

COALS USED IN THE ENTRAINED FLOW REACTOR STUDY

COAL	TYPE	WT% (DAF)					
		C	H	N	S	O	ASH (Dry)
Savage	Montana Lignite	71.2	4.6	1.1	1.3	21.8	10.6
Jacobs Ranch	Wyom. Subbituminous	74.3	5.2	1.1	.6	18.8	7.8
Illinois #6	Bituminous	73.9	5.1	1.4	4.2	15.4	11.0
Pittsburgh #8	Bituminous	83.5	5.5	1.6	3.3	6.1	9.2

Gas Analysis in the Furnace

Figure 2 shows the in-situ gas analysis. There is an acceptable noise level and no drastic effects from the particle scattering. The analyses are for the coal injector at positions from 5 to 66 cm above the optical port. The species which can easily be seen are CO, CO_2, H_2O, CH_4, C_2H_2, C_2H_4, and heavy paraffins. Additional species could be observed through the use of software signal enhancement techniques which can be used to detect species whose absorption lines are smaller than the noise (32). These techniques consider all of the absorption lines for a species, rather than a single line.

FTIR spectra obtained directly within the hot furnace allows the observation of heavy products such as tar which don't appear in the gas phase at room temperature and provide a means to determine whether reactions occur during the quenching and sampling of the gas stream. The in-situ observation also permits gas temperatures to be measured as described below.

Temperature Measurements by FTIR

It appears possible to use the ratios of lines from a given species to determine gas temperatures in the furnace. As the temperature of a gas changes, the populations in its higher energy levels increases. In terms of its absorption spectrum, this generally means that more absorption lines are visible. The effect is illustrated in Fig. 3 which compares CO spectra at a number of temperatures. The energy is clearly shifted from the central lines toward the wings as the temperature increases. Lines at 2250 and 2000 cm^{-1} which are too small to be observed at room temperature are clearly visible at the higher temperatures. The ratio of these lines to the lines at the center of the distribution can be used to determine temperature.

Gas Analysis in a Cell

Figure 4 shows the gas analysis from the room temperature cell. This cell was filled with the effluent gas stream from the furnace after passing through the cyclone and filter. The cell provides higher sensitivity detection because the path length is about 12 times longer than in the furnace. The spectra compare the pyrolysis gases from Jacobs Ranch coal injected at 66 cm above the optical port at furnace temperatures of 800 and 1200°C. Important differences in the product mix at these two temperatures can be observed. The top pair of spectra show the region between 3500 and 2800 cm^{-1}. At 1200°C there is HCN, C_2H_2 and CH_4. At 800°C there is less methane and little HCN or C_2H_2 but significant amounts of ethane and heavy paraffins (indicated by the broad background). This observation is consistent with the cracking of paraffins to form olefins, acetylene and soot which has been discussed previously (12,14). The region between 2600 and 1900 cm^{-1} shows the CO_2 and CO. The CO_2 increases by 50% but the CO increases by a factor of 3 in going from 800°C to 1200°C. This is consistent with previous observations of low temperature production of CO_2 and high temperature production of CO (11-15). The evolution of CO_2 and CO may be related to the early disappearance of carboxyl groups and the retention of ether lingages observed in the infrared spectra of chars discussed below. The region between 1800 and 1200 cm^{-1} shows water and methane. The region between 1200 and 500 cm^{-1} shows olefins, acetylene, HCN and CO_2. The ethylene and heavier olefins are lower and acetylene is higher at the higher temperature (consistent with cracking of olefins to form acetylene and soot).

A comparison of the pyrolysis gas composition from different coals is presented in Fig. 5. The coals were all injected at 66 cm above the optical window at a furnace temperature of 800°C. The spectra show the kind of variation with rank which has been discussed previously (11-15). The low rank coals, which are high in the oxygen functional groups, produce pyrolysis gases which are high in the oxygen containing species, CO, CO_2 and H_2O. The higher rank coals, which are higher in aliphatic functional groups, yield higher concentrations of hydrocarbons.

Data of the kind illustrated above were collected at several reaction distances at 800°C . Curves of concentration vs reaction distance differed among the species. On a normalized basis, however, these curves were similar for the various coals even though the concentration varied from coal to coal. This result is also in agreement with earlier work (11-15).

Changes in Char Chemistry

The infrared spectra of chars provide a convenient means of monitoring the chemical changes occurring during the pyrolysis process. The changes in functional group concentration can be correlated with the appearance of gas species to determine the sources for the species. FTIR spectra of chars from pyrolyzing Jacobs Ranch Coal at 800°C are shown in Fig. 6. The techniques for preparing, drying and making scattering corrections have been discussed previously (13, 33). The aliphatic groups (peak near 2900 cm^{-1}) and carboxyl groups (shoulder near 1650 cm^{-1}) are observed to decrease with reaction distance. The hydroxyl groups (broad peak between 3500 and 2500 cm-1) also decrease although not as rapidly. As the residence distance (and time) is increased, the char aromatic hydrogen peaks near 800 and 3100 cm^{-1} are observed to increase. The O-C bond concentration (peak near 1200 cm^{-1}) shows little change. These changes in the functional group concentrations during pyrolysis are in agreement with results from earlier experiments (14, 15, 21). The changes in char chemistry will be correlated with evolution of gas species and compared with the pyrolysis model predictions.

Conclusions

Preliminary results have been obtained in a newly constructed Entrained Flow reactor with on-line in-situ analysis by FTIR. These results indicate that:

1. Gas concentration measurements for CO, CO_2, water, methane, acetylene, ethylene and heavy paraffins can be routinely made in a hot furnace with an FTIR.

2. Gas temperature measurements appear feasible using ratios of CO lines.

3. On-line gas analysis in an external gas cell is also extremely effective,

Several observations which have previously been reported for other pyrolysis experiments appear to be supported by the preliminary data. These are:

1. Gas kinetics appear to be relatively insensitive to coal rank.

2. The gas composition varies sytematically with the functional group composition of the coal.

3. There is temperature dependent cracking of paraffins to form olefins and acetylene and olefins to form acetylene.

4. Functional groups in the chars disappear in the following order: First aliphatics, then hydroxyl, and then aromatic hydrogen and ether linkages. The present results show that carboxyl groups also disappear quickly.

ACKNOWLEDGEMENT

The authors would like to thank N. Y. Nsakala, G. J. Goetz, R. W. Seeker and R. C. Flagan for their advice on various details of the reactor and acknowledge the able technical assistance of R. M. Carangelo in running the experiments. The authors also express their appreciation for the encouragement given to this program by J. Yerushalmi, George Quentin and Leonard Naphtali.

REFERENCES

1. Howard, J. B., Fundamentals of Coal Pyrolysis and Hydropyrolysis, in Chemistry of Coal Utilization. Second supplementary volume. Martin A. Elliot, Editor, Wiley, pg. 665 (1981).

2. Howard, J. B., Peters, W. A. and Serio, M. A., Coal Devolatilization Information for Reactor Modeling. EPRI report AP-1803, April, (1981).

3. Anthony, D. B. and Howard, J. B., Am. Inst. Chem. Eng. J. 22, 625 (1976).

4. Anthony, D. B., Howard, J. B., Meissner, H. P. and Hottel, H. G., Rev. Sci. Instrum., 45, Pg. 992 (1974).

5. Anthony, D. B., Howard, J. B., Meissner, H. P. and Hottel, H. G., Fifteenth Symposium (International) on Combustion, p. 1303, The Combustion Institute, Pittsburgh, PA (1975).

6. Suuberg, E. M., Rapid Pyrolysis and Hydropyrolysis of Coal, Ph.D Thesis, MIT (1977).

7. Suuberg, E. M., Peters, W. A. and Howard, J. B., Ind. Eng. Process Des. Dev., 17, #1, p. 37 (1978).

8. Suuberg, E. M., Peters, W. A. and Howard, J. B., Seventeenth Symposium (International) on Combustion, p. 117, The Combustion Institute, Pittsburgh, PA, (1979).

9. Juntgen, H. and van Heek, K. H., Fuel Processing Technology, 2, 26 (1979.

10. Gavalas, G. R. and Oka, M., Fuel 51, 285 (1972).

11. Solomon, P. R. and Colket, M. B., 17th Symposium (International) on Combustion, p. 131, The Combustion Institute, Pittsburgh, PA (1979).

12. Solomon, P. R., ACS Div. Of Fuel Chemistry Preprints, 24, #3, 154 (1979).

13. Solomon, P. R., In Coal Structure, Advances in Chemistry Series, 192, page 95 (1981).

14. Solomon, P. R. and Hamblen, D. G., Understanding Coal Using Thermal Decomposition and Fourier Transform Infrared Spectroscopy, Proceedings of the Conference on the Chemistry and Physics of Coal Utilization, Morgantown, WV, June 2-4 (1980).

15. Solomon, P. R., Hamblen, D. G. and Carangelo, R. M., Coal Pyrolysis, AIChE, Symposium on Coal Pyrolysis (Nov., 1981).

16. Solomon, P. R. and Colket, M. B., Fuel, 57, 749 (1978).

17. Badzioch, S. and Hawksley, P. G. W., Ind. Eng. Chem. Process Des. Dev., 9, 521 (1970).

18. Nsakala, N. Y., Essenhigh, R. H. and Walker, P. L., Jr., Combustion Science Technol., 16, 153 (1977).

19. Kobayashi, H., Devolatilization of Pulverized Coal at High Temperatures, Ph.D. thesis, Dept. of Mechanical Eng., Mass. Institute of Technology, Cambridge, MA (1976).

20. Kobayashi, H., Howard, J. B. and Sarofim, A. F., Sixteenth Symposium (International) on Combustion, The Combustion Institute, Pittsburgh, PA, 411, (1977).

21. Solomon, P. R., Hamblen, D. G., Goetz, G. J. and Nsakala, N. Y., ACS Div. of Fuel Chemistry Preprints, 26, #3 (1981).

22. Ubhayaker, S. K., Stickler, D. B., von Rosenberg, Jr., C. W. and Gannon, R. E., 16th Symposium (International) Combustion, Combustion Inst., Pittsburgh, PA p. 427, (1977).

23. Scaroni, A. W., Walker, Jr., P. L. and Essenhigh, R. H., Fuel, 60 71 (1981)

24. McLean, W. J., Hardesty, D. R. and Pohl, J. H., 18th Symposium (International), on Combustion, The Combustion Institute, Pittsburgh, PA p. 1239 (1981).

25. Samuelson, G. S., Trolinger, J. D., Heap, M. P. and Seeker, W. R., Combust. Flame 38, #3 (1980).

26. Solomon, P. R., Fuel, 60, 3 (1981).

27. Solomon, P. R., Hobbs, R. H., Hamblen, D. G., Chen, W. Y., La Cava, A. and Graff, R. S., Fuel, 60, 342 (1981).

28. Solomon, P. R., Coal Structure and Thermal Decomposition, ACS Symposium Series, (In Press).

29. Solomon, P. R., Characterization of Coal and Coal Thermal Decomposition, Chapter III of EPA Monograph on Coal Combustion, (In Press).

30. Mims, C. A., Neville, M., Quann, R. and Sarofim, A., Laboratory Study of Trace Element Transformation During Coal Combustion, presented at the National 87th AIChE Meeting, Boston, MA, Aug. 19-22 (1979).

31. John, W. and Reischl, G., A Cyclone for Size-Selective Sampling of Ambient Air, Journal of the Air Pollution Control Assoc., 872 (1980).

32. Haaland, D. M., Easterling. R. G., Applied Spectroscopy, 34, #5, 539 (1980)

33. Solomon, P. R. and Carangelo, R. M., FTIR Analysis of Coal: I. Techniques and Determination of Hydroxyl Concentrations, submitted to Fuel (1981).

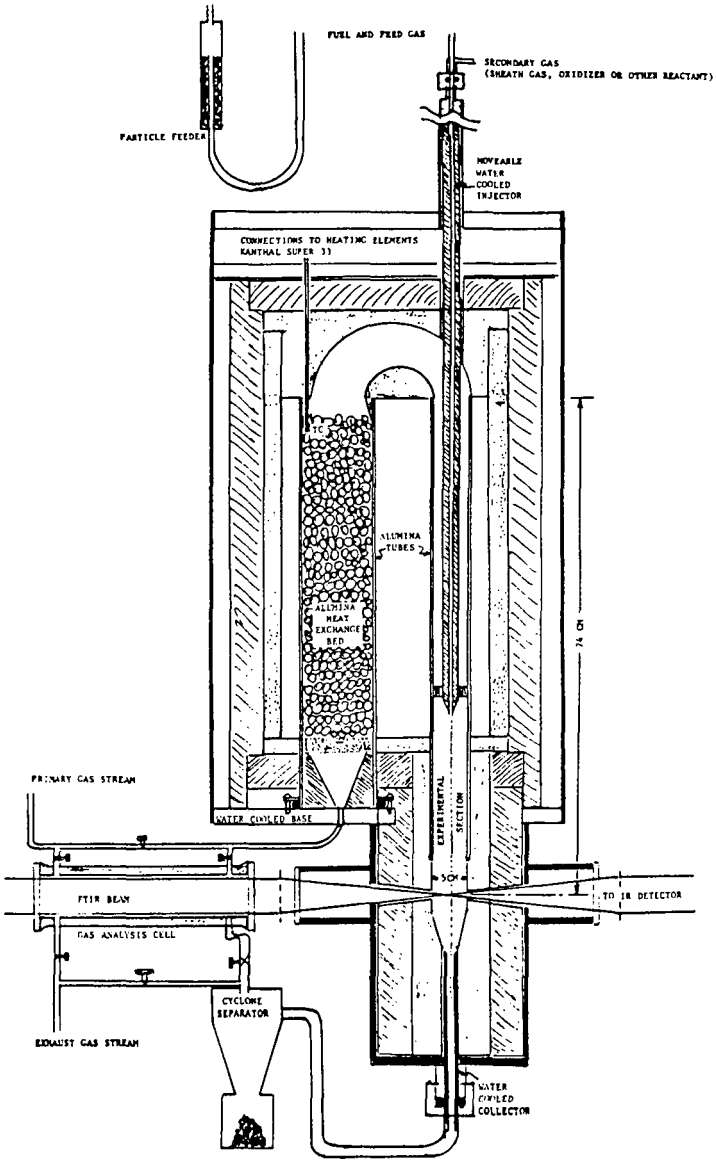

Figure 1. Entrained Flow Reactor.

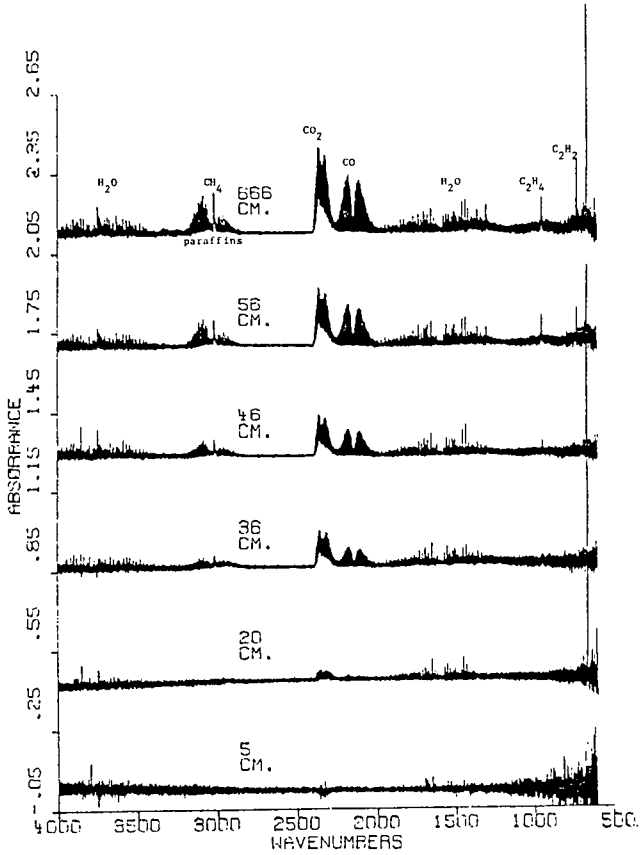

Figure 2. In-Situ FTIR Spectra of Pyrolysis Gases from Jacob's Ranch Coal at 1000°C.

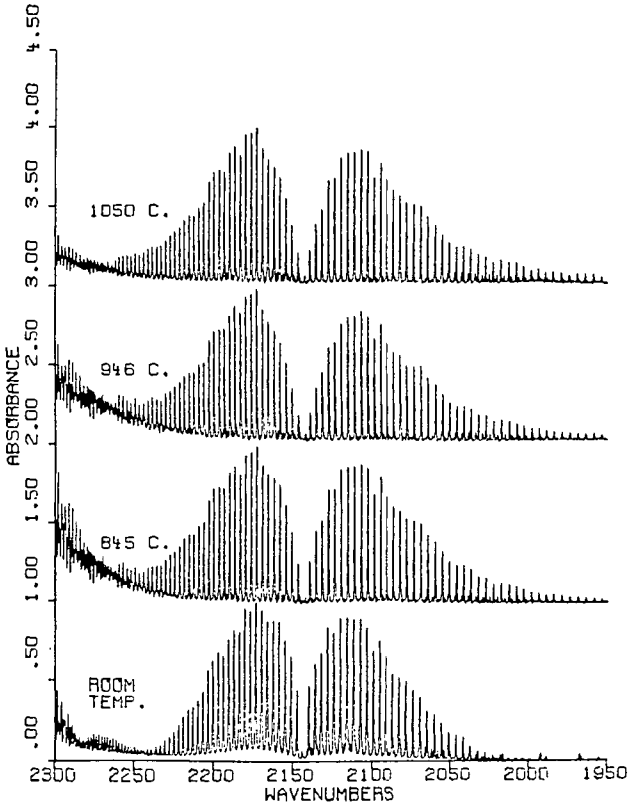

Figure 3. Spectra of CO at Elevated Temperatures.

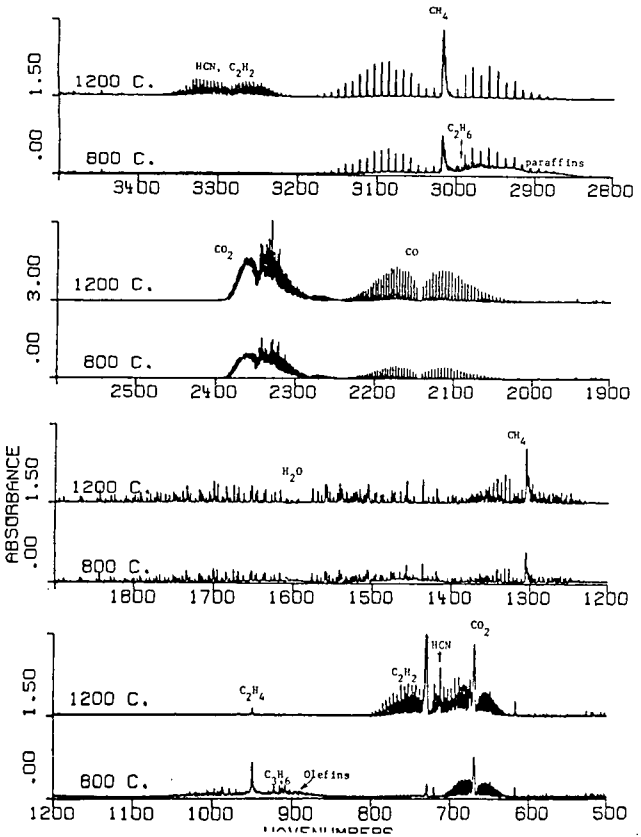

Figure 4. FTIR Spectra of Pyrolysis Gases from Jacob's Ranch Coal at 800°C and 1200°C in Room Temperature Cell. 66cm Residence Distance.

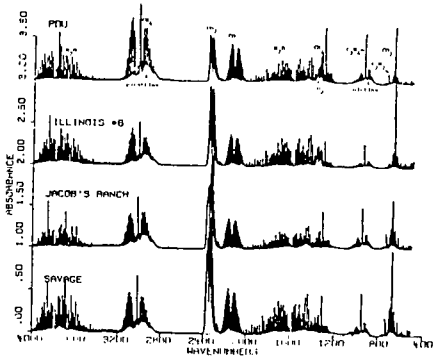

Figure 5. Comparison of FTIR Spectra from 4 Coals Pyrolized at 800°C at 66 cm Residence Distance.

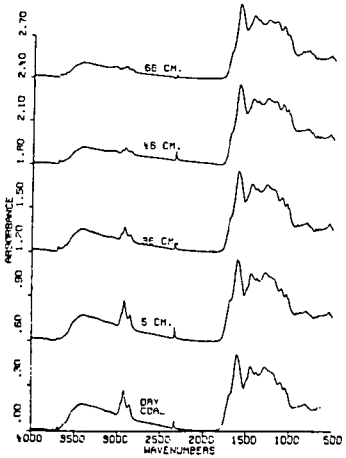

Figure 6. FTIR Spectra of Char from Jacob's Ranch Coal Pyrolized at 800°C.

COAL PYROLYSIS AT HIGH TEMPERATURES AND PRESSURES

S. S. Tamhankar, J. T. Sears and C. Y. Wen

Dept. of Chemical Engineering, West Virginia University, Morgantown, W.Va. 26506

INTRODUCTION

In coal conversion processes, such as combustion or high-temperature gasification, the extent of pyrolysis is an important parameter which is affected by temperature. Increasing amounts of coal converted directly to gaseous species would reduce the remaining material which must be converted by the relatively slow char-gas reactions. Studies on this aspect, particularly at pressure and high temperatures, are scarce.

ASTM standard methods obtain the amount of coal converted to volatile matter at low temperatures, slow heating rates and long exposure times. Other procedures have generally used either direct electric-resistance heating (1, 2) or a laminar-flow furnace (3, 4, 5, 6) to obtain high heating rates and high temperatures.

Menster et al. (1) and Kobayashi et at. (6) have indicated that the maximum temperature affects the extent of pyrolysis, with an apparent plateau or a peak in the weight loss curve at 900-1100°C, followed by an increase in the extent of pyrolysis. Scaroni, et al. (7) suggest that there is no direct heating rate effect on the extent of pyrolysis, but rather the preponderance of secondary char-forming reactions of the primary volatiles may yield an apparent heating rate effect as well as a sample-weight effect. There is evidence that the char formed by rapid heating at high temperatures is very reactive (3, 8). The previous work on pyrolysis at temperatures > 1000°C has been at 1 atm pressure.

To help fill in the data gaps, the present work has therefore been focused on the examination of pyrolysis at high temperatures (800-1600°C), pressures (1-15 atm) and in various reacting and nonreacting gases.

EXPERIMENTAL

A new design of a HPHT (high pressure, high temperature) TGA was utilized in this research. The details of the design and its performance have been discussed elsewhere (9). The system is depicted in Figure 1, which mainly consists of two chambers. The chambers are designed for 1200 psi, although supporting inlet lines limited the operating pressure to 450 psi. The small Grayloc flange was used as a port to introduce samples into the TGA. By raising the top chamber, attaching the sample, then lowering the chamber and securing the flange, a cumbersome, leaky port is avoided. A rugged electrobalance with a continuous weighing system, driven by an electric motor, is employed to lower the samples into the hot zone for weight-loss data. The heating system is a yttrium-stabilized ceramic "Kanthal" heating element. These elements are capable of 1800°C surface temperature, and work best in oxidizing gases. Temperatures were monitored throughout by Pt-Rh/Pt thermocouples. Steam can be introduced via a separate stainless steel flow system from gas lines, and condensation was avoided by maintaining the entire lower chamber at elevated temperatures.

This design has capability for quickly bringing the sample from a cold zone into the hot zone in less than 5 seconds, taking subsequent weight-loss data, and then removing the sample as quickly. The temperatures at various points in the system were calibrated at each reactor temperature and pressure. The temperature profile is such that the heating of the sample in the pyrolyzing-temperature region was achieved at a rate of 500-1500°K/sec depending on the reaction zone temperature. There is provision for several ports for gas input. Pyrolysis, external gas-

diffusion limitations, and char kinetic reactivity were analyzed from the weight-loss data by both varying time in the reaction zone and gas flow rate.

The coals studied included lignite (PSOC-246), bituminous (PSOC-309) and subbituminous (PSOC-240) samples. Samples of 50-100 mg were weighed, loaded and lowered in the sample holder into the heated chamber as described. Most runs used a platinum-mesh folded screen (52 mesh) as the sample holder. For some studies on particle size, the sample holder was a disked platinum foil. The results obtained on pyrolysis and gasification using the two different sample holders matched very well, indicating no effect of sample holder geometry.

The coal particle sizes used were 35-48, 48-60, 60-80, and 80-100 mesh ($\bar{d}_p$ = 358, 273, 213 and 163 μm, respectively). The gaseous environments were nitrogen, carbon dioxide, nitrogen-steam. Pyrolysis and subsequent in-situ reaction with gas following pyrolysis were run at 800-1600°C, 1-15 atm.

RESULTS AND DISCUSSION

Typical weight-loss data obtained at 1200°C in both nitrogen and nitrogen-steam for the lignite coal are shown in Figure 2. Note that the determination of percent pyrolysis in the inert nitrogen is straightforward, while in a reacting environment it is obscured by the rapid chemical reactions of the volatiles and char. If the break in the curve is identified by extrapolating the primary pyrolysis and reaction curve portions, respectively (p) and (r), this weight-loss can be called the apparent pyrolysis; and the apparent percent pyrolysis determined. The values thus obtained for the apparent percent pyrolysis as well as the pyrolysis time were found consistent and reproducible under a given set of conditions, as confirmed by repeated runs. It may be noticed from Figure 2 that the ultimate pyrolysis in nitrogen is greater than the apparent pyrolysis in the reacting gas, while in the same time period the amount pyrolyzed is more or less the same in the two cases.

In Figure 3 are presented the apparent percent pyrolysis of lignite as a function of temperature for different gases. Note that the apparent percent pyrolysis in CO_2 and N_2-H_2O is less than that in nitrogen, in agreement with the above discussion.

There is a plateau in the curve of percent apparent pyrolysis (devolatilization) versus temperature in the region 1200-1400°C. This type of phenomena can be found in the data of Menster et al. (1) and Kobayashi et al. (6). Suuberg et al. (10) observed two stages (or plateaus) in coal pyrolysis up to a temperature near 1100°C, and a third stage was envisaged above that temperature. This third stage was assumed to remove primarily CO and CO_2. The data of Kobayashi et al. (6) indicate percent weight-loss near 60 percent at temperatures above 1500°C. The present results are consistent with the results reported by these authors and confirm a third plateau stage.

Figure 4 presents devolatilization results at various temperatures for predried coal and for various particle sizes in a CO_2 gas. There appear to be significant effects of the moisture content in coal and various particle sizes. Although these results are inconclusive, they can be explained by either an effect of heating rate on pyrolysis or by secondary pyrolysis reactions which are influenced by available surface area, moisture and other gases which could result in internal volatile decomposition and coke formation.

Figure 5 presents the effect of pressure on the apparent pyrolysis in a steam environment. At lower temperatures (800-1100°C) the apparent pyrolysis increases slightly with pressure, while at higher temperatures (1200-1400°C) there is a decrease in apparent pyrolysis with pressure. One possible explaination is that at lower temperatures the increased gas concentration increases the gas-volatile re-

actions, decreasing the secondary char formation reactions; at higher temperatures the increased pressure prevents some volatiles from escaping the solid and thus participating in secondary char-formation reactions. Similar results have been reported earlier (8) in a hydrogen atmosphere, wherein the amount of pyrolysis was found to increase only beyond about 20 atm pressure. Notably, in steam this effect is observed at lower pressures. The present studies also bring out the effect of temperature on this behavior. Further work in this area is necessary to confirm the anomalous results.

Table 1 presents results of subsequent reactivity of chars formed by coal devolatilization. A comparison is shown of chars formed in-situ, as in the present mentod with chars formed separately and then reacted. Note that in-situ-formed char is a factor two to ten times more reactive than chars formed separately. Thus, keeping the char at high temperatures for longer times before reaction apparently renders the char less reactive, and can be interpreted as a morphological rearrangement. These results are in agreement with previous results at this laboratory (11), and extend these results to higher temperature regimes. It is suggested that the char preparation method dramatically affects subsequent char reactivity. These effects must be considered in models of char reactivity and in the use of char reactivity data in coal-conversion reactor models and in the interpretation of pilot-unit data.

CONCLUSIONS

Devolatilization generally increases with temperature in a manner consistent with the proposed three-stage mechanism for the evolution of volatiles. Results here show a plateau at 1200-1400°C and a maximum devolatilization above 1500°C. Reactive gases can interact with the freshly formed volatiles and affect the secondary char-forming reactions which can cause changes in the apparent percent pyrolysis. This was evident from the effects of moisture content, particle size, pressure and gaseous environment on the extent of pyrolysis. Reactivity of char formed in-situ and immediately reacted was found to be higher than reactivity of chars formed separately and then brought into the reactive environment. It is suggested that morphological rearrangements may be important in pyrolysis and subsequent char reactions.

ACKNOWLEDGMENT

This work was made possible by a grant from the Department of Energy, Contract No. ET-78-S-01-3253.

REFERENCES

1. Menster, M., O'Donnell, H. J. and Ergun, S., "Rapid Thermal Decomposition of Bituminous Coals," Am. Chem. Soc., Div. of Fuel Chem. Preprints 14 (5) 94 (1970).

2. Menster, M., O'Donnell, J. J., Ergun, S. and Friedel, R. A., "Devolatilization of Coal by Rapid Heating, " in Coal Gasification, p. 1, Advances in Chemistry Series No. 131, Am. Chem. Soc., Washington, D.C. (1974).

3. Nsakala, N.Y., Essenhigh, R. H. and Walker, P. L., Jr., Fuel 57 605 (1978).

4. Nsakala, N.Y., Essenhigh, R. H. and Walker, P. L., Jr., Comb. Sci. & Technol. 16 153 (1977).

5. Badzioch, S. and Hawksley, P. G. W., Ind. Eng. Chem. Process Des. & Dev. 9 (4) 521 (1970).

6. Kobayashi, H., Howard, J. B. and Sarofim, A. F., "Coal Devolatilization at High Temperatures, " 16th Intern. Symp. on Combustion, p. 411, The Combustion Institute, Pittsburgh, Pa. (1977).

7. Scaroni, A. W., Walker, P. L., Jr. and Essenhigh, R. H., Fuel 60 71 (1981).

8. Anthony, D. B., Howard, J. B., Hottel, H. C. and Meissner, H. P., Fuel 55 121 (1976).

9. Sears, J. T., Maxfield, E. A. and Tamhankar, S. S., "A Pressurized Themobalance Appartus for Use in Oxidizing Atmospheres at High Temperatures," Ind. Eng. Chem. Fundamentals (submitted 1981).

10. Suubert, E. M., Peters, W. A. and Howard, J. B., Ind. Eng. Chem. Process Des. & Dev. 17 37 (1978).

11. Agarwal, A. K. and Sears, J. T., Ind. Eng. Chem. Process Des. & Dev. 19 364 (1980).

12. Linares-Solano, A., Mahajan, O. P. and Walker, P. L., Jr., Fuel 58 327 (1979).

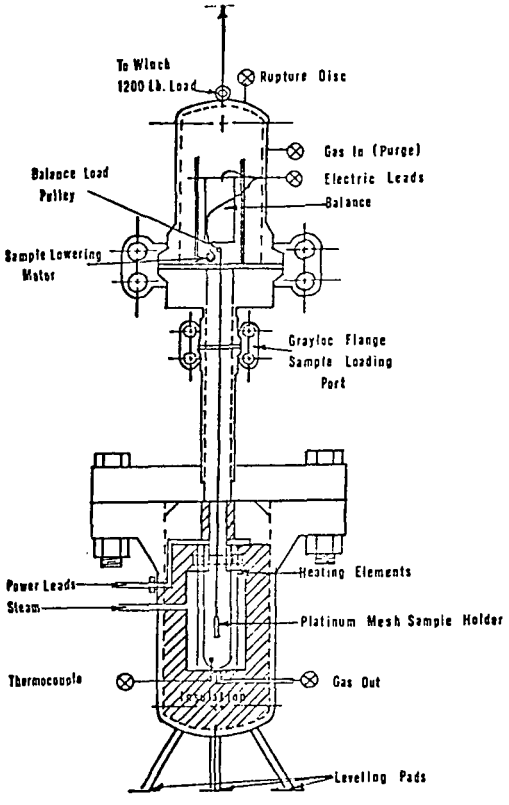

FIG. 1. SCHEMATIC OF HIGH PRESSURE/TEMPERATURE THERMOBALANCE APPARATUS.

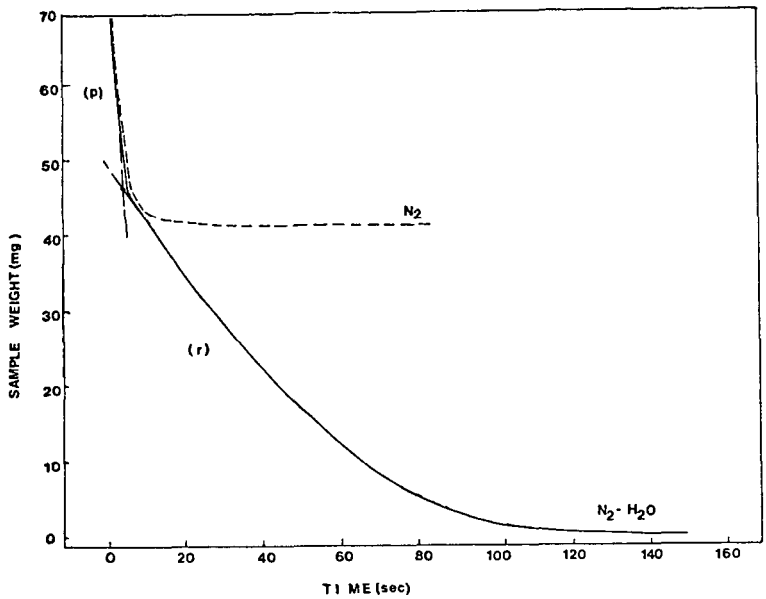

FIG. 2. REPRESENTATIVE WEIGHT LOSS CURVES OBTAINED AT 1200°C WITH PSOC-246 LIGNITE.

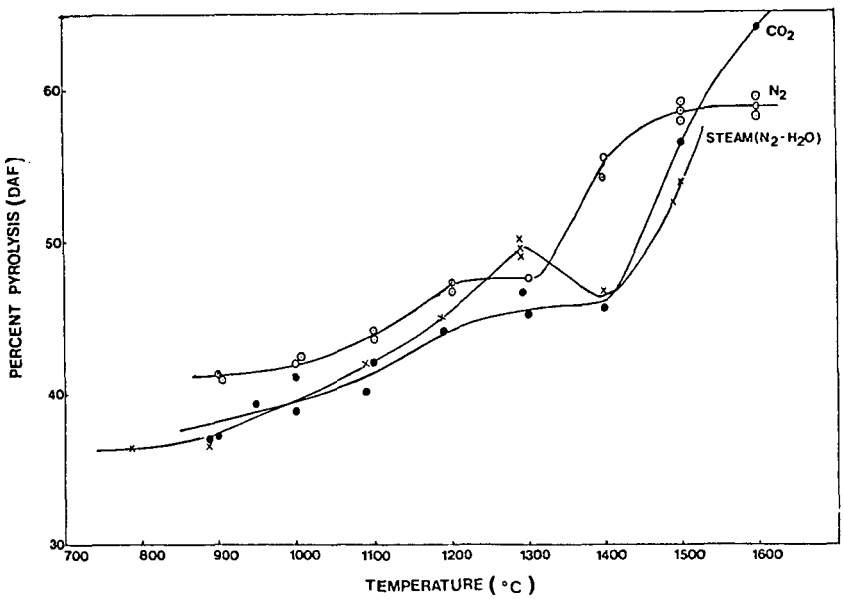

FIG. 3. EXTENT OF PYROLYSIS AS A FUNCTION OF TEMPERATURE FOR PSOC-246 LIGNITE.

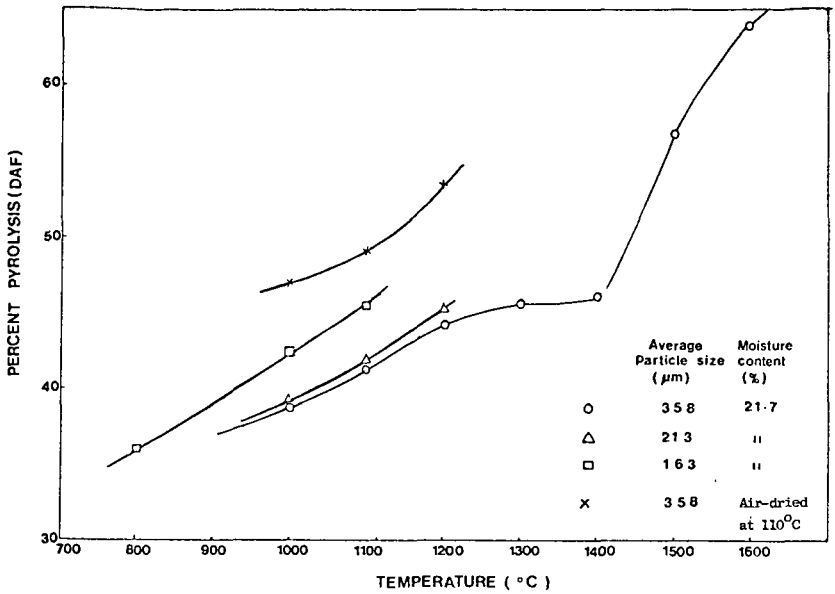

FIG. 4. EFFECTS OF PARTICLE SIZE AND MOISTURE CONTENT ON THE EXTENT OF PYROLYSIS IN CO_2 ATMOSPHERE.

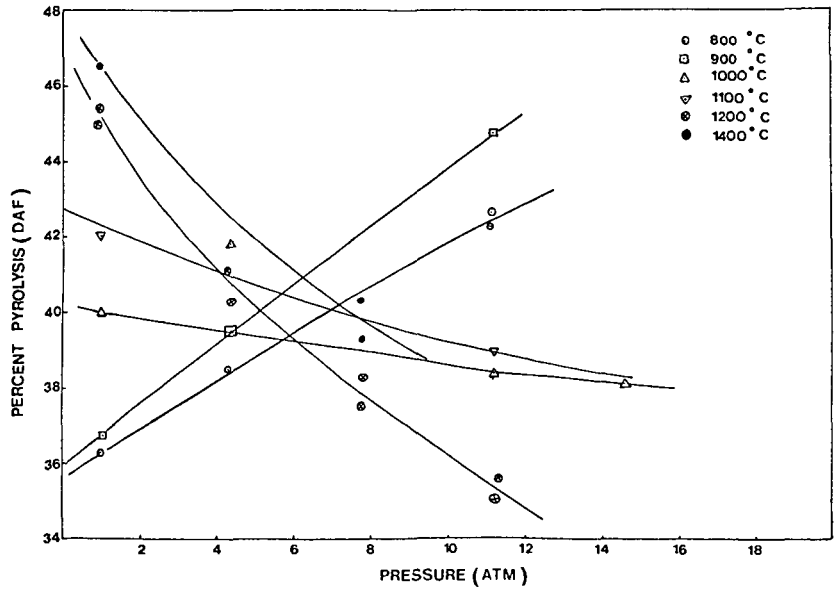

FIG. 5. VARIATION OF PERCENT PYROLYSIS WITH TEMPERATURE AND PRESSURE IN N_2-H_2O.

Table 1

REACTIVITY OF CHARS AS A FUNCTION OF PREPARATION CONDITIONS

(A) Reactivity of N.D. Lignite (PSOC-246) in CO_2

Reaction Temperature °C		900	950	1000	1050	1200	1250	1300
Initial Reactivity mg/mg Min.	In-situ	0.30	0.40	0.69	0.80	2.14	2.15	2.15
	Preformed Char*	0.26	0.32	0.57	0.62	0.88	0.89	1.02

(B) Reactivity of a Subbituminous Coal (PSOC-314) in CO_2

Reaction Temperature °C		1250	1300	1350	1400
Initial Reactivity mg/mg Min.	In-situ	0.54	0.67	1.13	1.30
	Preformed Char*	0.50	0.60	0.76	0.79

(C) Comparison of In-situ Reactivities with Other Reported Results

Coal Type	Method/Treatment	Reaction Temp. °C	Gas	Maximum Reactivity mg/mg Min.	Ref.
N.D. lignite (PSOC-246)	In-situ	910	N_2-H_2O (excess H_2O)	0.48	Present study
N.D. lignite (PSOC-87)	Coal heated in N_2 at 10°C/min to 1000°C, kept for 2 hrs, cooled. Reheated in N_2 at 20°C/min to 1000°C, cooled to 910°C, held for 20 min, reacted.	910	N_2-H_2O (excess H_2O)	0.0467	12
HVC bituminous (PSOC-309)	In-situ at ~ 600°C/sec	920	CO_2	0.20	Present study
HVC bituminous (PSOC-309)	In-situ at ~ 200°C/min.	920	CO_2	0.088	11

*Char prepared by pyrolyzing coal in N_2 at 1100°C for 2 min.

SIMULATION OF ENTRAINED FLOW HYDROPYROLYSIS REACTORS

A. Goyal
Institute of Gas Technology
Chicago, Illinois 60616

D. Gidaspow
Chemical Engineering Department
Illinois Institute of Technology
Chicago, Illinois 60616

The phenomena of coal pyrolysis and hydropyrolysis have become of considerable interest in recent years because of their significance in the efficient conversion of coals to clean fuels. The proposed hydropyrolysis commercial reactors are usually based on the entrained flow concept in which coal particles are rapidly heated in a dilute phase by mixing with hot hydrogen (or a gas mixture rich in hydrogen). A wide variation in the product distribution can be obtained in such reactors by manipulating temperature, residence time, and other operating parameters. Mathematical models incorporating hydrodynamics, coal kinetics, heat transfer characteristics, etc. are needed for understanding the influence of design variables, feed materials, and process conditions on the reactor performance. The literature is lacking in coal hydropyrolysis entrained flow reactor models. Such a model has been developed in this study.

Mathematical Formulation

A one-dimensional mathematical model has been formulated here. The physical system considered is an entrained flow hydropyrolysis reactor. Pulverized coal mixes with the hot gas feed at the reactor entrance. As coal particles are carried by the gas, their temperature increases and hydropyrolysis takes place.

The single coal particle hydropyrolysis kinetic model used in this study is described by Goyal (1). The model is primarily based on Johnson's kinetic model (2, 3, 4) supplemented by Suuberg's kinetic model (5) for rapid reactions. In this model, the coal is assumed to consist of eleven solid species while the gas of nine species (Table 1). Gaseous species $(CH_z)_a$ represents gaseous heavy hydrocarbons while $(CH_M)_b$ represents vaporized oils and tars.

The kinetic model has been combined here with reactor flow model and heat and mass transfer characteristics of the multiparticle system to derive a reactor model. Because of the significant amount of coal weight loss and gas generation in such systems, hydrodynamics may also be very important. The equations describing the system are given in Table 2. In this formulation, it is assumed that the heat of reaction of the solid-gas phase reaction affects the solid temperature only while that of occurring solely in the gas phase affects the gas phase temperature only. Also, the extent of swelling of the coal particles is directly proportional to the extent of devolatilization. Furthermore, the expression giving the gasification rate of the solid species CH_x (semichar) is somewhat complex. This rate is dependent on the time-temperature history of the particle and involves a double integration. The mathematical manipulation performed to simplify the complexity resulted into several additional differential equations, the details of which are given by Goyal (1).

The solid species production rate (S_i) is given by equation (18). The gas species production rates can be related to the solid species production rates (1).

Furthermore, coal hydrogenation experiments in the laboratory are often carried out in helical reactors (4, 6). The relationship between the particle

and the gas velocity is often represented in terms of a slip velocity factor (ϕ_s). In such reactor, the centrifugal forces are often more important than gravitational force. This slip velocity factor depends on the tube diameter, helix diameter, solids to gas ratio, particle size, gas velocity, etc. Thus for helical reactors:

$$D(v_s) = \phi_s D(v_g) \qquad 24)$$

This equation replaces equation (5) in Table 2.

This set of equations (Table 2) also requires a large number of auxiliary, algebric equations as component model parts; for example relationships for f_s, f_w, h_{gp}, h_{gw}, ε_{app} etc. These relationships are taken from the literature and the details are given by Goyal (1).

Furthermore, the model has been developed here for coal hydropyrolysis. Nevertheless, the formulations and the method of solution are flexible and can be easily manipulated for other entrained flow gasifiers, for example, peat gasification.

Solution Methodology

The entrained flow hydropyrolysis reactor has been modeled in the preceding section by a set of fifty three simultaneous nonlinear first order ordinary differential equations. The solutions to the formulations are sought in the form of time histories of quantities such as particle and gas temperature, their compositions, velocities, densities, and other derived quantities such as conversion etc. This system of equations is very stiff primarily due to the high temperature dependence of various hydropyrolysis reactor rates (1). A computer program based on implicit backward differentiation formulas of orders one through five (Gear's method) has successfully been used here in solving this set of stiff equations.

Comparison With Experimental Data

Cities Service Research and Development Company has performed studies on the hydropyrolysis of Montana Rosebud subbituminous coal, Western Kentucky No. 9/14 bituminous coal, and North Dakota lignite. Experiments were conducted in a bench-scale system of 2-4 lb/hr nominal capacity entrained-downflow tubular reactor. Different types of reactors (free fall, vertically-entrained, helically-entrained) were used in this study. The reactor was mounted inside an electric furnace designed for isothermal operation. Preheated hydrogen and coal were mixed inside a high-velocity coaxial injector nozzle located near the entrance to produce very high heating rates. The coal-hydrogen mixture moved to the reactor outlet where it was quenched to below 1000°F directly by a stream of cryogenically-cooled hydrogen, which terminated reactions. A more detailed description of the reactor system has been given by Hamshar et al. (7).

The reactor and coal types, flow rates, and operating conditions used in different test runs have been summarized along with experimental results by Cities Service Research and Development Co. (6). Operating conditions were varied in the nominal ranges of 1400°-1700°F reactor temperature, 34-170 atm reactor pressure, 0.18-1.3 hydrogen/coal weight ratio, and 0.3-25 sec vapor residence time. A few runs utilized a 78/22 (vol.) mixture of hydrogen/methane feed gas; the remainder used high purity hydrogen. The reactor temperature was measured by a series of removable skin thermocouples tacked along the wall of the reactor. However, these measured temperature profiles have not been reported. Instead, the mix temperature, maximum gas temperature and equivalent isothermal temperature for each run have been reported.

A total of twenty-one runs having good carbon and ash balance closures have been simulated in this study. The operating conditions for these runs are given by Goyal (1). The coal feed in these runs was dry. Also, several of their tests were conducted in helical coil reactors. Oko et al. (8) from Cities Service have recently reported the results of a helical glass cold-flow study. In this apparatus, average particle velocities were measured in the same flow regimes that were experienced in the bench-scale hydropyrolysis apparatus. The following empirical equation was derived to estimate the slip velocity factor:

$$\bar{\phi}_s = \bar{v}_s/\bar{v}_g = 1 - k_o \, Re_g^{p} R_c^{q} \, (D_H/D_t)^r \qquad 25)$$

where k_o, p, q, and r are empirical constants.

Several important reactor performance parameters have been compared here in Figures 1 through 4. Figure 1 shows a comparison of calculated and experimental carbon conversion for different types of coals. As seen from this figure, the computer model calculations agreed quite closely with the actual experimental results. Figure 2 compares the predicted moisture-ash-free (MAF) coal conversions with the experimental values of these conversions. The comparison is quite good; however, the model somewhat underpredicts this coal conversion. This is primarily due to the fact that Johnson's model allows for only 89% of coal oxygen evolution whereas the experimental oxygen evolution is approximately 97%. If this additional oxygen were allowed to evolve, then the predicted coal conversion would increase by approximately 1.5%. This would result in an excellent comparison.

Figure 3 compares the predicted carbon conversion to light hydrocarbons methane + ethane with experimental values. The predicted methane + ethane yield is somewhat higher. The comparison of carbon oxides yield is shown in Figure 4. The model underpredicts this yield. Again, it is probably because Johnson's model allows for only 89% coal oxygen removal while reported coal oxygen removal is in the range of 95% to 100%.

As mentioned earlier, the model is capable of predicting time histories of quantities such as conversions, particle and gas temperatures, their flow rates, compositions, velocities, etc. As an example, some of the important reactor variables have been summarized (as a function of reactor length) in Figures 5 to 7 for Run No. KB-5 with Western Kentucky bituminous coal feed. In this test, a 17.7 ft long and 0.26 inch ID reactor was operated at 1557°F (EIT) and 1500 psia hydrogen pressure. The superficial gas velocity, vapor residence time and hydrogen/coal weight ratio were 12.3 ft/sec, 1.44 sec, and 1.17 respectively. The wall temperature was assumed to be 1581°F which is the average of reported maximum reactor temperature and EIT. The data points shown in these figures are the actual experimental results at the reactor's exit.

Figure 5 shows carbon and MAF coal conversions as a function of reactor length. As seen from the figure, a significant conversion (12% to 14%) takes place within 0.1 ft reactor length. Note that the reactor length has been shown on a log scale, which allows to show the significant conversions occurring in the extremely short distance near the entrance. The particle residence time is also calculated by the model and is shown at the top of the graph.

Figure 6 shows the carbon conversion to different species over the length of the reactor. It shows that oil is evolved first and very rapidly. Again, log scale has been used to represent the reactor length. The change in the gas composition over the reactor length is shown in Figure 7. Pure hydrogen feed gas was used in this test and 96% of the exit product gas was hydrogen. This is so because excess amount of hydrogen was used in this run.

The mathematical model developed here has been used successfully to describe these hydropyrolysis reactors. Reasons for small discrepancies in experimental and predicted reactor performances are attributable to inadequacies in model formulation, unavailability of experimental data particularly reactor wall temperature profiles, and uncertainties in the experimental data.

A detailed parametric study has been performed using this model to identify important reactor parameters for the design of commercial entrained flow hydropyrolysis reactors. The results are given elsewhere (1).

Acknowledgement

The authors are grateful to Dr. S. Weil for providing many helpful suggestions and criticisms throughout this entire study.

Nomenclature

a	Contact area between solids and gas per unit reactor volume
a	Number of carbon atoms per mole of gas species $(CH_z)_a$
A	Reactor cross-sectional area
b	Number of carbon atoms per mole of gas species $(CH_M)_b$
B_j	Rate of gas species j going from solid phase to gas phase (i.e. crossing boundary) per unit reactor volume
C	Fractional coal conversion (moisture-free)
C_{af}	Fractional coal conversion (moisture-ash-free)
C_{pgj}	Heat capacity of gas species j
C_{psi}	Heat capacity of solid species i
D	Derivative with respect to distance along reactor (x)
D_H	Helix diameter
D_p	Particle diameter
D_t	Reactor diameter
f_s	Drag force exerted by fluid on the particles per unit volume of particles
f_w	Frictional force between the gas and the wall of the reactor
F	Solids flow rate per unit reactor cross-sectional area
g	Gravitational acceleration
g_c	Conversion factor (32.2 lbm-ft/sec^2/lbf)
G	Gas flow rate per unit reactor cross-sectional area
h_{gj}	Total enthalpy of gas species j
h_{gp}	Overall heat transfer coefficient between gas and solid particle
h_{gw}	Overall heat transfer coefficient between gas and wall
h_{si}	Total enthalpy of solid species i
H_{2gs}	Rate of gaseous hydrogen reacting with solid phase per unit reactor volume
H_{ls}	Wall heat losses from reactor per unit reactor length (due to convection between gas and wall)

H_{lsa}	Total wall heat losses from reactor per unit reactor length per unit reactor cross-sectional area
M	Atomic ratio of hydrogen to carbon in oils and tars (also in species CH_M)
M_j	Molecular weight of gas species j
P	Total reactor pressure
Q_{ash}	Ash flow rate per unit reactor cross-sectional area
R	Universal gas constant
R_c	Char to gas weight ratio
Re_g	Gas Reynolds number
$\dot{R}_i$	Reaction rate ($d\xi_i/dt$) for i^{th} reaction
$(S_i)_s$	Mass rate of solid species i produced per unit reactor volume
$(S_j)_g$	Mass rate of gas species j produced per unit reactor volume
t	Time
T_g	Gas temperature
T_s	Solids temperature
T_w	Wall temperature
v_g	Gas velocity
v_s	Solids velocity
V_R	Ratio of particle volume at anytime to its initial volume
x	Distance along reactor
x	Atmoic ratio of hydrogen to carbon in species CH_x (semichar)
y	Atmoic ratio of hydrogen to carbon in species CH_y (final product char)
y_j	Mass fraction of gas species j
z	Atmoic ratio of hydrogen to carbon in hydrocarbon gases other than CH_4 and C_2H_6 (also in solid species CH_z)
θ	Angle between horizontal line and the reactor axis
θ_g	Gas residence time
θ_s	Solids residence time
ρ_{ash}	Ash density
ρ^{o}_{ash}	Ash density of raw coal
ρ_g	Gas density
ρ_s	Solids density
ϵ	Voidage
ϵ_{app}	Effective emmissivity
σ_B	Stephen-boltzman constant
γ_s	Swelling parameter

ξ_i Fraction of solid species i not yet gasified ($i \neq CH_y$)

ξ_i° = 1 for $i \neq CH_y$

$\omega_{CH_y}^\circ$ Maximum lbs of CH_y that can be formed per lb of ash (equation 21)

ω_i° Lbs of solid species i in raw coal per lb of ash ($i \neq CH_y$)

ϕ_s Slip velocity factor defined as the ratio of solids velocity to gas velocity

Subscript

i Refers to solid species

j Refers to gas species

References

(1) Goyal, A., Mathematical Modeling of Entrained-Flow Coal Gasification Reactors, Ph.D. Thesis, Illinois Institute of Technology, Chicago, IL, May (1980).

(2) Johnson, J. L., ACS, Div. of Fuel Chem. Preprints, 20, No. 3, 61 (1975).

(3) Johnson, J. L., ACS, Div. of Fuel Chem. Preprints, 22, No. 1, 17 (1977).

(4) Johnson, J. L. and D. Q. Tran, "Kinetics of Devolatilization and Rapid-Rate Methane Formation," Final Report, AGA Project IU-4-11, GRI Contract No. 5010-322-0025, Report No. GRI-78/0049, Institute of Gas Technology, Chicago, IL, Nov. (1980).

(5) Suuberg, E. M., W. A. Peters and J. B. Howard, Ind. Eng. Chem. Process Design Develop., 17, No. 1, 37 (1978).

(6) Cities Service Research and Development Company, "Hydrogasifier Development for the Hydrane Process," Final Technical Progress Report, Feb. 1977 to July 1978, Subcontract to Rocketdyne Division of Rockwell International Corporation of DOE Contract No. EX-77-C-01-2518, Cranbury, NJ, July 31 (1978).

(7) Hamshar, J. A., S. J. Bivacca and M. I. Greene, Paper presented at 71st Annual AIChE Meeting, Miami Beach, FL, Nov. (1978).

(8) Oko, U. M., J. A. Hamshar, G. Cuneo and S. Kim, ACS, Div. of Fuel Chem. Preprints, 24, No. 3, 82 (1979).

(9) Gidaspow, D., "Hyperbolic Compressible Two-Phase Flow Equations Based on Stationary Principles and the Fick's Law," in Two Phase Transport and Reactor Safety, edited by S. Kakac and T. N. Veziroglu, 1, p. 283, Hemisphere Publishing Corp., Washington, D. C. (1978).

Table 1. Solid and Gas Species

Solid Species	Gas Species
1. HOH	1. CO
2. O·O	2. CO_2
3. OH	3. H_2
4. CO	4. H_2O
5. COO	5. CH_4
6. CHH	6. C_2H_6
7. CH_z	7. $(CH_z)_a$
8. CH_M	8. $(CH_M)_b$
9. CH_x	9. Inert gas
10. CH_y	
11. Ash	

Table 2. Differential Equations Model

Total Solids Mass Balance: $D[(1-\varepsilon)\rho_s v_s] = \Sigma(S_i)_s = D(F)$ 1)

Total Gas Mass Balance: $D(\varepsilon\ \rho_g v_g) = \Sigma(S_j)_g = D(G)$ 2)

Solids Species Balance: $D(Q_{ash}\omega_i{}^{\circ}\xi_i) = (S_i)_s$ 3)

Gas Species Balance: $D(\varepsilon\ \rho_g v_g y_j) = (S_j)_g$ 4)

Constitutive Equation for the Mixture: (Ref. 9)

$$-(1/2)D\ [|v_g - v_s|(v_g - v_s)] = f_s/\rho_s - g \sin\theta \qquad 5)$$

Mixture Momentum Balance: $g_c D(P) = (v_g - v_s)\Sigma(S_i)_s - (1-\varepsilon)\rho_s v_s D(v_s)$

$$-\varepsilon\ \rho_g v_g D(v_g) - f_w - [\rho_s(1-\varepsilon)+\rho_g\varepsilon]\ g \sin\theta \qquad 6)$$

Solids Density: $D(\rho_s) = D[\Sigma(\omega_i{}^{\circ}\xi_i)\rho_{ash}^{\circ}/V_R]$ 7)

Gas Density: $D(\rho_g) = D[(P/RT_g)(\Sigma y_j/M_j)^{-1}]$ 8)

Table 2. Differential Equations Model (Cont.)

Solids Phase Energy Balance: $D(T_s) = -[\{(-H_{2gs})(h_{gH_2})_{T_g} + \Sigma(B_j)(h_{gj})_{T_s} + h_{gp}a(T_s - T_g) - 4\sigma_B\varepsilon_{app}(T_w^4 - T_s^4)/D_t\}/Q_{ash} + \Sigma(\omega_i^\circ(h_{si})_{T_s}D(\xi_i)]/[\Sigma(\omega_i^\circ\xi_i C_{psi})]$ 9)

Gas Phase Energy Balance: $D(T_g) = [(-H_{2gs})(h_{gH_2})_{T_g} + \Sigma(B_j)(h_{gj})_{T_s} + h_{gp}a(T_s - T_g) - H_{1s}/A - \Sigma(h_{gj})_{T_g}(S_j)_g]/[\Sigma(Gy_j C_{pgj})]$ 10)

Fractional Coal Conversion: $D(C) = D[1-\Sigma(\omega_i^\circ\xi_i)/\Sigma(\omega_i^\circ\xi_i^\circ)]$

$= D[-\Sigma(S_i)_s/\{Q_{ash}\Sigma(\omega_i^\circ\xi_i^\circ)\}]$ 11)

Particle Relative Volume: $D(V_R) = D[(1 + \gamma_s C_{af})^3]$ 12)

Average Particle Diameter: $D(D_p) = (D_p/3V_R)D(V_R)$ 13)

Gas Residence Time: $D(\theta_g) = 1/v_g$ 14)

Particle Residence Time: $D(\theta_s) = 1/v_s$ 15)

Total Heat Loss: $D(H_{1sa}) = H_{1s}/A - 4\sigma_B\varepsilon_{app}(T_w^4 - T_s^4)/D_t$ 16)

Useful Algebric Equations:

$\Sigma(S_i)_s = -\Sigma(S_j)_g$ 17)

$(S_i)_s = (1-\varepsilon)\rho_{ash}\omega_i^\circ\dot{R}_i$ 18)

$Q_{ash} = (1-\varepsilon)v_s\rho_{ash}$ 19)

$G = \varepsilon\rho_g v_g$ 20)

$\omega^\circ_{CH_y} = (M_{CH_y}/M_{CH_x})\omega^\circ_{CH_x}$ 21)

$H_{1s} = \pi D_t h_{gw}(T_g - T_w)$ 22)

$C_{af} = C[\Sigma(\omega_i^\circ\xi_i^\circ)/\Sigma\{(\omega_i^\circ\xi_i^\circ)-1\}]$ 23)

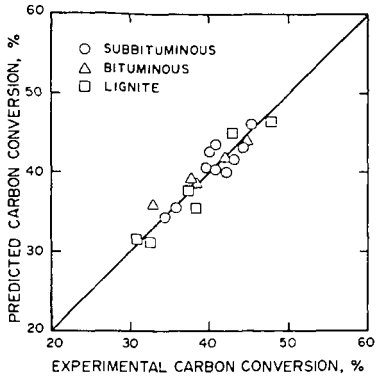

Figure 1. Comparison of Experimental and Predicted Carbon Conversion

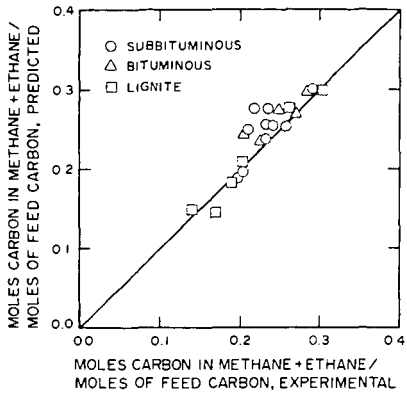

Figure 3. Comparison of Experimental and Predicted Methane + Ethane Yields

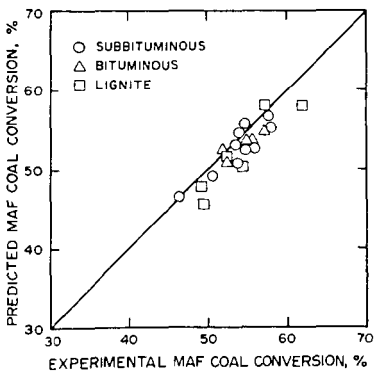

Figure 2. Comparison of Experimental and Predicted Moisture-Ash-Free Coal Conversion

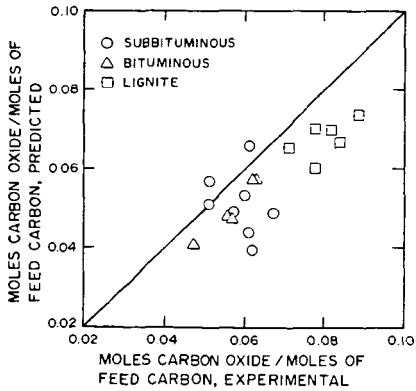

Figure 4. Comparison of Experimental and Predicted Carbon Oxides ($CO + CO_2$) Yields

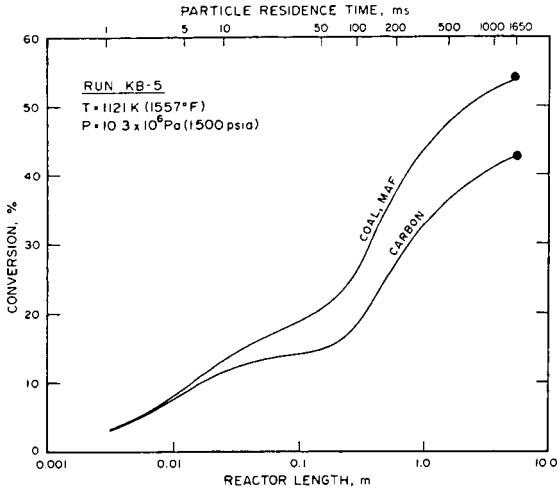

Figure 5. Carbon and Moisture-Ash-Free Coal Conversions along Reactor Length

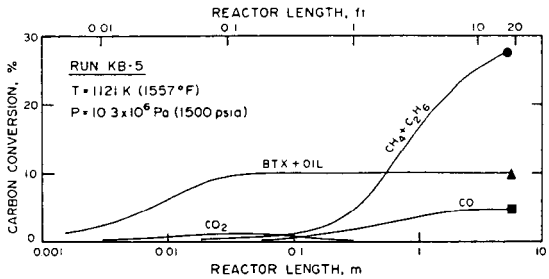

Figure 6. Distribution of Total Carbon Conversion to Different Species along Reactor Length

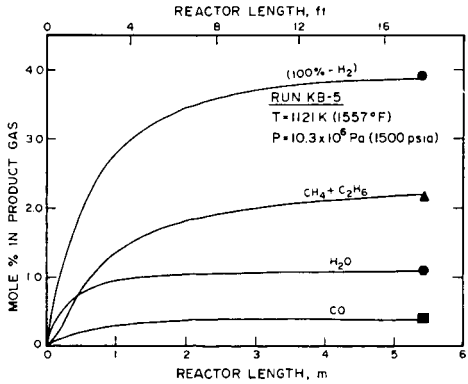

Figure 7. Gas Composition along Reactor Length

The Effect of Potassium Carbonate on the Gasification of Illinois No. 6 Coal

A.H. Pulsifer and J.F. McGehee, Department of Chemical Engineering and Engineering Research Institute, Iowa State University, Ames, Iowa 50011.

L. Saroff, U.S. Department of Energy, Pittsburgh Energy Technology Center, Pittsburgh, Pennsylvania 15213.

Catalyzed coal gasification can lead to reduced gasifier size and lower gasification temperatures which give greater thermal efficiencies. Therefore, an investigation of the steam gasification of a bituminous coal under moderately high pressures was conducted. The primary objective of the study was to determine the influence of an alkali metal carbonate catalyst on the kinetic parameters of the gasification reaction.

The coal chosen for the study was an Illinois No. 6 coal and this material was gasified both with and without the addition of potassium carbonate. Experiments were carried out at temperatures between 700 and 900°C and at a pressure of 2.17 MPa (21.4 atm). The partial pressures of steam, carbon dioxide and hydrogen were also varied during the investigation. The carbon gasification rate was modeled using an unreacted, shrinking-core model and kinetic constants and activation energies were determined.

Experimental Methods

The apparatus used to gasify the coal was a high-pressure, tubular, fixed bed reactor with an external heat supply. One of the unique features of this apparatus was its charging system. A 10 g sample of coal was held at a temperature near ambient in a pressurized vessel located above the reactor. Actuation of a ball valve allowed the sample to fall into the reactor, commencing the experimental run.

The apparatus was able to gasify a sample of coal with steam, or mixtures of steam and H_2,N_2, or CO_2. Carbon gasification rates were determined from the product gas flowrate and composition. The essential features of the apparatus are shown in Fig. 1.

The reactor and coal charging vessel were constructed from type 316 stainless steel. The reactor body was a 21-inch (53.3 cm) long, 3/4-inch schedule 160 tube with an outside diameter of 1.050 in. (26.7 mm) and an inside diameter of 0.614 in. (15.6 mm). A 0.125-in. (3.2 mm) thick porous stainless steel disc was located inside the tube, 6.5 in. (16.5 cm) from the bottom. This disc supported the bed of coal inside the reactor.

The coal charging vessel, a cylindrical funnel-shaped container with a volume of approximately 50 cm^3, was connected to the top of the reactor by a vertical 3/4-inch schedule 160 tube with an inside diameter of 0.464 in. (11.8 mm). At the bottom of this vessel was a ball valve. Charging the reactor was accomplished by opening the valve by means of a pneumatic actuator. The coal then fell a distance of 11 in. (27.9 cm) into the reactor.

The heat necessary to generate steam and gasify the coal was supplied externally through electric resistance heaters. There were three separate electrical heating circuits. These supplied the gas preheater and steam vaporizer, the reactor furnace, and the bottom flange heater.

Water for steam generation was delivered to the system by a high-precision

metering pump. The water used was high purity, liquid chromatography solvent grade material. The flowrate of the other gases supplied to the reactor were controlled by means of two electronic thermal-type mass flow controllers.

After exiting the reactor, the hot product gases and unreacted steam were filtered using glass wool to remove tar and liquid products. The gases were then cooled to condense excess steam, the pressure of the cooled gases was reduced to atmospheric, and they were then analyzed. A quadrapole mass spectrometer was used to determine the product gas compositions. The flowrate of product gas was determined with a wet test meter.

All of the material used in this study was Illinois No. 6 coal. Its proximate and ultimate analyses, free swelling index, and heating value are listed in Table 1. The coal had been previously pulverized, and particles with sizes between 0.297 mm and 0.149 mm(50 x 100 U.S. mesh) were retained.

The catalyst used in this investigation was anhydrous reagent quality potassium carbonate. The catalyzed samples used in the gasification experiments were produced by solution impregnation of the raw coal with K_2CO_3 in an autoclave at 285°C and 7.0 MPa with the product being dried by flash evaporation. The uncatalyzed samples were subjected to mild oxidative pretreatment. This was necessary to prevent agglomeration of coal in the fixed-bed reactor.

An experimental run was carried out in the following manner. Appropriate conditions of reaction temperature and reactant gas partial pressure were selected. The flowrates of nitrogen and carbon dioxide or hydrogen were adjusted to meet these specifications as measured by timed readings of the wet test meter. Steam flow was commenced by adjusting the water metering pump. Finally the ball valve was opened and the coal entered the reaction zone.

During the first five minutes of the run, the flow of products was rapid due

Table 1. Analyses of Illinois No. 6 coal.

	Moisture free coal	Moisture and ash free coal
Proximate analysis (wt. %)		
Volatile matter	40.5	46.5
Fixed carbon	46.5	53.5
Ash	13.0	- -
Ultimate analysis (wt.%)		
Hydrogen	4.7	5.4
Carbon	67.7	77.8
Nitrogen	1.1	1.3
Sulfur	3.8	4.3
Oxygen	9.8	11.2
Ash	13.0	- -
Heating Value	12307 Btu/lb (28619 kJ/kg)	14148 Btu/lb (32900 kJ/kg)
Free swelling index	3.5	3.5

to the devolatilization of the coal and the time at every one-quarter revolution of the wet test meter (0.0125 cu ft, 354 cm^3) was recorded. After five minutes, the volume reading of the wet test meter was recorded at 3-minute intervals. Discrete values of the concentration of each gas were also read from a digital display and recorded by the operator at intervals of 2.5 minutes, beginning at 5 minutes.

The length of time of each experiment varied. In the experiments conducted at 800°C and 900°C, the 10 g coal sample was usually allowed to react until 80-90% conversion of carbon had been achieved. At 700°C, the experiments were terminated after approximately two hours.

At the end of the experiment, flow of water to the steam vaporizer and flow of gases were terminated. All heaters were shut down, and the reactor furnace was opened. When the apparatus was cool, the reactor was depressurized and opened. The char and ash were withdrawn and weighed. All condensate was drained from the trap and the volume of water recorded. The tar filter was removed and weighed immediately.

Results

In this study, the influence of the following parameters on the steam gasification rate of Illinois No. 6 coal was investigated: the presence of K_2CO_3 as a catalyst; the partial pressures of steam, CO_2 and H_2; and reaction temperature. The total pressure of the system was held at a constant value of 2.17 MPa (21.4 atm) throughout the study. The total flowrate of gases into the reaction zone was also kept fixed in each experiment at some value between 980 and 1020 sccm. Variation of the reactant gas composition was accomplished by increasing the mass flowrate of steam, CO_2 or H_2 and simultaneously decreasing the mass flowrate of the inert carrier gas, nitrogen. Nitrogen was both a diluent and a carrier gas for product removal.

Runs were made at 700, 800 and 900°C with the pretreated coal and coal impregnated with 10 wt.% K_2CO_3. The effect of CO_2 concentration on the gasification rate of K_2CO_3-impregnated coal was studied at a constant steam partial pressure in a series of 6 runs. An additional 6 runs were made with a mixture of steam, N_2, and H_2 of constant composition to evaluate the magnitude of hydrogen inhibition of the steam gasification rates. Runs were made at each of the three temperatures, 700, 800 and 900°C, with both the pretreated coal and coal impregnated with 10 wt.% K_2CO_3.

Using the data of each experiment, a number of calculations were performed. The gasification rate and carbon conversion were calculated from a balance of carbon-containing reaction products. The extent of reaction of the steam was determined from a balance of hydrogen-containing or oxygen-containing products. Reactant and product gas partial pressures were computed at the reactor inlet and outlet. From these partial pressures, the apparent equilibrium constants of the water-gas shift, carbon-steam, and carbon-H_2 reactions were calculated. Finally, product gas sums and overall material balances were determined for each experiment.

Gasification rate

The carbon gasification rate was generally high initially, decreased rapidly and then slowly decreased throughout the remainder of the run. Fig. 2 shows typical results obtained at 700°C with a catalyzed coal sample. The initial peak in the curve seemed to be caused by devolatilization of the coal, which was followed by gasification of the base carbon in the sample.

To obtain a quantitative measure of the reaction rate, the shrinking, unreacted-core model for the case of complete gasification of a spherical, solid particle under conditions of chemical reaction rate control was used to describe the carbon

conversion-time data.* The integrated form of the equation based on this model is

$$1 - (1 - X_c)^{1/3} = \frac{kC_s^n t}{\rho_p R}$$

where X_c = carbon conversion
k = reaction rate constant
C_s = concentration of gaseous reactant at particle surface
n = reaction order
ρ_p = molar density of particle
R = initial radius of particle
t = time

In general, the model did not fit the initial data where devolatilization was occurring, but a good fit was obtained over the range of carbon conversions from 0.3 to 0.8. Applying the model to data from all the runs over the range of conversions from 0.3 to 0.7 using linear regression analysis gave correlation coefficients of 0.98 or larger except for two runs where the coefficients were 0.95 and 0.91.

To determine the reaction order with respect to steam concentration, n, a multiple linear regression analysis was performed on the data from the gasification experiments where only steam and nitrogen were used. Within the standard error of the estimate, the overall reaction order was one for both K_2CO_3-catalyzed and uncatalyzed steam gasification.

Assuming first order kinetics and using the Arrhenius expression, the frequency factor and activation energy were calculated for both catalyzed and uncatalyzed steam gasification of Illinois No. 6 coal. The derived reaction rate parameters are summarized in Table 2. As expected, the overall activation energy was somewhat lower for catalyzed gasification.

Apparent Equilibrium Constants

The value of the apparent water-gas shift equilibrium constant, $K_S = (pCO_2)(pH_2)/(pH_2O)(pCO)$, tended to decrease from the time of peak gasification rate until devolatilization was complete. From the time devolatilization was complete until the carbon had completely gasified, the value observed was approximately constant. The value of K_S for each experiment, over the time for which it was approximately constant, is compared in Fig. 3 with a literature value of K_S over the range of temperatures from 700°C to 900°C.

Table 2. Arrhenius parameters for steam gasification of Illinois No. 6 coal.

Material Gasified	Parameter	Estimate	Standard error of estimate	Correlation Coefficient
10% K_2CO_3-impregnated coal	Activation energy	133.7 kJ/mol (31.7 kcal/mol)	13.8 kJ/mol (3.3 kcal/mol)	0.931
	Frequency factor, min^{-1}	1.32×10^8	4.5	
Oxygen-pretreated coal (uncatalyzed)	Activation energy	151.5 kJ/mol (36.2 kcal/mol)	6.3 kJ/mol (1.5 kcal/mol)	0.986
	Frequency factor, min^{-1}	2.94×10^8	2.1	

*For a derivation of the model, see Levenspiel, O. 1972. Chemical Reaction Engineering. 2nd ed. Wiley, New York.

The values of K_S fall both above and below the theoretical curve. Some deviation is due to the sensitivity of K_S to errors in calculation of product gas partial pressures. At 700°C, the gasification rate was slow and steam conversion was slight. Therefore, equilibrium of the water-gas shift reaction may not have been reached. At 800°C and 900°C apparent values of K_S for both catalyzed and uncatalyzed gasification are closer to the theoretical curve than were the values at 700°C. If a 20% margin of uncertainty is assumed, the K_S values of most experiments at 900°C indicate the attainment of water-gas shift equilibrium.

In contrast, the carbon-steam and carbon-H_2 reactions did not appear to be in thermodynamic equilibrium. Neither equilibrium constants reached a consistent value at any time during the burnoff of the carbon and both values were at least an order of magnitude smaller than their theoretical value during the char gasification period.

Influence of CO_2 on the gasification rate

To determine the effect of CO_2 partial pressure, a series of 5 runs was made at constant steam flowrate while varying the CO_2 concentration. These runs were carried out with 10 wt.% K_2CO_3-impregnated coal at 800°C and the CO_2 partial pressure was varied from 97 kPa (0.96 atm) to 576 kPa (5.68 atm) using a constant steam pressure of 1.35 MPa (13.3 atm).

The calculated kinetic constants for these runs were generally somewhat lower than the value determined with pure steam. However, the deviation was within the expected range introduced by experimental errors. Therefore, the only conclusion that may be drawn from this set of experiments is that CO_2 concentration, over the range used, exerted a relatively small effect on the steam gasification rate of K_2CO_3-impregnated coal when compared with the effects of steam concentration and temperature.

Influence of H_2 on the reaction rate

Runs were made at 700, 800 and 900°C with both 10 wt.% K_2CO_3-impregnated coal and untreated coal. All 6 runs were done with the same hydrogen and steam partial pressures, namely 428 kPa (4.22 atm) and 1.69 MPa (16.7 atm), respectively.

Hydrogen inhibited the steam gasification rate of both coal samples. The results of the experiments with the K_2CO_3-impregnated coal showed that the magnitude of this inhibition decreased with increasing temperature for the catalyzed reaction. Comparison of the k values obtained with and without H_2 present show that the ratio of $k_{H_2O/H_2}/k_{H_2O}$ increased from 0.13 at 700°C to 0.38 at 900°C. The ratio of the k values was higher for uncatalyzed coal and did not change systematically. This ratio was 0.51 at 700°C, 0.27 at 800°C and 0.47 at 900°C. At atmospheric pressure, the inhibition of the carbon-steam reaction by hydrogen is expected to decrease with increasing temperature because of the relative magnitudes of the elementary activation energies. At higher pressures, the trend is probably more complicated, since the reaction steps leading to CH_4 production are significant. CH_4 generation rates were approximately the same in the char gasification periods for reactions both in pure steam and in the steam/H_2 mixture. CH_4 represented a greater percentage of the total product gas in the experiments with the steam/H_2 mixture than in those with pure steam.

Conclusions

The overall gasification reaction was found to be first order with respect to steam concentration, with the rate being unaffected by CO_2 and inhibited by hydrogen. The variation of gasification rate with carbon conversion was described by the unreacted, shrinking-core model, with the rate constants for runs catalyzed by K_2CO_3 being about four times those for uncatalyzed runs. The activation energies for the

catalyzed and uncatalyzed runs were 134 and 152 kJ/mol, respectively. The principal products of both catalyzed and uncatalyzed steam gasification were H_2 and CO_2. The water-gas shift reaction reached equilibrium for most experiments at 900°C and some at 800°C, with the presence of K_2CO_3 having little effect on the approach to equilibrium.

Acknowledgement

The experimental portion of the study was carried out with the cooperation and financial support of the United States Department of Energy, using the facilities of the Pittsburgh Energy Technology Center in Bruceton, Pa. Mr. John W. Courts assisted in the operation of the experimental apparatus.

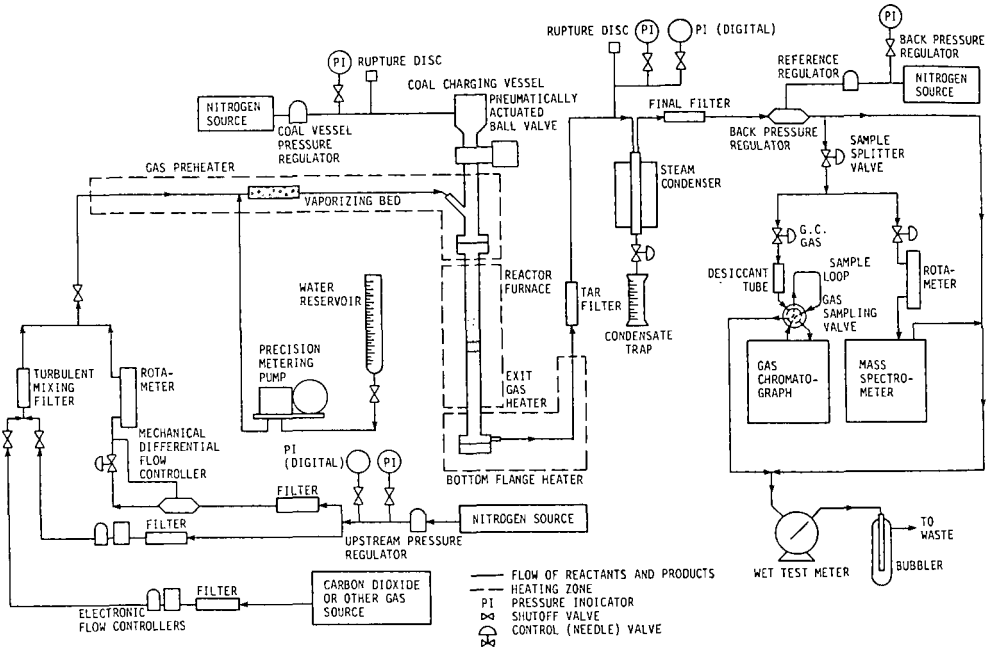

Figure 1. Flow diagram for experimental apparatus

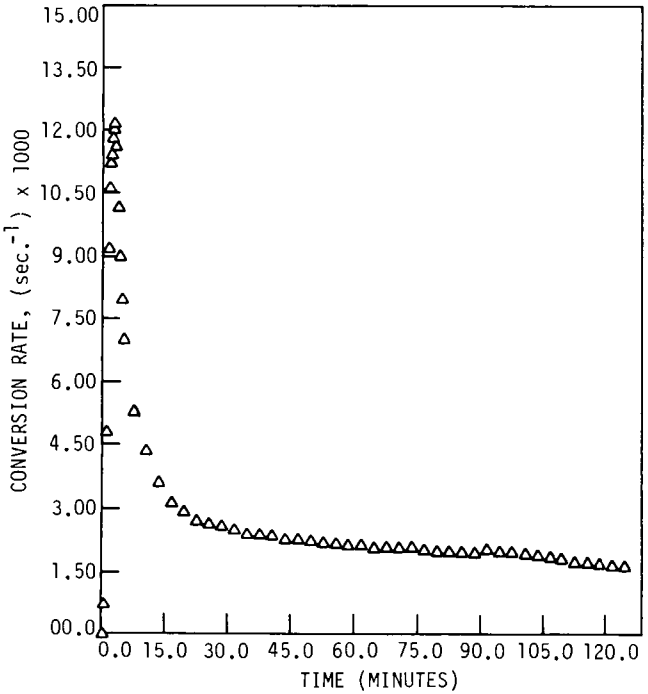

Figure 2. Rate of carbon conversion versus time; conditions = 700°C, 10 wt.% K_2CO_3-impregnated coal, and N_2-steam as reactant gas

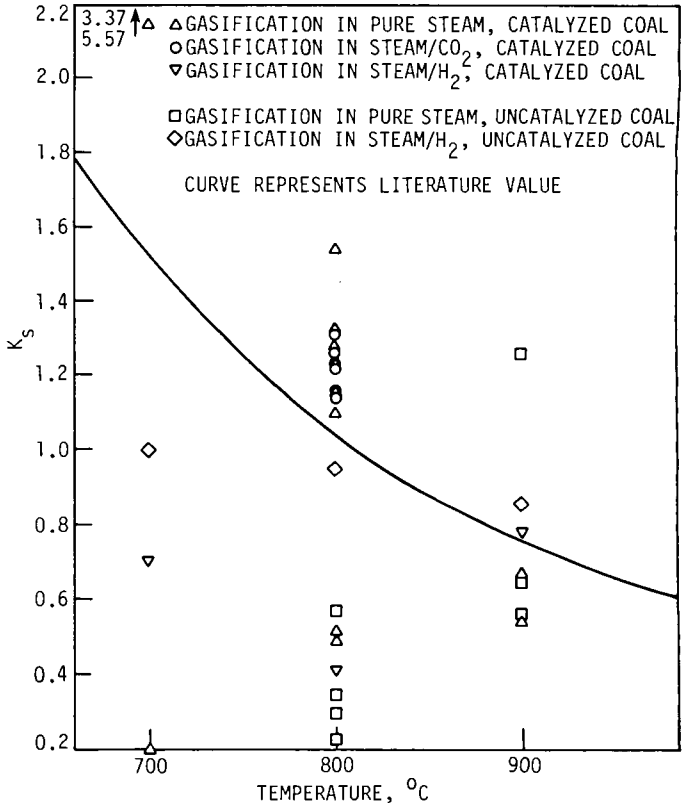

Figure 3. Approach of product gases CO, CO_2, H_2, and H_2O to thermodynamic equilibrium of the system: $CO + H_2O \rightarrow CO_2 + H_2$

CATALYTIC EFFECTS OF ALKALI METAL SALTS IN THE GASIFICATION OF COAL CHAR

D. W. McKee, C. L. Spiro, P. G. Kosky and E. J. Lamby

General Electric Corporate Research & Development
Schenectady, NY 12301

INTRODUCTION

Coal is a complex and variable carbonaceous rock which is composed basically of two types of materials. The macerals or carbonaceous remains of plants constitute the organic fraction of coal, with the remainder comprising minerals or inorganic impurities present in the parent vegetation or deposited subsequently. The major mineral components of coal include clays, alkaline carbonates, metallic sulfides, oxides and quartz, but the minor and trace impurities may include most of the elements of the Periodic Table.[1]

The reactivity and properties of coal can be profoundly influenced by these inorganic impurities.[2-4] Currently, there is interest not only in the effects of mineral matter on the chemical behavior of coal but also in the possibility of adding catalysts to coal in order to lower the temperature required for gasification processes. For example, it has been known for over one hundred years that the reactivity of coal and char towards steam is promoted by the addition of alkalis, such as caustic soda or lime.[5] There are a number of processes under development today which utilize the catalytic properties of alkali carbonates to improve the reactivity of coal in the gasifier.[6-8] Earlier work has shown that the carbonates and oxides of the alkali and alkaline earth metals are among the most active catalysts for the gasification of carbonaceous materials in steam and carbon dioxide.[9-11] However, there is still no generally accepted explanation for these catalytic effects.[12]

This paper describes the results of a continuing study of the catalytic behavior of salts of the alkali metals in the gasification of coal char by steam and CO_2. The main purpose of this work is to investigate possible mechanisms of the catalysis and to elucidate the effects of mineral impurities on the reactivity of coal char. For this purpose the behavior of a typical char and a pure graphite powder have been compared in the presence and absence of added alkali catalysts. In a companion paper (13), the effects of char pyrolysis temperature, surface area and mode of catalyst addition are described.

EXPERIMENTAL

Materials

The char used in this work was prepared from a large sample of Illinois #6 HVB bituminous coal from Inland Mine #1, Sessor, Illinois. Proximate and ultimate analyses of this coal sample are given in Table I. The results of x-ray diffraction on ash residues after low temperature ashing (LTA) showed major amounts of kaolinite and minor amounts of quartz and pyrite.

Initially the coal was coarse ground, homogenized, vacuum dried at 105°C and then stored in a vacuum desiccator. In some cases salt catalysts were added to coal samples before pyrolysis. Thus, about 15 g. of the dried coal was micronized in a nitrogen-driven fluid grinding mill to give a particle size of the order of several microns. A known amount, generally 5 percent, of the dried powder salt, e.g., K_2CO_3, CH_3COOK, was then added to the coal and the mixture rolled for four hours in a rolling mill. The doped samples were then placed in alumina crucibles and pyrolyzed in nitrogen at 700°C for 2 hours. Observed weight losses of the coal

samples during this pyrolysis were of the order of 30 percent. In other cases the catalysts were added after charring at 700°C by mixing weighed amounts of salts and char together in a Fisher Minimill. The char samples had surface areas of approximately 280 m^2/g., as determined by CO_2 adsorption at 195°K.

Spectroscopic grade graphite powder (-325 mesh, Type UCP-2^R, highest purity) was obtained from Ultra Carbon Corp. This material had an initial surface area of 7.5 m^2/g., as determined by nitrogen adsorption at -195°C.

The salt additives were Analytical Reagent or Certified ACS Grade materials and were used without further treatment. The gaseous atmospheres used included Linde Instrument Grade carbon dioxide and Linde Ultra-High Purity Grade helium. For experiments in steam (water vapor), the helium was passed through a distilled water bubbler at 25°C to give a water vapor pressure of 23 mm. (3.1 kPa) in the gas stream.

Proximate Analysis

	% Moisture	% Ash	% Volatiles	% Fixed C	BTU/lb
As Received	0.72	9.68	39.45	50.15	12979
Dry Basis	-	9.75	39.74	50.51	13073

Free Swelling Index = 5

Ultimate Analysis

	% Moisture	% C	% H	% N	% Cl	% S	% O (diff.)
As Received	0.72	73.06	5.04	1.68	0.39	1.20	8.23
Dry Basis	-	73.59	5.08	1.69	0.39	1.21	8.29

Table I: Analyses of Illinois #6 Coal Sample

Procedure

Thermogravimetric studies and measurements of the isothermal kinetics of the catalyzed gasification of char and graphite in CO_2 and water vapor were carried out in the Mettler Thermoanalyzer-2 automatically recording balance as previously described.[14] Kinetic measurements at a series of constant temperatures between 600 and 1000°C were made on 200 mg. samples of the doped carbons, using flowing CO_2 at 1 atm. (1.02×10^2 kPa) and a flow rate of 200 ml.min^{-1}. Gasification in water vapor was accomplished in a water vapor-saturated helium stream (23 mm. H_2O, 3.1 kPa) at a flow rate of 300 ml.min^{-1}. Kinetic data were generally plotted in the form of Arrhenius plots (rates vs. $1/T$°K), the gasification rates at each temperature being derived experimentally from the relation,

$$\text{Rate } (\text{min}^{-1}) = \frac{dW/dt}{W_o}$$

where W_o is the initial weight of the sample. In all cases, in order to minimize the effects of changing surface area and catalyst concentration, the total weight loss during gasification of each sample was kept below 15 percent.

Some thermogravimetric measurements of the reactions between the salts and the carbons and between the salts and selected minerals were carried out by heating appropriate mixtures in the thermobalance at a linearly increasing temperature of $10^{o}Cmin^{-1}$ using flowing atmospheres of pure dry helium or carbon dioxide.

RESULTS

Catalyzed Gasification in Steam

As expected, the carbonates of the alkali metals proved to be effective catalysts for the gasification of both char and graphite in steam. In the case of the char, the addition of 5 percent by weight of the salts resulted in slightly more active chars when the catalysts were introduced prior to charring at 700°C rather than physically mixed with the char after charring (13). In general, the reactivity of the doped chars in steam decreased on successive thermal cycles and with time at a constant gasification temperature. This effect will be discussed in more detail below. Figure 1 shows Arrhenius plots (gasification rates vs. $1/T^{o}K$) for the 700°C char doped with 5 percent by weight of alkali carbonates after charring. These data were obtained during the second thermal cycle in each case. A similar order of catalytic activity was observed previously for graphite,[15] although in this case Na_2CO_3 was slightly less active than K_2CO_3. Pure graphite was considerably less reactive than the uncatalyzed char sample, however the catalytic effects of the added salts were more marked in the former case, so that the catalyzed gasification rates in steam were quite similar for both graphite and char over the 600-900°C temperature range. Gasification rates for graphite doped with 1 and 5 wt. percent of the alkali salts were about the same, whereas with the char a progressive increase in rate was observed with increasing carbonate concentration up to 20 weight percent, as shown in Figure 2. This marked difference in behavior between graphite and char was probably related to the large difference in surface area between the two materials although the active site area was not known in either case. However, with a series of chars, prepared in the presence and absence of added catalysts, there was no significant correlation between reactivity and surface area. In fact, surface areas were generally somewhat smaller for catalyst-doped samples than for uncatalyzed chars. Also there was little difference in gasification rates when the char particles were ground from ca. 1 mm. size to ca. 1 μm.[13] These results indicate that surface areas and particle size are not important parameters in determining char reactivity, at least for chars of the same type and the same heat treatment history. In the steam environment, Li_2CO_3 was clearly the most active catalyst, with Na_2CO_3 and K_2CO_3 exhibiting somewhat lower activity. Other additives, such as KNO_3 and K_2SO_4, also showed substantial catalytic activity, whereas KCl was somewhat less active.

As noted above, the catalyzed char samples showed a progressive loss in reactivity towards steam during the experiments. This phenomenon, which was not observed with graphite, was studied in some detail. Figure 3 shows kinetic data obtained with a char sample doped with 5 weight percent K_2CO_3 during three successive thermal cycles. The initially high gasification rates in steam fell by a factor of about two on the second cycle with progressively smaller deactivation effects on subsequent cycles. Figure 4 shows the results of isothermal rate measurements obtained at 800°C for char samples initially doped with 2, 5 and 10 percent K_2CO_3. In all three cases a rapid drop in gasification rate occurred during the first hour with more gradual decreases during the subsequent four hours of the experiments. In the case of the sample containing 10% K_2CO_3, the gasification rate was so high that the rate began to decrease after about 3 hours because of loss of contact between the catalyst phase and the residual char substrate.

In steam (water vapor) catalyst deactivation was observed for every catalyst additive tested, regardless of whether the salt was added before or after charring. Figure 5 shows data obtained from a char sample to which 5 wt. % potassium acetate had been added before

charring at 700°C. Again a marked progressive loss in activity was found on successive thermal cycles, accompanied by an increase in the apparent activation energy from 18 to 51 Kcal/mole during the four cycles shown.

As it was found that this progressive deactivation did not occur during the catalyzed steam gasification of graphite, it appeared unlikely that the effect was due to sintering, agglomeration or vaporization of the salt catalyst. It seemed more probable that catalyst deactivation was related to reaction of the alkali salts with minerals such as quartz, clay, kaolin, and pyrite present in the char samples. Some experiments were therefore carried out in the thermobalance, using mixtures of K_2CO_3 with these mineral species, to determine if solid state reactions might occur at temperatures in the gasification range (600-1000°C).

Figure 6 shows thermograms (weight change vs. temperature) for 200 mg. pure K_2CO_3 (dashed curve) and for a mixture of 200 mg. K_2CO_3 and 200 mg. powdered quartz (solid curve) on heating in a stream of dry helium during a linear temperature rise of 10°C/min. Following an initial dehydration at 100-150°C, the pure salt showed no further weight loss on heating to 980°C and a slight loss at higher temperatures due to vaporization above the melting point. On the other hand, the mixture of salt and quartz lost weight rapidly at temperatures above 750°C, probably as a result of evolution of CO_2 by reactions of the type

$$K_2CO_3 + SiO_2 = K_2SiO_3 + CO_2$$

A variety of silicate-forming reactions are in fact possible. The extent of these reactions at a given temperature and the temperature of inception of the solid state reactions would be expected to depend on the particle size and interfacial contact area between the solid phases. Also the presence of CO_2 in the gas phase would tend to suppress these reactions. Similar thermogravimetric data for (A) 200 mg. pure K_2CO_3, (B) 200 mg. of powdered illite clay, and a mixture of 200 mg. K_2CO_3 and 200 mg. illite, are shown in Figure 7. The curve labelled (A+B) is the sum of curves (A) and (B) and represents the weight changes expected for a salt-illite mixture if no reaction occurred between the two phases. It is evident from the lower solid curve in Figure 7 that a reaction between the clay and the salt took place above 700°C with a continuous loss in weight of the sample, probably as a result of liberation of CO_2. The composition of the mineral illite, a complex aluminosilicate, is, however, indefinite, so no equation can be written for this reaction. Illite, however, is an important major mineral constituent in many coals. Similar data for kaolin-K_2CO_3 mixtures are shown in Figure 8. A comparison of curve (A+B) for kaolin + K_2CO_3 with no reaction and curve C, the experimental thermogram for the mixture, indicates that a reaction between the mineral and the salt took place at temperatures above 700°C with the loss of a volatile product, most likely CO_2. In a CO_2 atmosphere, this reaction was inhibited (curve D), but even in this case a marked loss in weight occurred above 900°C. A possible reaction between the salt and the kaolin is

$$Al_2Si_2O_5(OH)_4 + K_2CO_3 = 2KAlSiO_4 + 2H_2O + CO_2$$

The expected weight loss for the completion of this reaction is 60 mg, which corresponds closely to the experimental loss in weight of the kaolin-salt mixture between 650 and 1100°C. The reaction of potassium salts with the mineral constituents of fly ash to produce the water-insoluble mineral kalsilite ($KAlSiO_4$) has been reported by Karr et. al. to occur in the presence of steam at 850°C.[16]

Catalyzed Gasification in CO_2

As expected, the alkali metal carbonates were found to be active catalysts for gasification of coal char in CO_2. Results for the catalyzed gasification of graphite have been reported previously.[14] With coal char the kinetic data were much more reproducible in CO_2

than in steam. Figure 9 shows data obtained for a char-5% K_2CO_3 (the same sample as that used in Figure 3) on gasification in 1 atm. CO_2 between 600 and 900°C. In this case, during four successive thermal cycles the kinetic data were remarkably constant, with only a slight decrease in rates between the first and second cycles. The apparent activation energy for this series of experiments was 49.3 Kcal/mole. Similar data for a char sample to which 5 % K_2CO_3 had been added before the 700°C charring step are shown in Figure 10. Again, following a small reduction in gasification rates between the first and second cycles, the reactivity on further cycling was reproducible, with an apparent activation energy of 53.8 Kcal/mole. Comparison with Figure 9 indicates that the catalytic effect of the K_2CO_3 was similar regardless of whether the salt was added before or after charring. Similar data for a CH_3COOK-doped char sample are shown in Figure 11. In this case also, following a slight reduction in reactivity between cycles 1 and 2, subsequent kinetic data were quite reproducible. Comparison with Figure 5 shows the marked difference in behavior of this doped char sample in the two gaseous environments.

Gasification data in CO_2 for char doped with 5% Li_2CO_3, Na_2CO_3 and K_2CO_3 (added prior to charring) are shown in Figure 12. In this environment there was no significant difference in activity between the three salts when compared on a weight % basis. The effect of increasing concentration of K_2CO_3 (added prior to charring) on the CO_2 gasification kinetics is illustrated in Figure 13. Reactivity generally increased with K_2CO_3 concentration, at least up to the 20% level, however, the effect on apparent activation energy was small.

Reaction between Alkali Carbonates and Carbon

When K_2CO_3 is heated with carbon in an inert atmosphere, a solid state reaction takes place between 600 and 900°C, depending on the particle size and extent of physical contact between the two phases. The products of this reaction are CO and potassium vapor which sublimes into the cooler parts of the apparatus.[15] Figure 14 shows thermograms (weight changes vs. temperature) for K_2CO_3-char and K_2CO_3-graphite mixtures on heating in dry helium in the thermobalance at an increasing temperature of 10°C/min. In the case of graphite, loss in weight became marked above 800°C and the reaction was essentially completed at 1000°C. The char had a much larger surface area than the graphite and reaction with the salt began at about 600°C. This solid state reaction, which takes place in the gasification range, is believed to play an important role in the gasification of carbon with CO_2 or steam in the presence of the K_2CO_3[10,14] as discussed in the next section.

DISCUSSION

The reactivities of coal chars are obviously strongly influenced by a number of factors such as charring temperature and thermal history, pore size distribution and the presence of ubiquitous mineral impurities. However, the catalytic behavior of additives such as the alkali metal carbonates is similar for char and graphite and the same mechanisms probably operate in both cases.

The main effect of the salt catalysts (Figures 1,2,12,13) in both gasification reactions is to increase the pre-exponential factor of the rate equation. Changes in the apparent activation energy are small from catalyst to catalyst and on increasing the salt concentration. The most likely explanation of this effect is that the salt reacts with the char substrate to produce active sites on the surface where gasification can proceed. Increasing the amount of salt present increases the effective concentration of these active sites up to the point at which the surface becomes saturated.

A plausible mechanism which has been proposed previously[10,14,15] to account for the catalytic effects of Na_2CO_3 and K_2CO_3 in these reactions is shown in Table II. A common first

step, reaction (1) is suggested for both reactions, with the subsequent steps being different for CO_2 and H_2O as the gaseous oxidant.

C - CO_2 REACTION

$$M_2CO_3 + 2C = 2M + 3CO$$
$$2M + CO_2 = M_2O + CO \quad (2)$$
$$M_2O + CO_2 = M_2CO_3 \quad (3)$$
$$C + CO_2 = 2CO$$

C - H_2O REACTION

$$M_2CO_3 + 2C = 2M + 3CO \quad (1)$$
$$2M + 2H_2O = 2MOH + H_2 \quad (4)$$
$$2MOH + CO = M_2CO_3 + H_2 \quad (5)$$
$$C + H_2O = CO + H_2$$

Table II: Carbon Gasification Catalyzed by Na_2CO_3 or K_2CO_3

Although reaction (1) possesses a positive free energy change at temperatures in the 600-1000°C range, at low partial pressures of CO the reaction can proceed rapidly, as shown by the TGA data in Figure 15. Figure 15 shows the equilibrium stability regions of K_2CO_3 and K(g) for reaction (1), calculated from free energy data, as functions of temperature and the partial pressures (in atmospheres) of K(g) and CO. The sloping lines at each temperature separate the region of stability of K_2CO_3 (upper left) from that of K(g) (lower right). An overall gasification rate of $5 \times 10^{-3} min^{-1}$ (about the maximum attained in this study at 900°C) would give an ambient partial pressure of CO of about 10^{-3} atm. above the gasifying char sample. At this value of P_{CO}, and with a similar value of P_K, Figure 15 indicates that reaction (1) would be thermodynamically possible for all temperatures above about 800°C. At a temperature of 600°C the measured gasification rate, and the ambient value of P_{CO}, are about two orders of magnitude less than at 900°C and Figure 15 shows that reaction (1) is again possible for $P_K = P_{CO} = 10^{-3}$ atm. The steady state values of P_K reaction will in fact be much less than P_{CO} because of the occurrence of reactions (2) and (4). Direct evidence that reaction (3) does occur has recently been obtained by Wood et al.,[16] using high temperature Knudsen cell mass spectrometry. On heating K_2CO_3 and carbon together at temperatures of 500°C and above, the evolution of K vapor and CO could be measured. Thus, reaction (1), which is inhibited by increasing amounts of CO in the gas phase, is probably the rate determining step in the case of the gasification reactions catalyzed by Na_2CO_3 and K_2CO_3. Reactions (2) and (3) and also (4) and (5) have large negative free energy values at gasification temperatures and are thus favored thermodynamically, although little is known about their kinetics.

A somewhat different pathway probably operates in the case of the reactions catalyzed by Li_2CO_3 as Li_2O is more stable than the oxides of Na and K, also Li_2CO_3 is more easily hydrolyzed to hydroxide than the carbonates of Na and K. A possible sequence of reactions that might be involved in the catalysis process in the case of Li_2CO_3 is shown in Table III below. Evidence for the occurrence of these individual reactions is still, however, indirect and future efforts will be directed to exploring the catalytic process by the aid of isotopic tracers and in determining the relative rates of the elementary steps involved in the catalyzed gasification process.

C - CO_2 REACTION

$$Li_2CO_3 + C = Li_2O + 2CO \quad \text{(i)}$$
$$Li_2O + CO_2 = Li_2CO_3 \quad \text{(ii)}$$
$$C + CO_2 = 2CO$$

C - H_2O REACTION

$$Li_2CO_3 + H_2O = 2LiOH + CO_2 \quad \text{(iii)}$$
$$2LiOH + C = Li_2O + CO + H_2 \quad \text{(iv)}$$
$$Li_2O + H_2O = 2LiOH \quad \text{(v)}$$
$$C + H_2O = CO + H_2$$

Table III: Carbon Gasification Catalyzed by Li_2CO_3

The above mechanistic schemes, although feasible for the alkali carbonates, cannot readily explain the observed catalytic activity of the alkali halides in these reactions. Such salts as KF, NaF and LiCl have been found to be moderately active catalysts for the gasification of both char and graphite in steam and CO_2. The route by which the alkali halides function as catalysts in these reactions is not clear at this point. Direct reduction of these salts to alkali metal by reaction with the carbon substrate seems unlikely on thermodynamic grounds. However, although the direct hydrolysis reaction

$$KF + H_2O = KOH + HF \quad \Delta G^{o}_{1100K} = +24 \text{ Kcal/mole}$$

has a positive free energy change at gasification temperatures, appreciable and catalytically active concentrations of KOH might be formed in a flowing gas in which the partial pressure of HF is low. KF-char mixtures have, in fact, been observed to evolve appreciable amounts of HF during steam gasification,[18] hence dissociation and hydrolysis of the KF salt evidently does occur in the presence of carbon and steam. In CO_2 the mechanism of catalysis by KF cannot be interpreted on this basis. It is interesting, however, that the alkali halide salts are also moderately active catalysts for the oxidation of carbon by molecular oxygen.[19] On heating a mixture of graphite powder and pure KF in air at 900°C until the carbon was completely gasified, the residue was found by analysis to contain appreciable amounts of K_2O (2.4% by weight). A similar experiment with pure NaCl produced lower (0.4%) amounts of Na_2O. As no oxides could be detected in the original halide salts, the catalytically active alkali oxides may have resulted from the oxidation of the halides during the gasification of the carbon, possibly by a reaction of the type

$$2NaCl + C + 3/2\, O_2 = Na_2O + CO_2 + Cl_2 \quad \Delta G^{o}_{1100K} = -11 \text{ Kcal/mole}$$

though other halogenated species, such as HX, COX_2, HOX and the like could be formed in low concentrations.

CONCLUSIONS

The catalytic effects of alkali carbonates and other salts in the gasification of coal char and graphite in steam and CO_2 have been studied. Although the patterns of catalytic activity for the various additives were similar for both char and graphite, the reactivity of the char was influenced by factors such as charring temperature, porosity and the presence of mineral impurities.

On increasing the charring temperatures from 700°C to 900°C, there was a marked decreased in reactivity towards both steam and CO_2, presumably due to loss in porosity of the

char or annealing of active sites at the higher temperature. Non-porous graphite had a much lower surface area than the char and a lower reactivity, in the absence of catalysts. However, within a series of char samples prepared at the same temperature, there was no significant correlation between reactivity and surface area. In fact, surface areas were slightly reduced when salt catalysts were added to char samples, even though the reactivity was increased considerably. Also, the reactivity of the catalyzed samples proved not to be strongly dependent on the mode of addition of the catalyst and physical mixing of the salt with the pre-carbonized char was almost as effective as adding the catalyst prior to charring.

An observation of important practical implication was the progressive and rapid initial loss in catalytic activity during gasification at constant temperature and on thermal cycling between gasification temperatures and ambient. This effect, which was much more marked in steam than in CO_2, appeared to be the result of reaction of the salt additives with mineral matter in the char to form stable inert silicates and aluminosilicates.

Thermodynamically feasible mechanisms for the alkali carbonate catalysts which involve sequences of oxidation/reduction reactions with the intermediate formation of alkali metal or oxides have been discussed. The moderate catalytic activity of certain alkali halide salts is however difficult to explain on this basis.

ACKNOWLEDGEMENT

Support of this work by the US Department of Energy (Contract No. DE-AC21-80MC 14591) is gratefully acknowledged.

References

1. N. Berkowitz, "An Introduction to Coal Technology," Chapt. 2, Academic Press, NY (1979).
2. K. Otto, L. Bartosiewicz and M. Shelef, Fuel 58, 85 (1979).
3. A. Linares-Solano, O. P. Mahajan and P. L. Walker, Jr., Fuel 58, 327 (1979).
4. K. J. Huttinger and W. Krauss, Fuel 60, 93 (1981).
5. T. du Motay, British Patent 2458 (1967).
6. J. E. Gallagher, Jr., and C. A. Euker, Jr., Energy Research 4, 137 (1980).
7. A. L. Kohl, R. B. Harty, J. G. Johanson and L. M. Naphtali, Chem. Eng. Prog., 74, 73 (1978).
8. A. E. Cover, W. C. Schreiner and G. T. Skaperdas, Chem. Eng. Prog., 69, 31 (1973).
9. N. Kayembe and A. H. Pulsifer, Fuel 55, 211 (1976).
10. M. J. Veraa and A. T. Bell, Fuel 57, 194 (1978).
11. D. W. McKee, Carbon 17, 419 (1979).
12. D. W. McKee, "Chemistry and Physics of Carbon," P. L. Walker and P. A. Thrower, Eds., Vol. 16, p. 1, Marcel Dekker, NY 1981.
13. C. Spiro, D. McKee, P. Kosky, E. Lamby, and D. Maylotte, to be published.
14. D. W. McKee and D. Chatterji, Carbon 13, 381 (1975).
15. D. W. McKee and D. Chatterji, Carbon 16, 53 (1978).
16. C. Karr, P. Waldstein and J. Kovach, J. Inst. Fuel 47, 177 (1974).
17. B. J. Wood, K. M. Sancier, J. G. McCarty and H. Wise, "The Mechanism of the Catalytic Gasification of Coal Char," Technical Progress Report, SRI International, January 1981, DoE Contract No. DE-AC21-14593.
18. R. Lang, Exxon Research and Engineering Co., unpublished observations.
19. D. W. McKee, unpublished observations.

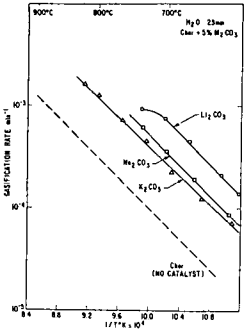

Figure 1 Catalytic effects of alkali metal carbonates on the gasification of coal char in water vapor. 5% salt added after charring at 700°C. Second cycle rate data vs. $1/T°K$.

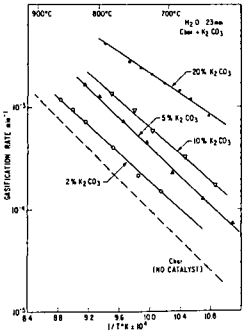

Figure 2 Effect of K_2CO_3 concentration on the rate of gasification of coal char in water vapor. Salt catalyst added after 700°C charring. Second cycle rate data vs. $1/T°K$.

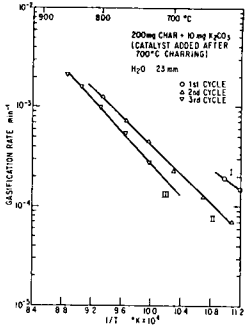

Figure 3 Gasification kinetics (rate vs. $1/T°K$) in water vapor for a 5% K_2CO_3-doped char (salt added after charring), for three successive thermal cycles.

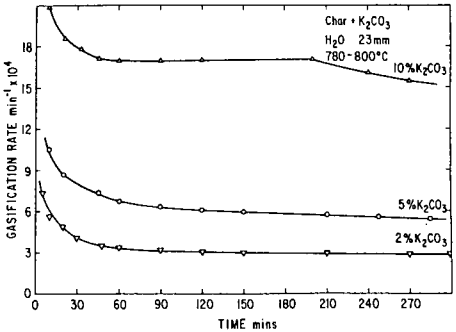

Figure 4 Gasification rates in water vapor vs. time at 800°C for a char with various concentrations of added K_2CO_3.

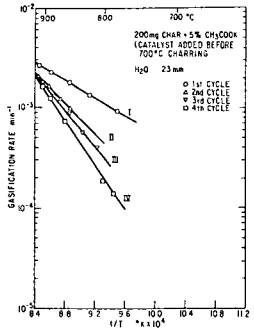

Figure 5 Gasification kinetics (rate vs. $1/T^{0}K$) in water vapor for a char containing initially 5% CH_3COOK (salt added before 700°C charring). Rates measured during four successive thermal cycles.

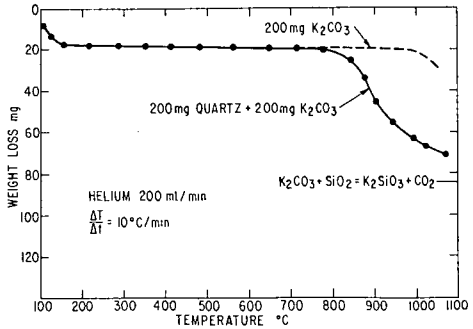

Figure 6 Thermograms (weight loss vs. temperature) for K_2CO_3 and a 1:1 quartz-K_2CO_3 mixture on heating in helium at 10°C/min.

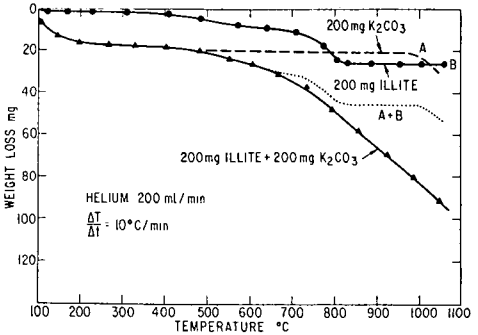

Figure 7 Thermograms (weight loss vs. temperature) for (A) K_2CO_3, (B) Illite and an illite-K_2CO_3 mixture on heating in helium at 10°C/min.

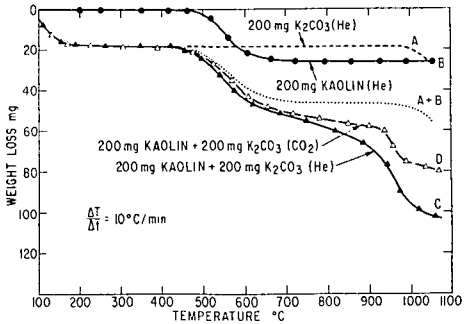

Figure 8 Thermograms (weight loss vs. temperature) for (A) K_2CO_3, (B) Kaolin and a kaolin-K_2CO_3 mixture on heating in helium (C) and CO_2 (D) at 10°C/min.

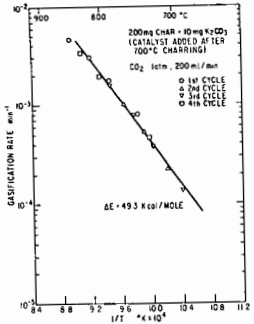

Figure 9 Gasification kinetics (rate vs. $1/T^{o}K$) in CO_2 for a char with 5% K_2CO_3 added after charring. Rates shown for four successive thermal cycles.

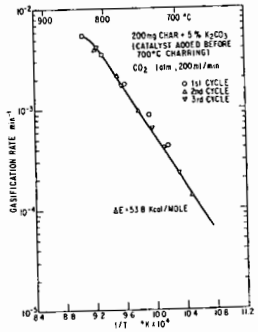

Figure 10 Gasification kinetics (rate vs. $1/T^{o}K$) in CO_2 for a char containing initially 5% K_2CO_3 (salt added before 700°C charring). Rates shown for three successive thermal cycles.

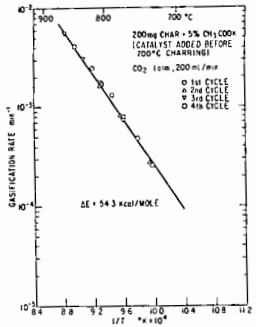

Figure 11 Gasification kinetics (rate vs. $1/T^{o}K$) in CO_2 for a char containing initially 5% CH_3COOK (salt added before 700°C charring). Rates shown for four successive thermal cycles.

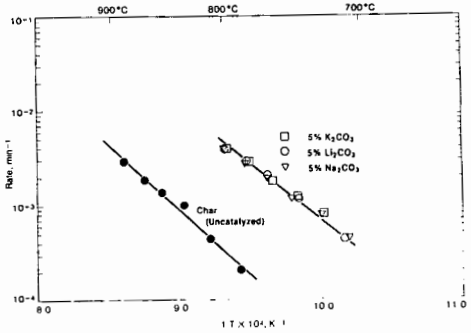

Figure 12 Gasification kinetics (rate vs. $1/T^{o}K$) in CO_2 for chars doped with 5% Li, Na and K carbonates (added prior to 700°C charring).

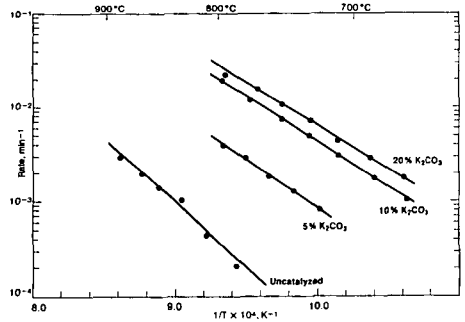

Figure 13 Gasification kinetics (rate vs. $1/T^{o}K$) in CO_2 for chars doped with 5%, 10%, and 20% K_2CO_3 (added prior to 700°C charring).

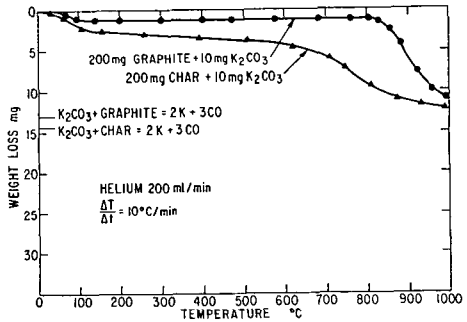

Figure 14 Thermograms (weight loss vs. temperature) for graphite-5% K_2CO_3 and char-5% K_2CO_3, on heating in helium at 10°C/min.

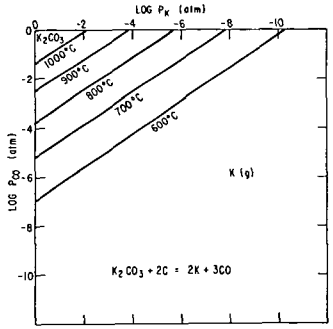

Figure 15 Equilibrium stability regions of K(g) and K_2CO_3 for the reaction $K_2CO_3 + 2C = 2K + 3CO$, as functions of temperature, P_{CO} and P_K.

5360-096bw

KINETICS OF POTASSIUM CATALYZED GASIFICATION

P. Knoer and H. W. Wong. Exxon Research and Engineering Co., Baytown Research and Development Division, P. O. Box 4255, Baytown, Texas 77520.

Commercial applications of the potassium catalyzed coal gasification reaction (CCG) are envisioned to include high pressure (2000 to 4000 kPa) and high concentrations of hydrogen in the gasification reactor (1, 2, 3). Published literature regarding CCG, however, report studies conducted at low pressure or with low concentrations of hydrogen or both (4, 5, 6). The present study was conducted to investigate the gasification reaction under commercially representative conditions. Thus, pressure was varied from 100 to 3500 kPa and hydrogen concentration was varied from 0 to 60%. Other reaction conditions, such as temperature and catalyst loading, were also varied in this study to check published results at these more representative conditions. The data from this study were combined with mechanistic information from the literature (6). Only one kinetic model was found which fit both the data and the literature mechanism. The two adjustable constants for this model were regressed using over 1200 pieces of data. The overall fit between the model and the data is very good.

Experimental Apparatus

This experimental program was carried out using a one atmosphere mini-fluid bed reactor and a fixed bed reactor capable of operating at high pressure. The atmospheric pressure unit was used to study variations in catalyst loading and temperature. These studies were conducted using both H_2O only and H_2O/H_2 mixtures, using chars from steady state pilot plant operations and chars prepared by devolatilization in the laboratory.

A schematic diagram of the mini-fluid bed reactor unit is shown in Figure 1. The reactor portion of the unit consists of a 0.6 cm I.D. quartz U-tube inside a hot steel block. Water is fed to the U-tube using a small syringe pump and is vaporized in the reactor. Argon or hydrogen gas is also fed to the unit. Ceramic beads are placed in the inlet leg of the U-tube to enhance the vaporization of water and to help disperse the gas flow. The exit gases from the reactor flow into an oxidizer where all carbon species are converted to carbon dioxide. After condensing any unreacted steam, the gas stream is bubbled through a sodium hydroxide solution where the amount of total carbon converted is automatically monitored by measuring the conductivity of the solution.

The argon or hydrogen gas fed to the mini-fluid bed serves to fluidize the char particles. The gas rate is typically about 40 cc/min STP which is equivalent to about 7 cm/sec linear superficial velocity in the reactor at 700°C. The minimum fluidizing velocity of the char particles is 3-4 cm/sec. Char sample sizes varied from 0.25 grams to 1.00 gram in the minifluid bed. The water feed rate ranged from 0.2 to 2.5 ml/hour.

The fixed bed reactor was used primarily to study pressure effects. All runs in the fixed bed were made at 700°C using laboratory prepared char. Variations were made in feed gas composition and flow rate. A simplified flow diagram of the fixed bed unit is shown in Figure 2. The unit consists of a high pressure water pump, steam generator, fixed bed reactor, condenser for unreacted steam, gas chromatographs, and dry gas flow measurement system.

The reactor itself is a one-inch Schedule 80 type 316 stainless steel pipe. The pipe holds a char sample inside a split tube furnace.

Effect of Varying Potassium-to-Carbon Ratio

If the overall carbon conversion is altered in the CCG reactor, the ratio of potassium-to-carbon (K/C) in the reactor will change as well. Therefore, the effect of catalyst loading on kinetics must be known in order to be able to optimize initial catalyst loading as well as overall carbon conversion for the CCG process. Experiments were conducted in the atmospheric mini-fluid bed reactor to determine the effect of carbon conversion and catalyst loading on the gasification rate.

Plotting the initial gasification rates against the water soluble K/C ratio reveals an approximately linear relationship between the two as shown in Figures 3 and 4. This is consistent with the earlier findings by others (6).

This suggests that the rate of gasification is proportional to the concentration of a (C-K) species rather than carbon or potassium concentrations per se. At high carbon concentrations and low K/C ratios, the concentration of the (C-K) species is proportional to the concentration of (K) since there is an overabundance of (C). The gasification rate thus appears to be independent of carbon concentration (i.e., zero order kinetics). At low carbon concentrations and high K/C ratios, there is an overabundance of (K). The gasification rate will then appear to be first order with respect to carbon. From studies of pilot plant chars, the demarcation between high and low K/C ratios appears to be about 0.2 mole C/mole water soluble potassium.

Variation of Reaction Temperature

The dependence of gasification rate on temperature was studied in the mini-gasifier, both with and without H_2 in the feed gas.

Figure 5 shows the measured reaction rates as a function of temperature for experiments both with and without H_2 in the reactor. The apparent temperature dependence changes as the composition of the gas fed to the reactor changes. From Figure 4 it is seen that for $H_2O + H_2$ in the feed gas, gasification rate is very sensitive to temperature changes. Gasification rate approximately halves for each 25°C drop in reactor temperature below 700°C.

There is an interaction between feed gas composition and apparent temperature dependence because the mini-reactor is an integral reactor. For example, when pure steam is introduced at the bottom of the bed of char, a mixture of $H_2O + H_2$ issues from the top of the bed. As the rate of reaction changes, the gas composition at various locations in the reactor changes even though the feed gas remains the same. Therefore, as temperature changes, some of the change in rate is due to activation energy, but some of the change is due to gas composition. A reactor model which performs an integration over the bed is required to account for both effects. Our modeling work discussed in the next section of this report has identified the true activation energy as about 50 kcal/g mole.

Gasification Rate Expression

During an earlier phase of research on the CCG process, a screening of gasification reaction rate models was reported by Vadovic and Eakman (5). In this screening, all combinations of from one to four inhibition terms involving the partial pressures of H_2, CO, H_2O, and the cross products of the partial pressures of H_2 and CO, and H_2 and H_2O were tested in the denominator of the gasification rate expression. In all, they tested thirty models. Those models which gave negative coefficients on regression were discarded as being physically unreal. Four additional models were discarded because they gave an infinite rate for a pure steam environment. Of the thirty models tested, three models remained which gave good fit to their data. These three are listed below.

$$\text{(A)} \quad r_G = \frac{k(P_{H_2O} - P_{CO}P_{H_2}/2K_G)}{P_{H_2} + 0.1775\ P_{H_2O}}$$

$$\text{(B)} \quad r_G = \frac{k(P_{H_2O} - P_{CO}P_{H_2}/2K_G)}{P_{H_2} + 0.210\ P_{H_2}P_{CO} + 0.0595\ P_{H_2O}}$$

$$\text{(C)} \quad r_G = \frac{k(P_{H_2O} - P_{CO}P_{H_2}/2K_G)}{P_{H_2} + 1.26\ P_{CO} + 0.349\ P_{H_2O}}$$

For their screening of gasification rate models, Vadovic and Eakman used data from runs in which only pure steam was fed to the bed of coal char. Mixtures of H_2O and H_2 or H_2O, H_2, and CO were introduced and studied in the present program.

In addition to the empirical data, mechanistic considerations were used to discriminate among the three models for catalytic gasification kinetics. Several mechanisms have been proposed for the steam-carbon reaction in the past (7). Recent work by Mims and Pabst (6) indicated that the overall gasification kinetics are consistent with a simple surface oxide mechanism:

$$H_2O + \tau \underset{k_{-1}}{\overset{k_1}{\rightleftharpoons}} \overset{O}{\tau} + H_2 \qquad \text{oxygen exchange}$$

$$\overset{O}{\tau} \xrightarrow{k_2} CO + \tau \qquad \text{surface oxide decomposition}$$

With the larger data base and the proposed mechanism, it was possible to better distinguish among the three rate models identified earlier. Only Model A was found to be consistent with both the mechanism studies and the new data. This model is shown in general form below:

$$r_G = \frac{k(P_{H_2O} - P_{H_2}P_{CO}/2K_G)}{P_{H_2} + b\,P_{H_2O}} \qquad (1)$$

r_G = the rate of gasification in moles per hour per ft^3 of reactor

K_G = the equilibrium constant for steam and β-graphite

P_i = the partial pressure of component i in the reactor

k = the rate constant; it contains the catalyst loading and temperature dependence.

Parameter Estimation for the Gasification Reaction

A total of 28 successful fixed bed runs were made at pressures ranging from 100 to 3500 kPa, H_2 flows ranging from 0 to 1.0 moles per hour, CO flows ranging from 0 to 0.17 moles per hour and steam flows ranging from 0.3 to 1.3 moles per hour. It was observed that the total gas make and gas composition changed during the runs as carbon was depleted from the bed. It was also observed that the methane and carbon dioxide were nearly in chemical equilibrium with the other gas phase components for the conditions studied.

A combination of kinetic constants k and b in Equation 1 were sought which would make the predictions of the fixed bed model best fit the fixed

bed data. Best fit is defined by a small deviation between predicted and observed molar flow rates. Thus, one expression of the objective function would be as follows:

$$\text{minimize } s^2 = \sum_k \sum_j \sum_i (\tilde{N}_{ijk} - N_{ijk})^2 \qquad (2)$$

where,

S = the sum of the squares of the deviations

$\tilde{N}_{ijk}$ = a predicted molar flow rate
N_{ijk} = an observed molar flow rate
i = a particular gas component (H_2, CO, CO_2, CH_4, or H_2O)
j = a particular level of carbon in the fixed bed reactor
k = a particular fixed bed reactor run

Hunter (8) has shown that use of this objective function will yield the maximum likelihood estimates for k and b only if the following three criteria are met:

(1) The measurement errors on each of the five gas species are normally distributed and these errors are independent.

(2) The variances on the measurement errors of all of the five gas species are identical.

(3) There is no correlation between the measurement errors for any two gas species.

From the design of the experiment we know that the measurements on the four fixed gases were related in that they were all sampled simultaneously by the gas chromatograph and the composition was normalized. Therefore, an error in the measurement of any one of the four fixed gases would be distributed among the other three fixed gases as well. Furthermore, any error in the measurement of CO or CO_2 would result in an error in the measurement of H_2O as well since H_2O yield was calculated by oxygen balance. As a result of these considerations, equation 2 was not used as the objective function for this study.

Box and Draper (9) have derived the following objective function for use in cases where unquantified covariance exists in the experimental measurements:

$$\text{minimize} \qquad \Delta = \det | S_{nm} |$$

where,

Δ = the determinant of the 5 x 5 matrix composed of elements S_{nm}

and,

$$S_{nm} = \sum_k \sum_j (\tilde{N}_{njk} - N_{njk})(\tilde{N}_{mjk} - N_{mjk})$$

where,

n,m = particular gas components
j,k = as above.

Hunter (8) recommends the use of this objective function when covariance might exist in the experimental measurements.

Rosenbrock's hill climbing method (10) was used to search for the optimum values of k and b in equation 1. For each set of k and b, the fixed bed reactor model equations were numerically integrated 28 times; i.e., once for each fixed bed reactor run being estimated. For each of the 28 fixed bed reactor runs, comparisons between calculated and observed molar flow rates were made for 8 to 10 different levels of carbon in bed. With five different gas species being estimated, there were over 1200 comparisons made for each guess of a k,b pair. For each guess, the appropriate cross products of deviations were calculated and accumulated to form the 5 X 5 matrix of elements S_{nm}. The determinant of this matrix was calculated and used by the Rosenbrock routine to make a new guess at k and b.

Results of the Regression

The initial guesses for k and b were taken from the results of Vadovic and Eakman (5). For 700°C and the K/C ratio used these were as follows:

k = 0.0204
b = 0.1775

The routine returned the following values:

k = 0.0173
b = 0.2080

Figures 6 through 10 are parity plots of the predicted and observed values of the molar flow rates of H_2, CO, CO_2, CH_4, and H_2O. The parity plots show that the fixed bed reactor model does a good job of predicting all of the gas species from the fixed bed reactor runs over a wide variety of conditions with the exception of CH_4. A slight overprediction of CH_4 yield is observed.

Conclusions

The potassium catalyzed gasification of Illinois No. 6 bituminous coal was found to fit a Langmuir-Hinshelwood type kinetic model. This model provides a good fit to fixed bed and miniature fluid bed data over pressures

ranging from atmospheric to 3500 kPa and over broad ranges of gas composition. The model closely predicted the observed flow rates of each specie in the product gas over a range of an order of magnitude or more. This model is consistent with the surface oxide mechanism for the steam-carbon reaction which was proposed in earlier literature. A sophisticated statistical regression technique was used to choose the two adjustable constants for this model by comparison with over 1200 pieces of data.

The kinetic constants were regressed from data taken over the range of practical commercial interest. This kinetic model may be combined with independently verified correlations for bubble growth and mass transfer in a fluidized bed and used directly to study larger pilot plant data or scale-up issues.

ACKNOWLEDGEMENT

This work was supported by the United States Department of Energy under Contract No. ET-78-C-01-2777 and by the Gas Research Institute.

REFERENCES

1. N. C. Nahas and J. E. Gallagher, Jr., "Catalytic Gasification Predevelopment Research," Proceedings of the Thirteenth Intersociety Energy Conversion Engineering Conference, (August 1978).

2. B. T. Fant and C. A. Euker, Jr., "Exxon's Catalytic Coal Gasification Process," Presented to The First International Research Conference, (June 9-12, 1980).

3. D. Hebden and H. J. F. Stroud, "Coal Gasification Processes," in Chemistry of Coal Utilization Second Supplementary Volume, M. A. Elliot ed., (1981), pp. 1649-1650.

4. H. G. Hipkin, Carbon-Steam System at Low Temperatures and Under Pressure, PhD Thesis, M.I.T. (1951).

5. C. J. Vadovic and J. M. Eakman, "Kinetics of Potassium Catalyzed Gasification," presented at the meeting of the American Chemical Society (September, 1978).

6. C. A. Mims and J. K. Pabst, "Alkali Catalyzed Carbon Gasification II. Kinetics and Mechanism," presented at the meeting of the American Chemical Society (August, 1980).

7. P. L. Walker, Jr., F. Rusinko, Jr., and L. G. Austin, Advances in Catalysis XI, (1959).

8. W. G. Hunter, "Estimation of Unknown Constants From Multi-response Data," I & E C Fundamentals, Vol. 6, (1967), pp. 461-463.

9. G.E.P. Box and N. R. Draper, Biometrika, V52, (1965), p. 355.

10. H. H. Rosenbrock, "An Automatic Method for Finding the Greatest or Least Value of a Function," Computer J., 3 (1960).

81B-10-88

FIGURE 1

SCHEMATIC OF MINI-FLUID BED REACTOR UNIT

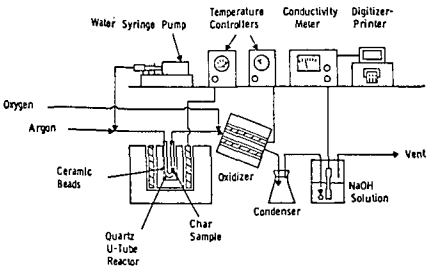

80B-12-1259

FIGURE 2

SIMPLIFIED FLOW DIAGRAM OF BENCH SCALE GASIFICATION UNIT

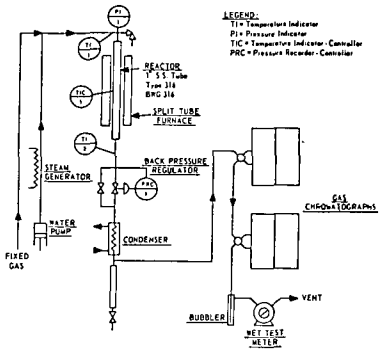

81B-3-37

80B-9-204

FIGURE 3

GASIFICATION RATE INCREASES LINEARLY WITH (K/C) RATIO

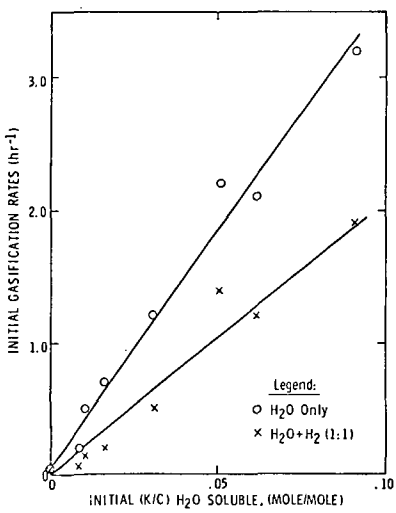

FIGURE 4

EFFECT OF CATALYST LOADING ON GASIFICATION

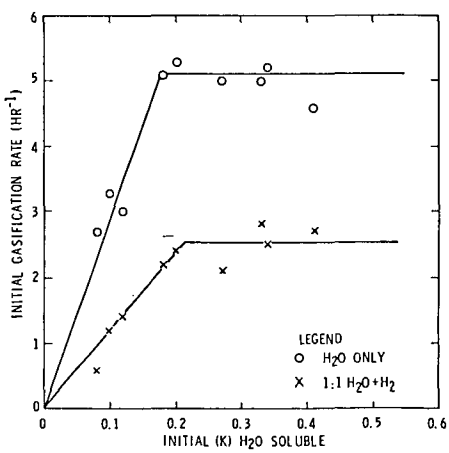

818-3-38

FIGURE 5

APPARENT ACTIVATION ENERGY DEPENDS ON FEED GAS COMPOSITION

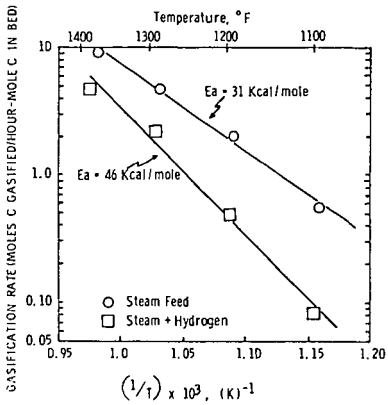

808-6-5-22

808-12-1130

FIGURE 6

CALCULATED AND OBSERVED FLOW RATES OF HYDROGEN

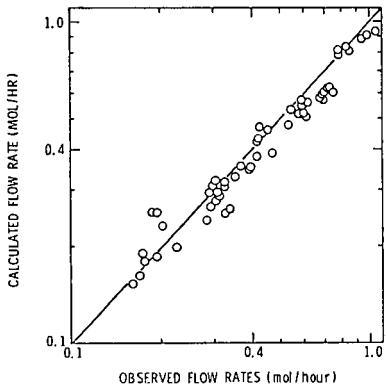

808-12-1131

FIGURE 7

CALCULATED AND OBSERVED FLOW RATES OF CARBON MONOXIDE

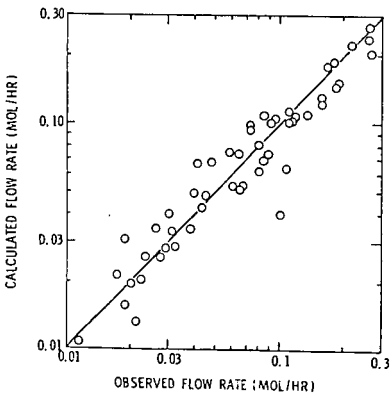

808-12-1132

FIGURE 8

CALCULATED AND OBSERVED FLOW RATES OF CARBON DIOXIDE

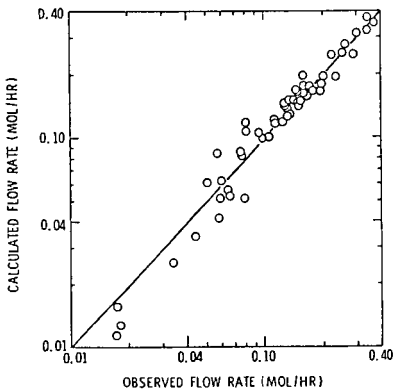

808-12-1133

FIGURE 9

CALCULATED AND OBSERVED FLOW RATES FOR METHANE

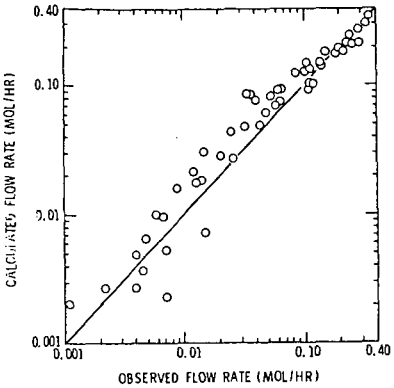

808-12-1134

FIGURE 10

CALCULATED AND OBSERVED FLOW RATES FOR STEAM

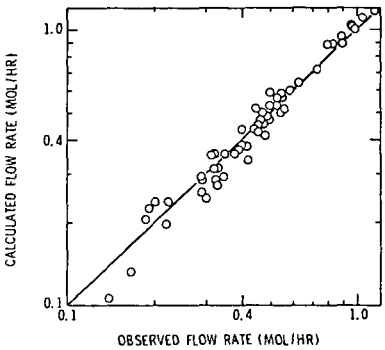

EVOLUTION AND REMOVAL OF POLLUTANTS FROM THE GASIFICATION OF A SUBBITUMINOUS COAL IN A FLUIDIZED BED REACTOR

R.M.Felder, J.K.Ferrell, R.W.Rousseau, M.J.Purdy, and R.M.Kelly

Department of Chemical Engineering
North Carolina State University
Raleigh, North Carolina 27650

INTRODUCTION

As a part of a continuing research program on the environmental aspects of fuel conversion, the U. S. Environmental Protection Agency has sponsored a research project on coal gasification at North Carolina State University in the Department of Chemical Engineering. The facility used for this research is a small coal gasification-gas cleaning pilot plant. The overall objective of the project is to characterize the gaseous and condensed phase emissions from the gasification-gas cleaning process, and to determine how emission rates of various pollutants depend on adjustable process parameters.

A complete description of the facility and operating procedures is given by Ferrell et al., Vol I, (1980), and in abbreviated form by Felder et al. (1980). A schematic diagram of the Gasifier, the Acid Gas Removal System (AGRS), and other major components is shown in Figure 1.

In an initial series of runs on the gasifier, a pretreated Western Kentucky No. 11 coal was gasified with steam and oxygen. The results of this work are given by Ferrell et al., Vol II, (1981), and were presented at the EPA Symposium on Environmental Aspects of Fuel Conversion Technology V, held in St. Louis, Mo., September, 1980.

The second major study carried out on the facility was the steam-oxygen gasification of a New Mexico subbituminous coal (from the Navaho mine of the Utah International Co.) using refrigerated methanol as the AGRS solvent. This paper presents a brief summary of the gasifier operation using this coal, shows examples of analyses of some of the gasifier effluent streams, and presents a summary of the results of the operation of the AGRS using the gasifier make gas as feed.

SUMMARY OF GASIFIER OPERATION

The fluidized bed gasifier and raw gas cleaning system (cyclone, venturi scrubber, filters and heat exchanger) used for these studies was originally designed for the gasification of a devolatilized coal char with a very low volatile matter content. Extensive modification of the upper part of the gasifier, the venturi scrubber system, and the heat exchanger was required for operation with the high volatile matter New

Mexico coal. Table 1 shows an analysis of the char and coal used in studies to date. After modification, the system functioned well in providing a clean, dry gas to the acid gas removal system.

All of the experimental work so far has been carried out with the solid coal particles fed into the reactor several feet above the top of the fluidized bed. The particles are thus in contact with the hot product gases for several seconds before mixing into the fluidized bed, a mode of operation that tends to maximize the production of tars and other organic liquids from the coal. It is an excellent mode of operation for our present purpose since it produces relatively high concentrations of environmentally important elements and compounds.

TABLE 1
COAL AND CHAR ANALYSIS

	Coal Char	New Mexico Coal
Proximate Analysis		
Fixed Carbon	86.0	42.0
Volatile Matter	2.4	35.4
Moisture	0.9	10.5
Ash	10.7	22.6
Ultimate Analysis		
Carbon	83.8	52.5
Hydrogen	0.6	4.8
Oxygen	2.2	18.3
Nitrogen	0.1	1.2
Sulfur	2.6	0.6
Ash	10.7	22.6

A total of 15 gasifier runs were made covering a range of reactor parameters. For this series of runs, the average temperature of the fluidized bed was varied from about 1600°F to 1800°F, and the molar steam to carbon ratio was varied from about 1.0 to 2.0. The coal feed rate and the reactor pressure were kept nearly constant. Several of the first reactor runs were made with mixtures of coal and char, but all integrated runs reported on later were made with 100% coal. At the lower temperatures the production of methane and of tars and other hydrocarbons is maximized. As the temperature is increased, the make gas rate increases, the production of methane and other hydrocarbons decreases, and the concentration of CO_2 increases.

GASIFIER MODELING RESULTS

To aid in the formulation of gasifier performance correlations, a simple model has been developed which considers the gasification process to occur in three stages: instantaneous devolatilization of coal in a zone above the fluidized bed, instantaneous combustion of carbon at the

bottom of the bed, and steam-carbon gasification and water gas shift reaction in a single perfectly mixed isothermal stage. The model is significant in and of itself, but its particular importance to the project is that it enables the specification of gasifier conditions required to produce a feed to the acid gas removal system with a predetermined flow rate and composition.

In a previous report (Ferrell et al., 1981), the structure of the model was presented, and the ability of the model to correlate data on the gasification of a devolatilized bituminous coal was demonstrated. The model was subsequently extended to include the evolution of volatile gases in the pyrolysis stage of the gasification process, and used to fit the data from the present series of runs with the New Mexico subbituminous coal. The model takes as input the average reactor bed temperature and pressure, the bed dimensions, feed rates of coal, steam, oxygen, and nitrogen, solids holdup in the bed, and ultimate analysis of the feed coal, and calculates carbon conversion and make gas flow rate and composition. A complete description of the model in its present form will be given in an EPA report now in preparation. A lot of model predictions vs measured values of carbon conversion is shown in Figure 2. The reasonably close proximity of most points to the 45 degree line on this and similar plots for total make gas flow rate and individual species (CO, H_2, CO_2) emissions is gratifying in view of the simplicity of the model.

AGRS OPERATION AND RESULTS

Top feeding coal into the gasifier allows a substantial amount of devolatilization to take place before the coal enters the fluidized bed. While most commercial fluidized bed gasifiers will use a deep-bed injection method of feeding coal into the fluidized bed, it was decided not to modify our system in order to maximize the formation of tars, oils, and other hydrocarbons and to provide a more complete test of the AGRS.

It should also be noted that the relatively simple acid gas removal system used in this study lacks the complexity of the selective systems found in many physical absorption processes. These systems, which use more than one absorber and stripper, and often several flash tanks, separate sulfur gases from carbon dioxide before further processing of the acid gas. This is done to concentrate the sulfur gases before they are fed to a sulfur recovery unit, and to recover the CO_2 or vent the CO_2-rich stream to the atmosphere. While the AGRS used in this study could have been modified to emulate an existing selective absorption process, it was decided that data obtained from a relatively simple but well-characterized system would be of more use than data obtained from a fairly complex system, similar but not identical, to existing commercial systems. Through judicious use of computer simulation and engineering calculations, the data obtained from our system should be extrapolatable to more industrially significant situations.

Complete results from all runs carried out will be published in a forthcoming EPA report. Illustrative results from a single run will be presented here. Gas analyses from the six different locations shown in Figure 1 are given in Table 2. The paragraphs that follow summarize the principal conclusions derived from analyses of the run data.

TABLE 2
GAS ANALYSIS SUMMARY FOR AMI-57/GO-76

Species	Sample Train	PCS Tank	Sour Gas	Sweet Gas	Flash Gas	Acid Gas
H_2	31.60	31.11	31.29	42.38	15.58	0.00
CO_2	23.51	23.91	21.98	-----	25.99	64.74
C_2H_4	0.52	0.53	0.56	0.0242	1.28	1.54
C_2H_6	0.72	0.72	0.76	0.0164	1.92	2.13
H_2S	0.250	0.284	0.287	0.0048	0.090	0.66
COS	0.0078	0.0076	0.0076	0.0001	0.0041	0.027
N_2	19.36	19.61	19.93	26.79	19.27	23.06
CH_4	6.56	6.46	6.57	7.54	14.20	2.36
CO	17.29	17.47	17.92	23.35	21.55	1.80
Benzene	0.087	0.097	0.234	TRACE	0.0031	0.15
Toluene	0.031	0.034	0.534	0.0054	0.0033	0.030
Ethyl Benz.	0.0016	0.0017	0.0450	-----	-----	-----
Xylenes	0.0080	0.0094	0.1557	-----	-----	-----
Thiophene*	44	44	127	-----	-----	-----
CH_3SH*	16	29	28	TRACE	5	TRACE
C_2H_5SH*	TRACE	-----	8	-----	-----	-----
CS_2	TRACE	3	TRACE	TRACE	TRACE	TRACE
Propylene*	1505	1521	1811	107	995	4640
Propane*	208	198	253	301	172	2203
Butane*	185	150	143	54	91	71
Methanol**	-----	-----	-----	-----	-----	3.68

*Parts per Million (volume) **Estimated

Acid Gas Removal

The primary function of the AGRS is to remove CO_2 and sulfur compounds from the gases produced during coal gasification. When using refrigerated methanol, the absorber also acts as an excellent trap for any other compound which condenses or disolves in the methanol at absorber conditions.

The run data show that for the range of conditions studied, the most significant factor in high acid gas removal efficiencies is stripping efficiency. With the use of more extreme operating conditions and "cleaner" methanol fed to the absorber, the levels of CO_2, COS and H_2S in the sweet gas can be reduced to acceptable levels. This is a particularly important point in the case of COS removal which poses

problems for many coal gas cleaning systems. The data show that refrigerated methanol is effective in removing COS and no unusual solubility characteristics were evident at moderate pressures and low liquid temperatures.

Trace Sulfur Compounds

There are several sulfur compounds besides H_2S and COS present in the gas fed to the AGRS which must be removed. Table 2 shows the distribution of several of these compounds in the AGRS. While there is some scatter in the analyses for methyl mercaptan, thiophene, CS_2, and ethyl mercaptan/dimethyl sulfide, it appears that in most runs they are removed to very low levels in the absorber.

A point of potential environmental significance is that while these compounds are removed to low levels, they are not completely accounted for in the flash and acid gas streams. This can be seen for methyl mercaptan and thiophene, which are present in relatively high levels in the feed gas. These compounds will accumulate in the recirculatory solvent and most likely eventually leave the system in one of three exit streams: sweet gas, flash gas, or acid gas. Because most sulfur recovery systems cannot treat mercaptans and thiophene, they will present emission problems if some additional method of treating these gases is not used. This can be a significant problem because the total sulfur from mercaptans, organic sulfides, CS_2, and thiophene is approximately half of the total sulfur associated with COS. If these compounds appear with the sweet gas, they are likely to affect adversely downstream methanation catalysts. The presence of these compounds in the sweet gas stream is also a problem if the gas is to be burned for immediate use because the sulfur in these compounds will be converted to SO_2.

In examining the results from all runs, there appears to be some pattern of trace sulfur species distribution. An increase in stripper temperature from -5.6°F to 48°F resulted in substantially greater amounts of mercaptan and thiophene in the acid gas stream. CS_2 seems to distribute to all exit streams in most of the runs despite the differences in process conditions.

Perhaps the most significant finding here is that over a wide range of processing conditions, the presence of at least small amounts of several different sulfur species is to be expected in all AGRS exit streams, and provision must be made for handling the associated problems.

Aliphatic Hydrocarbons

As the amount of volatile matter present in a particular coal increases, the production of aliphatic, aromatic, and polynuclear aromatic compounds produced during gasification also increases. Over the range of conditions studied here, the most significant point to be made about the distribution of aliphatic hydrocarbons is their presence in significant quantities in the flash and acid gases. Although flashing of

the methanol down to atmospheric pressure prior to stripping would release most of the hydrocarbons, the CO_2-rich flash gas would still contain substantial amounts of several hydrocarbon species. This stream would require further processing before it could be vented.

In a run in which the gasifier was operated at a lower temperature to increase the production of hydrocarbons, the aliphatics (excluding methane) made up almost 4.5% of the acid gas stream and 3.5% of the flash gas stream. While staging the flashing operations may result in a better distribution of these compounds, the total product from the flashing and stripping operations must be either recovered as product, fed to a sulfur recovery unit, or vented to the atmosphere. Since it is unlikely that all of the aliphatic hydrocarbons will appear in the sweet gas stream, as evidenced by the data collected here, additional treatment will be necessary to prevent their eventual appearance in a vent stream.

There appears to be no unusual pattern of distribution of aliphatic hydrocarbons in the AGRS. The lighter hydrocarbons-- methane, ethylene, and ethane-- seem to distribute as would be indicated from an examination of their pure-component solubilities in methanol. The magnitude of their solubilities, however, are greater than would be expected from Henry's law, especially at the high pressures used in the absorber. This is evident from the lower than predicted levels of ethane and ethylene in the sweet gas in several of the runs.

Aromatic Hydrocarbons

Because large amounts of aromatic hydrocarbons are produced during coal gasification, the potential for environmental problems is great. These compounds, which range from benzene to polynuclear species of many forms, must be prevented from escaping from the gas cleaning process and their distribution throughout the gas cleaning system is of great concern.

The simpler aromatics, benzene, toluene, and xylene, typically make up 0.1% (by volume) of the gas stream entering the AGRS. (See Table 2.) Analyses performed for selected runs indicate that significant quantities of these compounds are found in the solvent leaving the stripper. Eventually these compounds would build up in the solvent to the point of saturation. If the solvent is not effectively purged of these compounds periodically, they would begin to appear in several of the process streams.

Methanol Analysis

In order to identify the various hydrocarbon species that accumulate in the methanol, samples of the methanol leaving the stripper were taken for several runs. These samples were then analyzed by gas chromatography/mass spectrometry. The compounds detected are shown in Table 3. The presence of several siloxanes and phthalates was probably related to some contamination of the sample during processing.

Results from these runs indicate that most of the compounds accumulating in the methanol are simple aromatics, primarily substituted benzenes. A few C_{10} and C_{11} isomers were identified, indicating that napthalene is probably present but at trace levels. The presence of trace amounts of C_{14} and C_{15} isomers were found in but they could not be better identified. These may be polynuclear aromatics but they were present in very small amounts relative to the simpler aromatics.

Samples of liquid condensing in the knockout tank downstream from the sour gas compressor were collected and analyzed by GC/MS. This condensate contains most of the heavier hydrocarbons fed to the AGRS. Results of these analyses are presented in Table 4, and show that the compounds identified are very similar to those found in the stripped methanol. Again, mostly simple aromatics were found. No polynuclear aromatics were present, which supports the findings of the earlier analyses.

Results from these analyses indicate that very little, if any, polynuclear aromatic compounds were present in the gas fed to the AGRS. This is a particularly important finding. Analyses of the water used to quench the gasifier product gas stream showed that a substantial amount of polynuclear aromatics were present. Evidently, scrubbing of the raw product gas with water effectively removes these compounds.

Although polynuclear aromatics are removed by the quenching process, substantial amounts of simpler aromatics will be present in the sour gas fed to the AGRS. The use of cold traps may remove some of these compounds but provision must be made to prevent their release to the atmosphere through vent streams or through the sulfur recovery unit. The accumulation of these compounds in the methanol further complicates the problem because of the increased likelihood of their distribution to a number of process streams. Achieving efficient solvent regeneration is, therefore, a key step in avoiding environmental problems.

SUMMARY

A cyclone, a cold water quench scrubber, and a refrigerated methanol absorber have been used to clean the make gas from the steam-oxygen gasification of a New Mexico subbituminous coal in a pilot-scale fluidized bed ractor. A model developed for the gasifier provides the capability of predicting the make gas amount and composition as a function of gasifier operating conditions. The methanol functioned effectively for acid gas removal. Removal of CO_2, COS, and H_2S to sufficiently low levels was achieved with proper choice of operating conditions and effective solvent regeneration.

TABLE 3

COMPOUNDS IDENTIFIED IN STRIPPER EXIT METHANOL

1. sat'd hydrocarbon	21. toluene	42. C_3 alkyl benzene
2. CO_2	22. methyl thiophene isomer	43. C_3 alkyl benzene
3. C_4H_8 isomer	23. C_8H_{16} isomer	44. $C_{10}H_{22}$ isomer
4. tetramethylsilane	24. C_8H_{16} isomer	45. $C_{10}H_{22}$ isomer
5. trichlorofluro-methane	25. C_8H_{16} isomer	46. C_4 alkyl benzene
6. C_5H_{10} isomer	26. C_8H_{16} isomer (trace)	47. $C_{10}H_{22}$ isomer
7. unknown	27. C_8H_{14} isomer (trace)	48. $C_{10}H_{20}$ isomer
8. Freon 113	28. hexamethyl cyclotrisiloxane	49. unknown hydrocarbon
9. cyclopentadiene	29. C_9H_{20} isomer	50. C_9H_{10}
10. C_6H_{12} isomer	30. C_9H_{18} isomer	51. C_9H_8 isomer
11. C_6H_{14} isomer	31. ethyl benzene	52. alkyl benzene isomer
12. C_6H_{10} isomer	32. xylene (M,P)	53. $C_{11}H_{24}$ isomer
13. benzene	33. styrene	54. $C_8H_{10}O$ isomer
14. C_7H_{14} isomer	34. xylene (O)	55. $C_{11}H_{24}$ isomer
15. C_7H_{16} isomer	35. C_9H_{18} isomer	56. $C_8H_{10}O$ isomer
16. C_7H_{16} isomer	36. C_9H_{20} isomer	57. unknown siloxane
17. C_7H_{12} isomer	37. C_3 alkyl benzene	58. unknown siloxane
18. C_7H_{12} isomer	38. $C_{10}H_{22}$ isomer	59. unknown siloxane
19. C_7H_{12} isomer	39. unknown hydrocarbon	60. $C_{14}H_{30}$ isomer
20. unknown hydrocarbon	40. unknown hydrocarbon	61. $C_{14}H_{30}$ isomer
	41. $C_{11}H_{24}$ isomer	62. unknown
		63. $C_{15}H_{32}$ isomer

TABLE 4

COMPOUNDS IDENTIFIED IN COMPRESSOR KNOCKOUT SAMPLE

1. 1-pentene	10. substituted benzene
2. hydrocarbon	11. C_8 hydrocarbon
3. benzene	12. C_9 hydrocarbon
4. hydrocarbon	13. propyl or ethyl methyl substituted benzene
5. Toluene	14. propyl or ethyl methyl substituted benzene
6. cyclo C4-C5	15. 1-decene
7. hydrocarbon	16. 2-propyl benzene
8. ethyl benzene	17. 1-ethyl-4-methyl benzene
9. dimethyl benzene	

The presence of several trace sulfur compounds--mercaptans, thiophenes, organic sulfides, and CS_2--complicates the gas cleaning process because these compounds were found to distribute among all exit streams from the AGRS. Since no provision is made to specifically treat these forms of sulfur, the possibility of their emission into the atmosphere exists and must be dealt with to avoid significant environmental problems.

A wide variety of aliphatic and aromatic hydrocarbons are present in the gas stream fed to the AGRS. The aliphatic hydrocarbons, ranging from methane to butane, cover a wide range of solubilities. Their presence in all AGRS streams must be anticipated to prevent their emission to the atmosphere.

While a wide range of simple aromatics were identified in the gas stream fed to the AGRS, essentially no polynuclear aromatic compounds were found. Apparently, the water quenching process effectively removes these compounds from the gasifier product gas. However, significant quantities of simple aromatics were found to accumulate in the recirculating methanol, indicating a potential for their eventual discharge to the atmosphere. Provision must be made to periodically purge the solvent of these compounds and/or remove them prior to the AGRS through cold traps.

REFERENCES

1. Ferrell, J. K., R. M. Felder, R. W. Rousseau, J. C. McCue, R. M. Kelly, and W. E. Willis, "Coal Gasification/Gas Cleanup Test Facility: Vol I. Description and Operation", EPA-600/7-80-046a, (1980).

2. Felder, R. M., R. M. Kelly, J. K. Ferrell, and R. W. Rousseau, "How Clean Gas is Made from Coal", Env. Science and Tech., Vol 14, 658, (1980).

3. Ferrell, J. K., , R. M. Felder, R. W. Rousseau, S. Ganesan, R. M. Kelly, J. C. McCue, and M. J. Purdy, "Coal Gasification/Gas Cleanup Test Facility: Vol II. Environmental Assesment of Operation with Devolatilized Bituminous Coal and Chilled Methanol", EPA, (1981).

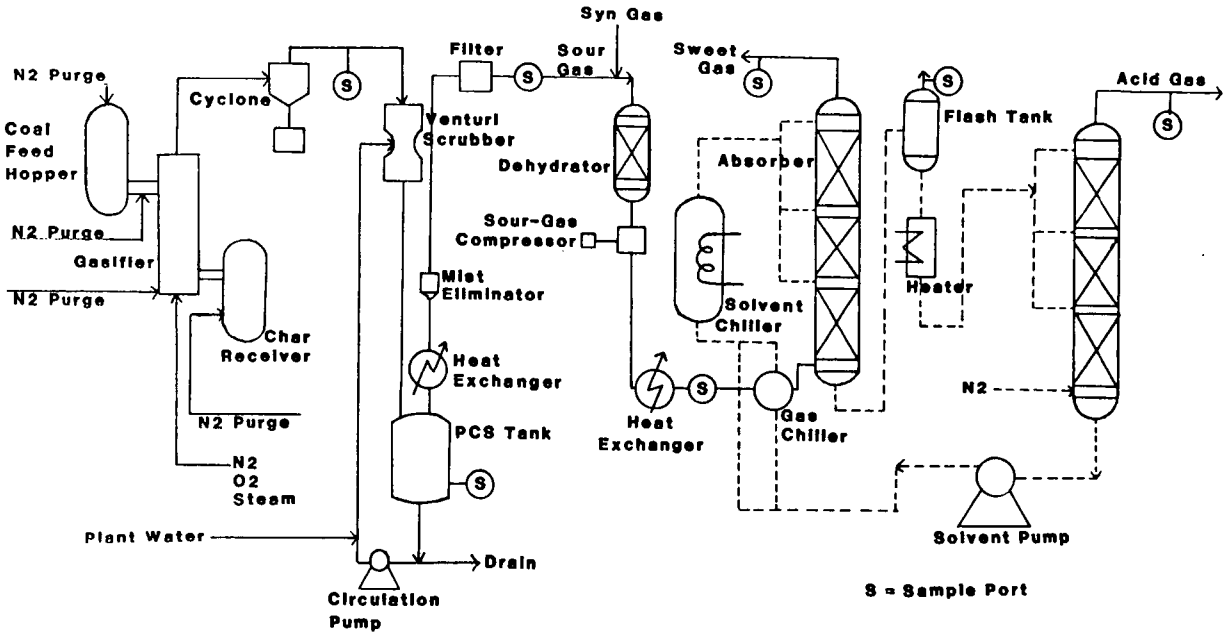

Figure 1

Pilot Plant Facility

Figure 2

Predicted vs. Experimental Carbon Conversion,
Gasification of New Mexico Coal

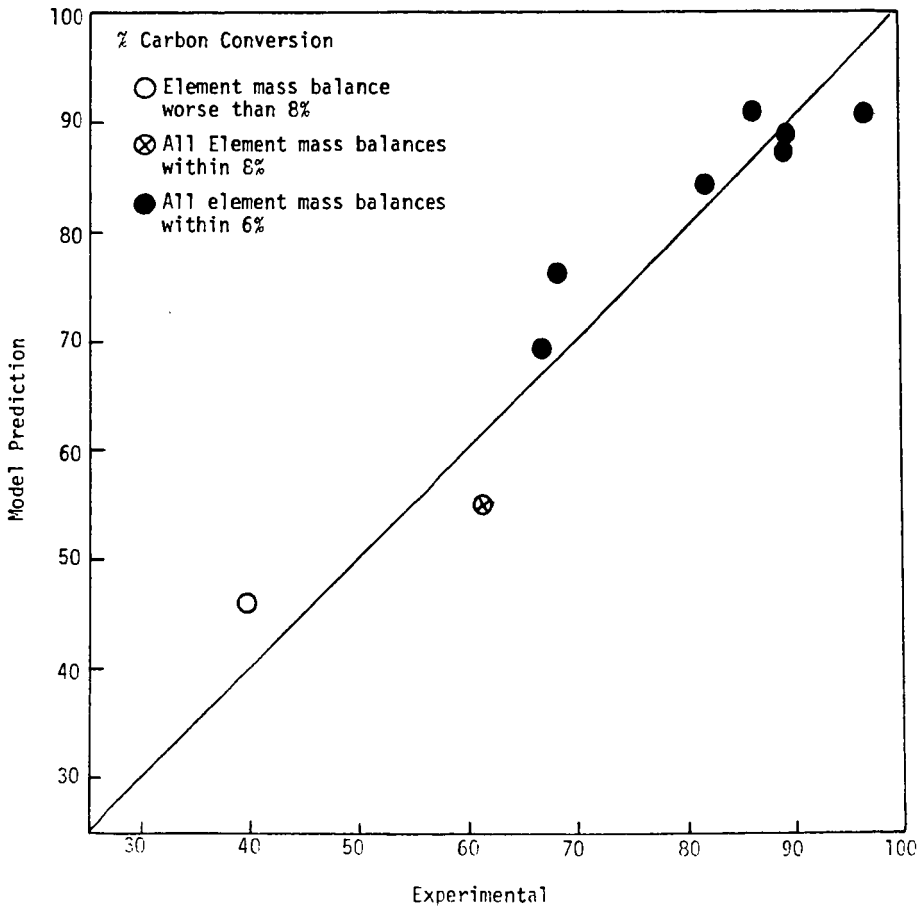

DIRECT METHANATION - A NEW METHOD OF CONVERTING SYNTHESIS GAS TO SUBSTITUTE NATURAL GAS

Howard S. Meyer, Vernon L. Hill, Ab Flowers

Gas Research Institute
8600 West Bryn Mawr Avenue
Chicago, Illinois 60631

John Happel, Miguel A. Hnatow

Catalysis Research Corporation
450 E. Edsall Boulevard
Palisades Park, NJ 07650

I. INTRODUCTION

The United States has vast resources of energy in the form of coal. One method of distributing this energy source to the consumer is to gasify the coal and distribute the gas through the existing natural gas pipeline distribution system. However, raw synthesis gas from a coal gasifier is not of sufficient purity and does not provide heating value suitable for use directly as substitute natural gas (SNG). The synthesis gas produced by a coal gasifier requires extensive purification and upgrading before it can be interchanged with natural gas. The current raw gas conversion systems were not specifically designed with the production of pipeline quality gas from coal in mind. Potentially, significant cost reductions could result from the development of an improved, integrated processing system.

As part of the strategic objective of improving reliability, operability, or reducing gas costs of coal gasification processes, the Gas Research Institute (GRI) is developing a new process for converting synthesis gas to SNG. The key to this process is the development of a sulfur-resistant, direct methanation catalyst. Preliminary cost estimates show that the direct methanation process could decrease capital costs by over 20% and operating costs by 10%, resulting in gas costs savings of about 15% over state-of-the-art methanation and combined shift-methanation processes.

II. METHANATION PROCESSES

A conventional gas processing system, as shown in Figure 1A, includes gas quench, water-gas shift, gas cooling,acid gas removal, methanation, dehydration, and compression. These clean-up processes produce separate streams that require further purification so that by-products, such as sulfur, phenols, ammonia, BTX, and tars, can be isolated for sale whenever possible. The gas quench utilizes oil and/or water to cool the raw gas and to remove particulates, tars, and oils, and other condensible components.

Water-gas shift (Equation 1) is required to adjust the H_2/CO ratio to over 3

$$CO + H_2O \rightleftharpoons H_2 + CO_2 \qquad 1)$$

as needed for methanation. Added steam reacts with the carbon monoxide to produce the required hydrogen. The use of new sulfur-insensitive shift catalysts show an economic advantage by allowing the shift process to be upstream of the gas cooling and acid gas removal systems. The acid gas removal system removes water, carbon dioxide, and sulfur-containing compounds. The current methanation process uses nickel-based catalysts for

converting (methanating) carbon monoxide and hydrogen to methane (Equation 2). After methanation, dehydration is required to remove the water formed during methanation; after which the gas is compressed to pipeline standards.

$$3H_2 + CO \rightleftharpoons CH_4 + H_2O \qquad 2)$$

Nickel catalysts have demonstrated their effectiveness for converting synthesis gas to methane. However, there are very strict process restrictions for successful use of nickel catalysts. Satisfying these restrictions can require process steps that are costly. A major restriction of nickel catalysts arises from their extreme sensitivity to poisoning by sulfur compounds that are always present in coal-derived synthesis gas. Although "sweet" pipeline gas can contain 4 ppm hydrogen sulfide (0.25 grains/100 scf), gas processed by nickel catalysts must be purified to 0.1 ppm sulfur to avoid irreversible poisoning of the catalyst. The nickel catalyst can also be irreversibly poisoned by carbon fouling, unless the hydrogen/carbon monoxide ratio of the input gas is maintained above 2.85 and/or excess steam is added. Nickel catalysts are also deactivated at high temperatures (above 950°F), such as those that can occur during the exothermic methantion reaction. Nickel catalysts cannot be exposed to oxygen after activation. They require special handling and pretreatment procedures to maintain reactivity.

Improvements to the conventional methanation process are those embodying combined shift-methanation, such as those developed by Conoco, R. M. Parsons, United Catalyst, ICI, and UOP. These processes utilize the water formed in methanation for water-gas shift. (Equations 1 and 2 simultaneously.) A combined shift-methanation process is shown in Figure 1B. Since nickel-based catalysts are used, removal of sulfur is required prior to shift-methanation. All the combined shift-methanation processes require steam addition for stoichiometry, temperature moderation, and/or to prevent carbon formation. An additional acid gas removal system is required downstream of the shift-methanation process to remove the high concentration of CO_2.

The direct methanation process being developed for GRI shows significant improvements over the conventional methanation and combined shift-methanation processes. The direct methanation process, shown in Figure 1C, methanates the raw gas directly using equal molar concentrations of carbon monoxide and hydrogen to form carbon dioxide and water. The chemistry of the process is such that steam is not needed either to suppress carbon formation or to drive the water-gas shift reaction. Although the overall reaction for combined shift-methanation is the same as for direct methanation (Equation 3), the mech-

$$2CO + 2H_2 \rightleftharpoons CH_4 + CO_2 \qquad 3)$$

anism appears different in that CO_2 is produced directly rather than by the water-gas shift, thus eliminating the high steam requirement. The process shows potential savings in steam usage and acid gas removal. Other process advantages are expanded upon in the remainder of the paper.

III. DIRECT METHANATION CATALYST DEVELOPMENT

Catalysis Research Corporation (CRC), located in Palisades Park, New Jersey, is responsible for iteratively developing novel catalyst formulations, performing scoping tests to evaluate the effectiveness of the formulations, and proposing process sequences that best utilize the advantages of the most promising catalysts. During the last six years, CRC has tested over 600 new catalyst formulations resulting in several compositions that have promise for application both in a conventional methanation process and in a new direct methanation process.

The catalyst development program for a sulfur-resistant methanation catalyst, from 1974-1978, lead to two patented catalyst formulations. In 1977, Patent 4,151,191 was issued to CRC for a cerium-molybdenum catalyst, designated as GRI Series 200 (GRI-C-284). In 1981, Patent 4,260,553 was issued to CRC for a cerium-molybdenum-aluminium catalyst, designated as GRI Series 300 (GRI-C-318). Both patents were assigned to GRI. These catalysts satisfied the original project objective of developing a sulfur-resistant methanation catalyst; however, they also lead to a new area of study.

In 1979, a second breakthrough was made in the CRC catalyst formulation work. A new family of catalysts, the GRI Series 400 and 500 catalysts, were developed that promote the direct methanation reaction (Equation 3) rather than the water-gas shift reaction (Equation 1). These catalysts provide the key to the new direct methanation process. The overall project objective was changed to reflect this breakthrough, and subsequential work concentrated on developing a direct methanation process.

The present series of catalysts are the most active catalysts yet developed. These catalysts show sufficiently high conversion and selectivity such that they can be used in a direct methanation process that involves no gas recycling and uses only a single acid gas removal system. They can operate with feed gases containing high levels of sulfur compounds and CO_2. Carbon formation has not been observed, even with H_2/CO ratios as low as 0.1 and with no steam addition, and the catalysts have high maximum operating temperatures. The catalyst are very easy to handle; they can be exposed to air at room temperature with no loss of activity, and therefore, they require little or no pretreatment.

IV. DIRECT METHANATION CATALYST CHARACTERIZATION

SRI International, located in Menlo Park, California, is responsible for characterizing the promising catalysts developed by CRC. The studies are intended to define the bulk and surface properties that affect the specific methanation activity, thermal stability, and deactivation resistance of these catalysts as an aid in further development and improvement. SRI has been involved with the Direct Methanation Project since 1977, but also has developed catalysts under contracts to the American Gas Association (A.G.A.) since 1972.

The direct methanation process requires a catalyst that selectively promotes the direct methanation reaction (Equation 3). Catalyst selectivity and activity can be strongly dependent upon both the composition and morphology of the catalyst. Development of basic methods to relate microcompositional and morphological properties of the catalyst to selectivity and activity is vitally important in the development of improved catalysts and gas processes for coal conversion plants. Work being performed by SRI is intended to refine measurement techniques suitable for understanding the observed behavior of the direct methanation catalysts.

In order to evaluate catalyst structure, SRI had to develop or improve new experimental techniques utilizing (1) x-ray photoelectron spectroscopy (XPS or ESCA), (2) scanning electron microscopy (SEM), and (3) BET surface area measurements to provide information on structural changes of catalysts. Dispersion and sintering stability studies have been performed using x-ray diffraction (XRD), SEM, and ESCA to define changes in the properties that control methanation activity. Solid state properties of the catalysts have been determined by a variety of surface science techniques.

Because of its nature, most of the work performed by SRI is proprietary; a general discussion of some aspects of the work follows. First, tests were

performed to study structural changes of the catalyst during methanation. This resulted in the discovery of a critical formulation variable that controls the specific methanation activity. Later, discovery of a correlation between methanation activity and surface acidity, as measured by quantitative absorption of a weak base (ammonia), simplified catalyst evaluation. Finally, a preliminary explanation of the mechanism by which the GRI Series 400 and 500 catalysts operate was developed.

V. DIRECT CATALYST METHANATION EVALUATION

The Institute of Gas Technology (IGT), located in Chicago, Illinois, is responsible for evaluating the promising catalyst formulations prepared by CRC using feed gases that simulate gasifier effuents and developing the process design data for promising catalysts in various processing sequences. The studies are intended to test the catalysts for longer times and at more severe and realistic conditions than the scoping tests performed by CRC. IGT has been involved with the Direct Methanation Project since 1978, but also has evaluated catalyst under contracts to A.G.A. since 1972.

The GRI Series 500 catalysts are the best methanation catalysts tested to date. They are capable of promoting the methanation reaction at temperatures from 600° to 1200°F, at all pressures from 200 to 1000 psig, at feed gas H_2/CO mole ratios from 3 down to 0.5, and in the presence of up to 3 mole % sulfur (H_2S, COS, CS_2, CH_3SH, C_2H_5SH, C_3H_7SH, and C_4H_4S). No carbon formation was detected under any of the above mentioned conditions. The presence of CO_2 in the feed retarded the total CO conversion but did not promote any other reactions. Hydrocarbon additions of up to 2 mole % C_6H_6, 0.05 mole % C_6H_5OH, and 0.3 mole % NH_3 did not poison or foul the catalysts. Life tests were conducted on the GRI Series 200 catalysts for more than 5000 hours, and ongoing life tests of the GRI Series 500 catalysts have extended for more than 2500 hours.

The promising catalysts were also tested in various processing sequences to provide process design data. IGT tested the effects of space velocity, temperature, pressure, and feed composition on the conversion of CO and H_2 to CH_4 and CO_2 by the direct methanation process. The feed gas simulated a gasifier effluent. The product composition of each reactor was used as the feed composition for each successive reactor stage, and runs at identical temperature and pressure were conducted. This approach generated information on the process variables at each reactor stage, provided input for process design, and served as a guideline for catalyst improvement.

Quench gases simulating those from the dry-bottom Lurgi, Slagging Lurgi, Westinghouse and HYGAS processes were tested. For cases where the H_2/CO ratio is less than 1, as in the Slagging Lurgi case at $H_2/CO = 0.4$, a preconditioning shift was required to increase the H_2/CO ratio to 1.1 to 1.3. The process steam requirements are therefore much lower than required for shifting the gas to 3 as needed for nickel methanation catalysts. The shift was performed with a CRC developed, GRI Series 300 catalyst and required only 16% steam in the feed gas to the methanation step, as shown in Figure 2. Typical data for a Slagging Lurgi flowsheet are shown in Figure 3 for the first reactor stage.

VI. DIRECT PROCESS METHANATION EVALUATION

C F Braun & Company, located in Alhambra, California, is the engineering/construction firm responsible for developing conceptual processes from the design data collected by IGT and from the process sequences recommended by CRC. First-cut economic evaluations are then performed based on the conceptual process design. The conceptual process design work includes

preparing process flow diagrams and sizing equipment. Capital cost and operating requirements estimates are used in the economic evaluation to determine gas costs.

A preliminary economic evaluation was conducted in 1979, based on the use of a GRI Series 300 catalyst. The results indicated the concept would not be competitive because the design required CO_2 removal prior to methanation. However, CO_2 removal is not required with the use of the GRI Series 400 and 500 catalysts, because these catalysts have good activity in streams with a high CO_2 content.

A first-cut analysis of the direct methanation process for a Slagging Lurgi gasifier raw gas was just completed. The analysis compared a 250 billion Btu/day Slagging Lurgi gasification plant with a combined shift-methanation process to a plant designed around the direct methanation process. The design of the gasifier was not changed, but the overall downstream process, utilizing commercially available subsystems, was redesigned to best exploit the direct methanation process advantages. A simplified flowsheet, based on a GRI Series 500 catalyst, is shown in Figure 4.

The preliminary results show the direct methanation process could reduce capital costs over 20%, operating cost by 10%, and reduce the gas cost by about 15%. The savings are realized in reduced steam requirements and more efficient sulfur management processes specifically for this application. Further savings were anticipated when new subsystems are developed specifically for use with direct methanation.

VII. CONCLUSIONS

The current GRI project to develop a direct methanation process is making excellent technical progress. Direct methanation processes utilizing the CRC catalysts could potentially realize the following advantages over existing technology:

- Reduced plant investment, operating costs, and gas costs
- Effective hydrogen utilization
- One acid gas removal step
- Smaller acid gas removal feed stream
- Higher energy efficiency
- Sulfur tolerance
- Carbon fouling tolerance
- Lower process steam requirements
- Decreased heat exchange area

If the development continues to be successful, the direct methanation process will be pursued through the pilot plant scale to provide the technology base required for commercial application.

ACKNOWLEDGEMENT

The authors wish to acknowledge the contributions made by Dr. Henry Wise at SRI International, Mr. Anthony L. Lee at IGT, Dr. Roger Detman at C F Braun & Co. and their staffs for their contributions to the overall progress of this project.

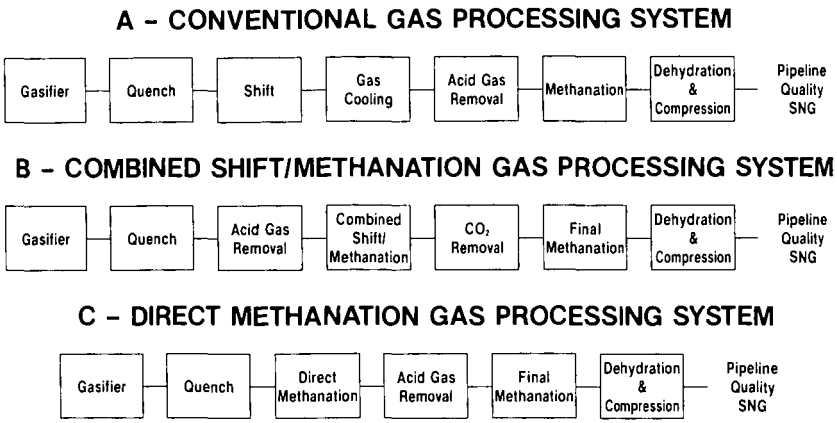

FIGURE 1. METHANATION PROCESSES

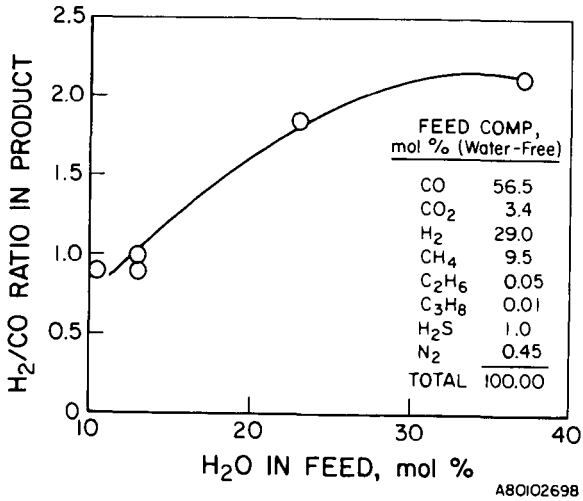

FIGURE 2. PRECONDITIONING SLAGGING LURGI RAW GASES (1000 psig, 580°F, 4500 SCF/hr-ft^3 GRI-C-318 Catalyst)

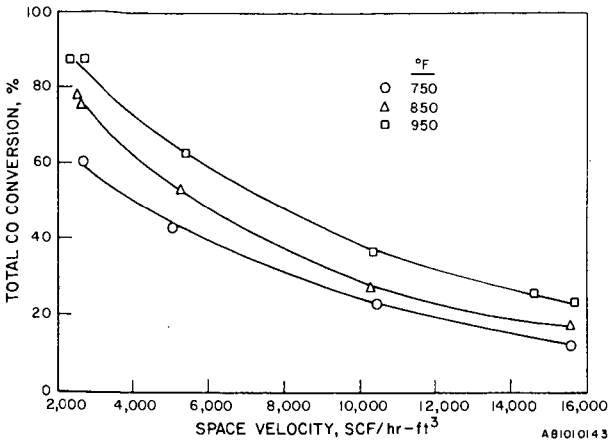

FEED COMPOSITION, mol %	
CO	34.27
CO_2	14.43
H_2	37.02
CH_4	10.60
C_2H_6	0.34
C_3H_8	0.11
C_4H_{10}	0.05
H_2S	0.98
COS	0.02
N_2	0.33
H_2O	1.85
TOTAL	100.00

FIGURE 3. CO CONVERSION IN THE FIRST DIRECT METHANATION STAGE FOR SLAGGING LURGI RAW GASES (450 psig, GRI-C-525 Catalyst)

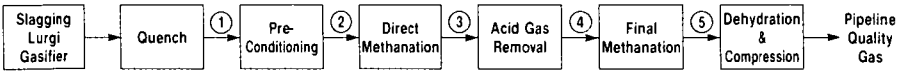

Gas Analysis, Vol %
(H_2O and N_2 Free Basis)

Stream Component	1	2	3	4	5
CO	58.9	37.6	1.7	4.1	0.1
CO_2	6.5	19.1	56.1	0.7	0.8
H_2	25.9	35.8	6.7	16.1	4.7
CH_4	6.1	5.3	32.3	77.6	92.7
C_2^+	0.5	0.4	0.6	1.5	1.7
H_2S	2.1	1.8	2.6	0	0

FIGURE 4. CONCEPTUAL FLOWSHEET FOR DIRECT METHANATION OF SLAGGING LURGI RAW GASES

VARIATIONS IN THE INORGANIC CHEMISTRY OF COAL

W.S. Fyfe, B.I. Kronberg, Department of Geology, The University of Western Ontario, London, Canada

J. R. Brown, Energy Research Laboratories, Department of Energy, Mines and Resources, Ottawa, Canada

INTRODUCTION

The composition of coal reflects its complex physical and chemical history. Throughout coal genesis, from accumulation of plant debris and during subsequent coalification, solute species in ground waters are constantly exchanged with the porous and reducing carbonaceous debris. From existing geochemical data (e.g., Wedepohl, 1969; Kronberg et al., 1981), it appears that coal and coal-related materials (peat, lignite, etc.) may incorporate and accumulate a complex array of elements. To some extent coal deposits acts as gigantic carbon filters through which ground waters wash the products of rock leaching. Very little is known concerning the exact siting of trace elements in coal and these elements at times attain ore grade (e.g., U, Mo).

The modern large-scale (10^{15} g a^{-1}) burning of coal may have ramifications not only for the global carbon cycle but contingent on their fates during combustion, also for the global cycle of other elements concentrated in coal. For example the deposition over the past five decades of charcoal as well as several metals (Cr, Fe, Co, Ni, Cu, Zn, Cd, Sn and Pb) in Lake Michigan sediments correlates with variations (oil, coal, wood, installation of control devices) in fuel use (Goldberg et al., 1981). Associated with coal combustion is the accumulation of easily leachable ash. Other recent work (Chapelle, 1980) shows that some metals (Cr, Ni, Zn, Cd, Pb) sorbed onto surfaces of Fe-Al-O phases in ash are easily leached by percolating waters.

Here discussion is confined to the coal chemistry of the transition metals, some of which are known to play catalytic roles in coal combustion and to the coal chemistry of the halogens. The presence of F and Cl at the per cent levels in some coals is significant for combustion technologies (concerned with corrosion problems, etc.) and for problems related to atmospheric emissions.

EXPERIMENTAL

The analytical data reported here pertain to samples of raw coal, ash from coal, lignite and tar sand, as well as NBS standard reference coals and coal ash. The non-reference coals are bituminous coals from Western Canadian mines, hosted in Cretaceous formations. The lignites are from North Dakota and Ontario, and the tar sand from Fort McMurray, Alberta. The British Columbia coals (samples 2-6, Table 1) are from different seams in the same mine, as are the Alberta coals (samples 7-9). The sample numbers correspond to those appearing in more detailed analytical reports (Kronberg et al., 1981; Brown et al., 1981a, b). The analytical techniques employed in all these studies are spark source mass spectroscopy (SSMS) and electron spectroscopy for chemical analysis (ESCA).

SSMS is useful for surveying the concentrations of 60-70 elements in a single analysis. However, it is necessary to pre-ash or otherwise pre-treat samples containing substantial material of low mass number, which easily forms polyatomic positive ions. Coal, due to its high carbon content exemplifies this difficulty, and an unmanageable number of interferences appear in the mass spectral record of raw coal. In this study the samples of coals, lignites and tar sand were dry ashed for 4-6 hours at 600°C in a muffle furnace. Sample electrodes, prepared by mixing the ash with pure graphite (Taylor, 1965), were sparked in a JEOL mass spectrometer

(JMS-01BM-2). The mass spectra were recorded photographically and interpreted semi-quantitatively using USGS standards (Flanagan, 1973). With regard to the analysis of coals and other geological materials (soils, Mn nodules, rocks, volcanic ash, deep-sea sediments, etc.) the analytical uncertainty is within the variation encountered using normal sampling techniques.

ESCA is a spectroscopic surface sensitive technique by which the concentrations of all elements (except H) can be surveyed semi-quantitatively to a surface depth of 1-5 nm. Detection limits are $\approx 10^{-9}$ g cm^{-2} of surface ($\approx$0.1 bulk wt. %). Thus for geological materials, semi-quantitative information can be obtained for major elements and for surface concentrated minor and trace elements (Brown, 1978; Bancroft et al., 1979). There are several advantages of ESCA for coal analysis: (1) ESCA is non-destructive. (2) It is often possible to gather details on the in situ chemistry of elements (oxidation state, coordination number, etc.). (3) Both raw coal and coal ash may be analysed. Ashing effectively concentrates the mineral fraction in coal by an order of magnitude, permitting concentration measurement of additional elements. Surface concentration of elements (e.g., F, S) during combustion by surface sorption reactions may be monitored. (4) ESCA multi-element scans may be done quickly ($\sim$ 1 hour) and may be useful in fingerprinting coals.

ESCA spectra were recorded using a McPherson 26 spetrometer equipped with an aluminum anode operating at 200 watts. Details of the ESCA procedures used for this study are available elsewhere (Brown et al., 1981a, b).

RESULTS AND DISCUSSION

The concentrations, obtained by SSMS (Table 1), of transition metals and halogens for some North American coals and coal-related materials are compared (Table 2) to data available for coal from various sources and to crustal abundances. The chaotic concentration patterns for many elements are a reflection of the complexity of chemical and physical processes associated with coal formation. The extreme variation is possibly related to local ground water chemistry and to the local permeability of coal and enclosing strata. With respect to crustal abundances (CA), both the transition metal and halogen concentrations, range from strongly depleted (less than 10-fold CA) to strongly enriched (greater than 10-fold CA). The data from other sources include those from coal deposits on other continents, and the wide concentration ranges may be an expression of the type of Earth processes leading to coal deposition and formation.

Of the transition metals (Table 1) Sc, Y and Zr appear the least mobile. The variations in Nb concentrations are intriguing and Nb may be more mobile or may be hosted in phases distributed more unevenly. The variation in Ti concentrations is noteworthy, and chemical migration of Ti in association with coal diagenesis has been noted (Degens, 1958). Moreover, there is evidence for the chemical coupling of Ti (and Zr) compounds to enzymes and other biologically active macromolecules (Kennedy, 1979). Further, Taylor et al. (1981) have shown that Mg, Ca, Ti, Fe, Cu, Zn species in coal may be extracted by organic solvents.

Our knowledge of the sources of halogens and their mode of concentration in coal is vague. River and ground waters flowing into coal basins would contribute substantial amounts of Cl. It could be introduced by rain and aerosols either directly or transferred via the biosphere. The sources of Br and F are less certain. F could be added during deposition by the influx of fine-grained detrital minerals or volcanic ash. For example, fluorite (CaF_2) is observed in the ESCA scan of coal No. 8 (Table 3).

In the ESCA scans of raw coals (Table 3), the largest peaks correspond to the detection signals for carbon (C 1s) and oxygen (O 1s). Other elements detected included Al, Si, Ca, sometimes S, and in some samples substantial F and Cl. Large

variations, indicated by the number of counts per second during ESCA analysis, are attributed to chemical variations in coal surfaces. The differences in carbon peak positions were of interest especially in sample no. 8, for which the C 1s peak position is indicative of graphitic carbon and this scan also contains the largest F 1s signal.

Recently, an examination of raw coal macerals by XPS indicates that fisinite displays characteristics (C 1s binding energy 284.4 eV) essentially identical to pure graphite. It was also observed that the vitrinite fraction of a western Canadian coal sample was greatly enriched (> 1 wt. percentage) in an organically found fluorine species, $^{a}(CF_2)_n$ type.

In the ESCA scans of ashed coals (Table 4) many more elements (Na, Mg, Ti and Fe) appeared and the F 1s and S 2s peaks are enhanced. S appearing both as SO_4^{2-} and S^{2-} is likely associated with Fe as iron sulphide (pyrite), the outer shell oxidized to sulphate by combustion. The concentrations of Al, Ca, Ti and Fe in NBS reference ash (1633a) measured by ESCA (using the Si 2s peak as a reference) agree well with recommended values. In the ash, F and S surface concentrations are much greater than those observed in the bulk samples, and this could be evidence for preferential siting of these elements on ash surfaces. Cl was not detected on the ash surfaces by ESCA, in contrast to the high signals noted on raw coal surfaces, and Cl may be removed in the volatile phase during combustion.

CONCLUSION

The combined use of SSMS and ESCA results was successful in part in overcoming the unique analytical difficulties presented by the heterogeneous chemical and physical distribution of intimately combined inorganic and organic species in coal. These techniques and modifications of them are applicable to the study of the combustion chemistry of coal as well as to the assessment of the environmental impact of coal utilization.

REFERENCES

Babu, S.P. (Ed.) 1975. Trace elements in fuels. Adv. Chem. Ser. 141. Am. Chem. Soc., Washington, D.C. 214 pp.

Bancroft, G.M., Brown, J.R., and Fyfe, W.S. 1979. Advances in, and applications of, x-ray photoelectron spectroscopy (ESCA) in mineralogy and geochemistry. Chem. Geol. 25, 227-243.

Brown, J.R. 1979. Adsorption of metal ions by calcite and iron sulphides: A quantitative XPS study. Ph.D. thesis, University of Western Ontario, London, Ontario, 220 pp.

Brown, J.R., Kronberg, B.I., and Fyfe, W.S. 1981,a. Semi-quantitative ESCA examination of coal ash surfaces. FUEL 60: 439-446.

Brown, J.R., Kronberg, B.I., and Fyfe, W.S. 1981,b. An ESCA examination of coal and coal ash surfaces, In: Proceedings "Coal: Phoenix of the '80's" (ed. A.M. Al Taweel), 64th Canadian Chemical Conference, Halifax, N.S.

Chapelle, F.H. 1980. A proposed model for predicting trace metal composition of fly-ash leachates. Environ. Geol. 3(3): 117-122.

Degens, E.T. 1958. Geochemische Untersuchungen zur Faziesbestimmung im Ruhrkarbon und im Saarkarbon. Glückauf, Jg. 94, Essen.

Fairbridge, R.W. (ed.) 1972, Encyclopedia of geochemistry and environmental earth sciences series, Vol. IVA, Van Nostrand Reinhold, New York, 1321 pp.

Flanagan, F.J. 1973. 1972 values for international geochemical reference samples. Geochim. Cosmochim Acta 37: 1189-1200.

Goldberg, E.D., Hodge, V.F., Griffin, J.J., Koide, M. and Edgington, D.N. 1981. Impact of fossil fuel combustion on the sediments of Lake Michigan. Envir. Sci. & Tech. 15 (4): 466-471.

Goldschmidt, V.M. 1954. Geochemistry, Claredon press, Oxford 730 pp.

Kennedy, J.F., 1979. Transition-metal oxide chelates of carbohydrate-directed macromolecules. Chem. Soc. Rev. 8 (2) 221-257.

Kronberg, B.I., Brown, J.R., Fyfe, W.S., Peirce, M. and Winder, C.G. 1981. Distribtuions of trace elements in western Canadian coal ashes. FUEL 6D: 59-63.

Taylor, S.R. 1965. Geochemical analysis by spark sourc-mass spectrography. Geochim. Cosmochim. Acta 29: 1234-1261.

Taylor, L.T., Hausler, D.W. and Squires, A.M. 1981. Organically bound metals in a solvent-refined coal: metallograms for a Wyoming subbituminous coal. Science, 213, 644-646.

Wedepohl, K.H. 1969. Handbook of Geochemistry. Springer-verlag, Berlin.

TABLE 1 - CONCENTRATIONS ($\mu g\ g^{-1}$) OF SOME ELEMENTS IN ASH FROM COAL, LIGNITE AND TAR SAND (SSMS DATA)

Sample	Yukon coal	British Columbia coals					Alberta coals			North Dakota lignite	Athabasca Tar Sand	Ontario lignite	NBS Reference Materials		
Element													coal ash	coals	
	1	2	3	4	5	6	7	8	9	10	11	12	1633a	1632a	1635
F	50	>500	>500	150	>500	>500	500	500	30	>500	>500	500	>500	500	>500
Cl	5	5	5	2	5	15	>50	50	10	1	50	50	50	>50	50
Sc	30	100	100	100	30	30	30	30	3	15	10	30	100(40)[a]	30	10
Ti	1,000				1,000			300		3,000			8000		
V	15	40	150	150	15	40	40	40	10	1,250	13	130	400(300)	130	40
Cr	15	15	15	5	5	15	15	5	0.3	15	18	3	18(196)	18	6
Mn															
Fe	100,000				10,000			1000		200,000			94,000	11,000[b]	2200[b]
Co	40	13	13	13	130	40	40	13	3	130	1	10	12(46)	12	360
Ni	150	15	15	15	450	150	150	50	5	60	1	15	5(127)	5	5
Cu	180	60	180	60	180	180	60	60	60	180	2	20	50(118)	18	18
Zn	40	400	40	12	120	40	40	120	3	85	4	4	35(220)	35	12
Br	0.5	0.5	0.5	0.2	0.2	0.5	0.5	0.5	0.2	0.2	0.05	1	0.2	0.2	0.2
Y	40	40	40	40	120	120	120	120	5	60	1	35	35	35	35
Zr	200	200	200	200	200	200	200	200	60	200	5	20	60	60	200
Nb	4	40	13	40	40	40	40	13	2	13	1	5	13	13	13
Mo	3	3	3	3	30	30	3	3	5	200	1	4	10(30)	4	1
I	1	0.3	1	<0.3	1	0.3	<0.3	3	30	1	1	1	1	<0.3	0.3

a NBS reference values

b raw coal analysis

TABLE 2

ELEMENT	RANGE[a]	DATA FROM VARIOUS SOURCES[b,c,d,e] coal	ash	CRUSTAL ABUNDANCE[f]
F	30->500	71-175		544
Cl	1->50	6-1000	186-3,000	126
Sc	3-100	3	10-1,000	25
Ti	300-8000	180-960	~30,000	10,500
V	10-1250	4-50	0.2-24,600	136
Cr	0.3-15	< 2-27	116-800	122
Mn		70-130	250-280	
Fe				
Co	3-130	3-25	10-39	29
Ni	5-450	4-100	5-80,000	99
Cu	60-180	3-180	15->500	68
Zn	3-400	20-200	160-10,000	76
Br	0.2-0.5	0.1-23	7-12	2.5
Y	5-120	3-25	100	31
Zr	60-200	10-300	115-5000	162
Nb	2-40	5-41		20
Mo	3-200	trace-3000	8-500	1.2
I	<0.3-30		142-587	0.46

[a]this study [b]Babu, 1975 [c]Goldscmidt, 1954 [d]Wedepohl, 1969 [e]Yudovich et al., 1972

[f]Fairbridge, 1972.

TABLE 3 - ESCA Chemical Analysis of Raw Coal Surfaces

Element (wt %) 15%	Raw Coal Samples[a]													
	N8S Standards				North American Coals									
	1632a		1635		1		5		8		10		12	
	ESCA	bulk[b]	ESCA	bulk[b]	ESCA	bulk[c]	ESCA	bulk[c]	ESCA	bulk[c]	ESCA	bulk[c]	ESCA	bulk[c]
Si	7.7	5.8	1.3	0.52	10.5	6.0	1.0	1.0	2.7	1.0	N.D.	2.0	4.1	N.A.
Al	5.20	3.1	0.8	0.30	10.6	2.0	2.5	2.0	7.4	1.0	1.2	2.0	3.4	N.A.
Fe	N.D.[d]	1.1	N.D.	0.22	N.D.	2.0	0.4	0.1	N.D.	0.50	0.9	1.0	1.0	N.A.
Ca	N.D.	0.24	1.5	0.54	N.D.	5.0	1.7	2.0	2.4	0.30	N.D.	0.5	1.7	N.A.
Ti	N.D.	0.15	N.D.	0.02	N.D.	0.1	N.D.	0.5	N.D.	0.1	0.9	0.3	N.D.	N.A.
S	N.D.	1.59	0.8	0.32	N.D.	2.0	N.D.	3.0	N.D.	2.0	3.1	3.0	N.D.	N.A.
F	1.25	N.A.[e]	1.4	N.A.	N.D.	N.A.	1.9	N.A.	3.8	N.A.	N.D.	N.A.	N.D.	N.A.
Cl	N.D.	0.08	N.D.	0.003	0.8	N.A.	1.1	N.A.	0.9	N.A.	1.5	N.A.	2.2	N.A.
N	1.2	1.27	1.5	1.0	0.3	N.A.	2.0	N.A.	1.4	N.A.	N.D.	N.A.	62.0	N.A.
C[f]	59.3	{86.7	73.8	{97.1	48.1	{82.9	74.0	{91.4	60.0	{95.1	71.8	{91.2	25.6	N.A.
O[g]	25.3		18.9		29.7		15.3		21.4		20.6			

[a]Surface concentrations are calculated from equation 1 using ESCA peak intensity ratios normalized to Si 2s except Sample No. 10, where Al 2s had to be used. Note the surface compositions have been calculated on a hydrogen free basis as hydrogen cannot be detected by ESCA.

[b]Accepted values from US N8S certificate of analysis (14)and/or reference (15).

[c]Bulk analysis by XRF and/or SSMS (4); note carbon and oxygen (a combined value) are determined by difference; coal 12 not analyzed.

[d]N.D. not detected. [e]N.A. not analyzed.

[f]Carbon content measured by ESCA includes a small sorbed portion (hydrocarbons) derived from the UHV system.

[g]Oxygen content measured includes a small portion of adsorbed oxygen due to handling in air prior to analysis.

TABLE 4 - ESCA Chemical Analysis of Coal Ash Surfaces

Element (wt %) 15%	Ashed Samples[a]											
	NBS Standard		North American Coal Ash									
	1633a		1		5		8		10		12	
	ESCA	bulk[b]	ESCA	bulk[c]	ESCA	bulk[c]	ESCA	bulk[c]	ESCA	bulk[c]	ESCA	bulk[c]
Si	16.9	22.8	10.9	10.0	21.5	25.0	2.8	3.0	5.1	10.0	4.6	5.3
Al	10.0	(14.0)	8.2	7.0	10.0	10.0	6.4	3.0	11.3	9.0	9.5	6.6
Fe	2.7	9.4	1.4	6.1	N.D.	1.0	1.1	0.1	4.2	10.0	8.0	5.4
Ca	2.2	1.1	5.8	10.0	0.9	0.5	2.9	0.1	5.1	4.0	9.8	25.7
Ti	1.3	(0.8)	1.5	0.1	2.5	1.0	0.6	0.03	0.6	0.3	N.D.	0.2
S[d]	4.2	[≥0.05]	1.87	N.D.	N.D.	N.D.	1.6 1.6	N.D.	3.74	N.D.	3.9	4.9
F	2.0	[≈0.05]	0.9	0.05	N.D.	N.D.	1.0	0.05	N.D.	0.05	N.D.	N.A.
Ba	N.D.	(0.15)	0.8	0.2	N.D.	0.06	1.5	0.6	N.D.	0.3	N.D.	N.A.
Mg	N.D.	0.50	0.9	5.0	N.D.	0.10	N.D.	N.D.	6.7	10.0	14.5	5.8
Na	N.D.	N.A.	N.D.	N.A.	N.D.	N.A.	N.D.	N.A.	3.2	N.A.	N.D.	0.7
C[e]	14.1	{51.14	40.5	{61.55	31.4	{62.34	66.5	{93.12	34.4	{56.35	28.1	{45.4
O[f]	46.6		27.3		33.7		14.0		25.7		21.7	

[a]Surface concentrations are calculated from equation 1 using XPS peak intensity ratios normalized to Si 2s.

[b]Accepted values from US NBS certificate of analysis (14); values in brackets listed but not certified, values in square brackets determined in concomitant SSMS study (4).

[c]Analysis by XRF and/or SSMS (4).

[d]Sulphur is present as the sulphate species (S^{6+}) except for ashed sample No. 8 where sulphide (S^{2-}) was also detected.

[e]As per Table 1; note some of this carbon is probably carbonaceous surface sited residue deposited during the coal ashing step.

[f]As per Table 1; some of this oxygen will be from oxygen species such as CO, CO_2, etc., associated with the carbonaceous coating (see e).

ANALYSIS OF SUB-MICRON MINERAL MATTER IN COAL VIA SCANNING TRANSMISSION ELECTRON MICROSCOPY*

Robert M. Allen and John B. VanderSande**

Materials Science Division
Sandia National Laboratories
Livermore, California 94550
**Department of Materials Science and Engineering
Massachusetts Institute of Technology
Cambridge, Massachusetts 02139

The mineral matter present in coal plays a deleterious role during the combustion of pulverized coal fuel in power generating boilers. Recent papers (1-3) on such problems as heat exchanger fouling and the emission of particulate pollutants from boilers have indicated that a fundamental understanding of these problems (and hence clues as to how they may be mitigated) may not depend solely on analyzing the fraction of mineral matter in the coal and its gross chemical composition. It may also prove necessary to obtain data on the actual size distribution of the original mineral particles and inclusions, and the distribution of these minerals among the particles of the pulverized fuel.

Such detailed information cannot be obtained by the traditional means of coal minerals analysis. However, recent advances in electron optical instrumentation and techniques, such as the use of a scanning transmission electron microscope (STEM) for high spatial resolution chemical microanalysis, show great promise for this type of characterization and have already been applied to coal research (4-7). The present work involves the use of a STEM both to obtain quantitative information about the ultra-fine (<100nm diameter) mineral inclusions present in several coals, and to examine the inorganic elements (hereafter referred to as inherent mineral matter) atomically bound into the organic matrices of these coals. It is anticipated that this type of information will be useful in modeling the combustion of pulverized fuel particles.

Sample Preparation

Samples of three different coals were examined in the present study: A lignite from the Hagel Seam in North Dakota, a semianthracite from the #2 Seam in Pennsylvania, and a sample of pulverized bituminous coal obtained courtesy of the Tennessee Valley Authority. The gross inorganic chemical analyses of the high temperature ash (HTA) of these three coals is shown in Table I.

Preparation of specimens for STEM examination was straightforward. Samples of each coal were ground to a fine powder using a mortar and pestle (except for the fuel coal which was already in pulverized form). A standard 3mm diameter 200 mesh copper transmission electron microscope grid coated with a thin carbon support film was then dipped into the powdered coal. Upon removal the grid was tapped several times to shake off excess and oversize particles. The final result was a sample consisting of a thin dispersion of fine coal particles clinging to the carbon support film.

Specimens prepared in this manner are well suited for STEM viewing and have several advantages compared to specimens thinned from the bulk by microtoming or ion milling. Their most notable advantage is of course the ease of preparation. Along with this, since nearly all the particles clinging to the grid have at least some area transparent to the electron beam, a much greater amount of thin area more randomly dispersed in origin from within the coal is potentially available for STEM examination than would be found in specimens thinned from bulk samples. Results obtained from powdered coal specimens should therefore be more representative of the overall mineral content of the initial coal sample.

*This work supported by U.S. Department of Energy, DOE, under contract number DE-AC04-76DP00798.

Table I: Compositions of High Temperature Ash (HTA)

Coal Name	Hagel Seam*	Cumberland Fuel**	Pennsylvania #2 Seam*
Coal Rank	Lignite	High Volatile Bituminous	Semianthracite
%HTA	9.66	18.8	30.74
SiO_2(%a)***	28.20	51.3	80.00
Al_2O_3(%a)	9.35	19.8	12.10
TiO_2(%a)	0.58	0.2	3.09
Fe_2O_3(%a)	8.20	17.0	1.47
MgO(%a)	5.91	1.2	0.05
CaO(%a)	24.50	4.9	0.30
Na_2O(%a)	2.81	0.9	0.05
K_2O(%a)	0.33	2.8	0.35
P_2O_5(%a)	0.10	0.2	0.05
SO_3(%a)	17.40	1.6	0.30
Trace Elements >1000ppm of HTA (in ppm of HTA)	Ba-6700 Sr-3150	Not Available	None Reported

*Information courtesy of the Penn State Coal Data Base
**Information taken from reference (8).
***%a - oxide % of HTA of dry coal

Experimental Procedure

The STEM used in the present study was a JOEL 200CX equipped with a Tracor-Northern TN2000 energy dispersive spectrometry (EDS) system for x-ray analysis. The features of STEM operation pertinent to this work are illustrated in Figure 1. The sample was illuminated by a narrow probe of 200kV electrons which was scanned across its surface. Transmitted electrons were used to form an image of the sample volume being scanned. The probe could also be stopped and fixed on some feature of interest in the sample, at which point the characteristic x-rays emitted by the atoms under the probe could be analyzed to obtain chemical information from a sample region with a diameter approaching that of the probe diameter. Chemical characterization could be accomplished in this manner for all elements with atomic number $Z \geq 11$.

For studies of mineral matter embedded in particles of powdered coal, advantage was taken of the difference in image contrast between the crystalline mineral particles and the surrounding amorphous organic matrix. The crystalline particles are capable of diffracting electrons, and so appeared in strong contrast when held at specific angles to the incident electron beam. The sample thus needed only to be tilted through some moderate range of angles (generally $\pm$ 45° from the horizontal) to quickly establish the locations of the minerals within a given coal particle. During the tilting such particles abruptly "winked" in and out of strong diffraction contrast, while the amorphous matrix changed contrast only gradually as a function of the change in sample thickness intercepted by the electron beam. An example of an image of a mineral particle visible by strong diffraction contrast amidst an amorphous coal matrix is shown in Figure 2. It is estimated that the imaging procedure could detect mineral particles with diameters >~2nm. Particles smaller than this would most likely remain indistinguishable from the amorphous matrix.

With the location of an embedded mineral particle thus determined, the probe was fixed on the mineral and an x-ray spectrum was acquired. Except in the instance where the mineral extended through the full thickness of the coal particle intercepted by the probe, this spectrum consisted of a superposition of a particle spectrum and a matrix spectrum. To determine the signal associated with the inclusion, the probe was subsequently moved 1-2 particle diameters away to a region of the matrix known to be free of other minerals (within the resolution limitation

discussed in the preceeding paragraph), where a second spectrum was collected. Comparison of the two x-ray spectra generally quickly revealed the primary elemental constituents of the mineral (again, for elements of atomic number $Z \geq 11$). Two examples of this type of analysis are shown for a Ti-rich particle in the Cumberland fuel coal in Figure 3, and a particle rich in Ba and S in the Hagel Seam coal in Figure 4.

Results and Discussion

The results of the STEM examination of the three coals are summarized in Table II. The first half of the table deals with the data obtained in a random sampling of mineral inclusions with mean diameters <100nm which were found embedded in the coal particles. Quantitative results are presented for the two most frequently observed mineral types in this size range for each of the three starting coals.

The second half of the table describes the results of the matrix measurements which were undertaken concurrently with the particle analyses. Aside from being necessary to correctly identify the constituents associated with the discrete mineral particles, the matrix spectra themselves provided additional information on the inherent mineral elements atomically bound into the organic coal matrix, without the danger of confusion from elements in discrete mineral particles (at least for particles larger than ~2nm in size). Recent work has suggested that such inherent mineral matter may comprise >15% of the total mineral matter in pulverized fuels (8).

Table II: Results of STEM Analysis

Coal Name		Hagel Seam	Cumberland Fuel	Penn.#2 Seam
Total # of Particles Analyzed (dia. $\leq$100nm):		29	30	27
Predominant Particle Types*				
#1	Major Elements	Fe	Ti	Ca
	Number Observed	15	14	11
	Average Diameter (nm)	43±17	45±22	45±27
	Possible species**	-	TiO_2(Rutile)	$CaCO_3$(Calcite)
#2	Major Elements	Ba,S	Ca	Ti
	Number Observed	7	5	10
	Average Diameter(nm)	60±28	50±17	36±13
	Possible species**	$BaSO_4$(Barite)	$CaCO_3$(Calcite)	TiO_2(Rutile)
# of Different Matrix Areas Analyzed:		25	21	24
Most Common Signal From Organic Matrix:		Ca	Si, Al	S
Frequency of Observation of Most Common Signal (% of Total # of Areas Analyzed):		96%	90%	42%
Frequency of Observation of S Signal from Matrix (% of Total # of Areas Analyzed):		28%	43%	42%

*The two most frequently observed particle types for particles with mean diameters $\leq$100nm. Categorization into types is based on major elements ($Z \geq 11$) observed in x-ray spectra attributable to particles.

**Tentative identification based on major elements ($Z \geq 11$) found in spectra. Species listed are the most common minerals found in coal which could produce the observed spectra. No clear choice exists for the Fe-rich particles in the lignite.

For all three coals, the predominant mineral species observed in the ≤100nm size range would not be predicted from the results of the chemical analyses of the high temperature ash of the coals. None of the major elements (Z>11) observed (with the exception of sulfur in the Ba,S-rich particles) constitutes more than 10% of the HTA for the respective coals; indeed, Ba in the lignite, Ti in the bituminous coal, and Ca in the semianthracite all make up less than 1% of the respective ashes. Encountering these elements as the major constituents in the predominant mineral species observed in a random sampling of particles <100nm in diameter indicates that the distribution of inorganic elements must not be uniform over all size ranges of mineral inclusions. In particular, for all three coals, the predominant mineral species observed in the <100nm size range must therefore differ from those species predominating at larger size ranges.

In analyzing the background spectra obtained in this work, it was found that for two of the coals a particular element or combination of elements was observed in greater than 90% of all matrix measurements: Ca for the Hagel Seam lignite and a combination of Si and Al for the Cumberland bituminous. Examples of these two characteristic elemental signatures may be found in the two matrix spectra in Figures 3 and 4.

The semianthracite had no elements of Z≥11 which were nearly as consistently observed in association with the matrix. In this coal, the most frequently observed matrix signal was from S, which only appeared in 42% of the observations. Indeed, in all three coals a S signal was detected in association with organic matrix, but only on an irregular basis (i.e., in less than 50% of the areas examined). Other elements, such as Fe, were also occasionally observed in the coal matrices. Such a point-to-point variation in inherent (atomically bound) mineral content may be expected to further complicate attempts to model the evolution of pulverized fuel particles into fly ash during combustion processes.

Conclusions

1. The STEM is an instrument well suited for the characterization of the sub-micron sized mineral matter in coal and can also be used to identify inorganic elements atomically bound in the organic coal matrix.
2. For the three coals studied, a random survey was taken of mineral inclusions <100nm in mean diameter observed within coal particles in powdered coal samples. The results indicate that the predominant mineral species making up these inclusions differ from those species predominating in mineral particles at larger size ranges.
3. Two of the coals examined showed characteristic matrix "signatures" of inorganic elements which were observed in ≥90% of the matrix areas examined. The third coal did not. All three coals exhibited various elements with Z≥11, most notably S, which were only irregularly associated with the matrix signal (i.e., found <50% of the time).

References

1. R.W. Bryers, J. Eng. Power (Trans. ASME) 101, 506 (1979).
2. T.F. Wall, et. al, Prog. Energy Combust. Sci. 5, 1 (1979).
3. R.D. Smith, Prog. Energy Combust. Sci. 6, 53 (1980).
4. L.A. Harris, et. al, in Microstructural Science Vol.5, ed. by J.D. Brown, et. al, Elsevier North-Holland, Inc. (New York 1977) p. 351.
5. J.A. Little, et. al., in Proc. 38th Annual EMSA Meeting, ed. by G.W. Bailey, Claitors Publishing Division, (Baton Rouge, 1980) p. 220.
6. H. Heinemann, in Proc. Int. Conf. Coal Science, Dusseldorf, 7-9 Sept. 1981, Verlag Gluckauf (Essen, 1981) p. 567.
7. C.A. Wert and K.C. Hsieh, in Proc. Int. Conf. Coal Science, Dusseldorf, 7-9 Sept. 1981 Verlag Gluckauf(Essen, 1981) p. 780
8. J.H. Pohl, Energy and Environmental Research Corp., 8001 E. Irvine Blvd. Santa Ana, CA 92705, private communication

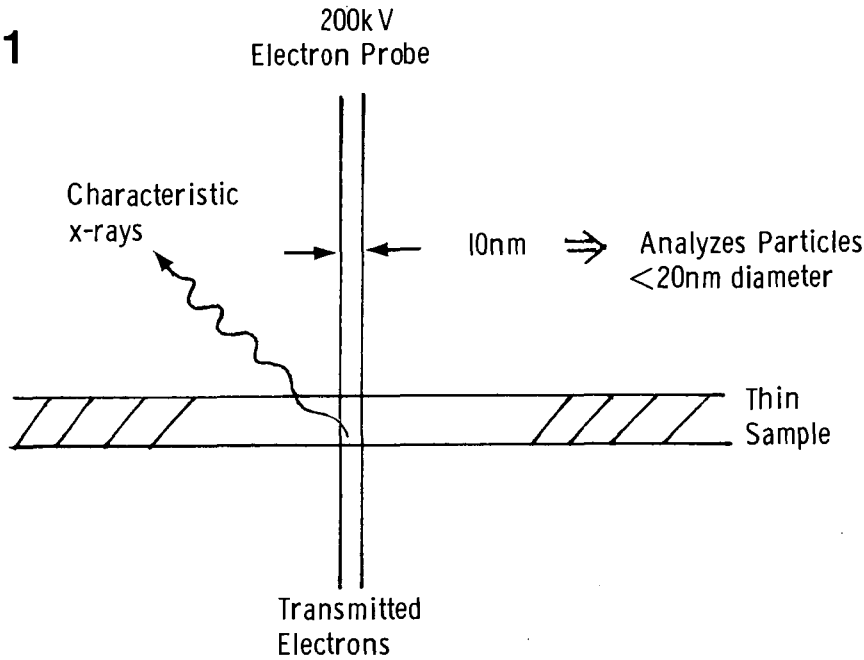

Figure 1: Schematic diagram of STEM operation during chemical microanalysis.

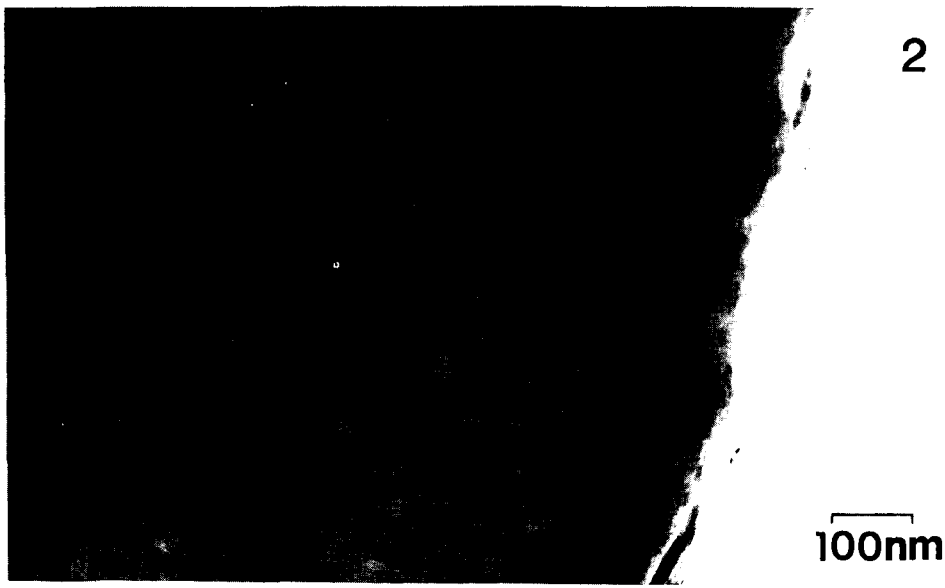

Figure 2: A transmitted electron image of a portion of a coal particle from the bituminous sample. A mineral inclusion is visible in strong diffraction contrast at A.

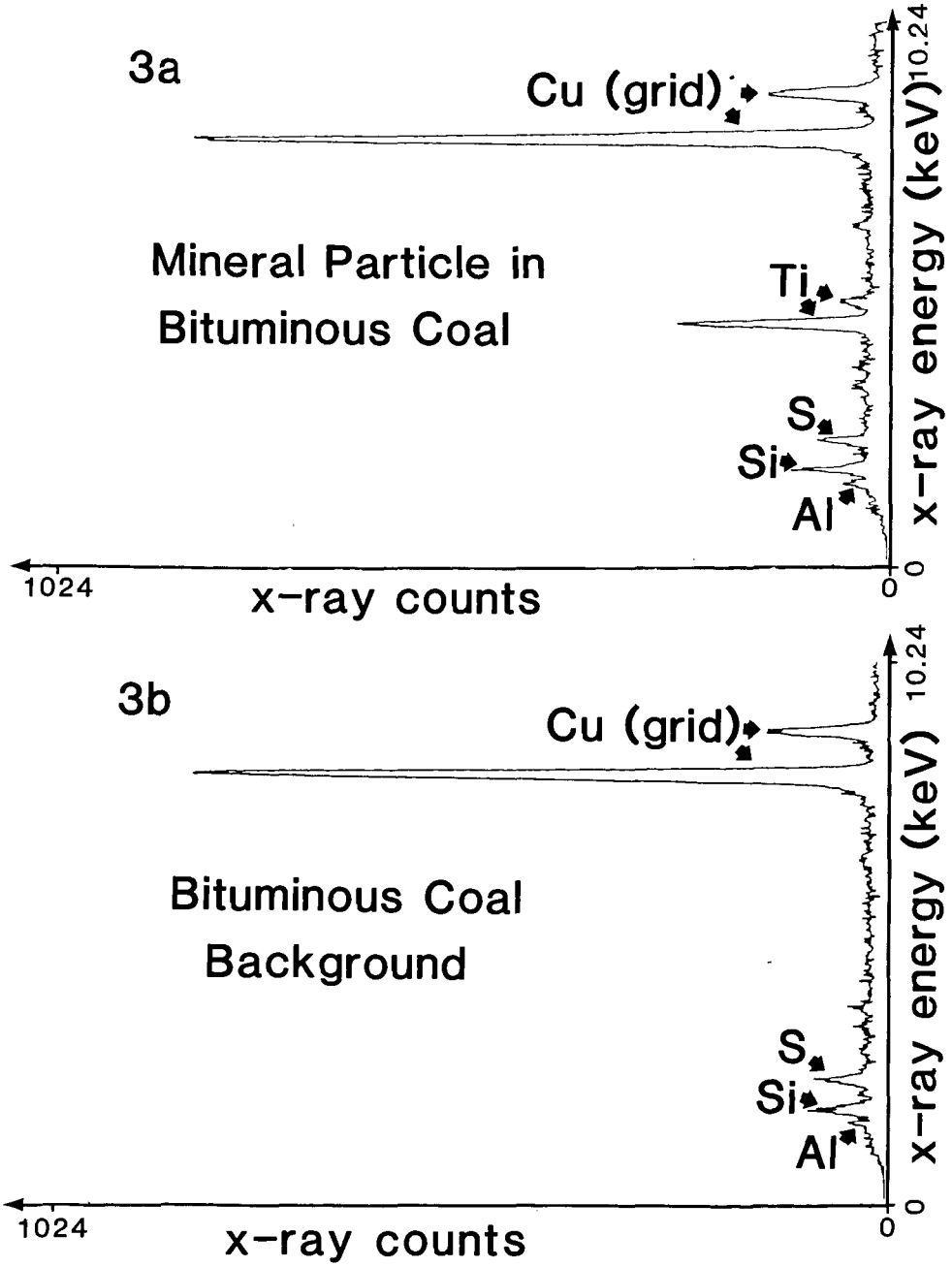

Figure 3: Examples of x-ray spectra from the bituminous sample.
a. Spectrum from particle shown in Figure 2.
b. Accompanying background spectrum.

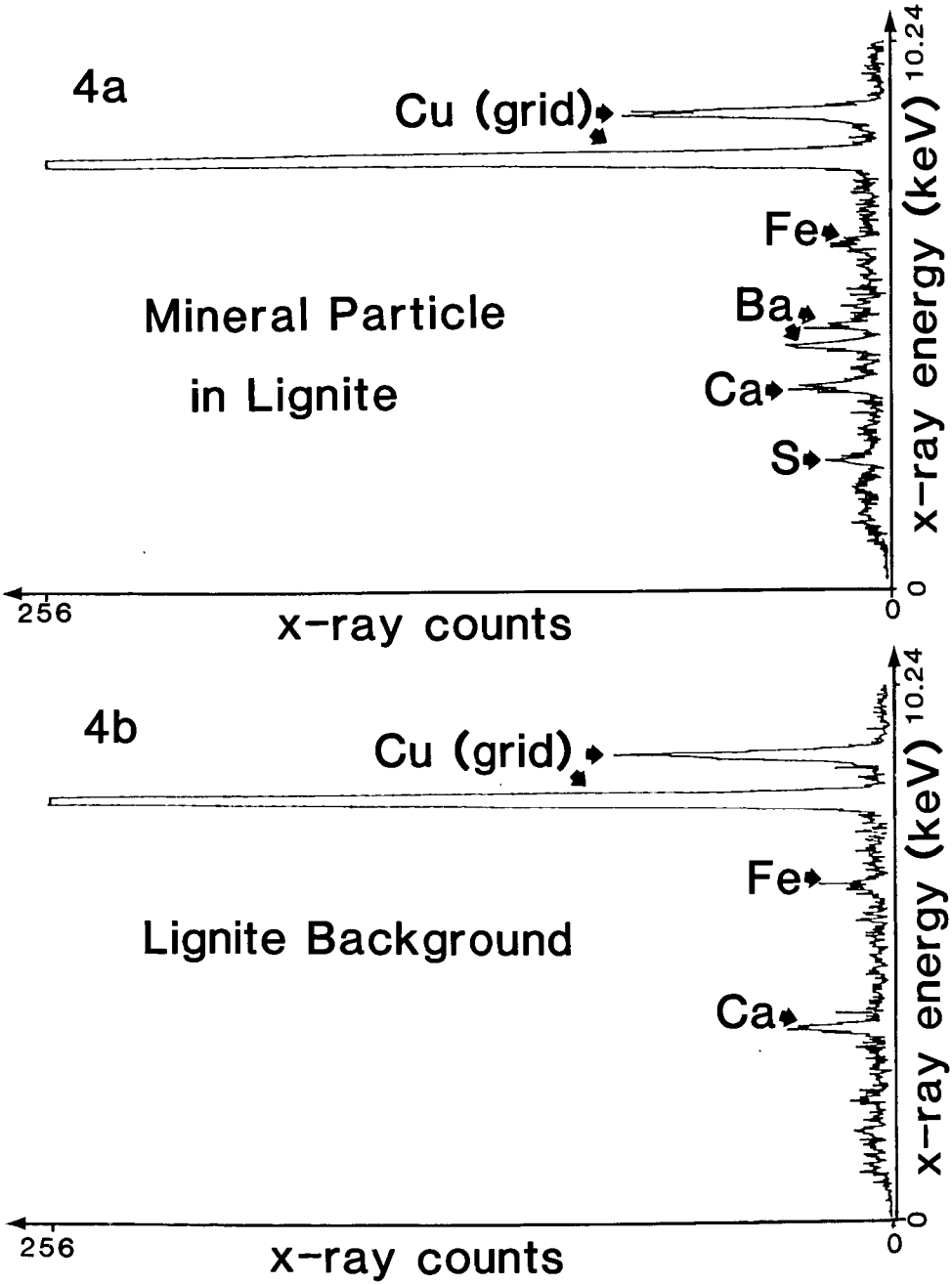

Figure 4: Examples of x-ray spectra from the lignite sample.
a. Spectrum from 40nm diameter particle.
b. Accompanying background spectrum.

The Determination of Mineral Distributions in Bituminous Coals by Electron Microscopy*

L. A. Harris

Oak Ridge National Laboratory
P. O. Box X
Oak Ridge, Tennessee 37830

INTRODUCTION

The chemistry and concentration of mineral matter in coals are factors that play important roles in coal combustion. For example, fouling, slagging, corrosion, and erosion are all mineral dependent processes that occur in coal-fired steam plants. Of these processes, fouling and slagging are probably the most detrimental to steam plant efficiency. Attempts to predict the fouling and/or slagging potential of a given coal have led to the development of equations based upon the ratios of base to acid minerals multiplied by either the sulfur or sodium content. (1,2) Essentially, these ratios take into account the lowering of the ash fusion temperature as a function of increased alkali bearing minerals.

In addition to the impact of mineral matter on steam plant operations, mineral matter also contributes to atmospheric particulates via steam plant stack emissions. Methods for reducing and/or altering the effects of minerals in coal are limited by the size and distribution of the minerals which is in turn related to the origin of the minerals, namely, whether syngenetic or epigenetic. As reported by Mackowsky (3) epigenetic minerals can be more readily removed from the coal because they are not as intimately mixed with the organic constituents (macerals) as syngenetic minerals. Furthermore, the epigenetic minerals may be considerably different from the syngenetic minerals due to differences in environments at the time of deposition and/or growth.

Currently, a common procedure for identifying minerals in coals consists of firstly low temperature ashing (L.T.A.) the coal and secondly analyzing the inorganic residue by means of x-ray diffractometry. Added information about the minral residue may be attained by utilizing a scanning electron microscope (SEM) with energy dispersive x-ray analysis (EDX) this procedure helps identify the minor minerals as well as locate trace elements. An advancement over the aforementioned SEM technique is one utilized by Finkelman (4) in which polished blocks were used so that not only the identity of minerals were obtained but also their relationship to the organic constituents could be determined.

In recent transmission electron microscopical studies of coals, (5,6) ultrafine minerals were observed (<1 μm). The observation and identity of these submicron minerals would have been difficult to achieve by use of the scanning electron microscope (SEM). However, the scanning transmission electron microscope (STEM) with energy dispersive x-ray analysis is an ideal analytical tool since it is capable of supplying elemental and diffraction data for particles as small as 30 nm in diameter. In this paper, we present observations and analyses of mineral matter in coals obtained through use of electron microscopes. These data significantly increase our knowledge of the mineral matter in coals as related to their affects on coal combustion.

---

*Research sponsored by the Division of Basic Energy Sciences, U.S. Department of Energy under contract W-7405-eng-26 with the Union Carbide Corporation.

EXPERIMENTAL

Sample Selection and Preparation

The samples used in this study were obtained from several high volatile bituminous coals of Eastern United States - Illinois No. 6, Kentucky No. 9, Elkhorn No. 3, and Hazard No. 4. Specimens were prepared for the transmission electron microscope studies from the above coals using a technique previously reported.[7] Optical thin sections approximately 10–15 μm thick were prepared. The thin sections were removed from the glass slides using acetone and subsequently mounted in an ion milling machine. Specimens were thinned (ion milled) using Argon gas and a liquid nitrogen cooled stage to insure against thermal damage to the specimen. Additional specimens consisting of polished blocks of coal were prepared for observation with the scanning electron microscope.

A high-voltage TEM (1MeV), a STEM (120Kv), and a SEM (JEM-U3) were used in this study. The STEM and SEM were fitted with energy dispersive x-ray analysis systems utilizing Si(Li) solid state detectors. Microchemical analyses of minerals for elements of atomic number 11 or greater could be attained for particles as small as 20 nm by using STEM with EDX.

RESULTS AND DISCUSSION

Submicron size minerals have been observed in all the high volatile bituminous coals that have been studied at this laboratory. A representative TEM micrograph of these coals (Fig. 1) reveals that these ultra-fine minerals are typically enclosed in a matrix consisting of vitrinite. These minerals are considered as syngenetic in orgin; (i.e., contemporaneously deposited in the peat basin with the organic constituents). Limited selected area diffraction (SAD) and energy dispersive x-ray analyses (EDX) of several of these minerals, using the STEM, showed that kaolinite (clay) is the dominant mineral species. However it must be noted that this analysis is strictly qualitative.

Moza et al. (8), in a study of minerals in coal as related to coal combustion systems, suggested that mineral fragments less than 8 microns would not be expected to gain enough momentum to collide with heat transfer tubes and these minerals would escape in the gas stream. However, from our present study of submicron micerals one can conceive of these particles fusing together to become substantially larger fragments. For example, a cubic μm of vitrinite may contain as much as 300 minerals, many of which actually touch.

Additional ultrafine syngenetic minerals have been observed to be intimately mixed with exinite (usually sporinite) and fragments of inertinite and vitrinite. These durain-like bands were probably derived from sediments consisting of degraded organic materials and mineral detritus deposited together in the peat swamp. The mineral species comprising these deposits are much more varied than those found in the vitrinite. In fact, these minerals usually contain many of the minor and trace elements associated with the mineral matter in coal (5) such as tin, nickel, zirconium titanium, and chromium. Typically, these minerals have a wider range of sizes varying from submicron particles to grains several microns long.

The TEM microstructure presented in Fig. 2 shows sporinite (S_P) segments bounded by regions consisting of granular maceral fragments and minerals (designated M-M). An aggregate of euhedral pyrite (P_Y) crystals located at one of the sporinite (S_P) boundaries is not an uncommon feature in many of the coals examined at this laboratory. The size of these pyrite crystals (~1 μm) appears to be identical to the

pyrite crystals in framboids located in vitrinite bands. It is worth noting that these minerals should prove more easily removed from the coal than those within macerals.

In Fig. 3, another view of mineral matter in durain-like bands is shown. A section of sporinite (S_P) interfaces with the inertinite maceral semifusinite (S_F). The region between these two macerals contains fine granular material including minerals. Additional minerals and organic debris are located within the collapsed sporinite walls (C_E). A large quartz grain (~6 μm) is located in a crushed cell in the semifusinite (S_F). Usually mineral inclusions within the vacant cell cavities of inertinite are considered as epigenetic. This point can be more clearly demonstrated by viewing an optical micrograph (Fig. 4) that shows epigenetic pyrite (P_Y) filling the crushed cell cavities in semifusinite (S_F).

Common structures found in bituminous coals are microfractures and/or joints that formed perpindicular to the bedding plane of the coal. These fractures (joints) are called cleat and originated in the coal after consolidation due to tectonic forces acting upon the earth's crust. In Fig. 5, a SEM micrograph of a polished block of coal, one can observe the appearance of cleat (CL). The epigenetic mineral filling the cleat (CL) was identified as calcite based upon EDX and x-ray diffraction analyses, the latter determination being performed on segments detached from the coal. The calcite forms a uniform mineral deposit approximately 10 μm thick and entends over several millimeters. A segment of the calcite sheet removed for analyses exposes one of the cleat walls (CLW). Typically, minerals in cleat can be readily separated from the organic constituents in coal, this is in contrast to the pyrite (P_Y) framboids (Fig. 5) enclosed in the vitrinite (V) band which would be extremely difficult to remove from the coal.

In addition to the presence of calcite in cleat, pyrite and kaolinite are also commonly found in cleat (9). The massiveness of the epigenetic mineral deposits in contrast to the syngenetic mineral distribution makes it apparent that the former mineral type constitute the major fraction of minerals in coal. The relative absence of calcite as a syngenetic mineral and its presence as a dominant cleat mineral in these coals suggests that calcite could readily be removed from the coal by current beneficiation methods. Indeed such cleaning of coals would also result in considerable reduction of pyrite and kaolinite. In general, the removal of calcite and pyrite should tend to increase the ash fusion temperature and consequently lead to a reduction in fouling and slagging.

CONCLUSIONS

1. Syngenetic and epigenetic minerals can be observed and identified by electron microscopy in conjunction with energy dispersive x-ray analysis.

2. Submicron micerals that are not readily identified or observed by scanning electron microscopy are easily viewed by use of transmission electron microscopy.

3. Calcite appears to be relatively scarce as a syngenetic mineral whereas calcite is an important epigenetic mineral usually occurring as cleat deposits.

4. Important minor syngenetic mineral assemblages appear to be associated with detritus. These minerals probably contain the major portion of minor and trace elements in coal.

5. Most of the epigenetic minerals should be readily removed from the coal resulting in a probable reduction in fouling and slagging.

REFERENCES

1. L. J. Garner, *J. of Institute of Fuel*, 40, 107 (1967).

2. R. C. Attig and A. F. Duzy, Proceeding of Am. Power Conf., 31, 290 (1969).

3. M-Th. Mackowsky, in Coal and Coal-Beating Strata, (Eds. D. G. Murchison and T. S. Westall), Elsevier, 309 (1965).

4. R. B. Finkelman and R. W. Stanton, *Fuel*, 57, 763 (1978).

5. L. A. Harris and C. S. Yust, Anvances In Chemistry Series 192, (Eds. M. L. Gorbaty and K. Ouchi), *Am. Chem. Soc.*, 321 (1981).

6. L. A. Harris, D. N. Braski, and C. S. Yust, *Microstructural Science*, 5, 351 (1977).

7. L. A. Harris and C. S. Yust, *Fuel*, 55, 233 (1976).

8. A. K. Moza, D. W. Strickler, and L. G. Austin, *Scanning Electron Microscopy/1980/IV*, 91, (1980).

9. L. A. Harris, O. B. Cavin, R. S. Crouse, and C. S. Yust, *Microscopica Acta*, 82, 343 (1980).

By acceptance of this article, the publisher or recipient acknowledges the U.S. Government's right to retain a nonexclusive, royalty-free license in and to any copyright covering the article.

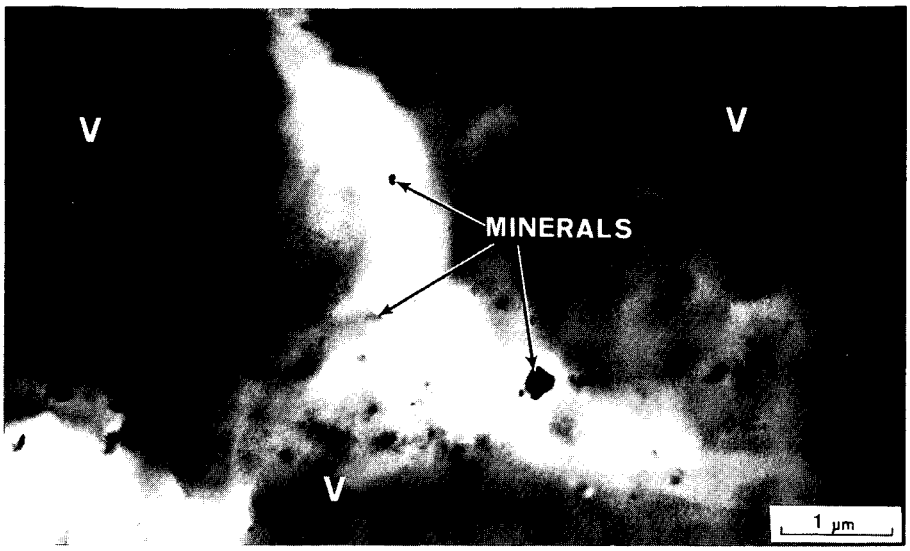

FIG. 1. TEM MICROGRAPH OF A HIGH VOLATILE BITUMINOUS COAL SHOWIN THE DISTRIBUTION OF SUBMICRON MINERALS (See Arrows) IN VITRINITE (V).

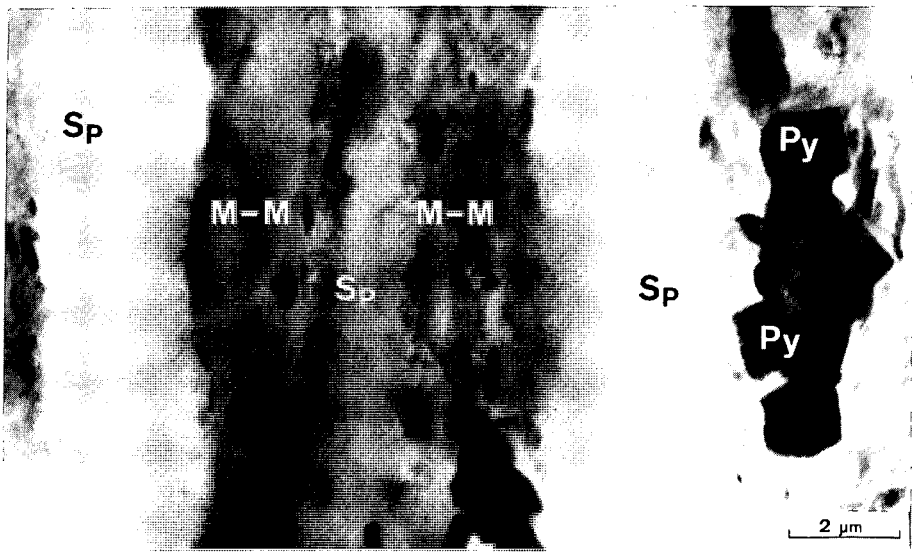

FIG. 2. TEM MICROGRAPH SHOWING THE RELATIONSHIP OF SPORINITE (S_p) WITH MINERAL BEARING BANDS (M-M). NOTE EUHEDRAL PYRITE (P_y) CRYSTALS AT SPORINITE (S_p) BOUNDARY.

FIG. 3. TEM MICROGRAPH OF MICROSTRUCTURE CONTAINING SPORINITE (S_P) AND SEMIFUSINITE (S_F). A QUARTZ GRAIN (See Arrow) IS LODGED IN A CELL CAVITY IN THE SEMIFUSINITE (S_F).

FIG. 4. OPTICAL MICROGRAPH SHOWING EPIGENETIC PYRITE (P_Y) FILLING THE CRUSHED CELL CAVITIES IN THE SEMIFUSINITE (S_F).

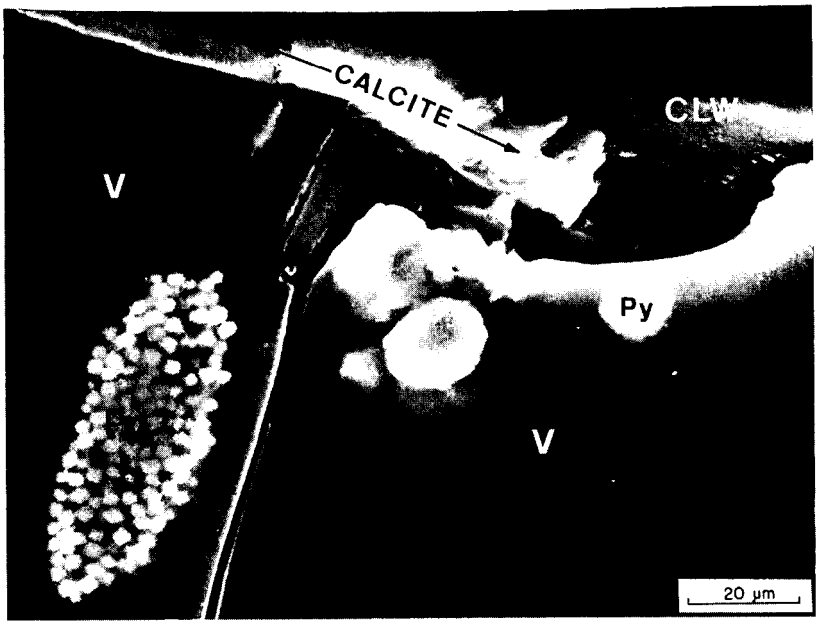

FIG. 5. SEM MICROGRAPH SHOWING CALCITE DEPOSIT (See Arrows) IN CLEAT. PYRITE (Py) FRAMBOIDS ENCLOSED IN VITRINITE (V) ALSO CAN BE SEEN.

THE FATE OF ALKALIS IN COAL COMBUSTION

G.W. Stewart and C.D. Stinespring
Aerodyne Research, Inc., Bedford, MA 01730

and

P. Davidovits
Aerodyne Research, Inc. and Department of Chemistry, Boston College
Chestnut Hill, MA 02167

INTRODUCTION

In the process of coal combustion, the ash particles deposited on various combustor components can cause serious materials damage. It has been shown that the alkali compounds contained in these particles are among the main causes of corrosion. Such corrosion may be especially damaging in proposed combined cycle power plants where the gas turbine blades are exposed to the combustor and therefore, are in direct contact with particles that escape filtering. To control the corrosive effects of the alkalis, it would be certainly useful to understand the mechanism governing the alkali contents of the particulates.

Over the past few years, a number of measurements have been made to obtain the concentration of trace elements in ash particles. Several of these studies measured the concentrations as a function of particle size.[1-6] In some of the experiments, the surface composition of the larger particulates has also been determined.[7-12] From these data, enrichment factors have been calculated for a large number of elements.[13] A selection from the available data is displayed in Figures 1 and 2 and Table I.

The composition of the smaller particles (a few microns or less) is of special interest since particles in this size range are more likely to escape filtering. It is commonly accepted that enrichment in the submicron particles, as well as on the surfaces of the larger particulates, is due to condensation of volatile species from the vapor phase. This would lead one to expect significant enrichment by elements that are themselves volatile or are found in coal as relatively volatile compounds. By and large, the measurements are consistent with these expectations. Thus, for example, elements such as Pb, Zn, Tℓ, Se, and As which are expected to be volatile, do indeed show significant enrichment in the smaller particles and, where data exist, also on the surfaces of the larger particles. However, an examination of the data shows that the alkalis exhibit a surprising departure from this trend. One would certainly expect the alkalis to be among the more volatile

species. In fact, combustion experiments done under laboratory conditions show significant vaporization of the alkalis.[14] Yet, the data gathered from actual coal combustion plants show that the smaller particles are not enriched by the alkalis. On the other hand, the surfaces of the larger particles do show significant enrichment by them.

The observation that the small ash particles are not enriched by the alkalis suggests that, contrary to expectations, the alkalis are not volatilized under actual case combustion conditions. If this is the case, the observed surface enrichment of the larger particles is not due to condensation, but must be produced by some other process, possibly diffusion from the interior to the surface.

Experiment Results

Evidence for these suggestions is found in the recent work of Stinespring and Stewart[15] and Stewart et al.[16] These experiments studied the behavior of the alkalis in model components under various coal combustion conditions. Since the alkalis are found in the organic as well as the inorganic components of coal, it is important to understand their behavior in both types of sites. Illite, which is a potassium containing aluminosilicate mineral, was chosen as a typical inorganic coal component. Sodium and potassium benzoate were chosen to represent the alkali containing organic fraction. These experiments examined the behavior of several elements; however, we will focus here only on the results relevant to the alkalis. Auger Electron Spectroscopy (AES) was used to determine the surface composition of aluminum silicate minerals which are heated in a well controlled environment. Differential thermal analysis (DTA) and thermogravimetric analysis (TGA) were performed on the model organic compounds to determine the extent of alkali release from the organic constituent.

The depth profiles for potassium indicate that the surface concentration of potassium begins to increase at temperatures as low as 200°C and it reaches an enrichment of about 13 at 1100°C. The depth of enrichment is about 100A. Order-of-magnitude calculations indicate that diffusion may occur on a time scale compatible with the residence time of ash particles in the combustor. From these results we conclude that alkali enrichment on the larger ash particles may indeed result from segregation rather than adsorption or condensation.

The DTA/TGA studies of sodium and potassium benzoate decomposition show that these model molecules initially decompose to form condensed ring organic molecules, alkali carbonate, and carbon dioxide. This initial decomposition process occurs over the temperature range of 400 to 600°C and is independent of the gas stream composition. Over this temperature range, there is no loss of alkali into the gas phase. Rather, all of the alkali is converted into the corresponding alkali carbonate. At higher temperature, the alkali carbonate decomposes and the course of this decomposition is determined primarily by the composition of the ambient gas. In an inert gas stream, the alkali carbonate decomposes over the temperature range of 700 to 900°C with release of carbon monoxide and atomic alkali. This decomposition has been confirmed by transporation mass spectrometer studies.[17] However, in a stream containing 20% CO_2 between 700 and 900°C, only carbon monoxide is released and the alkali is converted to alkali carbonate. This rection sequence occurs as long as residual carbon and carbon dioxide are present. Once the excess carbon has been converted to carbon monoxide, the alkali carbonate will decompose at temperatures in excess of 1200°C. Experiments were also performed with a combination of SO_2, CO_2, and O_2 in the gas stream. Here, it was found that the alkali carbonate is converted to the alkali sulfate with no indication of alkali loss over the temperature range studied (< 1300°K).

CONCLUSIONS

Thus, the results of the measurements and experiments discussed above do provide a plausible way to begin an explanation for the distribution of alkali in the ash particulates. To summarize:

1. Under typical coal combustion conditions in an atmosphere rich in CO_2 and/or SO_2, the alkalis in the organic fraction do not vaporize but remain bound in the ash as stable carbonates or sulfates.

2. The alkalis in the inorganic fraction diffuse to the surface producing enrichment by a factor of about 13 to a depth of about 100A.

The results, however, do not provide conclusive evidence about the fate of the alkalis. The effect of water vapor in the combustion stream has not yet been studied. Clearly, water could have an important effect on the vaporization process. Furthermore, the reasoning we have followed to explain the absence of alkali enrichment in the submicron particles requires that the volatilization of the alkalis in both the organic and inorganic fraction not be significant (say less than 20%).

It is possible to make a reasonably clear statement about the alkalis in the organic fraction under various combustion conditions. Here, the volatilization of the alkalis is primarily determined by the heterogeneous chemical reaction of the alkalis with the gas stream. Such detailed information, however, is not available for the alkalis in the inorganic fraction. Here, experimental data were not obtained under appropriate conditions. Thus, the combustion experiments of Mims et al., which do show significant alkali vaporization, were performed in an O_2 atmosphere without CO_2 or SO_2 enrichment. The experiments of Stinespring and Stewart, with the inorganically bound alkalis, measured only enrichment and did not study vaporization. The results of recent vaporization studies of Hastie et al.[18] were also not performed under conditions directly applicable to coal combustion. Clearly, a wider range of experimental data will have to be obtained. Specifically, the effects of surface chemistry on the alkali in the inorganic fraction will have to be studied before a more conclusive statement can be made about the fate of the alkali in coal combustion.

ACKNOWLEDGMENTS

This work was supported by the U.S. Department of Energy/Morgantown Energy Technology Center under Contract No. DE-AC21-81MC16244.

REFERENCES

1. D.F.S. Natusch and J.R. Wallace, Science 186, 695 (1974).

2. R.L. Davison, D.F.S. Natusch, J.R. Wallace, and C.A. Evans, Jr., Environ. Sci. & Technol. 8, 1107 (1974).

3. J.M. Ondov, R.C. Ragaini, and A.H. Biermann, Environ. Sci. & Technol. 13, 947 (1979).

4. D.G. Coles, R.C. Ragaini, J.M. Ondov, G.L. Fisher, D. Silberman, and B.A. Prentice, Environ. Sci. & Technol. 13, 455 (1979).

5. L.E. Wangen, Environ. Sci. & Technol. 15, 1081 (1981).

6. R.D. Smith, Prog. In Energy & Comb. Sci. 6, 53 (1980).

7. R.W. Linton, A. Loh, and D.S.F. Natusch, Science 191, 852 (1976).

8. J.A. Campbell, R.D. Smith, and L.E. Davis, Appl. Spectrosc. 32, 316 (1978).

9. S.J. Rothenberg, P. Denee, and P. Holloway, Appl. Spectrosc. 34, 549 (1980).

10. R.W. Linton, P. Williams, C.A. Evans, Jr., and D.S.F. Natusch, Anal. Chem. 49, 965 (1977).

11. L.D. Hulett and A.J. Weinberger, Environ. Sci. & Technol. 14, 965 (1980).

12. L.D. Hansen, D. Silberman, and G.L. Fisher, Environ. Sci. & Technol. 15, 1057 (1981).

13. Enrichment factors are obtained by normalizing to the bulk composition of the large particles (say > 30 μm).

14. C.A. Mims, N. Neville, R.J. Quann, and A.F. Sarofim, "Laboratory Studies of Trace Element Transformation During Coal Combustion," Presented at the 87th AIChE Meeting, August 1979, Boston, Mass.

15. C.D. Stinespring and G.W. Stewart, Atmos. Environ. 15, 307 (1981).

16. G.W. Stewart and A. Chakrabarti, High Temperature-High Pressure (In press) (1982).

17. A. Chakrabarti, D.W. Bonnell, G.W. Stewart, and J.W. Hastie, To be published (1981).

18. J.W. Hastie, E.R. Plante, and D.W. Bonnell, Interim Report No. NBSIR 81-2279, U.S. Department of Commerce, National Bureau of Standards, Washington, DC 20234 (1981).

SURFACE AND BULK ENRICHMENT OF COAL COMBUSTION ASH FOR SELECTED ELEMENTS

ELEMENT	ENRICHMENT		
	BULK*	BULK**	SURFACE***
As	9.4	13.4	---
Cd	11.5	---	---
Cr	2.4	6.2	3.3
Pb	3.8	8.4	11.0
Sb	7.9	---	---
Se	10.4	5.4	---
Tℓ	---	4.9	10.0
W	7.1	---	---
Zn	7.8	6.2	7.2
Aℓ	1.0	1.6	1.1
Ca	1.1	1.0	1.6
Cℓ	1.1	1.0	---
Cs	1.2	---	---
Fe	1.3	1.3	0.8
K	1.1	1.3	7.6
Mg	1.3	---	0.9
Mn	1.5	1.7	6.4
Na	1.5	---	15.2
Rb	1.1	1.7	---
Ti	1.2	1.2	0.9
Be	1.6	---	6.0
Cu	2.3	2.2	
V	3.8	2.7	2.0

*Bulk enrichment defined as the ratio of the concentration in a 1μ particles to that in an 18.5μ particle, from D.G. Coles, R.C. Ragaini, J.M. Ondov, G.L. Fisher, D. Silberman, B.A. Prentice, Environ. Sci. & Tech., 13, 455 (1979).

**Bulk enrichment defined as the ratio of the concentration in a 0.15μ particle to that in a 20μ particle, from R.D. Smith, Prog. in Energy & Comb. Sci., 6, 53 (1980).

***Surface enrichment defined as the ratio of the surface composition divided by the composition at 500 Å, from R.W. Linton, P. Williams, C.A. Evans, Jr., and D.S.F. Natusch, Anal. Chem., 49, 1514 (1977).

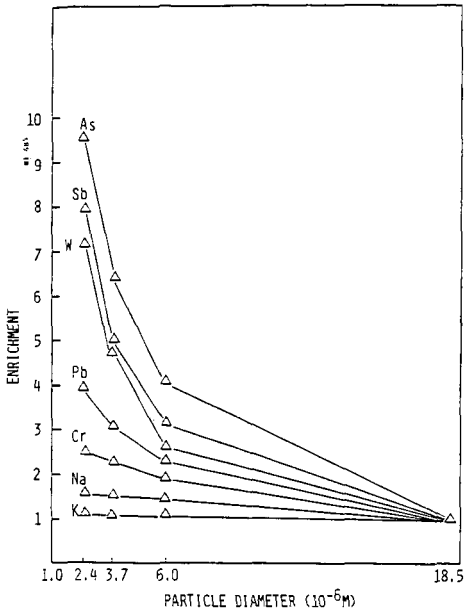

Figure 1, Enrichment vs. Particle Size, Based on Data from Coles et al., Environ. Sci. and Tech., 13, 455 (1979).

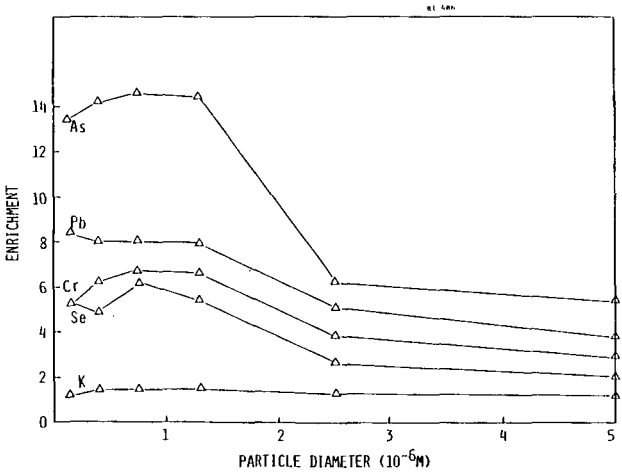

Figure 2. Enrichment vs. Particle Size, Based on Data by Smith, Prog. Energy and Comb. Sci., 6, 53 (1980).

Coal Ash Sintering Model and the Rate Measurements

E. Raask

Central Electricity Research Laboratories
Kelvin Avenue
Leatherhead, Surrey, UK

INTRODUCTION

In spite of innumerable laboratory investigations and the wealth of practical experience, there remains some enigmatic facets in the formation of sintered ash and slag deposit on heat exchange surfaces in coal-fired boilers. That is, occurrences of massive build-up of ash deposits can take boiler design and operation engineers by surprise. This would suggest that the engineers are receiving incomplete or incorrect information on the deposit-forming propensity of ash in different coals.

Traditional methods of assessing the behavior of deposit-forming impurities in high temperature boiler plants are based on ash fusion tests as described in different national standards for coal analysis and testing, e.g., ASTM (1968), British Standard (1970), DIN (1976) and Norme Francaise (1945). These ash fusion tests have been developed from refractory material technology, and are based on observations of the change in shape and size of an ash sample on heating. It has been realized that the results of ash fusion tests are frequently imprecise, and can lead to a mistaken assessment of the likely severity of boiler fouling and slagging.

There has been a number of suggestions made for ash fouling and slagging indices to predict more accurately the rate of deposit build-up with different coals as reviewed by Winegartner (1974). The empirical formulae, e.g., silica ratio, basic to acidic oxide ratio, and sodium and sulphur contents of coal, are based on the chemical analysis and have a limitation that they apply to particular coals. That is, there is no universal formula of predicting the severity of boiler fouling based on ash fusion tests and chemical analysis with all types of coal.

It is therefore evident that further research is necessary on the mechanism of ash particle-to-particle bonding at high temperatures. This work sets out to redefine an ash sintering model in terms of measurable parameters, surface tension, viscosity, electrical conductance, temperature, particle size and time. In the experimental work, novel methods of measuring the rates of ash sintering were applied, in order to test the validity of the sintering model.

SINTERING MODEL

Frenkel (1945) has derived an equation relating the growth of the interface between two spherical particles:

$$x^2 = \frac{3r\gamma t}{2\eta} \qquad (1)$$

where x is the radius of the interface, r is the original radius of the spheres, γ is the surface tension and t is the time. Rearranging the equation in terms of x/r and t, it becomes:

$$\frac{x}{r} = 1.225 \left(\frac{\gamma}{\eta r}\right)^{1/2} t^{1/2} \qquad (2)$$

and it is applicable when $\frac{x}{r} < 0.3$.

Sintering by viscous flow is the principal mechanism for the formation of deposits in coal fired boilers and the rate of sintering of different size particles for a given viscosity (10^8 N s m^{-2}) can be seen in Fig. 1 where the ratio of x/r is plotted against time on a logarithmic scale. The surface tension of fused ash was taken to be 0.32 N m^{-1} as measured previously by Raask (1966). Fig. 2 shows plots where the ratio of x/r represents the degree of sintering of 5 μm radius particles having different viscosities. Table 1 lists four arbitrary stages of sintering of ash deposit on boiler tubes from the initial contact between the ash particles to the formation of fused slag where the shapes of initial constituent particles are no longer distinguishable.

Table 1. Degree of Sintering Based on the Ratio of Neck Bond Radius to Particle Radius ($\frac{x}{r}$)

Ratio of x/r	Degress of Sintering	Comment
0.001	Onset of sintering	Deposit of this degree of sintering on boiler tubes would not have significant cohesive strength and would probably fall off under the action of gravity and boiler vibration.
0.01	Slightly sintered matrix	The deposit on boiler tubes would probably be removed by soot blowing.
0.1	Strongly sintered deposit	The deposit on boiler tubes would be difficult to remove by soot blowing.
>0.3	Slagging	The ash particles lose their original identity and the deposit on boiler tubes cannot be removed by soot blowing.

Rapid formation of sintered boiler deposits and slags is usually explained by the presence of a liquid phase or molten surface layer on ash particles. In high temperature glass and slag technology (blast furnace slag), a liquid phase is considered to have a viscosity value below 10 N s m^{-2}. The plots in Fig. 1 and 2 show that with small particles it is not necessary to evoke the presence of a liquid phase for a rapid sintering. For example, particles 0.1 m in diameter would require about 10 milliseconds to form a substantial sinter bond, when the viscosity has a high value of 10^8 N s m^{-2}. With the same viscosity 10 μm particles would require about 10 seconds to achieve the same degree of bonding.

The two parameters which govern the rate of sintering, namely the surface tension and the viscosity, both decrease with temperature as shown in Fig. 3. The temperature coefficient of surface tension is small (Curve A) and it is approximately proportional to the inverse of square root of temperature as discussed by Boni and Derge (1956) whereas the viscosity changes exponentially with temperature as shown by Curve B. It is therefore evident that the rate of sintering will show an inverse relationship with the viscosity and will increase exponentially with temperature.

PARTICLE-TO-PARTICLE NECK GROWTH MEASUREMENTS

The model for coal ash sintering discussed in the previous section is based on the viscous deformation and flow at the contact points between spherical particles. It would, therefore, be logical to consider determining the rate of sintering by a technique where the measurements are based directly on Frenkel's equation. Kuczynski (1949) has

carried out such sintering measurements by placing spherical particles on the surface of a glass slab of the same composition. Raask (1973) has reported some results of sintering rate measurements with coal ash slag particles based on a similar technique. The method requires spherical particles of ash and these can be prepared by passing ground coal minerals or slag through a vertical furnace as described by Raask (1969). Subsequently the particles were placed in a narrow groove on a platinum foil as shown in Fig. 4a. The particles were then introduced into a preheated furnace and kept at a constant temperature in air, or in a gas mixture for a period of five minutes to several hours. The radius of the sinter neck between the particles (Fig. 4b) was measured microscopically at the ambient temperature.

Fig. 5 shows the rate of neck growth between spherical particles of slag, 60 μm in radius, when heated in air. The spherical particles were prepared from boiler slag of a typical British bituminous coal ash which has caused some boiler fouling. The time for a firm degree of sintering, ($x/r = 0.1$, Table 1) was 135 seconds and 70 seconds at 1375 K and 1425 K, respectively. From these measurements the time required for a given degree of sintering can be calculated for the ash particles of different sizes. For example, the ash deposited on boiler tubes in pulverized coal fired boilers contains a larger number of particles of 0.5 to 1.0 μm in diameter, and these particles require only a few seconds to form a strongly sintered deposit in the same temperature range.

MEASUREMENTS OF ASH SINTERING RATES BY SIMULTANEOUS DILATOMETRIC AND ELECTRICAL CONDUCTANCE TECHNIQUES

Particle-to-particle sinter bonding usually results in a shrinkage of the external dimensions of a powder compact, and the dilatometric shrinkage measurements have been extensively used to determine the rate of sintering of glass and refractory materials. Smith (1956) has used a dilatometric shrinkage technique to study the sintering characteristics of pulverized fuel ash and an intercept of the shrinkage curve on the temperature axis was taken to define the sinter point. The measurements can give useful information and the results can be related to different degrees of sintering as outlined in Table 1. With some coal ashes, however, anomalous results can be obtained where the shrinkage measurements show no change although a significant degree of sintering has taken place. This deviation in the sintering behaviour from the Frenkel model makes it necessary to monitor another parameter which relates to the process of particulate ash coalescence.

Viscosity measurement by the rod penetration method has been applied by Boow (1972), Raask (1973) and Gibb (1981) to assess the sintering characteristics of different coal ashes. However, the rate of initial sintering cannot be measured by this technique, and Raask (1979) therefore considered the use of a method of electrical conductance measurements for monitoring the rate of sintering of coal ashes. Previously Ramanan and Chaklader (1975) had used the same technique to study sintering of glass sphere and nickel powder compacts.

The essential premise of this method is that the particulates are of an electrically conductive material, e.g., nickel, or that the glassy and ceramic materials contain some cations, e.g., alkali-metals which constitute an ionic conductance path when an electrical potential is applied. The method is, therefore, not applicable to measure the rate of sintering of nonconductive powders, e.g., alumina. This is not a limitation with coal ashes as all ashes contain sufficient amounts of cationic species; 0.1 per cent by weight quantity of sodium, potassium or calcium is likely to be adequate for the purpose of providing a conductance path.

A powder compact before sintering has a low conductance because of lack of particle-to-particle contacts. As the cross-sectional area of sinter bonds grows on heating the conductance is increased according to the equation:

$$\Lambda = A \left[\left(\frac{D}{D_o}\right)^{2/3} - 1 \right] \exp\left(\frac{-E}{RT}\right) \qquad (3)$$

where Λ is the conductance, D_o and D are the densities of sample before and after sintering, E is the energy of activation of sintering, R is the thermodynamic (gas) constant, T is the temperature and A is a constant. When the degree of sintering does not change, e.g., on cooling after the process of particle coalescence has reached the stage of density D, the equation (3) reduces to:

$$\Lambda = A_1 \exp\left(\frac{-E}{RT}\right) \qquad (4)$$

Rask (1975) has described a furnace assembly sketched in Fig. 6 for simultaneous measurements of the electrical conductance and the dilatometric shrinkage measurements. Fig. 7a shows the furnace in its down position for exposure of the sample well; sample crucible and three pellets of sintered ash from previous runs are shown at the well. Fig. 7b shows the furnace in the operation position. The heating rate of 0.1 K s^{-1} (6 K min^{-1}) was the same as that used in the ASTM (1968) ash fusion tests and the sinter tests can be carried in air or in simulated flue gas. Care is needed to stop heating when the ash sample has decreased 30 per cent in height to avoid slagging; once slag is formed it is difficult to remove the frozen material from the crucible.

Initial experiments were made with a soda glass, ground below 100 μm in particle size, of known viscosity/temperature characteristics published by Napolitano and Hawkins (1974). This was done to establish the validity of the simultaneous dilatometric and conductance measurements for determining the rate of sintering of powder compacts. The results are shown in Fig. 8 where Line A_1 depicts thermal expansion of the alumina support tubes and the sample, and Curve A shows the linear shrinkage of 10 mm high sample of powdered glass. The intercept of Curve A on the temperature axis, 875 K can be defined as the sinterpoint temperature.

The conductance plot (Curve B gives the same sinterpoint temperature and the results increase exponentially with temperature. On cooling Curve C shows a large hysteresis effect, that is, these are significantly higher than the corresponding results on heating. On reheating, however, the conductance measurements fit closely to Curve C. This behavior is in accord with the sintering model and the measurements on first heating when sinter bonds are formed, fit equation (3). Since on subsequent cooling and reheating, the process of particle coalescence is "frozen," the conductance change is governed by the exponential temperature as defined by equation (4).

Fig. 9 shows that there was in inverse relationship between the viscosity and the electrical conductance with respect to temperature. The conductance is dependent on the mobility, i.e., on the rate of diffusion of sodium and calcium ions in the glass matrix, and thus an inverse relationship between viscosity and self-diffusion is established as stipulated by Frenkel's sintering model. The results of conductance measurements plotted in Fig. 9 cover the viscosity range of 10^6 to 10^{10} N s m^{-2}, and it has been suggested previously by Raask (1973) that this is a relevant viscosity range for the formation of sintered deposits in coal fired boilers. That is, strong sinter bonds can form in this viscosity range within a few minutes or several days depending on the particle size (Figs. 1 and 2).

A number of British and US bituminous coal ashes have also been investigated for their sintering characteristics by the simultaneous shrinkage and conductance measurements. Fig. 10 shows typical shrinkage curve and the conductance plots on heating and on cooling which were obtained with an Illinois coal ash. It was evident that with

this ash and other bituminous coal ashes tested, sintering proceeded according to equation (3). The conductance data can be examined in more detail on the log n against 1/T plot as depicted on Fig. 11. The conductance plot on heating is nonlinear as expected from equation (3), whereas on cooling the plot was linear in accord with equation (4).

The conductance plot on heating can be divided into three sections where the logarithmic conductance values in S (micro-Siemen) are as follows: 1 to 10, 10 to 100 and 100 to 1000 units. Fig. 12 shows schematically the conductance path and shrinkage in three different degrees of sintering. The strength of the sintered pellet to crushing was determined at room temperature at the end of the sinter run. The presentation shows that an increase of 155 K from the initial sinter point temperature of 1125 K to 1180 K resulted in a high degree of sintering where the conductance readings were above 100 μS.

There are some coal ashes which exhibit in their sintering behavior a remarkable degree of divergence from the particle coalescence model as defined by equation (3). Fig. 13 shows that the nonbituminous coal ash, Leigh Creek, Australia, commenced to sinter at 1100 K according to the conductance measurements (Curve B). There was, however, no shrinkage of the ash pellet before temperature reached 1350 K (Curve A). That is, there was a gap of 250 K between the ash sinterpoint temperature indicated by the conductance measurements and that deduced from the shrinkage measurements. The reason for this nonconformist behavior must be that there was a significant degree of particle-to-particle bonding of the infusible material, e.g., quartz by a low viscosity phase at temperatures of 1100 to 1350 K. This may be an explanation for severe boiler fouling with high sodium coal ashes as discussed by Boow (1972) which is inconsistent with the results of conventional ash fusion tests. Leigh Creek ash had another unusual sintering feature; after an initial rise in conductance with temperature there was a decrease with an inflection point at 1325 K (Fig. 12). This was probably because the high amount of sodium in ash, 6.3 per cent of Na_2O by weight, resulted in crystallization of sodium alumino-silicate or aluminate in the temperature range of 1275 and 1325 K thus reducing the concentration of sodium ion in the glassy matrix.

Laboratory prepared ashes can be categorized according to the results of simultaneous measurements of shrinkage and the electrical conductance on sintering of an ash compact. The majority of ash compact coalesce and shrink according to the model as defined by equation (3) and particle-to-particle bonding is accompanied by the external shrinkage and a change in shape of an ash sample in early stages of sintering. With these ashes the conventional ash fusion tests, e.g., ASTM-Method (1968) usually give meaningful results. There are, however, some coal ashes rich in sodium which can give anomalous results when sinter tested as exemplified by the conductance and shrinkage curves in Fig. 12. That is, there can be a high degree of the internal particle-to-particle adhesion resulting in the formation of ash compact or deposit of high strength without the corresponding external shrinkage and these ashes should be tested by the electrical conductance technique to give meaningful results in the early stages of sintering.

NEED FOR AUGMENTING CONVENTIONAL ASH FUSION TESTS BY SINTERING RATE MEASUREMENTS

Ash fusion tests are based on the external change in shape, deformation, shrinkage, and flow of a pyramidic or cylindrical pellet of ash when heated in a laboratory furnace. A pyramidic shape is often used because it is easier to observe rounding of the pointed tip of the specimen than that of the edge of a cylindrical pellet. The methods are empirical, and strict observance of the test conditions is necessary to obtain reproducible results and these are laid down in the US ASTM (1968), British Standard (1970), German (DIN 1976) and French (Norme Francaise, 1945) procedures.

It has been recognized by many researchers that although ash fusion tests can given useful information regarding the fouling and slagging propensities of coal ashes, there are serious shortcomings. First, the tests are based on subjective observations and not precise scientific measurements, and they have a large margin of error. For example, the ASTM-method which is widely used in many countries allows for a 55 K margin of reproducibility in the initial deformation, softening hemisphere temperatures in an oxidizing atmosphere, and a 70 K margin of uncertainty in determining the initial deformation temperature in a reducing atmosphere. Within that 70 K margin the viscosity can change by an order of magnitude and consequently the rate of ash sintering will change by the same factor.

Another, more serious, shortcoming with the ash fusion method is that when testing some coal ashes there occurs an extensive degree of particle-to-particle bonding without any visible sign of deformation in the shape of an ash pellet. It is, therefore, evident that an additional method is needed to assess the sintering characteristics of coal ashes. A choice of sinter measuring techniques is given in Table 2.

TABLE 2. REVIEW OF ASH SINTERING TECHNIQUES

Measuring Technique	Equipment	Comments
Neck-growth measurements between spherical particles (Kuczynski, 1949), Raask, 1973)	A furnace and a microscope	This is suitable for homogeneous material when available in the form of spherical particles. It is not suitable for routine sinter testing of coal ashes.
Simultaneous shrinkage and electrical conductance measurements (Raask, 1979)	Needs a purpose-built furnace assembly for more accurate measurements. A simpler version uses platinum wire electrodes as described by Raask (1979) and by Cumming (1980)	Each ash could be provided with sintering rate curves. The method needs to be tested and assessed by different researchers.
Crushing strength measurements of sintered ash pellets (Atting and Barnhard, 1963; Gibb, 1981)	A furnace and a crushing strength measuring device	The method has been used by several researchers but there is no agreed procedure
Ash agglomeration by sieving test (Stallman and Neavel (1980)	A furnace and a sieving machine	This is one of the simplest methods of testing for initial sintering, and it warrants more systematic tests
Ash plug flow method	A tubular furnace tube with perforated plate to support an ash plug	So far no experimental results have been found in literature

The brief review in Table 2 shows that there are several laboratory methods of sinter testing coal ashes, which can give some useful information regarding their deposit

forming propensity. However, none of these techniques could be written as recommended methods, and a coordinated test program involving specialist researchers in different laboratories would be required to assess their general applicability.

CONCLUSIONS

1. Frenkel's sintering model is a useful introduction to understanding of the mechanism of formation of boiler deposits in the crucial early stages of particle-to-particle bonding. The model sets out unequivocally the rate controlling parameters in sintering, namely surface tension (the driving force for particle coalescence) viscosity (the temperature sensitive parameter) and particle size.

2. Measurements of the rate of neck-growth between the spherical particles demonstrate the validity of the sintering model, but the technique is not suitable for routine assessment tests of the sintering characteristics of different coal ashes.

3. A method of simultaneous measurements of dilatometric shrinkage and electrical conductance has been developed for assessing the deposit forming propensity of coal ashes. The measurements are based on a sintering model which stipulates that the formation of particle-to-particle bonding leads to enhanced conductance and increased density of ash test samples and boiler deposits.

4. There are some coal ashes, rich in sodium which do not behave as predicted from sintering models. With these ashes the sinterpoint temperature defined by the electrical conductance measurements can be over 250 K lower than that indicated by the results of conventional ash fusion tests.

ACKNOWLEDGEMENT

The work was carried out at the Central Electricity Research Laboratories and the paper is published by permission of the Central Electricity Generating Board.

REFERENCES

1. ASTM, Fusibility of Coal and Coke Ash, D1857-68 (1968).

2. R. C. Attig and D. H. Barnhardt, "A Laboratory Method of Evaluating Factors Affecting Tube Bank Fouling in Coal-Fired Boilers," Proceed. Int. Conf., Mechanism of Corrosion by Fuel Impurities, Marchwood, England, 1968, Butterworths Publ. p. 183.

3. R. E. Boni and G. Derge, "Surface Structure of Non-Oxidizing Slags Containing Sulphur," Trans. AIME, Journ. Metals, p. 59 (1956).

4. J. Boow, "Sodium and Ash Reactions in the Formation of Fireside Deposits in Pulverized Fuel Fired Boilers," Fuel, 51, 170 (1972).

5. British Standard, "The Analysis and Testing of Coal and Coke, BS Method 1016, Part 15 - Fusibility of Coal and Coke Ash," 8rit. Stand. Inst., London (1970).

6. J. W. Cumming, "Communication: The Electrical Resistance of Coal Ash at Elevated Temperatures," Journ. Inst. Energy, 53, 153 (1980).

7. DIN, "Determination of Ash Fusion Behavior," German Standard, DIN 51730 (1976).

8. J. J. Frenkel, "Viscous Flow of Crystalline Bodies Under the Action of Surface Tension," Journ. Phys. (Moscow) 9, 385 (1945).

9. W. H. Gibb, "The Slagging and Fouling Characteristics of Coals - 1. Ash Viscosity Measurements for the Determination of Slagging Propensity," Power Ind. Research, 1, 29 (1981).

10. G. C. Kuczynski, "Study of the Sintering of Glass," Journ. Appl. Phys. 20, 1160 (1949).

11. A. Napolitano and G. E. Hawkins, "Viscosity of a Standard Soda-Lime-Silica Glass," Journ. Res. US Nat. Bur. Stan. Sec. A., 68, 439 (1964).

12. F. Norme, "Determination of Ash Fusibility Curves," NF M03-012 (1945).

13. E. Raask, " Slag/Coal Interface Phenomena, "Trans. ASME for Power, Jan. p. 40, (1965a).

14. E. Raask, "Fusion of Silicate Particles in Coal Flames," Fuel, 48, 366 (1969).

15. E. Raask, "Boiler Fouling - The Mechanism of Slagging and Preventive Measures," VGB Kraftwerkstechnik, 53, 248 (1973).

16. E. Raask, "Sintering Characteristics of Coal Ashes by Simultaneous Dilatometry - Electrical Conductance Measurements," Journ. Therm. Anal., 16, 91 (1979).

17. T. Ramanan and A.C.D. Chaklader, "Electrical Resistivity of Hot-Pressed Compacts," Journ. Am. Ceram. Soc., 58, 476 (1975).

18. E. J. D. Smith, "The Sintering of Fly Ash," Journ. Inst. Fuel, 29, 1 (1956).

19. J. J. Stallman and R. C. Neavel, "Technique to Measure the Temperature of Agglomeration of Coal Ash," Fuel, 59, 584 (1980).

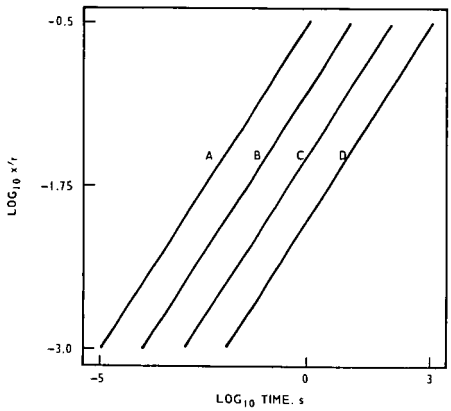

FIG. 1 LOG-LOG PLOT OF DEGREE OF SINTERING (x'/r) AGAINST TIME VISCOSITY – 10^8 N s m^{-2}

PARTICLE RADIUS: A – 0.05 μm B – 0.5 μm
C – 5.0 μm D – 50 μm

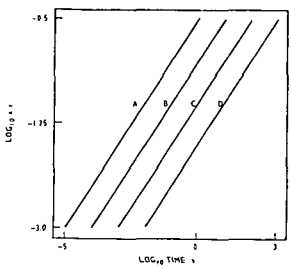

FIG 1 LOG-LOG PLOT OF DEGREE OF SINTERING (x r) AGAINST TIME VISCOSITY - 10^8 N s m^{-2}

PARTICLE RADIUS A - 0.05 μm B - 0.5 μm
C - 5.0 μm D - 50 μm

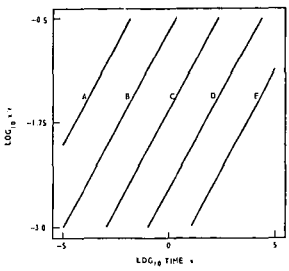

FIG 2 LOG-LOG PLOT OF DEGREE OF SINTERING (x r) AGAINST TIME PARTICLE RADIUS - 5 μm

VISCOSITY (N s m^{-2})

A - 10^4 B - 10^6
C - 10^8 D - 10^{10}
E - 10^{12}

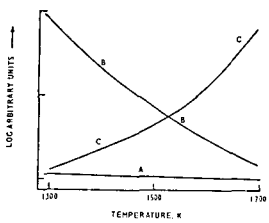

FIG. 3 THE EFFECT OF TEMPERATURE ON ASH SINTERING PARAMETERS

A - SURFACE TENSION B - VISCOSITY
C - RATE OF SINTERING

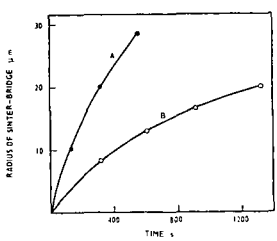

FIG 5 GROWTH OF SINTER BRIDGE BETWEEN PARTICLES, RADIUS - 60 μm

A - AT 1435 K B - AT 1375 K

10 μm

(a) SLAG PARTICLES ON PLATINUM PLATE BEFORE SINTERING

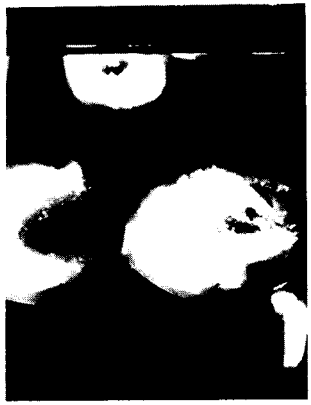

20 μm

(b) SINTER BRIDGED PARTICLES

FIG. 4 SINTERING OF SPHERICAL PARTICLES OF COAL ASH SLAG

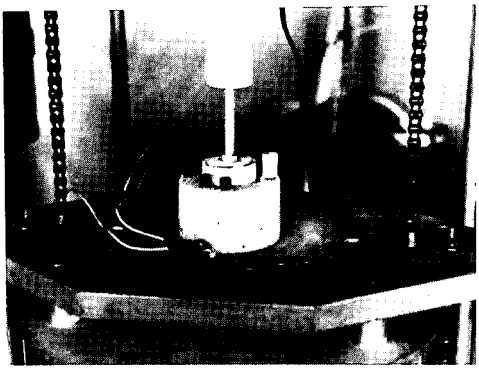

(a) DOWN POSITION FOR SAMPLE CHANGE

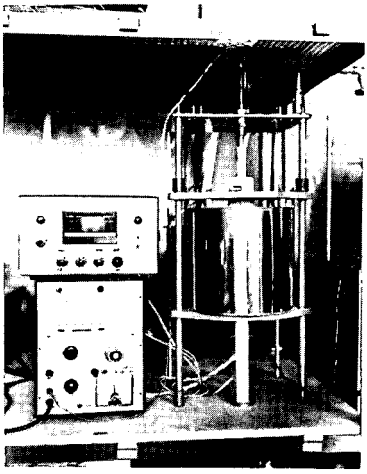

(b) OPERATION POSITION

FIG. 7 FURNACE ASSEMBLY FOR THE ASH SINTERING MEASUREMENTS

PLEASE RETURN THIS ORIGINAL TO DRAWING OFFICE

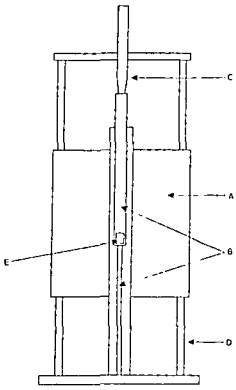

A FURNACE
B CONDUCTANCE LEADS AND THERMOCOUPLE
C DISPLACEMENT PROBE
D FURNACE HAS BALANCED LOWERING AND RAISING ACTION
E SAMPLE

FIG 6 SCHEMATIC OF FURNACE FOR SIMULTANEOUS SHRINKAGE AND CONDUCTANCE MEASUREMENTS

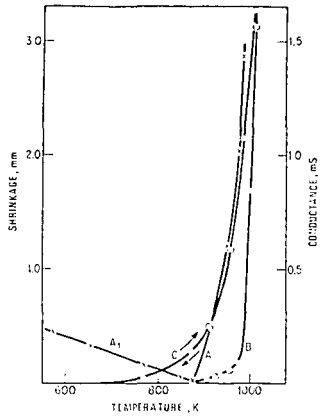

FIG 8 SIMULTANEOUS SHRINKAGE & ELECTRICAL CONDUCTANCE MEASUREMENTS OF SODA GLASS

A_1 - THERMAL EXPANSION
A - SHRINKAGE
B - CONDUCTANCE ON HEATING
C - CONDUCTANCE ON COOLING & REHEATING

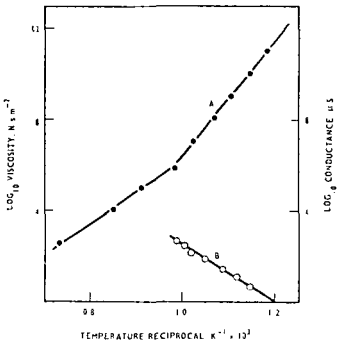

FIG 9 ARRHENIUS PLOTS OF VISCOSITY (A) AND CONDUCTANCE (B) OF SODA-GLASS

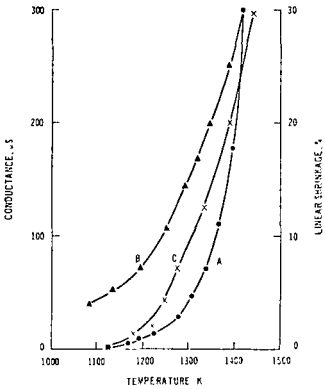

FIG 10 CONDUCTANCE AND SHRINKAGE PLOTS ON SINTERING OF ILLINOIS COAL ASH

A - CONDUCTANCE ON HEATING 5 K min^{-1}
B - CONDUCTANCE ON COOLING 5 K min^{-1}
C - SHRINKAGE ON HEATING 5 K min^{-1}

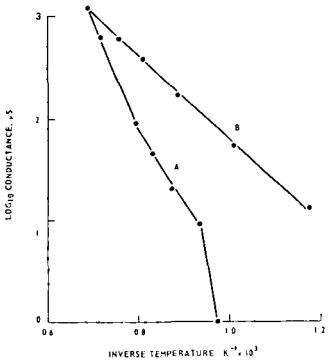

FIG 11 CONDUCTANCE LOGARITHM/INVERSE TEMPERATURE PLOT ON SINTERING OF COALITE BREEZE ASH

A – HEATING 5 K min⁻¹
B – COOLING 5 K min⁻¹

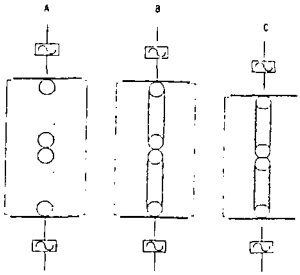

FIG 12 THREE STAGES IN THE SINTERING OF ILLINOIS COAL ASH – 12 mm HIGH, 8 mm DIA PELLET BETWEEN PLATINUM PLATES

	TEMP., K	COND, μS	SHRINK., %	STRENGTH, MN m⁻²
A FIRST CONTACT	1125	1.0	0.07	0
B INITIAL SINTER	1195	10	2.0	0.1
C RAPID SINTER	1280	100	10	1.3

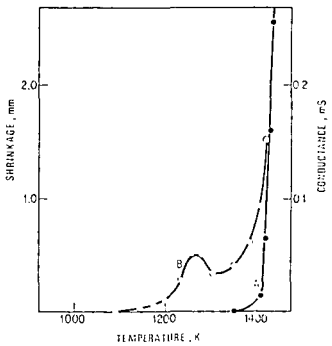

FIG 13 SIMULTANEOUS SHRINKAGE (A) & CONDUCTANCE MEASUREMENTS (B) LEIGH CREEK, AUSTRALIA COAL ASH

THE CAPTURE AND RETENTION OF SULFUR SPECIES BY CALCIUM COMPOUNDS DURING THE COMBUSTION OF PULVERIZED COAL

P. L. Case, M. P. Heap, C. N. McKinnon, D. W. Pershing and R. Payne

Energy and Environmental Research Corporation
8001 Irvine Blvd., Santa Ana, Calif. 92705

1. INTRODUCTION

Coal is the United States most abundant source of fossil fuel energy however its utilization poses several problems for society, among which are those associated with the formation of atmospheric pollutants during its combustion. Coal is not a pure hydrocarbon fuel, it contains inorganic matter (ash), nitrogen and sulfur which, in turn, form particulates (fly ash), nitrogen oxides and sulfur oxides. The emission of such pollutants to the atmosphere is undesirable and can be avoided by removing the pollutants from the combustion products, preventing their formation, or removing the constituents which form pollutants from the coal. This paper describes bench scale experiments which will establish whether and under which conditions calcium containing sorbents can be used to capture sulfur during pulverized coal combustion. Having established that sulfur capture is possible, the studies will then concentrate upon whether it is practical since sorbent injection into boilers could have a serious impact upon boiler operation. Sorbent injection will increase particulate mass loading, change slagging and fouling characteristics and will change fly ash properties.

The use of sorbents to control emissions of sulfur oxides from coal fired power plants is a conceptually simple process. A pulverized, calcium containing sorbent is injected into the combustion chamber of a boiler where it flash-calcines to lime (CaO) and, at the same time, reacts with sulfur dioxide and oxygen to form calcium sulfite and/or calcium sulfate. Considerable effort was expended in the late 1960's and early 1970's on development and demonstration projects (1), and although pilot plant studies showed promise, the results could not be duplicated in full scale systems. The lack of success was attributed to a combination of loss of reactivity of the lime due to deadburning and maldistribution of the sorbent. Recent pilot scale studies (2, 3) with low NO_x coal burners suggest that sorbent injection could be more effective under conditions which minimize NO_x formation in pulverized coal flames.

Nitrogen oxides are formed from two sources during pulverized coal combustion; molecular nitrogen which is part of the combustion air and nitrogen which is chemically bound in the organic coal matrix. Low NO_x pulverized coal burners are effective because they produce a fuel rich zone which minimizes fuel NO formation and lowers peak flame temperatures, which, in turn, reduces the rate of thermal NO production. If a sorbent is injected into a combustor fired with low NO_x burners it will experience lower peak temperatures and more reducing conditions than if the combustor was fired with "normal" burners. The opportunity to control both nitrogen and sulfur oxide emissions by preventing their formation may be given by the use of sorbent injection into low NO_x burners.

Sulfur capture by sorbent injection involves three processes, namely:

- Sorbent activation - the sorbent particles are heated and calcined. Ultimate particle reactivity will depend mainly upon initial properties and peak particle temperature. If the particle temperatures are too high, the sorbent loses its reactivity (deadburns).

- Capture - sulfur species (H_2S, COS or SO_2) react with the sorbent producing either sulfate or sulfide. The rate of absorption will depend upon

temperature, sulfur species concentration and sorbent characteristics.

- Regeneration - under certain conditions, the spent sorbent may decompose regenerating gas phase sulfur species.

The general reaction describing sulfur capture under oxidizing conditions is:

$$CaO + SO_2 + 1/2\ O_2 \rightarrow CaSO_4 \qquad 1)$$

The rate of this reaction, the rate of calcination, and the maximum calcium utilization imposed by pore blockage has been studied extensively in thin bed and dispersed flow reactors by several workers (4, 5). None of these studies duplicated the time temperature conditions that prevail in pulverized coal flames.

Borgwardt (6) has suggested that reactions such as:

$$CaCO_3 + H_2S \rightarrow CaS + H_2O + CO_2 \qquad 2)$$

$$CaO + H_2S \rightarrow CaS + H_2O, \qquad 3)$$

involving reduced sulfur species could become significant under fuel rich conditions. Extrapolation of rate data for such reactions (obtained by Ruth and Squires (7)) to pulverized coal flame conditions indicates that the reaction of H_2S with $CaCO_3$ is sufficiently fast to allow significant sulfur capture.

Consequently, it appears that there are two possible modes of sulfur capture by calcium based sorbents in a pulverized coal fired combustor operating under low NO_x conditions. Under oxidizing conditions, reduced peak temperatures will reduce deadburning and allow reaction 1 to proceed. If the sorbent is injected into the fuel rich region, reaction 2 may become significant, but calcium sulfide could be lost when the partially oxidized fuel is burned out. Thus retention of the sulfur becomes an important factor in the overall process. Figure 1 shows the effect of temperature and stoichiometric ratio on equilibrium calcium distribution. It indicates that under rich conditions (50% theoretical air) calcium sulfide is very stable compared to calcium sulfate under lean conditions (100% theoretical air or SR = 1.0). These calculations imply that if the sulfide is formed in the rich zone, then the transition to oxidizing conditions should be carried out quickly to prevent prolonged times under new stoichiometric conditions, and that the temperature during this transiton should be reduced. An experimental study has been carried out to determine whether either of the two routes referred to above are likely to allow simulataneous control of sulfur and nitrogen oxide emissions from pulverized coal fired boilers.

2. EXPERIMENTAL

A bench scale facility has been constructed which is capable of duplicating the history of the solid particles (coal and sorbent) and the products of combustion in a pulverized coal fired power plant. As shown in Figure 2, the system consists of three major components:

- The radiant furnace, a horizontal refractory lined cyclinder, which simulates the region close to the burners. Heat extraction is varied by adding or removing cooling tubes.

- The post flame cavity which simulates the volume above the burner zone of a boiler before the superheater.

- The convective section, cooled by banks of air cooled stainless steel tubes, which simulates the superheater, reheater and air heater sections of the boiler.

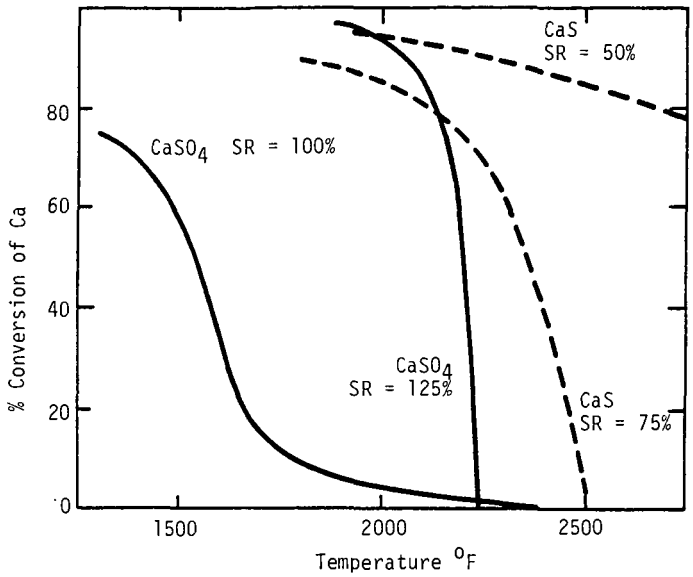

Figure 1. Effect of Temperature and Stoichiometric Ratio on Equilibrium Calcium Distribution - % Ca as $CaSO_4$ or CaS (Ca/S = 1)

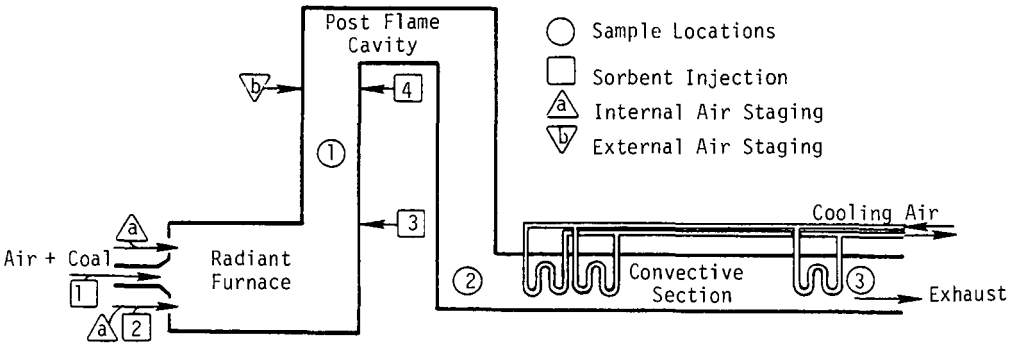

Figure 2. Schematic of Test Furnace Showing Location of Sample Ports, Staged Air Addition and Sorbent Injection.

The facility is fired with coal using a small scale low NO_x burner which could be operated in two modes - internally and externally staged. When the burner was operated with the second stage air supplied at the firing face through the staged air injectors, only the burner zone was fuel rich. This is referred to as internally staged. Alternatively, when the staging air was added downstream in the post flame cavity, the whole of the radiant furnace operated fuel rich. This is referred to in the text as external staging. The sorbent was added in any of four locations: 1) with the coal, 2) with the staged air at the burner face, 3) at the entry of the post flame cavity, and 4) with the downstream staged air when operating in the externally staged mode.

The measurement of sulfur species in combustion products containing active sorbents introduces several problems related to sample acquisition. A "phase discrimination" probe has been designed, constructed and tested which minimizes gas-solid contacting after sample extraction. SO_2 was measured with a non-dispersive ultra-violet absorption instrument. H_2S and COS were measured by gas chromatography using a flame photometric detector. Sulfur capture was based on SO_2 measurements with and without sorbent in every test case.

3. RESULTS

A series of experiments has been carried out with the coal and sorbent listed in Tables 1 and 2 in both the external and internal staging modes.

Indiana Coal

Ultimate Analysis, % Dry Basis

C	69.91
N	5.18
H	1.54
S	2.53
O	11.00
Ash	9.84

Calorific Value (dry bais) 12,515 Btu/lb

Moisture, average, as burned 7.0%

Table 1. Coal Properties

Vicron 45-3, Pfizer

Composition, typical, %

$CaCO_3$	97.0
$MgCO_3$	1.6
SiO_2	1.0
Al_2O_3	0.5
Fe_2O_3	0.05
Moisture	0.2

Specific Gravity	2.71
Particle Shape	rhombic
Oil absorption	14
Surface area (m^2/gm)	1.4

Table 2. Sorbent Properties

Internal Staging

Figure 3 shows the percentage capture as a function of the calcium to sulfur molar ratio when the sorbent was added with the staged air (location 2), and an additional 15% (over the normal heat loss) of the input heat was extracted from the radiant zone. Data are presented showing the relative capture in the radiant zone (sample port 1), the post flame section (between 1 and 2) and the overall capture (sample port 3). The capture in the post flame section is based upon the gas phase sulfur dioxide concentration entering the section and free calcium oxide (that which was not used in the radiant section). The data presented in Figure 3 indicate that when heat is extracted from the radiant zone capture occurs in both the radiant zone and the post flame section. These data were obtained with the burner zone operating at a stoichiometric ratio of 0.6 and a total air input equal to 120% of stoichiometric.

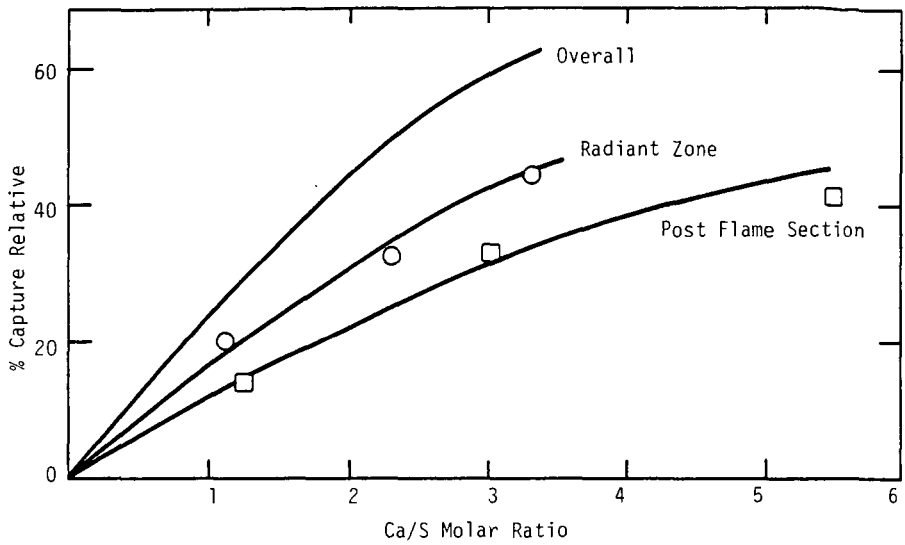

Figure 3. Relative SO_2 Capture, Sorbent Injected With the Staged Air Internal Mode With Heat Extraction in the Radiant Zone.

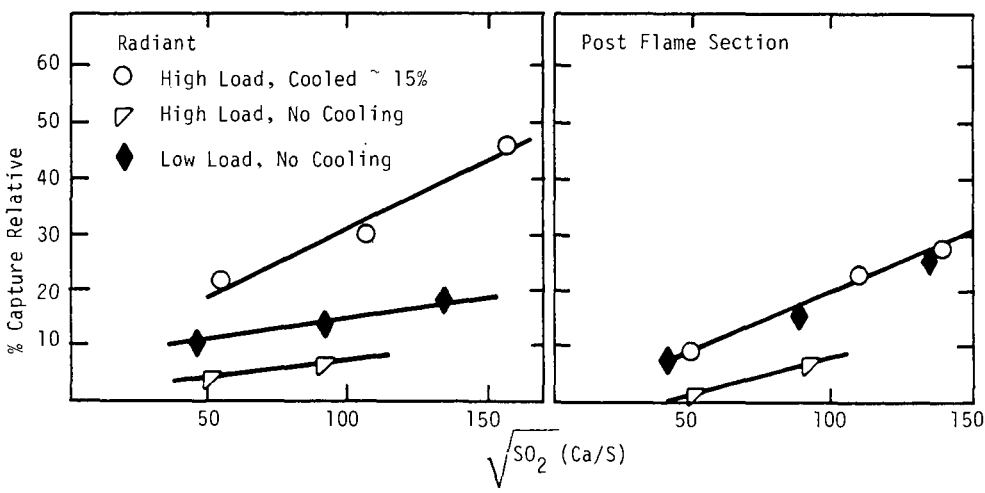

Figure 4. The Impact of Load and Radiant Zone Cooling on Sulfur Capture.

Tests have been carried out to determine the influence of burner zone stoichiometry on sulfur capture in the internally staged mode. Provided the burner zone stoichiometry does not rise above 80% the sulfur capture appears almost to be independent of burner zone stoichiometry. However as the staging air is reduced to a minimum and the burner zone becomes fuel lean the sulfur capture is reduced. In these experiments this reduction is probably caused by a reduction in sorbent velocity and because of the increase in peak flame temperatures as the burner zone stoichiometry increases.

In the internal staging mode thermal environment has a very significant impact upon sulfur capture. This is illustrated by the data presented in Figure 4 which shows the sulfur capture in both the first two zones as a function of the product of the calcium to sulfur ratio and the square root of the sulfur dioxide concentration in that zone. Three conditions are shown: high load with and without radiant zone cooling and low load without cooling. Reducing the load will lower temperatures and increase residence times. At high load cooling the radiant zone dramatically increases the sorbent reactivity. At low load reactivity in the radiant zone is less than that with cooling at high load but the reactivity in the post flame section is similar to the high load, cooled case.

External Staging

The purpose of the external staging tests was to determine whether sulfur dioxide emissions could be reduced by adding limestone under reducing conditions and then burning the fuel completely by the addition of second stage air downstream. This requires that the majority of the sulfur captured under reducing conditions be retained by the sorbent as the fuel burns out. Equilibrium calculations indicate that under fuel rich conditions hydrogen sulfide is the dominant sulfur species while measurements in the fuel rich region indicate that sulfur dioxide, hydrogen sulfide and carbonyl sulfide all are present. Sulfur dioxide concentrations decrease and hydrogen sulfide concentrations increase as the primary zone stoichiometry decreases. Thus, the sorbent may react with any of three sulfur species. Initial reaction rates for the reaction of H_2S and COS with CaO have been measured (7, 8) and are similar.

The data from two different external staging experiments are shown in Figures 5 and 6. In one experiment sorbent was added with the coal (location 1) and measurements of sulfur species at the exit of the rich zone (port 2) were made with and without sorbent. Figure 5 shows the percent capture of SO_2, COS and H_2S as a function of first stage stoichiometric ratio. It can be seen that all three species were captured. The data in Figure 6 are from an experiment comparing calcium utilization firing with two fuels, coal and propane doped with H_2S to give the same sulfur content as the coal. The sorbent was added at the base of the post flame section (location 2) and the staging air was added in the post flame cavity (location b). SO_2 was measured with and without sorbent for both fuels at sample port 3 (exit of furnace). Total calcium utilization as a function of first stage stoichiometry is shown in Figure 6. Measurements indicate that as much as 50 percent of the input coal remains as solid at the lower first zone stoichiometries. The data for coal presented in Figure 6 has been plotted as a function of the actual gas phase stoichiometry. It can be seen that the ultimate sulfur capture decreased with decreasing gas phase stoichiometric ratio for coal but increased for propane doped with H_2S. It should be noted that the data shown in Figure 6 represent the sum of sulfur species capture under reducing conditions in the first zone, retention of sulfur during burnout and the sulfur capture under oxidizing conditions in the second stage.

4. CONCLUSIONS

An investigation has been carried out in a bench scale facility to determine

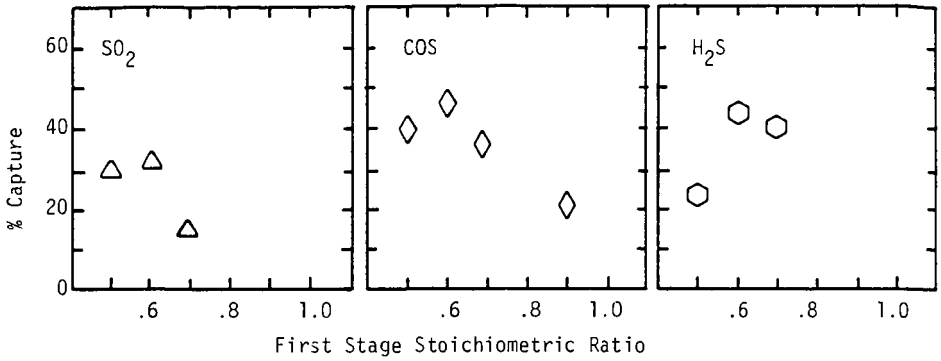

Figure 5. % Capture of Sulfur Specie in Rich First Stage (External Mode) Sorbent Injected With the Coal.

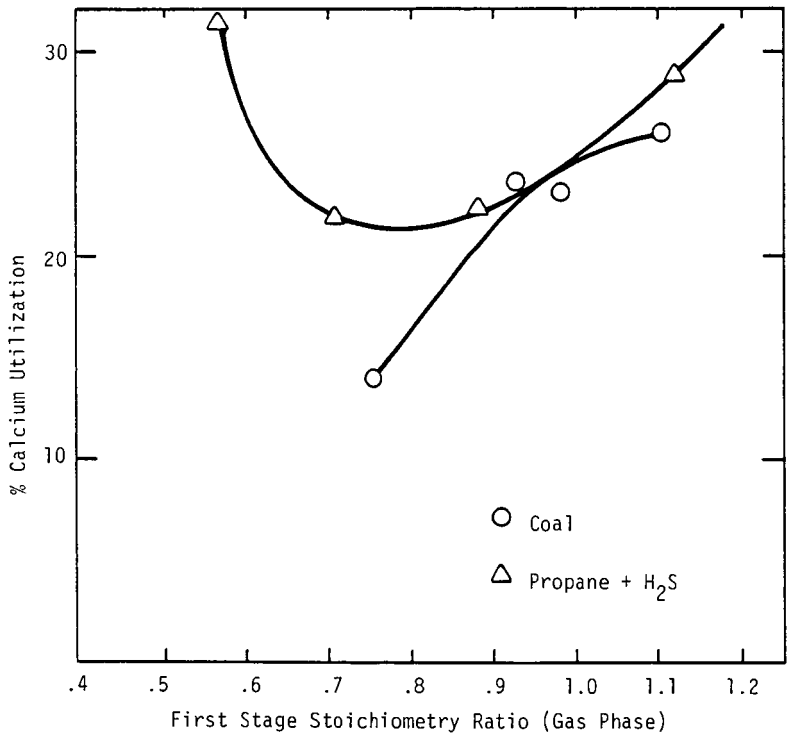

Figure 6. Capture and Retention of Sulfur Under External Staged Conditions for Coal and Propane Doped with H_2S.

under which conditions sulfur species generated during the combustion of pulverized coal can be captured and retained by calcium containing sorbents. Two series of experiments were carried out: one in which any capture would take place primarily under oxidizing conditions and the other in which significant residence times in the rich zone would allow capture under reducing conditions. Under oxidizing conditions the thermal environment experienced by the sorbent particle appears to be the dominant parameter controlling sulfur capture. This is probably because of deadburning. If a sorbent particle's temperature exceeds a certain limit (which depends on the particular sorbent) the sorbent deadburns and loses its reactivity (4).

The processes controlling capture and retention when the sorbent is maintained under reducing conditions for a prolonged time are more complex. The principle gas phase sulfur specie are H_2S, SO_2 and COS and, even though the sulfur species are absorbed the possibility that the sulfide will decompose during burnout exists. The data presented in Figure 6 shows a significant difference between the behavior of coal and propane doped with H_2S. This difference can be attributed to:

- With coal part of the fuel remains in the solid phase and for a given input stoichiometry the gas phase stoichiometry in the reducing zone is higher than with gas. Reference to Figure 1 indicates that the stability of calcium sulfide is strongly dependent upon stoichiometry ratio;

- With coal up to 50 percent of the sulfur remains in the solid phase under rich conditions thus the gas phase concentration is lower than the corresponding concentration with propane as the fuel;

- The conditions during burnout in the second stage will be different for the solid and gaseous fuels and this could affect retention of the sulfur during burnout.

These tests indicate that there is the potential to remove greater than 50 percent of the input sulfur with Ca/S molar ratios of two when coal is burned under low NO_x conditions. Further work is necessary to insure that the controlling conditions can be achieved in practical combustors and that the sorbent injection does not adversely impact combustor performance.

References

1. Gartrell, F.F., "Full Scale Desulfurization of Stack Gas by Dry Limestone Injection", EPA-650/2-73-019 a, b, c, 1973.

2. Zallen, D.M., Gershman, R., Heap, M.P., Nurick, W.H., "The Generalization of Low Emission Coal Burner Technology", Proceedings, Third Stationary Source Combustion Symposium, EPA-600/7-70-050 b, 1979.

3. Flament, G., "The Simultaneous Reduction of NO_x and SO_2 in Coal Flames by Direct Injection of Sorbents in a Staged Mixing Burner", IFRF doc. no. G 19/a/10, 1981.

4. Coutant, R.W., et al., "Investigation of the Reactivity of Limestone and Dolomite for Capturing SO_2 from Flue Gas", Batelle Memorial Institute, Final Report, EPA Contract PH-86-67-115, 1970.

5. Borgwardt, R.H., "Kinetic of the Reaction of SO_2 with Calcined Limestone", NAPCA, Vol. 4, p. 59, 1970.

6. Borgwardt, R.H., Presentation at the EPA SPO Contractors Meeting, Raleigh, North Carolina, October 1981.

7. Ruth, L.A., Squires, A.M, Gratt, R.A., "Desulfurization of Fuels with Half-Calcined Dolomite: First Kinetic Data", Environmental Science & Technology, Vol. 6, p. 1007, 1972.

8. Yang, R.T., Chen, J.M., "Kinetics of Desulfurization of Hot Fuel Gas with Calcium Oxide. Reaction Between Carbonyl Sulfide and Calcium Oxide", Environmental Science & Technology, Vol. 13, p. 549, 1979.

Acknowledgments

This work has been supported under EPA Contract 68-02-2667. The authors are pleased to acknowledge the encouragement and ideas provided by Dr. D. C. Drehmel and G. B. Martin of EPA and the contributions of their colleagues at EER in the execution of the experiments.

TITANIUM AS A TRACER FOR DETERMINING COAL BURNOUT

Ray S. Pace, Paul O. Hedman, and L. Douglas Smoot

Combustion Laboratory
Department of Chemical Engineering
Brigham Young University
Provo, Utah 84602

INTRODUCTION

Background. Extensive research on coal combustion at this laboratory (1-6) has focused on developing an understanding of the physical and chemical mechanisms and reaction rates of coal burnout and nitrogen and sulfur pollutant formation. Local samples of combustion products have been extracted from the pulverized coal combustor using water-quenched sample probes. To complete mass balances and determine important local parameters, chemically inert tracers have been used in the reactor. Argon added to the primary air has been used as the gas phase tracer to determine the mixing rates of the primary and secondary air streams and the volume of combustion gases from the coal. Carbon conversion is also determined from gas composition, coal feed rate, and a forced argon balance.

Coal burnout has been calculated from the percent ash in the residual char and in the raw coal in previous phases of this study (4-6). However, the use of ash as a particle tracer has not been satisfactory. Ash is not a suitable tracer because it contains many inorganic compounds which decompose and/or vaporize. Kobayashi, et al. (7) and Sarofim, et al. (8) have shown that as much as 20-60 percent of the original coal ash can be volatilized depending on the temperature history of the ash.

Collecting samples of combustion products with a water-quench probe produces a char-water mixture which is filtered and dryed to obtain the solid char sample. Many constituents of ash are soluble in the water and more losses are incurred in the total measured ash content. Harding, et al. (6) have shown that up to 10 percent of the ash can be dissolved in the probe quench water.

High losses of ash negate its usefulness as a solid tracer by introducing large errors into the mass balance and burnout calculations. Consequently, there has been an interest in finding another particle tracer which could more accurately determine coal burnout, and also to help understand the fate of the ash and slag.

Mims, et al. (9) have characterized the volatilization of ash with temperature. At higher temperatures, compounds formed from elements such as arsenic, manganese, magnesium, sodium and antimony showed strong vaporization trends. Aluminum, silicon and other known refractory compounds also showed significant losses at high temperatures. Compounds formed from such elements as titanium, scandium, barium and lanthanum were found to be more stable. Because of their low concentrations in the coals, scandium and lanthanum were not considered as feasible tracers. Titanium was selected as a possible tracer because it forms relatively stable high boiling point compounds (i.e., TiO, TiC, TiO_2, Ti_4O_7), and is found in most coals in easily detectable amounts.

Objectives. The purpose of this study was to develop an analytical procedure which could be used to measure the concentration of a solid particle tracer and apply the techniques to representative samples from the pulverized coal combustor. Techniques commonly used to analyze elements in the ash are atomic absorption (AA), instrumental neutron activation analysis (INAA), x-ray diffraction (XRD), and x-ray fluorescence (XRF). XRF was chosen because of the ease of analysis (sample preparation time 10-15 minutes and analysis time of 40-120 seconds), and availability of a suitable instrument. Comparison of AA, INAA and XRF results for

fly ash and coal analysis have been found to give good agreement for most elements (10).

This study was divided into three tasks: (1) set-up and calibration of the XRF instrument in order to measure titanium trace element concentration in char from the combustor, (2) analysis of char samples from combustor tests to determine the usefulness of titanium in the ash as a tracer, and (3) use of the titanium tracer data to compute mass balances and consequently coal burnout.

TEST FACILITIES

A diagram of the pulverized coal combustor with major dimensions is shown in Figure 1. The reactor, with a coal feedrate of about 13.6 kg/hour, was constructed of five interchangable sections of 33 cm (14 in.) schedule 40 pipe. Each section was 30.4 cm in length and lined with 6.4 cm of castable aluminum oxide refractory. One of the five sections contained a water-quench, traversing probe which was used to sample the flame at different axial locations in the reactor. This section could be interchanged with any of the other sections in order to obtain gas and char samples at various radial and axial locations, effectively mapping the reactor. A more detailed description of the combustor and its supporting facilities has been reported (4-6).

In order to obtain an adequate sample of combustion char for ASTM ash and XRF Ti analysis, a special larger exit sample probe was used. The probe detail of Figure 1 shows the design of the probe tip that permitted centerline char sample collection near the reactor exit without interfering with other combustor experiments. Both probes were similar in design, differing only in size. Complete details on the design and operation of the probes have been documented (6, 11, 12).

INSTRUMENTATION

A Phillips 1410 vacuum path x-ray fluorescence (XRF) spectrometer was used to analyze titanium in the coal samples. XRF is known for the relatively quick sample analysis time and sample preparation time (10). Quantitative measurements of Ti on the XRF required values for five correction factors: detector dead time, background count, peak overlap, absorption corrections, and instrument electronic and power drift. Each factor is briefly discussed below.

Dead Time. Dead time is the time required for the electronics and detector to register one count of radiation. If a second burst of radiation arrives at the detector before the first burst is registered, the second burst will not be registered. The bursts of radiation are assumed to be statistically random and a simple correlation is used to quantify the dead-time correction (13).

Background Counts. Natural scattering of the x-rays causes a small count to be present at every angle on the XRF. The background counts vary non-linearly and compensation is made by estimating the background at the peak using an average of the background at angles below and above the peak.

Peak Overlap. Peaks within one or two degrees of the measured peak may add to the number of counts at the desired peak position. Corrections for these overlaps are made by measuring pure disks of the interfering element and determining the height of the peak at the desired angle.

Absorption and Instrument Drift. Fluorescence from an element within the sample matrix could be absorbed by another element, altering the intensity of the peak of the desired element. Carbon and other lighter elements are strong absorbers at the wavelength of radiation from titanium. This causes major problems when organic concentrations in the char vary from 0 to 94 percent. This problem is circumvented by using the internal standard method of calibration. Instrument drift

on the XRF is caused by variations in the voltage, sample placement, and goniometer accuracy on the machine. These are also compensated by the internal standard method (14).

XRF Calibration. The internal standard method of calibration (14) was chosen as the calibration technique. Scandium as Sc_2O_3, which has an absorption edge near those of the element being measured, was added to the char sample in a known concentration. Since absorption effects are similar for the two elements, the ratio of the concentrations of the unknown to the standard element was related to the ratio of the intensities by a constant factor A:

$$W_{Ti}/W_{Sc} = A\ C_{Ti}/C_{Sc} \qquad (1)$$

where A is a constant factor, C_{Ti} and C_{Sc} are the measured counts of radiation at the peaks for titanium and scandium in the sample, respectively. This ratio technique eliminates the need for absorption corrections because the peaks are in the same sample, and the absorption correction factors are nearly equal. Calibration after every third sample prevented major errors due to machine drift. Calibration consisted of analyzing a cellulose blank to determine background factors and then analyzing a NBS fly ash standard (NBS Standard Reference Material 1633a) for titanium to determine the value of A in Eqn. 1.

XRF Error Analysis. The counting statistics and equations for the XRF error analysis are explained in detail by Jenkins and DeVries (13). The arrival of bursts of radiation from the sample can be modeled as a Chi Square distribution which approaches a Gaussian distribution. A total XRF counting error of ±0.4 percent (relative[1]) was realized for the tests conducted. This gave a limit of detection of 45 ppm (mass). The raw coal contained about 400-600 ppm titanium (dry basis), well above the minimum.

The XRF counting errors were very small. The major errors were introduced by the sample preparation techniques. Samples were prepared by weighing 400 mg of char, 40 mg of high purity cellulose and 10 mg of Sc_2O_3 into a small vial with a 6mm glass ball. A commerical dental mixer was used to mix and grind the sample for 3 minutes. The sample was then pressed onto a support with a cellulose backing at 4.58×10^6 kg/m^2. The major errors introduced in weighing the Sc_2O_3 accurately were ±1 to 2 percent. Increasing the percent Sc_2O_3 did not significantly increase the accuracy because of increased error due to increased scandium counts.

TEST PROGRAM

Fifteen combustor tests were performed at four different values of secondary air swirl number[2] (S_s^e = 0.0, 1.4, 3.2, and 4.5), and over a range of stoichiometric ratios[3] (SR) of 0.59 to 1.65. The coal used was a Wyoming subbituminous coal with about 5.0 weight percent ash (as received) and 0.8 weight percent titanium in the dry ash. The proximate analysis of the coal gave values of 27.8 percent, 32.9 percent, 34.3 percent, and 0.4 percent for moisture, volatiles, fixed carbon, and

---

[1]Relative error is error divided by percent titanium present times one hundred.

[2]Swirl number (S_s^e) is defined as the flux of angular momentum divided by the product of duct radius and axial flux of momentum.

[3]Soichiometric ratio (SR) is defined as the air/fuel ratio divided by the stoichiometric air/fuel ratio. SR values less than one are fuel rich while SR values greater than one are oxidizer rich.

sulfur respectively. The ultimate analysis on a dry basis gave 6.9 percent ash, 4.4 percent hydrogen, 76.3 percent carbon, 1.1 percent nitrogen, 0.5 percent sulfur and 10.8 percent oxygen. The char sample probe was located on the center line of the reactor near the reactor exit (ca 150 cm from the burner inlet). Coal burnout was determined at each test condition from ASTM analysis of the ash sample, and by XRF analysis for titanium in the char sample.

TEST RESULTS

Coal burnout results determined from a titanium mass balance in the char samples obtained are shown in Figure 2. Coal burnout was shown to be primarily a function of stoichiometric ratio, increasing from about 80-87 percent at SR = 0.6 (fuel rich) to greater than 95 percent at SR > 1.1 (Figure 2(a)). The tests were not all conducted at a consistent set of stoichiometric ratios. Nevertheless, interpolation of the curves (Figure 2(a)) at SR = 0.6, 0.9, and 1.2 has permitted the effect of swirl in the secondary air stream to be determined (Figure 2 (b)). The effect of stoichiometric ratio is still quite pronounced. The effect of secondary swirl on coal burnout is small. The combustion of pulverized coal is very complex and the influences of secondary swirl, mixing rate, stoichiometric ratio, etc. are just beginning to be understood (1-6).

An ASTM analysis of the char samples for ash and titanium as a tie component are given in Figure 3. Titanium burnout is higher in every case than the ash burnout, indicating that titanium is a better tracer than ash.

The extent of ash loss, equivalent to an ash burnout, has also been determined from the titanium data. A set of parametric ash loss lines have also been constructed on Figure 3 for comparison (10 percent, 20 percent, 30 percent, 40 percent, and 50 percent). Ash losses of 15 to 60 percent can be observed by the superposition of the data on the various ash loss lines. The extent of ash loss is large compared to earlier work at this laboratory with a bituminous coal (6). However, the difference in coal type, ash composition, and moisture level could account for these differences.

Ash loss has little effect on coal burnout at very high burnout levels. Figure 4 shows the error in burnout due to ash loss at several different burnout levels. At burnout values of 95 percent, ash losses of 40-50 percent create differences of only 2-3 percent in burnout estimates. Hence at moderate ash loss (20-40 percent) and high burnout values (greater than 95 percent burnout) the ash tracer burnout values are almost as accurate as the titanium-based burnout values. However, if burnout is below 95 percent then burnout based on titanium gave significantly improved results.

Asay (12) has recently completed as set of pulverized coal combustion tests at the same secondary swirl numbers and at nearly the same stoichiometric ratios for this Wyoming coal. Carbon burnout data obtained from these tests with a complete gas coumposition and an argon tracer mass balance are compared in Figure 5 to the titanium analysis coal burnout data reported above. In general, coal burnout is expected to be from 1-2 percent higher than carbon burnout because of the more complete release of the hydrogen from the coal. In general, the agreement between burnout values from the gas analysis and from the titanium analysis is good at SR > 0.9. At SR = 0.6 however, the burnout values determined from the gas analysis are much lower. Asay (12) is still reviewing this discrepancy but it is thought that the data from the titanium analysis are superior. One possible explanation is that the gas data represent an integration of radial gas composition profiles near the reactor exit while the titanium data are based on centerline samples.

CONCLUSIONS

Titanium can accurately be determined in char samples by using the internal standard method of XRF calibration. Errors of ± 2-3 percent are incurred mostly from sample preparation inaccuracy. X-ray fluorescence instrument error is less than ± 0.4 percent.

Titanium compounds in ash are more stable than the total ash constituents and hence provide a solid phase tracer to complete overall mass balances with increased accuracy. Burnout calculations are improved by as much as 20 percent at burnout values less than 95 percent and with high ash loss. When coal burnout level is above 95 percent, titanium provides only 1-2 percent increased accuracy in the burnout calculation.

Use of the titanium tracer also provides a method of calculating ash loss. Up to 60 percent of the ash was lost in these combustion tests. This loss is the sum of the losses due to vaporization in the flame and dissolution into the quench water.

ACKNOWLEDGEMENTS

Blaine Asay, Steven Zaugg, and Rodney LaFollette assisted in the combustion tests while technician, drafting, and secretarial services were provided by Michael R. King, Kathleen Hartman, and Ruth Ann Christensen, respectively.

This research project was supported by the EPRI under contract RP-364-2 with Mr. John Dimmer as project officer, and by the Brigham Young University Research Division.

REFERENCES

1. L.D. Smoot, P.O. Hedman. "Mixing and Kinetic Processes in Pulverized Coal Combustors." Final report prepared for EPRI, Contract No. RP-364-1, August 1978.

2. L.D. Smoot, P.O. Hedman, and P.J. Smith. "Mixing and Kinetic Processe in Pulverized Coal Combustors." Final report prepared for EPRI, Contract No. RP-364-1-3, October 1979.

3. L.D. Smoot, P.O. Hedman, and P.J. Smith. "Combustion Processes in a Pulverized Coal Combustor." Final report prepared for EPRI, Contract No. RP-364-2, August 1981.

4. J.R. Thurgood, L.D. Smoot, and P.O. Hedman. "Rate Measurements in a Laboratory-Scale Pulverized Coal Combustor." Combustion Science and Technology, 21, 1980, pp. 213-225.

5. D.P. Rees, L.D. Smoot, and P.O. Hedman. "Nitrogen Oxide Formation Inside a Laboratory Pulverized Coal Combustor." 18th Symposium (International) on Combustion, The Combustion Institute, Pittsburgh, Pennsylvania, 1981, pp. 1305-1311.

6. N.S. Harding, L.D. Smoot, and P.O. Hedman. "Nitrogen Pollutant Formation in a pulverized Coal Combusor: The Effect of Secondary Stream Swirl." accepted for publication in AIChE Journal, 1982.

7. H. Kobayashi, J.B. Howard and A.F. Sarofim. "Coal Devolatilization at High Temperatures." 16th Symposium (International) on Combustion, Combustion Institute, Pittsburgh Pennsylvaniz, 1977, p. 411.

8. A.F. Sarofim, J.B. Howard, A.S. Padia. "The Physical Transformation of the Mineral Matter in Pulverized Coal Under Simulated Combustion Conditions," Combustion Science and Technology, 16, 1977, pp. 187-204.

9. C.A. Mims, M. Neville, R.J. Quann and A.F. Sarofim. "Laboratory Studies of Trace Element Transformations During Coal Combustion." 87th AIChE National Meeting, August 19, 1979.

10. R.D. Smith. "The Trace Element Chemistry of Coal During Combustion and the Emissions from Coal-Fired Plants." Progress in Energy and Combustion Science, Vol. 6, Number 1, 1980, pp. 53-119.

11. R.S. Pace, "Titanium as a Tracer for Determining Burnout in a Laboratory Pulverized Coal Combustor," M.S. Thesis, Brigham Young University, in preparation, December, 1981.

12. B. Asay, "Measurement of Nitrogen Pollutants and other Combustion Products in a Swelling Pulverized Coal Flame," Ph.D Dissertation, Brigham Young University, in preparation, 1982.

13. R. Jenkins and J.L. DeVries. Practical X-Ray Spectrometry. 2nd ed., New York: Springer-Verlag Inc., Great Britain, 1969.

14. K. Norrish and B.W. Chappell. "X-Ray Fluorescence Spectrography." ed. by J. Zassman, Physical Methods in Determination Minerology, New York: Academic Press, 1967, pp. 201-272.

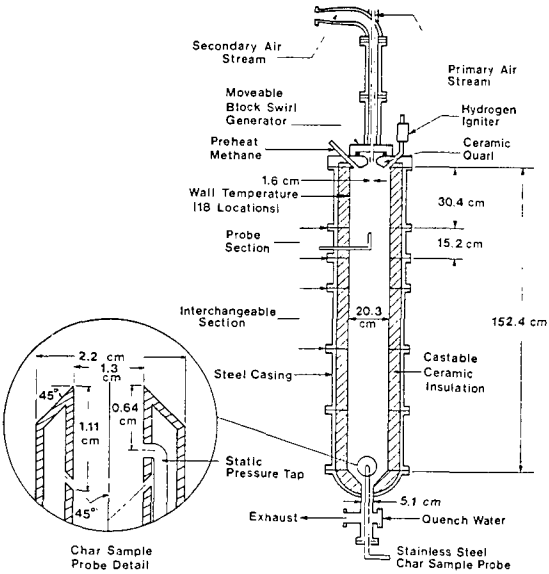

Figure 1. Schematic of atmospheric combustor (Adapted from Harding (6)).

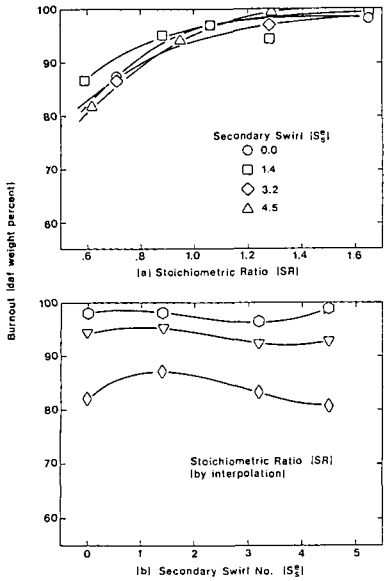

Figure 2. Effect of stoichiometric ratio and secondary swirl number on coal burnout by titanium analysis.

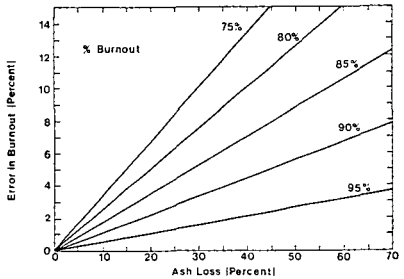

Figure 4. Percent change in burnout due to ash volatilization.

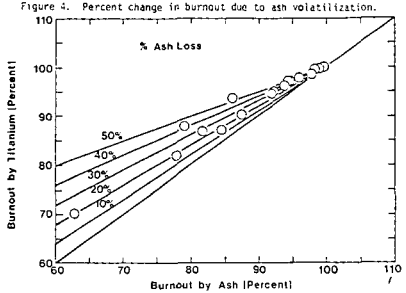

Figure 3. Burnout using titanium compared with burnout using ash as tracer.

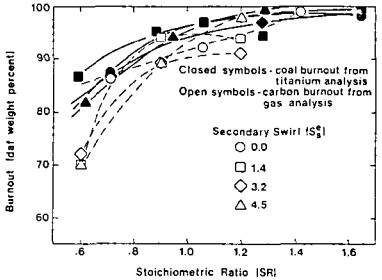

Figure 5. Comparison of carbon burnout by gas and analysis and coal burnout by ash tracer.

BED AGGLOMERATES FORMED BY ATMOSPHERIC FLUIDIZED BED COMBUSTION OF A NORTH DAKOTA LIGNITE

Steven A. Benson, Frank R. Karner, and Gerald M. Goblirsch
Grand Forks Energy Technology Center
U.S. Department of Energy
Grand Forks, North Dakota 58202

David W. Brekke
Department of Geology
University of North Dakota
Grand Forks, North Dakota 58202

INTRODUCTION

The goal of atmospheric fluidized bed combustion (AFBC) research at the Grand Forks Energy Technology Center is to provide a data base for design, operation, process control, and emission control requirements for low-rank coals. The application of the AFBC process has the potential to solve some of the problems associated with conventional combustion. These problems are ash fouling on heat exchange surfaces, the expense and reliability of SO_2 control devices such as scrubbers, and the system sensitivity to fuel variables (moisture, Na_2O concentration, etc.).

These problems can be reduced by the AFBC process for low-rank coals because the alkaline characteristics of the ash or sorbent added directly to the combustion zone provides the sulfur retention, which would eliminate or reduce the need for post combustion SO_2 controls. The temperatures in the combustion zone are at the right levels to provide maximum reaction of SO_2 and alkali to form solid alkali sulfate waste. One problem which the fluidized bed combustion of low-rank coals seems to exhibit is a tendency toward the formation of agglomerates of the material which are used to make up the bed. Agglomerates in this case are defined as a cluster of individual bed material particles held together by a substance not yet well understood, and manifest in many differing forms. The understanding of the mechanism of formation of these agglomerates is vital to their control, and therefore the full utilization of low-rank coal in AFBC.

Once formed these agglomerates will tend to decrease heat transfer, and fluidization quality resulting in poor combustion efficiency and loss of control of bed operational parameters (i.e., excess air, temperature, etc.). In severe cases the formation of agglomerates can lead to a forced premature shutdown of the system.

While the addition of limestone, or calcium bearing materials into the fluid bed, or the forming of the bed itself by limestone particles has shown a tendency to inhibit the formation of agglomerates, agglomerates of a severe nature have been observed in a bed of limestone alone, or limestone and sand particle mixtures while burning a high sodium coal for an extended period of time.

In general with a high sodium coal the agglomeration of limestone bed material is dependent only on the length of run time, if the run is long enough agglomeration in a limestone bed will occur, and can be as devastating as those which occur with a silica bed.

GFETC constructed a 0.2 square meter experimental AFBC. A detailed description of the unit is given by Goblirsch and others (1). The combustor can be operated over a wide range of conditions as listed below:

Average bed temperature	--	700 to 982°C
Superficial gas velocity	--	0.9-2.7 m/sec
Excess air	--	10 to 50%
Ash reinjection (% of primary cyclone catch)	--	0 to 100%.

The nominal coal feed rate is 80 kg/hr at 1.8 m/sec superficial gas velocity and 20% excess air.

This paper discusses the performance of quartz or limestone as a bed material during the combusting of high sodium North Dakota lignite. The lignite is from the Beulah mine of Mercer County, North Dakota. The composite coal and coal ash analysis is summarized in Table 1. The lignite was partially dried before this series of tests; its as-mined moisture content was 36%, and its heating valve 15,000 J/g.

TABLE 1. TYPICAL COAL AND COAL ASH ANALYSIS OF HIGH Na BEULAH LIGNITE

Ultimate Analysis, As Fired			Coal Ash Analysis, % of Ash	
Carbon	52.65	%	SiO_2	15.8
Hydrogen	4.59		Al_2O_3	12.1
Nitrogen	0.75		Fe_2O_3	9.9
Sulfur	1.33		TiO_2	0.8
Ash	9.7		P_2O_5	1.0
Moisture	20.0		CaO	17.5
Heating Valve (8372 Btu/lb)	19,459 J/g		MgO	6.2
			Na_2O	8.8
			K_2O	0.0
			SO_3	27.2

Other important considerations are the operation of the combustor and how operational parameters affect the performance of the bed material, sulfur retention on coal ash and bed material, and heat transfer. The most important operational parameters of the AFBC for the tests to be discussed here are listed in Table 2.

TABLE 2. AFBC OPERATIONAL PARAMETERS

Run Number	2181	2281	2481
Coal Type	Beulah	Beulah	Beulah
Bed Material	Quartz	Limestone	Limestone
Average Bed Temperature (°F)	1467	1460	1450
Superficial Gas Velocity (M/sec)	1.8	2.0	1.8
Excess Air (%)	25.49	22.65	24.98
Additive	None	*	*
Ash Reinjection (%)	None	100	100
Coal Feed Rate (kg/hr)	53	57	48

*Addition of supplemental bed material to maintain bed depth.

The tendency for the bed to agglomerate has been shown through extensive testing to depend on the following parameters:

1. Bed temperature (higher temperature increases tendency)
2. Coal sodium content (increased coal sodium content shows increased severity of agglomeration)

3. Bed material composition (high calcium content tends to delay, and decrease the severity of agglomerates formed)
4. Ash recycle (increased recycle of ash tends to increase agglomeration tendency)
5. There appears to be a bed design parameter such as position of coal feed points, and distributor plate performance which affect bed material agglomeration.

The bed material used in baseline run 2181 was 10 mesh quartz sand. Upon startup the bed was sampled every eight hours for the duration of the 69 hour run. At the end of the run the system was cooled and opened to expose the inside of the combustor. The bed material was removed and several agglomerates were found, which varied in size and shape, with the largest having a diameter of 6 cm. These agglomerates were found both free floating in the bed and attached to the inside wall of the combustor.

The limestone bed material was tested in run 2281 using 100% ash reinjection for a duration of 73 hours. The bed was sampled in the same manner as 2181. The formation of agglomerates in the run was very minimal with no major agglomerates found. On the other hand, run 2481 which used a limestone bed ran for 160 hours with 100% ash reinjection and had severe problems with agglomeration. After the run numerous agglomerates were found loose in the bed. In addition, a large agglomerate was found on top of the distributor plate at the bottom of the combustor. The agglomerate had dimensions of 30.5 cm X 30.5 cm X 12.5 cm; it weighed 10 kg and covered 30% of the distributor plate.

The bed material and agglomerates were characterized by polished thin section study, polarized light microscopy, and scanning electron microscopy/microprobe (SEM) - both secondary electron (SEI) and backscatter electron (BEI) images were used. Bulk samples were analyzed by x-ray diffraction and x-ray fluorescence. The goals in characterizing the bed material and agglomerates are to identify the stages which lead to agglomeration and possibly postulate a mechanism of their formation to thereby determine methods and procedures to control their growth.

RESULTS AND DISCUSSION

Quartz Bed Agglomerates

Agglomeration of quartz bed material is typified by run 2181 utilizing high-Na Beulah lignite and ash injection. Samples of bed material taken at various intervals during the run are illustrated in Figures 1 to 11 with chemical analyses data given in Table 3. The following four stages can be used to summarize the agglomeration process:

Stage 1. Initial ash coating.

Initial samples of bed material have a fine coating, about 50 microns thick, consisting of sulfated aluminosilicate particles (Figure 1). The coatings contain some coarser ash materials in the outer parts and the inner parts have penetrated the quartz grains slightly along gently curved or cuspate embayments. The quartz grains are extensively fractured, apparently as a result of thermal stresses.

Stage 2. Thickened nodular coatings.

Longer bed usage results in the development of thicker ash coatings about 100 - 300 microns thick with nodular outer surfaces resulting from incorporation of larger ash particles (Figure 2). Sulfating, shown by lighter colored areas in the SEM photographs, is common within both the finer and coarser ash particles of the coating.

Stage 3. Sulfated ash-cemented agglomerates.

In this stage the quartz grains are loosely held together by a cement of sulfated aluminosilicate ash (Figure 3). Penetration of quartz grains by fine grained ash is more extensive.

Stage 4. Glass-cemented agglomerates.

In the final stage quartz grains are bonded by sulfated ash which has partly melted and crystallized through reaction of the hot ash and the quartz grains. Resultant cooled agglomerates consist of quartz grains of the bed material bonded by a mixture of sulfated ash and Ca-rich, S-poor glass (Figure 4), with an intermediate reaction zone made up of an S-depleted, Si-enriched ash portion with a fringe of melilite or augite crystals projecting into the glass (Figures 5 and 6). Some quartz grains are partly melted and/or recrystallized to cristobalite or other phases.

Limestone Bed Agglomerates

Agglomeration of limestone bed material appears to be dependent on ash deposition and sulfation combined with extensive reaction and deterioration of the bed material.

Ash buildup on the grains and sulfating is comparable to reactions that occur with the quartz bed material. However, the limestone grains appear to undergo the following reactions:

1. Loss of CO_2 and conversion to CaO with addition of S, Fe, Na and other elements. These reactions produce concentric alteration zones, high Ca and S contents and the reddish color that characterizes typical grains (Figure 7).

2. Continued reaction produces thicker sulfated ash coatings and more thoroughly altered bed grains.

3. Bed grains disintegrate extensively and become mixed with ash coatings producing a weakly bonded agglomerate consisting of masses of sulfated ash and altered limestone bed grains and fragments (Figure 8). The altered limestone appears to recrystallize to coarse crystals of anhydrite in a fine-grained matrix containing abundant Ca, S and Si (Figure 9). Other phases, not yet identified, occur in the limestone agglomerates including crystalline Fe-Ca oxides as shown in Figure 10, and other iron-rich zones and coatings.

Where quartz and limestone bed materials are combined mutual interactions produce reaction zones on the quartz containing secondary needles of an unknown calcium silicate mineral (Figure 11).

Bulk x-ray diffraction analyses were performed on the bed material agglomerates to identify the phases present. The crystaline phases found in the quartz bed agglomerates from run 2181 include quartz, a member of the series $Ca_2Al_2SiO_7$-$Ca_2Mg_2SiO_7$ which includes melilite, and $CaSO_4$. The major phases identified in the limestone bed agglomerate are $CaSO_4$, $CaSiO_4$ and CaO. This data supports the SEM microprobe data.

X-ray fluorescence analysis was performed on bed material sampled continually throughout the run to determine the changes in composition of major ash constituents. The most appreciable changes which occurred in the quartz bed run were: SiO_2 decreased from 95 to 47% of the bed because of dilution; SO_3 increased to 24% because of adsorption by alkali constituents of the coal ash in the bed; CaO increased to 11% and Na_2O increased to 7% of the bed. The CaO and Na_2O reacted with the SO_3 and adhered to the quartz grains of the bed. Al_2O_3, Fe_2O_3 and MgO remained relatively constant throughout the run after the initial eight hours. The

components of the limestone bed of run 2481 changed as follows: CaO decreased by dilution to 37% by the coal ash; SO_3 increased to 28% by adsorption; and Na_2O increased to 7.7% of the bed. SiO_2, Al_2O_3, Fe_2O_3 and MgO remained constant throughout the run after the initial eight hours.

The concentrations of alumina and silica remain constant during the run indicating that the aluminosilicate clay particles leave the bed during combustion. On the other hand, the calcium oxide and sodium oxide which largely originate from the organic structure of the lignite are free to react with the SO_2 and bed material increasing their concentration.

TABLE 3. CHEMICAL ANALYSIS DATA FOR FIGURE 1 TO 11.
WT. %

OXIDE	A	B	C	D	E	F	G
SiO_2	10.76	12.45	8.22	12.16	31.20	47.80	48.32
Al_2O_3	11.70	11.20	18.94	8.94	19.13	10.03	10.61
FeO	4.82	0.55	6.94	3.02	13.14	9.95	9.48
MgO	5.71	1.14	11.86	5.73	10.27	4.44	6.26
CaO	18.11	32.86	12.63	12.83	19.82	20.28	20.29
Na_2O	12.70	3.99	10.14	17.97	2.04	6.11	3.73
SO_3	34.45	37.25	30.80	38.27	3.39	0.43	0.52

OXIDE	H	I	J	K	L	M
SiO_2	15.50	19.66	12.39	1.81	0.89	31.50
Al_2O_3	10.28	0.15	5.13	5.91	1.87	8.20
FeO	0.75	0.37	1.15	0.32	81.69	0.56
MgO	3.84	0.09	0.93	0.17	0.91	0.00
CaO	40.45	53.36	44.23	39.58	13.55	44.19
Na_2O	1.91	1.74	0.78	0.40	0.00	2.76
SO_3	21.49	24.39	35.37	51.66	6.33	11.89

CONCLUSIONS

Agglomeration of the bed material can be manifested in many different ways depending on the chemical composition of the bed. The elements which have a major effect are sodium, calcium and sulfur which react with the bed material possibly forming possibly a molten phase. This phase causes other ash constituents to adhere to the bed particles. As this phenomenon reoccurs many times, agglomeration becomes more severe.

REFERENCE

1. Goblirsch, G.M., Vander Molen, R.H., and Hajicek, D.R., AFBC Testing of North Dakota Lignite, Sixth International Fluidized Bed Conference, Atlanta, Georgia, April, 1980.

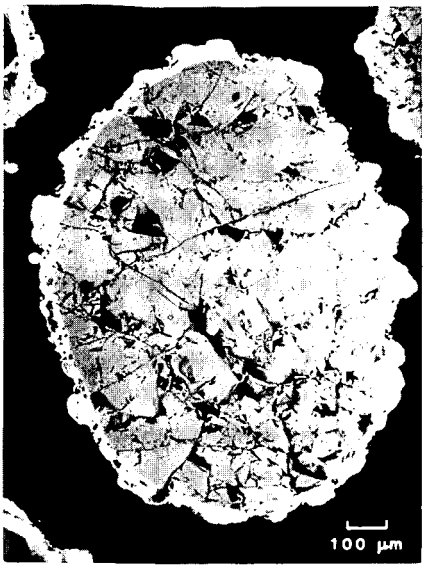

FIG. 1. Initial ash coating on quartz bed material. SEM/BEI image. Analysis A (Table 3). Run 2181, 40 hrs.

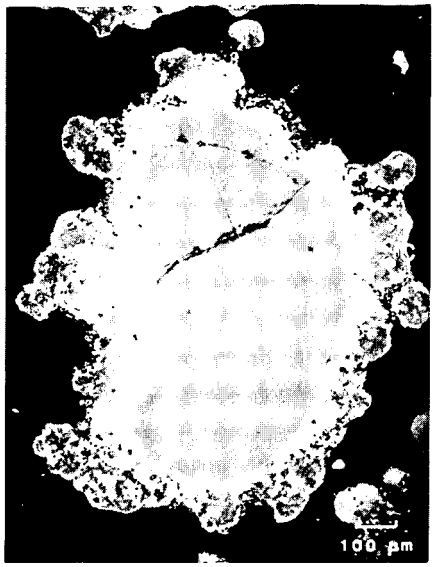

FIG. 2. Thickened nodular ash coating on quartz bed material. SEM/BEI image. Analysis B of fine light sulfated ash and C of darker interior of coarser ash particle (Table 3). Run 2181, 54 hrs.

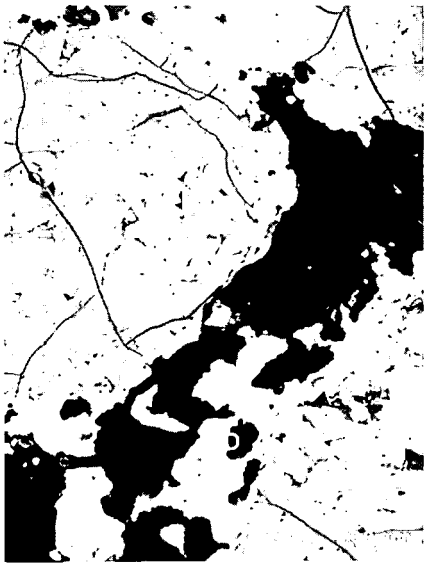

FIG. 3. Quartz bed grains loosely cemented by sulfated aluminosilicate ash. SEM/BEI image. Analysis D given in Table 3. Run 2181, 69 hrs.

FIG. 4. Quartz bed agglomerate bonded by altered sulfated ash, bottom of the dotted boundary (analysis E); Ca-rich, S-poor glass, top of the dashed line (analysis F); and intermediate fringe of melilite or augite crystals. SEM/BEI image. Run 2181, 69 hrs.

FIG. 5. Transmitted light image (partially crossed polars) of lower center of Figure 4 showing light quartz grain, gray glass, and crystals of melilite or augite crystals projecting into glass. Run 2181, 69 hrs.

FIG. 6. Detail of lower center of Figure 5, showing dendritic crystal form of melilite or augite. Analysis G given in Table 3. SEM/SEI image. Run 2181, 69 hrs.

FIG. 7. Concentric alteration zones and reacted limestone bed material. Analysis H given in Table 3. SEM/BEI image. Run 2481, 169 hrs.

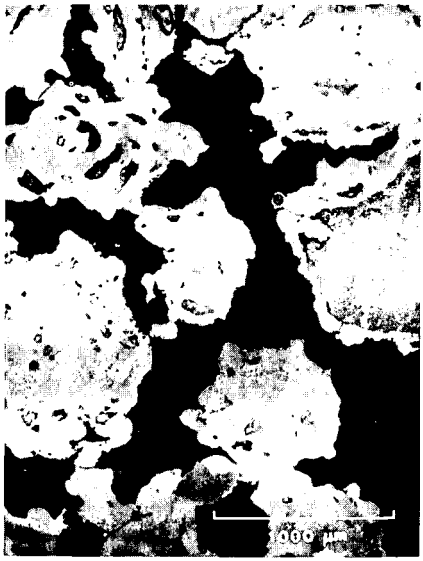

FIG. 8. Weakly bonded agglomerate of sulfated ash and altered limestone bed grains and fragments. Analysis I and J are given in Table 3. SEM/BEI image. Run 2481, 169 hrs.

FIG 9. Limestone bed material altered to coarse crystals of $CaSO_4$ in a fine-grained matrix of Ca, S, and Si. Light area to left is ash coating. Analysis K given in Table 3. SEM/BEI image. Run 2481, 169 hrs.

FIG. 10. Bladed crystals of Fe-Ca oxides in limestone agglomerate. Ash coating to right. Analysis L given in Table 3. SEM/BEI image. Run 2481, 169 hrs.

FIG. 11. Reaction zone consisting of secondary needles of an unknown Ca-silicate mineral on a quartz grain contained in the limestone bed. Analysis M given in Table 3. SEM/BEI image. Run 2481, 169 hrs.

Experimental Research on Lignite Fluidized Bed Combustion

Yang Min-Shin, Yang Li-Dan, Bao Yi-Lin, Chin Yu-Kun

Harbin Institute of Technology
The People's Republic of China

Burning Characteristics of Lignite Fuel

Lignite fuel is highly volatile and has a low ignition temperature, and is consequently easy to burn. In practice, however, when burning low grade lignite fuel in stokers or pulverized coal furnaces, some difficulties may occur due to high moisture content and low ash fusing point. In general, the moisture content of lignite fuel is above 30% and the sum of the moisture content and ash content is higher than 50%. Its heating value is about 2,000-2,500 kcal/kg and the ash-deformation temperature is higher than 1,100 C.

Burning lignite fuel in fluidized beds has many obvious advantages:

(1) High heat accumulation of the fuel bed. This provides a sufficient heat source to dry and preheat the lignite and helps high moisture lignite to ignite in time, resulting in a stable combustion condition.

As an example, a factory installed a fluidized-bed boiler with steam capacity of 10 t/hr. During the first winter of boiler operation, the air required for combustion was delivered into the furnace by drawing in outside air, which was approximately -30°C. In order to prevent the frozen coal from partially melting into a large lump in the coal bunker, the bunkers were installed outdoors. During the winter, frozen coal, together with ice particles, was delivered directly into the furnace via belts. The walls became covered with ice frost like the outside of a refrigerator. Despite such difficult conditions, the combustion process in the furnace was normal and the combustion was stable as long as the temperature of the fuel bed was above 600°C.

Another factory trial successfully fired three lignites with high moisture content. The measured characteristics of the fuels are given in Table 1.

Table 1. Typical Analysis of Lignites Fired in Trials

Type	I	II	III
Moisture content as fired (%)	27.21	46.01	56.82
Ash content as fired (%)	26.2	23.37	16.13
Volatile matter as fired (%)	24.1	19.83	14.91
Fixed carbon (%)	22.4	10.43	12.14
Lower heating value (kcal/kg)	2551	1470	1230

(2) The normal temperature range for fluidized beds is 850-950°C. This is much lower than the lignite ash-deformation point, and the temperature field is even, with no possibility of slagging.

(3) Ash erosion is not usually high. This is because the fly-ash particles flying out of the fluidized bed are not subjected to temperatures above their fusion point. Thus the erosion potential of the fly-ash is probably lower than that leaving conventional furnaces.

(4) Since the operating temperature for a lignite fluidized bed boiler may be relatively low, the load range can be much wider. As the temperature of the fluidized bed varies from 600°C to 900°C, the load range for a single fluidized bed can be easily varied from 50% to 100%. Using a separated fluidized bed operation, the minimum load can be further reduced, resulting in a much lower value than the low load stable operating range of a pulverized-coal furnace.

(5) The erosion of the submerged tubes in lignite fluidized-bed boilers is not serious due to the relatively loose character of lignite ash. In most fluidized bed boilers operated for many years, the erosion of the submerged tubes has not been a problem, although there may be some exceptions.

(6) The specific gravity of lignite ash is relatively low. For this reason the air pressure of the plenum may have a lower value than when using high low-grade coals. The plenum air is usually supplied at a pressure of 500 mm water.

(7) It's easier to ignite a lignite fluidized-bed boiler. We have ignited run of the mine (ROM) lignite fuel successfully many times when the temperature of the fuel bed was about 400°C.

(8) When lignite fuel is thrown into the high-temperature fuel beds, the fuel is suddenly heated and crumbles easily by itself, allowing coal particles as-fired to be very coarse. Operating experiments in Heilang Jiang and Yunnan provinces also proved that the maximum diameter of particles may be raised to 20-25 mm, slightly reducing power consumption for crushing and making it easier to sieve.

Fluidized Bed Boilers with a Rear-Installed Cyclone Furnace

At present, one of the main problems for existing fluidized-bed boilers is low combustion efficiency. The main reason for lower combustion efficiency and higher unburned combustible solids losses is the high carbon content in the fly-ash. The small particles may be blown off the high-temperature fluidized bed, resulting in an unburned carbon loss in the fly-ash.

Another important characteristic of lignite fuel is its high volatile content. The heat released from the volatile matter is about one-half of the coal heating value. In addition, lignite particles may break up during the burning process, forming many small coal particles. Therefore, one of the important characteristics for firing lignite in fluidized-bed boilers is possibly that more volatile matter and small coal particles are burning in the suspension chamber (freeboard).

The optimization of the combustion process in the suspension chamber to obtain better performance is an important factor in determining the combustion efficiency of lignite fluidized-bed boilers. One effective measure for reducing the fly-ash carbon content is using a fly-ash recycle for refiring in the fluidized beds or applying fly-ash refiring beds. However, this will complicate the system and its construction for small-capacity, fluidized-bed boilers. Practically, providing high temperature within the suspension chamber (freeboard) may exert an afterburning action for various fuels. For this reason, we suggest limiting the heat exchange surface as much as possible or not placing them in the freeboard. This will raise the gas temperature in the upper part of the furnace as high as possible. The ignition temperature for lignite fuel is relatively low. Thus, the increased temperature will exert sufficient afterburning action on the suspension chamber (freeboard). Providing a sufficiently high temperature in the suspension chamber is an important condition in achieving better combustion.

Another important condition is how to organize the aerodynamic field of the suspension chamber. In 1972, we designed a fluidized-bed boiler with a rear-installed cyclone furnace, shown in Fig. 1. Good results were obtained. Afterwards, we designed several dozen fluidized-bed boilers for lignite, the majority using rear-installed cyclone furnaces. The design of this cyclone furnace is based on the characteristics of a horizontal cyclone furnace. The aerodynamic field for a cyclone furnace is very complex. Its complexity assists in sufficient mixing of combustibles and oxygen in the gas flow. This is due to the increase in the relative velocity between the gas flow and the fly-ash and thus an increase in the diffusion velocity of oxygen to the fly-ash. These effects result in an increased burning velocity for coal particles. Furthermore, the residence time for fly-ash in the cyclone furnace is obviously prolonged. This is especially true for ash particles having a medium diameter. The carbon content for this part of the fly-ash, in general, gives the highest value. In addition, a cyclone furnace collects dust within the furnace. It may reduce erosion on the convection heating surfaces and reduce the load on the dust-collecting plants.

Note that although the dimension of the convex collar for cyclone furnace outlets is not large, its effect on the aerodynamic field is quite important. The scheme for an aerodynamic field in a cyclone furnace with and without a collar is shown in Fig. 2. It was also shown by cold modeling that the separation efficiency for cyclone furnaces with collars is much higher than for those without collars.

Aerodynamic Fields for Horizontal Cyclone Furnaces

In order to recognize the mechanism for the separating and afterburning action in the cyclone furnace and to investigate for a more reasonable construction, we have performed cold modeling for the horizontal cyclone furnace and tested the aerodynamic field in this type of furnace.

The maximum particle size leaving the cyclone furnace is expressed by the following relationship:

$$d_{max}^{1.6} = 13.88 \frac{W_r^{1.4} R''^2 r_g v^{0.6}}{W_t'^2 R_o r}$$

where

w_t' = velocity in inlet of cyclone furnace (m/sec)

w_r = radial velocity (m/sec)

R'' = radius of the exit (m)

r_g = specific gravity of gas (kg/m^3)

v = coefficient of kinematic viscosity of gas, (m^2/sec)

R_o = radius of the lower boundary of inlet (m)

r = specific gravity of particle (Kg/m^3)

From the above, we can approximate the diameter of a particle in cyclonic motion at the exit boundary of a cyclone furnace. Some large particles of diameter above d_{max} near the wall will be moved towards the wall and then pass down the wall. The other large particles will continue their circumferential movements in various values of the radius until the wall is reached or their diameter is reduced to less than d_{max}. The particles of diameter less than d_{max} may be moving with the air flow out of the cylone furnace, but the small particles near the wall may also be separated from the gas flow. Therefore, d_{max} may be considered as the limit of the

maximum particle diameter leaving the cyclone furnace. Because particles are not spherical d_{max} obtained from the above equation should be divided by a coefficient ϕ, called the particle shape coefficient, as a correction. Only after this may the value be considered as the actual size.

For the cold modeling experiment, the above expression for d_{max} gives a value of about 94 μm. Experimental measurements show a maximum particle diameter of 142 μm. If this value is corrected for particle sphericity (ϕ = .66) a value of 93.72 μm is found which is very close to d_{max} from the above expression.

For conditions typical of an operating cyclone furnace, the maximum particle diameter leaving the furnace from the above equation is about 320 μm. For some factory furnaces the experimental value is about 500 μm. This is equivalent to a spherical diameter of 330 μm (ϕ = 0.66) which is close to 320 μm.

Summarizing, the principal causes of afterburning action in cyclone furnaces are:

(1) Large particles of fly-ash are thrown by the high centrifugal force toward the wall. These particles then pass rapidly down the inner walls of the cyclone furnace. Although these particles are separated rapidly, due to the high relative velocity they can be burned up within a short time. Since large particles have partially burned within the fluidized bed, the carbon content of these particles would not be as high.

(2) Based on the above principle, medium particles will move around the circumference with different radii until they have burned to a size less than d_{max} and then leave the cyclone furnace. So the residence time of the medium particles within the cyclone furnace is greatly increased resulting in greater char combustion.

In addition, the action of the collar mounted at the throat forces the air flow at and around the throat to change its direction repeatedly (rotating 180°). This forms an intense turbulence and recirculating movement of the particles (see Fig. 1). The latter recirculates in the cyclone axially and at the same time rotates around the cyclone axis, also increasing the residence time of the particles within the cyclone furnace. Cold modeling has confirmed that some medium-size particles are rotating continually within the cyclone furnace until the fan is shut down.

Based upon theoretical analysis and some experimental data from the domestic research unit, it has been found that particles of medium size have the highest carbon content, and that this type of particles is in the majority. For example, experimental data obtained in the fluidized bed boiler burning local coal at Che-Jiang University has shown that the heat loss for particles ranging from 0.13 to 0.375 mm is over 70% of the total heat loss of fly-ash. The majority of these particles may be just the rotating particles within the cyclone furnace. Therefore, the cyclonic action of the cyclone furnace may be very effective in reducing the carbon-content of fly-ash.

Experimental Research on the Cyclone Furnace Under Thermal State

The carbon content of the ash samples taken from various parts of the boiler flue gas were determined and are summarized in the following table.

Table 2. Ash Size Distribution and Carbon Content in Various Parts of Flue Gas

Granularity mm	Ash separated in cyclone furnace		Ash in precipitating chamber		Ash in dust collector	
	proportion by weight %	carbon content %	proportion by weight %	carbon content %	proportion by weight %	carbon content %
	1.87	1.18				
1-2	5.83	1.76				
0.5-1	36.4	1.08	4.64			
0.28-0.5	25.8	1.3	15.4	18.48	1.25	35.86
0.09-0.28	24.8	0.93	59.3	9.91	33	18.89
0.09	5.2	1.05	20.66	4.12	65.18	8.53

In a typical boiler, a two-stage dust collector is used. About 60% of the total fly-ash is collected in the precipitating chamber. The remaining ash is then removed by the dust collector. Based on the above data, we can draw the following conclusions:

(1) The ash particle size in precipitating chambers and dust collectors is scarcely larger than 0.5 mm. It is reasonable to assume that particles greater than 0.5mm will not leave the cyclone furnace. This is in accordance with the results from the cold modeling experiment.

(2) Ash particles with diameters of 0.25 - 0.5mm in the fly-ash have the highest carbon content. However, most of this fly-ash size fraction has been separated from the gas flow in the cyclone furnace and its proportion by weight in the fly-ash is not high. When a boiler operates at normal capacity, the average carbon content for fly-ash is 11.85%. This value may be considered relatively low.

(3) The ash particles separating from the gas flow in the cyclone furnace have a significantly lower carbon content than that observed in the ash overflow. In general, the medium particles of fly-ash have higher carbon content, while the carbon content of ash particles ranging from 0.28 to 0.5 mm separated in the cyclone furnace is only 1.3%. This shows that the degree of burn-up for ash separated within cyclone furnaces is rather high.

(4) Since the separation efficiency for cyclone furnaces is rather high (about 50%), the ash particles burn more completely with the result that the boiler combustion efficiency increases. During operation periods at rated capacity, the unburned combustible solid losses are 3.8% and the unburned gas losses are 0.67% while the combustion efficiency can be as high as 95.47%.

When the temperature of fluidized bed section is 900°C at rated capacity, the gas temperature measured at the cyclone furnace exit is 920°C, that is the temperature difference between the latter and the former is 20°C. This shows that there are some combustibles still burning in the suspension chamber and in the cyclone furnace. According to calculations, the total fraction burned in the suspension chamber and cyclone furnace is 0.3.

In experimental tests with another lignite fluidized bed boiler of the same type, the fraction burned in the cyclone furnace itself was found to be 0.172.

The results of the data for the above two experiments are basically the same. It can be seen from the above summary that the total fraction of combustion in

suspension chambers and cyclone furnaces in fluidized bed boilers is relatively high. Thus the organization of the combustion process is highly significant in obtaining better boiler combustion efficiency.

The separation efficiency for cyclone furnaces, η_f, is the ratio of ash separated in the cyclone furnace, ΔG, to ash leaving the cyclone furnace, G", plus the ash separated, ΔG, that is

$$\eta_f = \frac{\Delta G}{G'' + \Delta G} \times 100\%$$

The unburned carbon content of the ash is included in the above expression. The results of the tests are summarized in Table 3.

Table 3. Separation Efficiency for a Cyclone Furnace as a Function of Ash Particle Size

Granularity mm	>1	0.5-1	0.28-0.5	0.09-0.28	<0.09
Separating efficiency η_f %	100	93.7	75.3	39.3	13.7

The average separating efficiency is about 50%.

Conclusions

(1) Lignite of high moisture content is not an easy to burn fuel. At present, for typical industrial boilers in our country, there has not been a furnace-type which has the ability to burn high moisture content lignite fuels economically with the exception of fluidized bed furnaces. Burning lignite fuel in utility boilers presents many significant difficulties also. Existing experiments show that fluidized bed boilers can successfully burn low-grade lignite fuel having moisture content up to 56.82% or ash content up to 46.8%.

(2) Rear-installed cyclone furnaces have an obvious effect of increasing oombustion efficiency for lignite fluidized bed boilers. The combustion efficiency for boilers of such types may be as high as 95%. Its main function consists of prolonging the residence time of the medium particles which contain higher carbon content within the furnace. This creates better conditions for carbon combustion. The total fraction of combustion in the suspension chamber and cyclone furnace is about 0.3.

(3) The separation efficiency for cyclone furnaces is about 50%. The majority of particles having diameters larger than 0.5mm may be separated from the gas flow in the furnace. The approximate maximum particle diameter leaving the cyclone furnaces may be obtained from the following formula.

$$d_{max}^{1.6} = 13.88 \frac{W_r^{1.4} R''^2 \quad 0.6}{W_t'^2 R_o r}$$

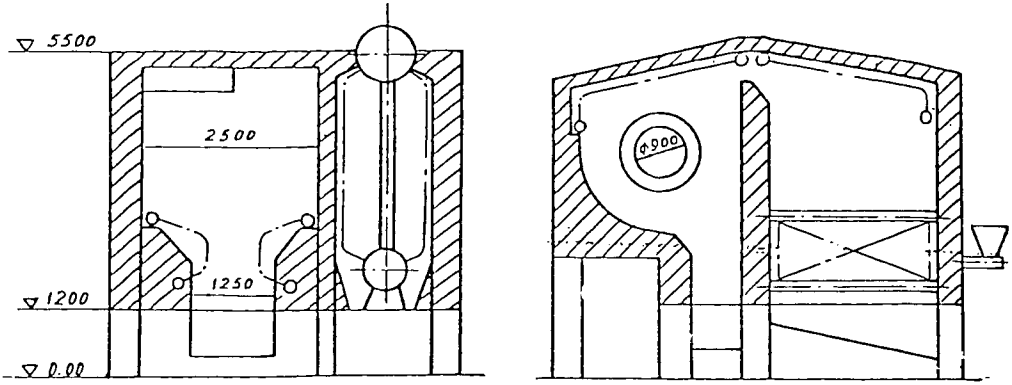

Figure 1. Fluidized-Bed Boiler with Rear-Installed Cyclone Furnace

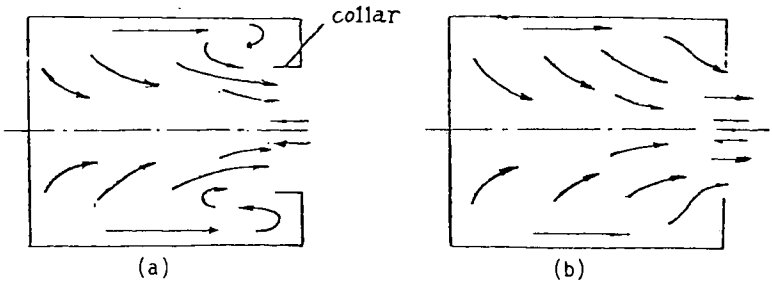

Figure 2. Effect of Collars on the Aerodynamic Field in a Cyclone Furnace: (a) With Collar. (b) Without Collar.

Pilot Plant of a Coal Fired Fluidized Bed Boiler in Japan

S. Tamanuki

The Coal Mining Research Center
Kanda Jinbocho 2-10 Chiyoda-ku
Tokyo, Japan

H. Karayama, S. Kawada

Kawasaki Heavy Industries, Ltd.
Babcock-Hitachi K.K.

A pilot plant of an atmospheric fluidized bed combustion boiler which is capable of evaporating 20 t/h at the steam conditions of 60 atg and 540°C was constructed and started operation at the beginning of April, 1981.
A description of the project and its results are presented in this paper.

1. Introduction

Brief History of FBC Development in Japan

The project named 'Research on Fluidized Bed Combustion Technology' was started in 1978 to support Japan's national effort for coal utilization technology development. This project has been financially supported by the government and steered by a joint committee of several related agencies and companies. The Coal Mining Research Center has been filling the leading role in this committee since it was organized in 1978.

During 1978 and 79 component tests and fundamental studies using bench scale units were performed. In parallel with these a feasibility study for a 500 MW power generation unit was carried out. The previously expected advantages of fluidized bed boilers over the conventional pulverised coal combustors were examined. It has been found that most of the advantages of fluidized bed combustion such as the possibility of eliminating flue gas desulfurization and denitrification and the capability of handling wide range of coal types are still effective for Japanese social and economical situations.

The whole program of the fluidized bed boiler development is shown in Table 1. A pilot plant with a 20 t/h evaporation capacity was constructed in Wakamatsu Thermal Power Plant of the Electric Power Development Co. and the test runs are performed for testing the instrumentations and components and determining the optimum operating conditions of the fluidized bed boiler. A survey program on the design conditions for various components and devices for a 240 t/h class

demonstration plant is also running.

Organization

To carry out this project effectively, the pilot plant program Steering Committee was organized by The Coal Mining Research Center, Electric Power Development Co., Kawasaki Heavy Industries, Ltd. and Babcock-Hitachi K.K. As a sub-committee of the Steering Committee, the Pilot Plant Executive Office was organized. This Office has taken charge of the construction, test and operation of the pilot plant.

Wakamatsu Pilot Plant Test Items

The planned pilot plant test items are as follows:

(1) NOx and SOx emission control
(2) Reduction of the required quantity of desulfurizing sorbent
(3) Controllability of the fluidized bed boiler
(4) Reliability of the fluidized bed boiler
(5) Suitable types of coal
(6) Performance of the dust collector

2. 20 t/h Pilot Plant

Basic Concepts

The fluidized bed boiler consists of a main bed cell (MBC) and a carbon burn-up cell (CBC). The design was made so that various imported coals and low grade coals can be burned.

Crushed coal has been used as a feed coal. Before feeding, the coal is pretreated-drying, crushing screening, etc. Coal feeding is done by both pneumatic feeders and overbed spreaders.

Fine grain coal is fed to the bottom of the bed through a pneumatic conveyer and coarse grain coal sprinkled over the fluidized bed by a spreader. The capacity of the feeders are designed so that total required quantity of coal can be fed by one of these two method. Natural limestone whose sizing has been completed at the mine is used as a desulfurizing sorbent. The sorbent is fed through a pneumatic conveyor.

A multi-cyclone is installed at the outlet of the MBC. The design was made so that the collected coal ash can be reburned either in MBC or CBC.

A balanced draft systems is used.

MBC was designed so that it can be diveded into two parts. The installation position of heat exchange tubes in the free board of MBC can be changed. The duct connected to the rear flue can be removed so that the height of free board can be changed.

Hot stoves and over bed burners are used for starting up the boiler. Steam generated by the boiler is changed back to water by an air condenser. The water can be reused. Discharged ash is wetted and transferred to the ash yard to be discarded.

After the fiscal year 1982, the following expansion or modification will be made.

A. A sorbent regeneration unit: applicable for both limestone and synthetic sorbent.

B. A new dust — collector for testing is planned for the dust discharge quantity 10 mg/Nm^3, and for the gas flow rate of approximately 1,000 Nm^3/h.

Design Conditions

(1) Main boiler specification

Boiler type:	Natural and forced circulation type drum boiler; indoor type.
Evaporation:	20 t/h
Steam pressure:	60 kg/cm^2 G at the outlet of the superheater
Steam temperature:	540°C at the outlet of the superheater
Feedwater temperature:	133°C at the inlet of the fuel economizer
Boiler efficiency:	87.37% (high calorific value base)
Fuel consumption:	2,450 kg/h (wet coal base)
Fuel calorific value:	7,100 kcal/kg (high heating value for dry coal.) 6,603 kcal/kg (high heating value for wet coal)
Combustion flue gas:	20,293 Nm^3/h (wet)

(2) Target value of emission control
SOx: 95% desulfurization for coal containing 3% S
NOx: 60 ppm for coal containing 1% N and O_2 6% equivalent.

(3) Properties of planned coal: Refer to Table 2.

(4) Desulfurizing sorbent: natural limestone and synthetic sorbent

Plant Outline

(1) Boiler

Fig. 1 shows a section of the boiler elevation.

The MBC consists of the combustion furnace which is composed of a natural circulation membrane structure water wall and the refactory wall rear flue. In the fluidized bed with a 2.17 m x 4.34 m area, the forced circulation type evaporator by a boiler circulating water pump and the primary and secondary superheaters are installed. The fluidized bed is divided into two parts so that one side operation can be done.

Outside the bed, the evaporator and flue economizer are installed. This evaporator, as shown in Fig. 2, can be removed to the free board of the combustion furnace or rear flue. This, together with a change in the installation level of the duct connecting to the rear flue, enables the test for a change in free board conditions. In the free board of the combustion furnace, double stage combustion air feeding ports (8 rows x 5 stages) are installed to enable various comparison tests to be conducted.

CBC is composed of a natural circulation water wall (0.91 m x 0.91 m). In the free board of the CBC, a fuel economizer is

installed.

The height of the overflow is variable. Overflow ash is cooled by air. To monitor the temperature distribution in the fluidized bed and the temperature behavior in the major parts of the boiler tubes, tens of thermocouples are installed and connected to a data processor evaluate and analyse the test operating conditions and performance of the boiler.

(2) Coal and Limestone Feeder

The coal charged into the feed coal hopper is temporalily stored in the feed coal bunker and sent to the dryer to remove moisture, then crushed screened for classification into fine and coarse fractions of coal.

The coal dryer of an indirect steam heating type.

Coal is crushed in two stages before drying. Limestone whose grain size has been adjusted at the mine is used and supplied into MBC together with fine grain coal through pneumatic conveying.

(3) Instrumentation

The instrumentation of this plant consists of the boiler control system, a centralized operation monitoring system and a precessing system. The data further can be displayed on the color CRT screen.

(4) Ash handling Equipment

Ash discharged from the overflow pipe of MBC and CBC is cooled and sent to the overflow tank, then sent to the ash storage silo by the pneumatic conveyer system.

3. Present State of the Test

Outline of the results of the operation up to June, 1981 together with several examples of the operation data are as follows:

(1) Operation Results

Since coal feeding started in early May, 1981, operation time has accumulated to 628 hours by September, 1981. Taiheiyo coal, typical low sulfur non swelling bituminous coal of Japan, is currently used. Properties of this coal and limestone are shown in Table 3 and Table 4 respectively.

The size of coal is -6 mm and the average particle diameter is about 2.5 mm. The limestone size is -3 mm.

Up to now so far, 10 cold starts and 17 hot starts have been carried out.

(2) Operation Data

Table 5 shows an example of operation data. In the Table, the NOx values are from the single stage and two stage combustion. These values are sufficiently low compared to the values of the government regulation. The SOx value is for the present low S coal. The desulfurization performance will be checked by using medium S coal in later test.

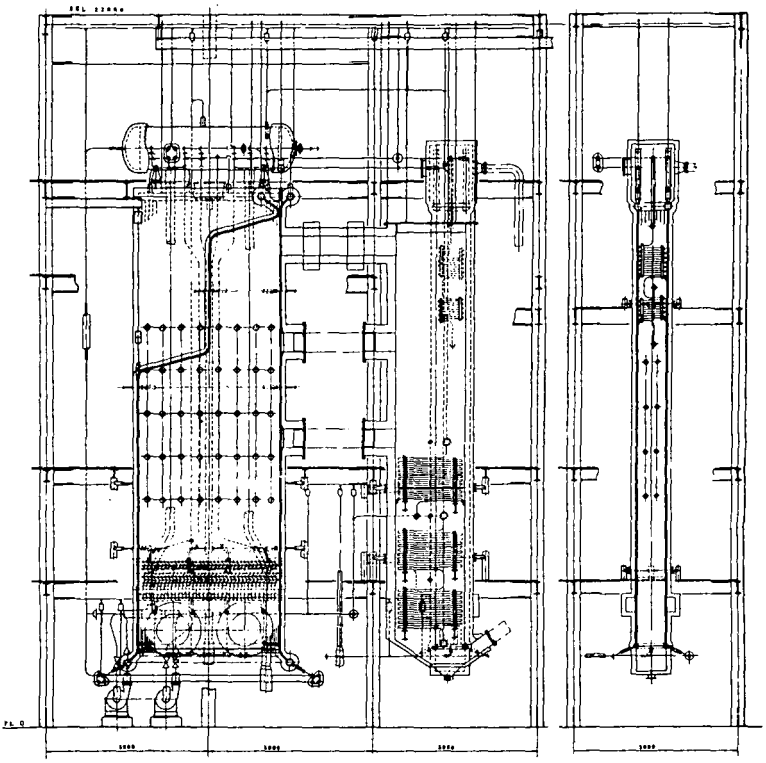

MBC CBC

Fig. 1 Boiler Structure

Fig. 2. Possible configulation of free board and tube arrangement in 20 t/h Fluidized Bed Boiler Test Module

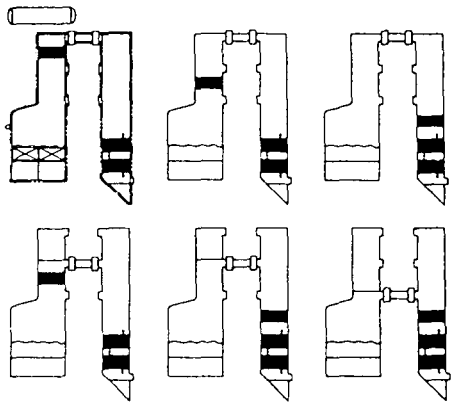

Table 1. Fluidized Bed Boiler Development Program

Item \ Fiscal year	1978	'79	'80	'81	'82	'83	'84	'85	'86
Preliminary study									
Feasibility study 500 MW plant									
20 t/h pilot plant		Design	Manufacture and installation	Operating test					
240 t/h demonstration plant (75 MW class)				Design		Manufacture and installation		Operating test	

Table 2. Coal Properties

Type of coal			Planned coal
Drycoal high heating value (kcal/kg)			7100
Surface moisture			7.0
Proximate analysis	Moisture	(%)	2.8
	Ash	(%)	9.5
	Volatile matter	(%)	28.5
	Fixed carbon	(%)	59.2
Ultimate analysis	C	(%)	73.8
	H	(%)	4.0
	N	(%)	0.8
	O	(%)	11.0
	Total sulfure	(%)	0.8

Table 4. Properties of Limestone

	Item		Analysis
Component	CaO	(%)	55.38
	MgO	(%)	0.30
	SiO_2	(%)	0.28
	Fe_2O_3	(%)	0.03
	Al_2O_3	(%)	0.10
	Others	(%)	0.90

Table 3. Properties of Coal

Type of coal			Taiheiyo coal
High Heating Value (Kcal/kg)			6330
Surface moisture (%)			1.6
Proximate analysis	Moisture	(%)	3.0
	Ash	(%)	15.3
	Volatile matter	(%)	44.2
	Fixed carbon	(%)	37.5
Ultimate analysis	C	(%)	64.1
	H	(%)	5.8
	N	(%)	0.8
	O	(%)	13.4
	Combustible S	(%)	0.1
	Incombustible S	(%)	0.1

RESEARCH AND DEVELOPMENT OF COAL-FIRED FLUIDIZED-BED BOILER

Bao Dong-wen and Ruan Yi-shao

Research and Development Division
Dong-fang Boiler Works
Zigong, Shichuan, China

INTRODUCTION

The power industry in many countries is now facing a problem: how to achieve the inevitable shift from oil and natural gas to coal and low-grade coals while remaining in compliance with the regulatory limits on emissions. Fluidized-bed combustion (FBC) has demonstrated its potential to solve this problem, because it has the advantages of adaptability to low-grade coals and feasibility for sulfur emissions control. Due to FBC's relatively low combustion temperatures, NO_x emissions from a fluidized bed are lower than those from conventional furnaces.

As a new technology it is natural that there are many technical problems to be investigated and difficulties to be overcome in the development of fluidized-bed boilers (FBB).

Since 1971, Dong-fang Boiler Works (DBW) has carried out developmental work in FBB in the following areas:

- Combustion efficiency.
- Arrangement of fluidized-bed heating surfaces.
- Immersed superheater.
- Erosion of immersed tubes.
- Start-up of fluidized bed.

A 463 x 324 mm FBC test unit was built to investigate methods of improving the combustion efficiency of the FBB. Later, a 24 t/h stoker-fired boiler was converted into an FBB by DBW. It has now been successfully operated for

more than 3 years, since 1977. The performance of the unit has been satisfactory to the user. Figure 1 shows the general arrangement of this modified boiler. Its major parameters are as follows:

Steam capacity	24 t/h
Steam pressure	32 kg/cm^2
Superheated steam temperature	450°C
Feed water temperature	150°C
Gas temperature at boiler exit	200°C
Designed fuel	Bituminous coal

Natural circulation was adopted for the immersed evaporating surface. To date no problem in water circulation has occurred. An experimental immersed superheater was placed in the bed and its behavior observed. For distribution of combustion air, a refractory covered bubble cap plate was installed. In order to facilitate bed start-up and load changes, the windbox was divided into four separate compartments. Because bituminous coal was to be used, no carbon recycling was considered; thus the uncertainty of a recycle system was avoided. The once-through combustion efficiency (i.e., without reburning of elutriated fines) was measured as 94.8 to 95.5 percent.

TEST RESULTS AND DISCUSSION

A. Combustion Efficiency

When compared with pulverized coal firing, carbon losses from a fluidized bed are high as a result of the relatively coarse coal particulates and low combustion temperature. Combustion efficiency depends on the bed velocity and temperature, excess air, and on the coal characteristics (which have significant influence on carbon losses). Coal with high ash content and less volatile matter would have lower combustion efficiency. The following experimental data from the test rig demonstrate that c.e. values in burning different coals may differ greatly, even when the superficial velocity, bed temperature, and excess air rate are approximately the same.

	Volatile matters on combustible basis	Ash on analytical basis	Total carbon losses
Bituminous coal	35.48	31.40	3.77
Lean coal	17.50	39.04	10.67
Colliery wastage	48.09	76.50	7.95

If anthracite is burned, carbon losses will be higher than the above values. It is evident that application of FBC in utility boilers will require significantly increased combustion efficiencies.

Two approaches for improving combustion efficiencies are: using a carbon burnup bed (CBB) and fly ash reinjection into the main fluidized bed.

The effect of the CBB was examined using the 463 x 324 mm rig. The tests showed that with the use of a CBB (an efficiency of 80 percent was assumed for the cyclone dust collector), combustion efficiencies may reach values of 97.5-98.0 percent when bituminous or lean coals are burned.

The recycling or reinjecting of elutriated fines has not been tested, but judging from the literature of other countries and experiences in application of carbon recycling in some FBB in China, we can say that particulate recycling (especially for coals with high volatile matter content) is also an effective measure. For example, the combustion efficiency of a bituminous coal-fired combustor may attain ~ 98 percent.

When a CBB is used, in order to avoid high dust loading, the gas stream from the CBB must be directed to an individual gas flue. Therefore, the CBB is in essence a separate fluidized-bed boiler, which operates at different conditions from the main bed and needs its own particulate removal system. In addition to being a more complex system, the reliable combined operation of a CBB with the main fluidized bed is rather difficult because of the inevitable fluctuation of coal characteristics and the main bed exploitation; the recycle system is much simpler. The main disadvantage of recycling the dust recovered from the dust collector is the resulting high dust loading of the gas stream. The erosive characteristics of the dust must be determined by operating a demonstration unit over an extended period of time.

In our view, with regard to industrial FBB, the carbon recycling system may be more desirable in most cases. Where less reactive coal such as anthracite is burned and the high combustion efficiencies which are required for a utility boiler are pursued, the CBB system may have to be used.

The even distribution of coal over the bed has proved to be of significance for attaining good combustion efficiency. It has been reported that satisfactory coal distribution can be achieved if one feed point is provided for every 0.84 m of bed area. This would result in nearly 70 points for a 130 t/h unit. In order to meet the above requirement, a pneumatic method of transporting crushed coal may be necessary. However, for large FBB (e.g., 200 MW units) the feed lines and control system would become very complicated; therefore, a method to improve the area per feed point must be found if the pneumatic feed system is to be simplified.

For purposes of this test a pneumatic feed system was not considered, but four screw-type coal feeders were installed on the front wall. The area of distributing plate for the 24th FBB unit was 8 m^2; this provided one feed point for every 2 m bed area. To promote even coal distribution, a coal spreading method was developed. During the tests of this method on the 24 t/h FBB unit only two feeders were put into operation,

which temporarily raised the area per feed point to 4 m^2. It was demonstrated that when the spreading device was used, combustion efficiencies were increased by 3.5-5.0 percent.

B. Arrangement of Bed Heating Surface

Vertical immersed tubes are generally used for small FBB. They are convenient for maintenance, and are more resistant to abrasion than horizontal tubes.

For larger units, to allow the necessary surface area required to be placed in the bed, horizontal or inclined buried tubes (staggered or in-line) are generally adopted. It is common knowledge that so far as convection surfaces are concerned, staggered tubes have higher heat transfer rates than tubes arrayed in-line. Given this information, is it still correct to use immersed tubes in FBB? To answer this question, special comparison tests were carried out. The results showed that, owing to the specific nature of the in-bed heat transfer, heat transfer coefficients for the in-line array of tubes fully compared with those for staggered tubes.

Initially, the immersed tubes of the 24 t/h unit were staggered. When the unit was put into operation, it was immediately discovered that excessive pulsations occurred and the erosion rates of the staggered inclined tubes and the fire brick walls were high.

On the basis of the above tests, it was decided to change the staggered tubes into in-line array. After the modification the steam output was maintained, the fluidizing quality became normal, and the abrasion rates were reduced.

C. Immersed Superheater

An industrial FBB can be designed with only an evaporating surface in the bed; this appears adequate to absorb the required amount of heat from the bed. In contrast, a certain portion of the superheating or reheating surface of a utility boiler must be placed in the bed in addition to the generating immersed surface. It seems useful to examine some problems of the buried superheater.

Because of the high heat transfer to immersed tubes (generally 220-250 kcal/m^2 •h• ^oC), it is of great importance to find out whether the wall temperatures of buried superheater tubes will exceed the limits. To this end, the character of the heat flux distribution along the periphery of an immersed tube must be determined. Special tests showed that this distribution was uneven, and surprisingly, the highest heat flux point was found at the upper part of a horizontal buried tube (Figure 2). The maximum heat flux exceeded the average value by 15-30 percent (in some cases even more), which means there exists an intense circulating flow of particulates within the "cap area" above the immersed tube. Figure 3 illustrates the approximate manner of particulate circulation.

ø42 x 5.5, 12 Cr/MoV steel tubes were used for the experimental submerged superheater. The steam velocity was ~ 35 m/s and the mean exit steam temperature ~ 420 °C. Thermocouples were placed on the outer surface of the lower part of two buried superheater tubes. No thermocouple was placed on the upper part of the tubes, because it was thought that the maximum heat flux area must be at the lower half periphery; thus, the maximum tube wall temperature was not measured. The temperatures taken from the lower half periphery were 530°-550°C. It was clear that the wall temperature at the top of the tubes must have been higher. After about 3 months of operation, a metallographic examination was made of the tube. It was found that grade 3 spheriodization had taken place at the top of the tube, which meant that although the steam temperature was as low as 420 °C, using the 12Cr/MoV steel tube was not safe. It appears that the tube wall temperature must be considered carefully and high-quality heat resistant alloy steel will have to be used when superheating or reheating surfaces need to be placed in the bed.

The protection of the immersed superheater during start-up and bed slumping was also of considerable concern. As operating experience had proved, the buried superheating tube temperature would not exceed the allowed value during start-up and slumping, provided the surface was arranged properly and partial bed start-up sequence (a portion of the bed where the immersed superheater is located, lit up only after an adequate steam flow is established) was adopted. When the boiler was to be shut down and the bed slumped, the immersed superheater would be safe. The immersed superheater was arranged above the slumped bed and its wall temperatures, measured during slumping, were all lower than 530°C. The temperatures measured in the space between the superheater and slumped bed did not exceed 600°C.

The temperature distribution over the bed was relatively even, and the deviation in heat absorption among the individual tubes was not great. Generally speaking, the deviation coefficient is about 1.1, provided the surface is appropriately designed. The temperature gradient along the feeder axis may be somewhat greater; therefore, the tubes of an immersed superheater would preferably be oriented in parallel with the feeder axis (as shown in Figure 1). If bed temperature unevenness along the feeder axis is significant and the superheater tubes are at right angles to the feeder axis, higher deviation coefficients of 1.20-1.26 may be reached, depending on the bed temperature gradient.

D. Erosion of Immersed Tubes

At present, rather coarse coal particulates are generally used in China. Consequently, high fluidizing velocity has been adopted. Many years of operational practice has shown that in most cases the abrasion of inclined buried tubes is very severe. For example, tubes (20 carbon steel) with a thickness of 3 mm may wear out after only ~ 4000 hours of operation. The most serious abrasion usually occurs in the first (lower) row of inclined buried tube surfaces. Along the inclined tubes certain more severely abraded sections can be observed. The abrasion rate is very uneven along the tube periphery. Figure 4 illustrates the severe abrasion of a 20-carbon steel tube with a thickness of 6.25 mm (no antiabrasive treatment used) after 8682 hours of operation. The

abrasion rate at the bottom of the tube is three times as high as that at the top. Several types of antiabrasive treatments for immersed tubes were tried, and some of them have showed effect. However, when relatively hard coals are burned these measures can only extend tube life to a certain degree, therefore the abrasion problem cannot be regarded as solved. Lignite-fired, fluidized-bed boilers may be the only exception. The erosion rate of their immersed tubes is not high, owing to the softness and light weight of the lignite.

It seems to us that low fluidizing velocity should be accepted as the primary measure for extending the life of immersed tubes, with additional antiabrasive treatment when necessary. This may be the final solution to the erosion problem. Besides the diminished tube abrasion, low fluidizing velocity may offer other benefits such as higher combustion efficiency, better SO_2 absorption (when limestone or dolomite is added to beds where high-sulfur coal is burned), and the possibility of using shallow beds to reduce the amount of blower power required. In order to lessen the abrasion rate, the immersed tubes should be reasonably arranged to avoid excessive pulsations and gas flow imbalances in the bed.

E. Start-up of Fluidized Bed

The process of start-up is, in essence, to heat the bed material to a temperature high enough for stable combustion of coal. It seems very simple, but when boiler service is initiated operators often run into trouble.

"Fixed state" start-up is a method adopted in the initial period of FBB development in China. In this process, the bed remains fixed at the beginning of start-up. When the bed material has been heated to the appropriate degree, the bed is tranformed from a fixed to a fluidized state and continues to be heated to the required temperature. During the start-up process, clinkering or flame failure may easily take place if the heat balance is not properly controlled. Exploitation depends to a great extent on the operator's experience, so it is not completely reliable. Furthermore, the time required for starting up is rather long.

Through the search for a better method, the so called "fluidized state" start-up technology has been developed. The major feature of this process is that the bed is brought to fluidization at the very beginning of start-up. The fluidized bed is heated up by an oil burner; the heating is uniform and steady. In 10-20 minutes, a bed with an area of 4 m^2 can be heated from ambient temperature to 900 -1000 °C. It is much quicker than the "fixed state" method, and oil consumption can thus be reduced. Figure 5 shows a typical bed start-up curve in which the "fluidized state" method was used.

CONCLUSION

The main reason for developing fluidized-bed boilers in China is to burn high-ash coal of low calorific value, and thus broaden the scope of energy resources. This appears to be especially important in the southern pro-

vinces. Practice over a number of years has indicated that FBB are promising, at least for industrial boilers and small electricity generating units in China. The application of FBB to utility power plants, however, depends on future development, economic factors, and the success of intermediate demonstration units.

There is no doubt that many areas still need further investigation and that equipment could be improved, but we are convinced that a good start has already been made. Dong-fang Boiler Works now produces commercial FBB with steam capacity of up to 35 t/h. Units of greater capacity are under consideration.

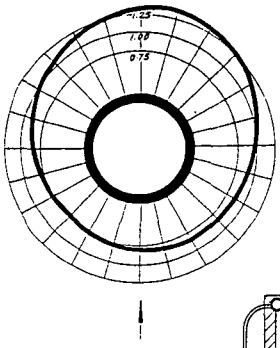

Fig.2 - Heat Flux Distribution

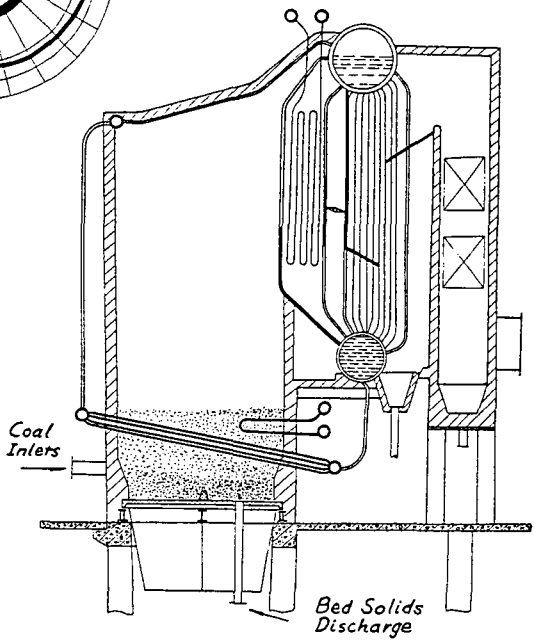

Fig.1 - 24 t/h Fluidized Bed Boiler (modified)

5:vm:513:4

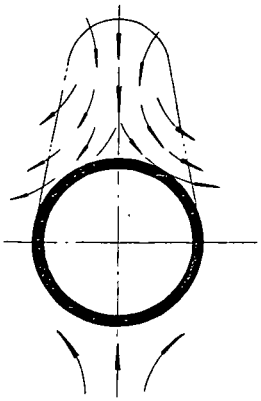

Fig. 3 - Particulate Circulation in "Cap Area"

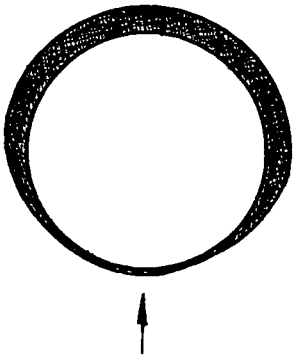

Fig. 4 - Wornout Tube

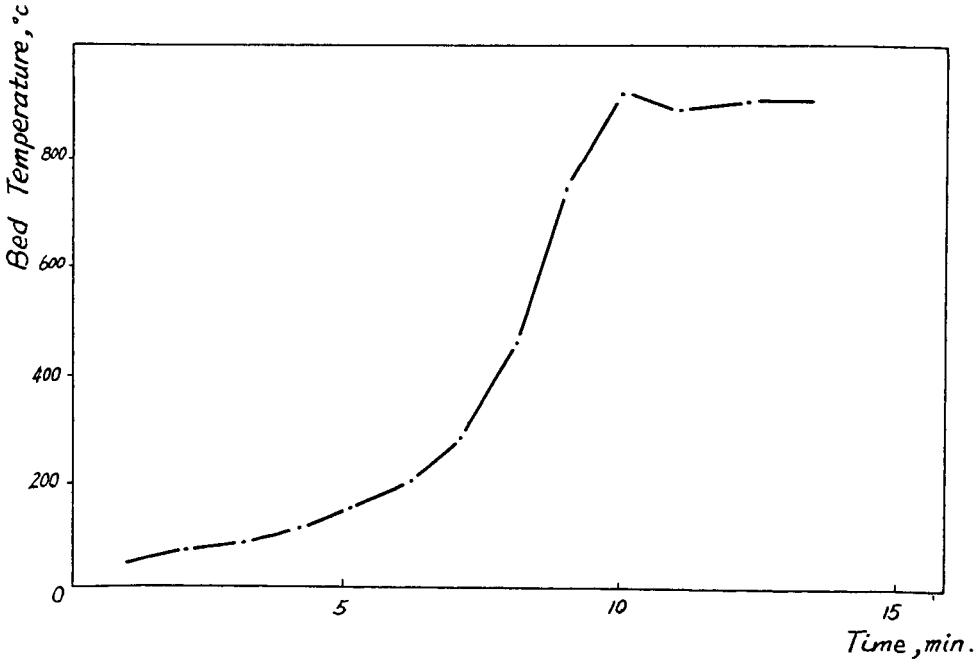

Fig. 5 - Bed Start-up Curve

A DATA ACQUISITION AND CONTROL SYSTEM FOR A FLUIDIZED BED COMBUSTION UNIT

D. W. Church and D. G. Pincock
Applied Microelectronics Institute, P. O. Box 1000,
Halifax, Nova Scotia B3J 2X4

INTRODUCTION

The Centre for Energy Studies at the Technical University of Nova Scotia is currently developing a small scale fluidized bed combustion unit for domestic heating purposes. The Electrical Engineering Department at the University was called upon to provide the electronics necessary to control and gather operating data on an improved prototype. The purpose of the present system is to develop an efficient control algorithm. If the fluidized bed proves feasible, the hardware can be simplified to an inexpensive microprocessor controller.

OVERALL SYSTEM DESIGN

The main requirement of the electronic system is to maintain the temperature of the fluidized bed between the limits of 750° - 950°C. The method of control is to monitor not only the bed temperature but also the stack temperature and concentration of pollutants and then adjust the ratio of fuel and air input to achieve complete combustion. Since the fluidized bed is integrated with a back-up domestic oil-fired hydronic heating system, control of boiler temperature is also a system requirement. In addition alarms are energized and appropriate actions taken when the fluid bed temperature is outside the desired range.

To aid in development of the control algorithm,the fluidized bed and back-up heating unit are fitted with a variety of sensors. Examples include thermocouples for temperatures, gas analyzers for oxygen and carbon monoxide, and pressure transducers for air flow rates. Since the total number and type of sensors is variable, expansion and modification of both hardware and software by the user is highly desirable. With these points in mind, the system of Figure 1. was developed.

The general philosophy is to employ the desktop computer in the role of a "host", controlling data flow and perfoming arithmetic calculations. The host also acts as an interface between the console (user) and the data acquisition unit when system configuration changes are desired. The printer provides a record of the system status and operating conditions.

The next section briefly describes the components selected to realize the system of Figure 1.

System Hardware

Since the project is of a developmental nature it was thought highly desirable to select major components which are general purpose in nature and, hence, useful in future applications. To this end, the STD BUS was selected as the basis of the microprocessor controlled data acquisition unit. The STD BUS was developed by Pro-Log and MOSTEK and is now quite popular. A wide variety of plug-in cards and complete systems are available from manufacturers such as Pro-Log, MOSTEK, Intersil and Analog Devices.

The STD BUS standardizes the physical and electrical aspects of modular 8-bit microprocessor card systems. The standard permits any card to work in any slot of the bussed motherboard which provides internal communication. All other connections to the outside world are by connectors at the opposite ends of the cards. Available cards include all the popular 8-bit processors, memory expansion, digital

I/O, analog I/O, industrial I/O (relays and triacs) and peripheral interfaces.

The data acquisition unit contains 4 plug-in cards, two of which are custom built. Figure 2 shows how the various functions are distributed. The processor card uses an 8085A and has sufficient random access and program memory on-board. With the exception of signal conditioning for low-level signals, the entire analog I/O subsystem is contained on the RTI-1225 card manufactured by Analog Devices Corp. It is designed specifically for interfacing real time analog signals to microcomputer systems. On the input side there are 16 channels multiplexed to a sample and hold amplifier and a 10 bit A to D converter. The output side has 2 channels with 8 bit resolution. Communication is memory mapped and appears as five contiguous address locations which are used to control the functions of the card and pass data to and from the microprocessor.

The custom built cards combine two functions on each. One handles thermocouple signal conditioning and digital I/O while the other contains a real time clock and a UART for interfacing to the desktop computer. Four thermocouples of any type can be handled by the present card, with gain and cold junction compensation software selectable. Additional cards may be added as required. All temperature channels are multiplexed into channel one of the A to D converter, leaving 15 single-ended 0-10 volt analog input channels.

Operating data other than temperatures are supplied by the monitoring instruments (e.g. oxygen analyzer). The outputs from such instruments are in general fully compensated and conditioned 4-20 mA currents or selectable low level voltages. Instruments with 0-10 volt outputs can thus connect directly to the A to D converter. In our system, carbon monoxide and carbon dioxide monitors produce only a 0 - 5 volt output, which still provides adequate resolution and accuracy with a direct connection. Instruments with current loop outputs also connect directly by terminating the loop at the A to D input with a 500 ohm resistor to produce a 2-10 volt signal range. If other low level sensors such as strain guages are required, they can be amplified externally with modules which produce either current loop or 0-10 volt outputs. Examples include the Analog Devices 2B50 series.

The host computer is a desktop unit which does the calculation of the control algorithm and prepares system status information for display at the console and printer. This computer is a Superbrain (Intertech Data Systems, Columbia, South Carolina) based on the Z-80A microprocessor and using the CP/M operating system. It is a self-contained unit having a CRT, keyboard, two floppy disk drives, 64K of memory and 2 I/O ports.

In keeping with the overall philosophy of hardware selection, the printer is a Decwriter LA-120 which provides the user with a very flexible and attractive hard-copy terminal for future use.

System Software

The system software was develpped in two stages. First the data acquisition unit program was written in PL/M. Compilation was done on a large time-shared system and the result downloaded to a PROM programmer. Included in the I/O portion is a segment which enabled testing and calibration of the analog hardware as the program was expanded. Following this the host computer program was written and tested a portion at a time with the working data acquisition unit. Rapid development of relatively unsophisticated processing, combined with ease of program maintenance by the users led to the selection of BASIC as the host language.

The main tasks assigned to the data acquisition unit are temporary storage of raw binary data from all sensors, conversion to ASCII of this same data, response

to requests by the host computer and monitoring alarm conditions in the fluidized bed. Single letter codes sent by the host initiate any desired actions. Examples include passing of the latest data, adjustment of fuel or air motors, or changes in system configuration such as number of active channels.

PL/M is a programming language designed for Intel's 8 bit microcomputers. The language is structurally similar to PL/I so that programs are somewhat self-documenting and easily altered and maintained. A memory map for the data acquisition unit is shown in Figure 3. The program is stored in read-only memory and the analog I/O subsystem is placed at the top of the 64k address space. This application uses about 1k bytes of the available on board ROM.

The supervisory BASIC program gets the latest data from all sensors, converts to appropriate units and formats and displays this information on the console and printer. Time of day and update interval are provided by the real time clock, which is software settable from the host. For non-linear sensor readings, disk files containing appropriate tables are used for interpolation. Such is the case for all thermocouple readings. The converted data is then utilized by the control algorithm to determine if fuel and air feed corrections are required. If so, this information is passed to the data acquisition unit and out the D to A channels to motor controllers. Finally, a second check on the fluidized bed temperature is done by the host to alert the operator in the event of a failure of the hardware alarms.

Conclusion

A data acquisition and control system for a fluidized bed combustion unit has been described. It should be re-emphasized that the developed algorithm can be easily moved to read-only memory in a low cost controller. It is believed that the choice of major components has resulted in a system which is sufficiently general in nature to not only serve the current project but also to prove useful in future applications. The type of system described should find application wherever monitoring, recording and control of analog or digital signals and processes is required.

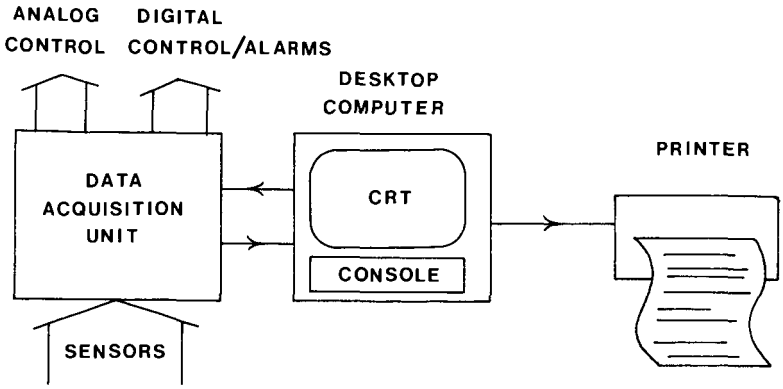

FIGURE I. OVERALL SYSTEM.

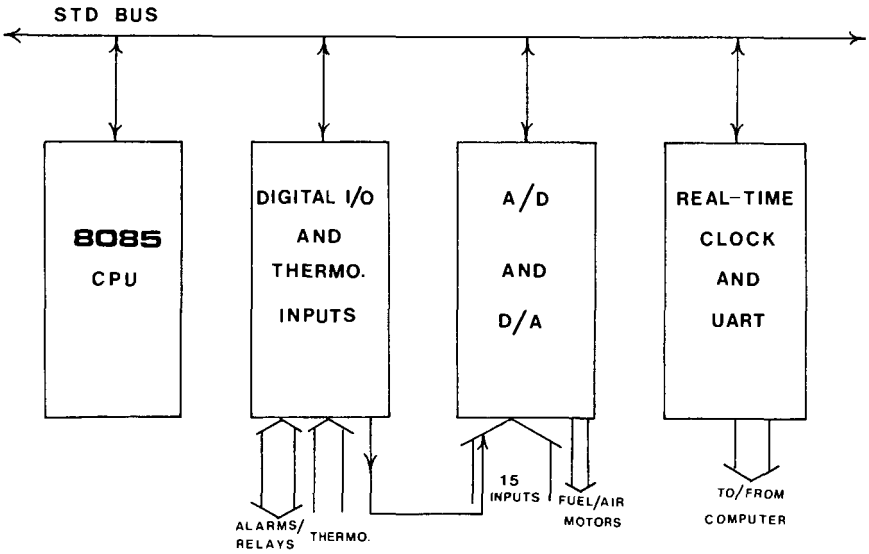

FIGURE 2. DATA ACQUISITION UNIT.

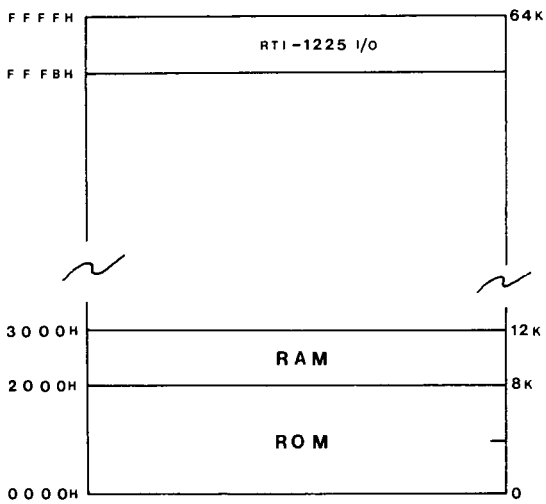

FIGURE 3. D.A.U. MEMORY MAP.

SAMPLING SYSTEM FOR FLUIDIZED BED APPLICATIONS - RESULTS OF FOUR YEARS OF TESTING ON B&W/EPRI's 6' x 6' FLUIDIZED BED TEST FACILITY

K. L. Loudin and P. W. Maurer

The Babcock & Wilcox Company
Research and Development Division
Alliance Research Center
Alliance, Ohio 44601

W. Howe

Electric Power Research Institute
Palo Alto, California 94304

INTRODUCTION

In cooperation with The Electric Power Research Institute (EPRI), The Babcock & Wilcox Company (B&W) has built and is operating a 6-foot x 6-foot (6' x 6') Atmospheric Fluidized Bed Combustion (AFBC) Development Facility at its Alliance Research Center in Alliance, Ohio. A complete description of the facility design details is contained in EPRI Final Report CS-1688. An artist's rendition (Figure 1) identifies the major components of the facility.

The 6' x 6' size was selected as being large enough to bridge the gap between bench-scale units then in operation and larger, future units in the proposal and/or construction stages. The facility design is flexible (versatile to modifications) in many areas -- number of feed points, immersed tube bundle configurations, ash recycle configurations, interchangeable gas sample systems, etc. -- and is highly instrumented (controls, interlocks, data acquisition, and sampling) to closely simulate utility boiler designs. The size, design, and equipment selections have produced a hot test facility with the capability of generating significant performance data over extended periods of steady operation for a multiple number of planned test conditions.

The facility construction was completed in October 1977. Following a 5-month startup and debugging phase, the first test series was conducted in April 1978. Since that time, approximately 2000 hours of testing (five to eight test series) per year have been logged.

GAS SAMPLING SYSTEMS

Evaluation of the performance of the 6' x 6' AFBC test facility mandated accurate sampling and gas concentration measurements. For example, measurements of CO_2, CO, and Hydrocarbons are used in calculating combustion efficiency while the measurement of SO_2 is needed to calculate sulfur capture. Oxygen measurements, also used in performance calculations, are used by the operators in setting the desired facility operating test conditions. Figure 2 shows the location of the main gas and solids sample points on the 6' x 6' unit.

Obtaining gas concentration data required the use of a sampling system that included the use of many special instruments and/or equipment. The original system layout and details are shown on Figure 3 and Table 1, respectively. The two independent systems that make up the complete system are identified as the mobile and furnace outlet systems. Sampling flexibility is gained by being able to

interchange systems and/or components. The original system has been expanded to include NO_x and Hydrocarbon measurements at the furnace outlet and CO_2 measurement at in-bed and freeboard locations.

Table 1

Tabulation of Gas Sampling System Details

Tank Farm Calibration Gases	SO_2, CO, O_2, NO, CO_2, Air, and N_2	
Instrument Air System	60 - 100 psig (2 - 3 SCFM)	
GAS SAMPLE SYSTEMS	Furnace Outlet Probe	Mobile Probe
SO_2, CO, O_2, NO_x, and CO_2 Analyzers	Yes	Yes
Hydrocarbon Analyzer	Yes	No
Common Tank Farm	Yes	Yes
Common Instrument Air Supply	Yes	Yes
Separate Sample Probes	Yes	Yes
Separate Filter-Cyclone Assemblies	Yes	Yes
Separate Heated Sample Lines	Yes	Yes
Separate Filter-Pump Systems	Yes	Yes
Instrument Air to Pump Control Switch	10 psig @ 1200 cc/minute	10 psig @ 1200 cc/minute
Cooling Water to Probes	20 gph maximum	20 gph maximum
GAS SAMPLING SOURCE	Stack (Furnace Out)	"In-Bed" and Freeboard
Approximate Source Gas Temperature	900°F	1650°F
Sample Gas Temperature @ Probe Discharge	310°F	310°F
Sample Gas Temperature in Sample Line	300°F	300°F
Sample Gas Temperature @ Pump Inlet	180°F	180°F
Sample Gas Temperature After Analyzers	Ambient (80°F)	Ambient (80°F)
Sample Gas Flow From Source	5 liters/minute	5 liters/minute
Sample Gas to O_2 Analyzers	250 cc/minute	250 cc/minute
Instrument Air to O_2 Analyzers	10 psig	10 psig
Sample Gas to SO_2, CO, and CO_2 Analyzers	1000 cc/minute	1000 cc/minute
Sample Gas to NO_x Analyzers	1200 cc/minute	1200 cc/minute
Instrument Air to NO_x Analyzers	35 psig	35 psig
Recorder "A" Gas Printout	SO_2, CO, O_2, and CO_2	
Recorder "B" Gas Printout		SO_2, CO, O_2, and NO_x

GAS SAMPLING WITH ORIGINAL PROBE-FILTER ASSEMBLIES

Furnace Outlet Gas Sample Location

The gas analysis from the furnace outlet is used in performance calculations and additionally to set and control the facility test conditions. This system must operate on a continuous basis. Figures 4 and 5, respectively, show the probe installation in the furnace outlet duct and the original probe-filter assembly. The water-cooled probe has an open-ended, concentric quartz tube for sample flow. In turn, the tube is connected to an in-line particulate filter assembly (glass cyclone collector/drop out bottle and frit-fiberglass filter unit) through which the gas sample flows enroute to the heated sample line. The particulate filter assembly, located in an electrically-heated cyclone oven (size - 9-1/2 inches square x 21-1/2 inches long), is maintained at 300°F. At normal operating conditions (no dust recycle), the particulate filter assembly had to be changed twice during each 24-hour operating period.

Freeboard Sample Locations

The mobile gas sampling system and probe installation shown in Figure 6 are used to traverse the freeboard at the locations previously shown in Figure 2. A typical traverse at one location would include taking gas samples at 12 or 13 points across the width of the facility. A complete traverse, conducted with the drive mechanism on either "hand mode" or "automatic mode", requires from 60 to 90 minutes to complete. Except for the difference in length, the furnace outlet and mobile probe-filter assemblies are identical.

In-Bed Sampling Locations

The in-bed gas sampling probe installation, shown in Figure 7, is used for traversing in the fluidized bed. The original in-bed probe-filter assembly is shown in Figure 8. The filters are 3/4 inches in diameter x 1-3/4 inches long with a pore size of approximately 1 micron. The ceramic collar is cemented to the filter at a position that is 1/4 inch away from the open end. The collar is clamped in the probe head at a location that presents an active filter flow area of approximately 2 square inches.

Typically, the ceramic filter had to be cleaned (nitrogen back-purged) at 15- to 20-minute intervals.

GAS SAMPLING PROBLEMS

The original gas sampling probes operated satisfactory and allowed accurate gas concentration measurements during no dust recycle test conditions. However, operation of the 6' x 6' AFBC unit has shifted to the use of dust recycle to improve performance. Dust loadings as high as 10,000 lb/hr have been run at temperatures up to 1750°F and at gas velocities of about 100 ft/sec. The high dust recycle increased the particulates that were entrained in the gas samples. This condition necessitated frequent filter changes, caused problems with glassware breakage due to increased handling, and required more frequent nitrogen back-purging of the in-bed filter.

Problems associated with gas sampling at the furnace outlet, freeboard, and in-bed locations are discussed in the following paragraphs.

Furnace Outlet Gas Sample Location

With high dust recycle rates, the filters required continual attention. Each filter change involved disconnecting and reconnecting five joints in the flow system. In a few instances, slight amounts of air infiltration (induced by negative pressure in the sample line) into the gas sample produced incorrect gas concentrations. Increased handling of the glassware and quartz tube produced some breakage problems. In certain instances, the breakage would occur as a crack that was difficult to detect. Undetected cracks, on a couple of occasions, permitted air infiltration into the sample in such a small quantity that the incorrect concentration readings went unnoticed for a few hours. These problems instigated a modified probe-filter assembly design that would provide more effective filtering. The modified design would eliminate the fragile components, such as glass and quartz, and would minimize the number of connection joints.

Freeboard Sample Locations

Problems with the probe-filter assembly were similar to those encountered at the furnace outlet location. Due to continual filter pluggage, the probe could not be used in the fringe area of the bed i.e., the lower sets of freeboard ports. Additionally, the long probe length (approximately 9 feet) and relocating the probe to all sample ports produced occasional breakage to the fragile components. Such actions also caused occasional air infiltration into the numerous connection joints.

In-Bed Sampling Locations

The solids density of the bed has always required the use of a nitrogen back-purge to clean the ceramic filter. A combination of the small active filter area (only 2 square inches) and the increased solids concentration increased the "blow-back-cleaning frequency". The resulting time required to conduct a traverse more than tripled that required for the no ash recycle test condition.

SOLUTIONS FOR SOLVING SAMPLING PROBLEMS

A review of sampling at all locations indicated that the components included in the probe-filter assemblies were responsible for the problems. Further review of the problems encountered at each location suggested that a modified probe-filter design could be adapted for sampling at all locations. The modified design actions included the following:

- Install a primary solids filter at the sample inlet to the probe. A ceramic filter, supplied by the Coors Porcelain Company, with an active filtering area of approximately 12 square inches was selected for this application. This filter (size - 1-1/4 inches OD x 3/4 inch ID x 4 inches long) with a pore size of 100 microns was included on the modified probe-filter assembly shown in Figure 9.

- Install a secondary filter between the sample probe and the heated sample line. A cartridge-type filter with two inches of kaowool insulation (also shown in Figure 9) was proposed to protect other components of the sample train in the case of a failure of the primary filter. This secondary filter would eliminate the glassware and plastic components which in turn would decrease the number of connection joints where possible air infiltration could occur. The insulation around the filter would eliminate the cyclone oven, controls, etc. thereby reducing the bulkiness of the installation.

- Remove the quartz tube (gas sample flow tube) from the center of the probe. This would eliminate another fragile component by allowing the sample to flow down the center (stainless steel tube) of the probe.

PERFORMANCE DATA SUPPORTS MODIFIED SYSTEMS

Primary Filter Performance

- The ceramic filter was initially tested at the furnace outlet gas sample location. At first, problems developed in sealing the ceramic filter and the metal tube. After obtaining a good seal, the ceramic filter performed to maximum expectations as shown by the following table:

Gas Temperature (°F)	Solid Flow Rate (lb/hr)	Gas Velocity (ft/sec)	Ceramic Filter Performance
800	3000	100	Sample system operated continuously for a period of 12 days (288 hours). Minimal wear to upstream side of filter.
800	10,000	100	Sample system required a filter change every 2 or 3 days. Minimal wear to upstream side of filter.

  The above tests were conducted without back-purging (with nitrogen) the filter. When the pressure drop across the filter reached its pre-determined maximum limit, the filter was changed.

- The filter tests in the freeboard area indicated that no pluggage occurred while sampling at any of the ports. No back-purge system was used and the filters showed no wear after extended periods of operation.

- The in-bed filter tests indicated that no pluggage occurred during a complete traverse across the bed. The original probe-filter assembly had to be back-purged with nitrogen every 15 or 20 minutes during each traverse. The nitrogen back-purge cleaning feature was available, but was not used during these latter tests. It appeared that the filters could be used indefinitely with no indications of wear.

Secondary Filter Performance

The secondary filter tests at the furnace gas outlet and freeboard sampling locations indicated the cartridge-type filter wrapped with two inches of kaowool insulation met all performance expectations. This filter served its initial purpose of protecting other components in the sample train in the case of a failure of the primary filter. It also replaced the fragile components and served to decrease the number of connection joints (possible air infiltration sources) in the sample train. The insulation contributed to the elimination of the cyclone oven which made the assembly less bulky and easier to handle. A combination of the insulated filter and controlled setting of the cooling water to the probe retained the gas temperature well above the dew point as the gas passed through the secondary filter enroute to the heated sample line. These tests were conducted in the most severe environment possible in both sampling locations. The secondary filter on the original in-bed

probe-filter assembly was not changed, thus no secondary filter tests were conducted at this sampling location.

Quartz Tube Versus Stainless Steel Tube Performance Data

The original probe-filter assemblies used at the furnace gas outlet and freeboard sample locations contained a quartz tube through which the gas sample was drawn. Due to the fragile nature of the quartz, it was desirable to eliminate the quartz tube and instead use a stainless steel tube. Some concern existed that a gas-stainless steel reaction -- more likely at high gas temperatures -- could possibly produce incorrect gas concentrations (particularly with NO_x). By adjusting the water cooling rate on the probe, the temperature of the gas along its path of contact with the stainless steel was reduced to a low, non-reactive temperature level (200° to 400°F).

The results of the quartz tube versus stainless steel tube tests, conducted at the furnace gas outlet and freeboard sample locations, are shown in the following performance tabulation:

Sample Location	Sample Tube Diameter/Material (Inch)	Source Gas Temperature (°F)	Sample Gas Temperature In Probe (°F)	Gas Concentration Comparisons
Furnace Outlet	5/8 SS	800	300 Max	Gas concentrations for O_2, CO_2, CO, SO_2, and NO_x were essentially identical for both the quartz and stainless steel tube sample probes.
Furnace Outlet	5/8 Quartz	800	300 Max	
Freeboard	5/8 SS	1700	280 - 305	Gas concentrations for O_2, CO_2, CO, SO_2, and NO_x were essentially identical for the quartz tube and the two (5/8" and 3/8" diameter) stainless steel tube sample probes.
Freeboard	3/8 SS	1700	325 - 400	
Freeboard	5/8 Quartz	1700	155 - 220	

SUMMARY

Gas sampling and analysis form a major portion of the performance evaluation of the 6' x 6' AFBC facility. The analysis requires measuring the concentration of six different gases at three sample locations -- in-bed, freeboard, and furnace gas outlet. Sample flow rates of 6 to 10 liters per minute are needed for analyzing these gases.

Accurate sampling and analysis from the high-temperature - high velocity, dust-laden environment of the fluidized bed unit requires the use of a system that includes certain special equipment. An "efficient particulate filter" is needed to clean the large-volume gas samples removed from the adverse environment of the 6' x 6' unit. A ceramic filter -- constructed of inert material, self-cleaning, having minimum pressure drop, and able to withstand high temperatures and abrasive wear -- served as the primary particulate filter in our final design.

A cartridge-type secondary filter eliminated the glassware and decreased connection joints, while serving its main function of protecting the remaining sample system components in the case of a failure of the primary (ceramic) filter. Eliminating the quartz tube has produced a design that includes no fragile (glassware or quartz) components.

The modifications have been combined to produce a refined gas sampling system that can be used at sample locations of interest in fluidized beds. It has been used for collecting and for accurately analyzing gas data over extended test periods for a multiple number of planned test conditions. These results have played a major role in the evaluation of the AFBC performance. The refined gas sampling system -- developed for the 6' x 6' fluidized bed application -- is recommended as a reliable system for fluidized bed units.

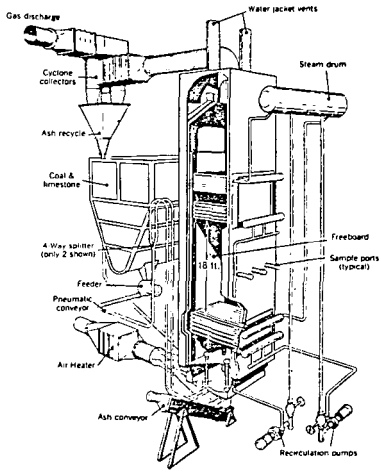

Figure 1 6' x 6' Fluidized Bed Combustion Facility

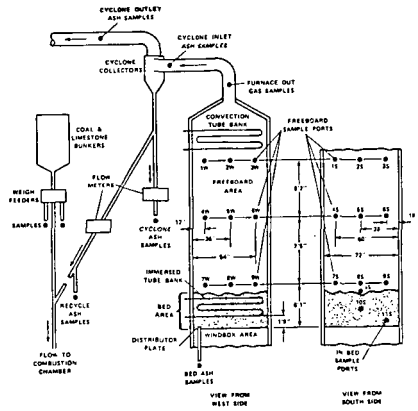

Figure 2 Relative Sample Locations for the 6' x 6' AFBC Facility

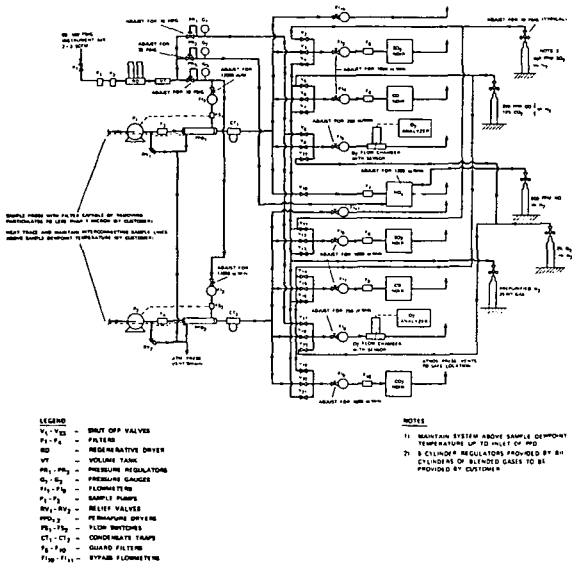

Figure 3 Complete 6' x 6' AFBC Facility Sampling System

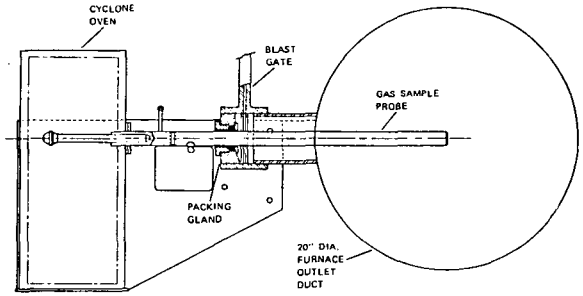

Figure 4 Furnace Outlet Gas Sampling Probe Installation

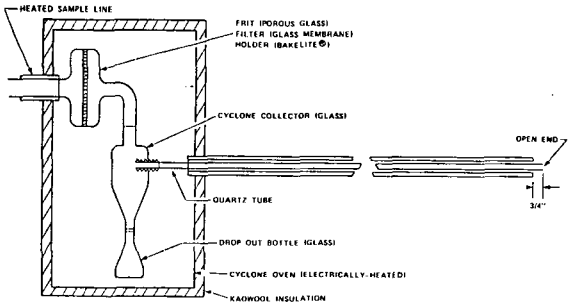

Figure 5 Original Furnace Outlet Gas Probe-Filter Assembly

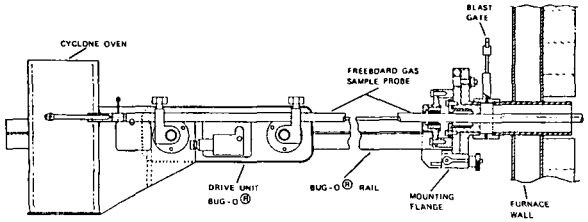

Figure 6 Freeboard Gas Sampling Probe Installation

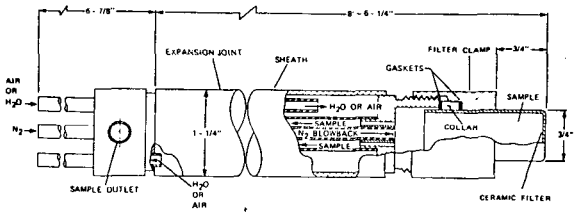

Figure 8 Original In-Bed Sampling Probe

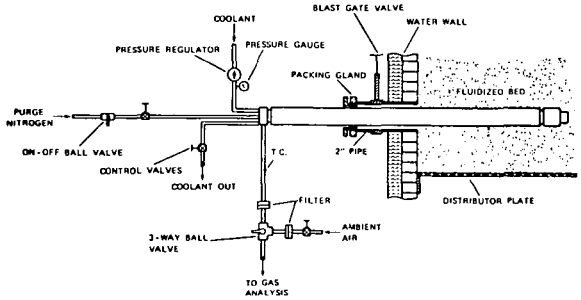

Figure 7 In-Bed Gas Sampling Probe Installation

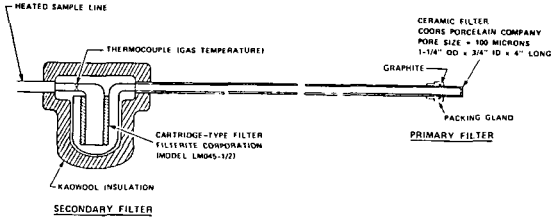

Figure 9 Modified Furnace Gas Outlet Probe-Filter Assembly

The Influence of Varying Operational Parameters on Both the Combustion Efficiency in and the Emission of Pollutants from Fluidized Bed Plants [1)]

by: Dr. H. Münzner, Dr. H.-D. Schilling VDI, Essen

Bergbau-Forschung GmbH, P.O. Box 13 01 40, 4300 Essen 13, Fed.Rep. of Germany

1. Methods and Apparatus

Our method of determining the influence of different operational conditions on fluidized bed plants consists in a stepwise alteration of one single operational parameter while maintaining the others as constant as possible (1). It is well known that this is easiest on a laboratory scale, whereas with increasing plant size the procedure becomes more and more onerous. If beyond operational parameters also the design concept and the size of a plant are varied, one obtains useful hints how to generalize and scale-up the results achieved.

Present findings were obtained using several types of laboratory equipment with thermal performances between 2 and 20 kW as well as from a semi-technical plant of 300 kW. Figure 1 is a schematic drawing of the shapes and dimensions of fluidized bed reactors used. Apparatus no. I is a tube reactor of 6 cm diameter and 60 cm height on top of which has been arranged a freeboard of approx. 35 cm hight and 10 cm diameter. Apparatus no. II is a tube reactor of 6 cm diameter and about 120 cm high. Here the ash is retained by an integrated inertial separator. Apparatus no. III represents a two-stage secondary air reactor with the following dimensions:

lower section:	6 cm diameter, 60 cm high,
upper section:	10 cm diameter, 80 cm high,

integrating an inertial separator. Unit no. IV is a pressurized reactor allowing combustion pressures up to 10 bar. Its reaction tube has a diameter of 6 cm and a height of 1 m, and incorporates an inertial separator. An early version of the pressurized reactor, operated at 4.5 bar, was of a similar shape and size as apparatus no. I. The reactor space provided by the semi-technical plant, finally, has a cross-section of 40 by 80 cm, a height of approx. 1 m, with a freeboard of 80 by 80 cm cross-section and approx. 2 m height.

The coal is fed pneumatically, along with all of the combustion air, to the electrically pre-heated laboratory units, whereas in the semi-technical plant coal is fed with a small fraction of the total air from one side into the fluidized bed. The atmospheric laboratory units, due to their high surface-to-volume ratio, are equipped with a heat insulation allowing to maintain a combustion temperature as high as approx. 950 °C. The pressurized unit, however, requires a variable heat exchanger for thermal discharge since in this case the heat release rate is higher by a factor of 10. As to the atmospheric semi-technical unit, it also needs heat exchangers which are immersed in the fluidized bed.

---

1) The present project has been sponsored by the Federal Ministry of Research and Technology (project no. ET 1024 B)

With regard to the similarity particularly of the laboratory equipment to bigger plants, one had to compromise on this. On the one hand a contact time between gas and solids comparable to that of a bigger fluidized bed plant had to be attained which requires an adequate height of the fluidized bed. On the other hand the thermal performance was to be kept low, i.e. within the limits of a laboratory unit. As a compromise between these requirements resulted an elongated reactor shape which, seen under the aspect of flow mechanics, due to its high length/diameter ratio can at first view not be compared with a bigger plant since it tends to aggregative fluidization and pulsations. In order to be able to use these easy to be handled reactors and to obtain reliable results nonetheless, elongated wire spirals were introduced in the reactor spaces. This helped to avoid the formation of big bubbles and strong pulsations and to bring about a more particulative fluidization (2).

An essential design difference of the laboratory units consists in the substitution of the enlarged cross-section of the free board by an inertial separator. The objective of this constructional modification is to determine the functionality and need of such a high-volume free-board.

2. Results

The results were obtained from an evaluation of analysis on the feed materials, flue gases, ash, and from the material balance of throughputs.

Figure 2 is a schematic summary of the variations of the main operational parameters, including their range and direction of variation as well as relevant standard values plus qualitative effects on: specific heat release rate, C-loss, CO-, SO_2-, and NO_x-concentrations in the flue gas.

Depending on the slope and inflexion of the arrow indicating the direction of parameter variations of a given component, such variation has a stronger or weaker influence on throughput and emission; a horizontal arrow stands for invariance in respect of the independent parameter. The specific heat release rate, expressed as MW/m^2, goes up along with both increasing fluidizing velocity and pressure, i.e. along with those parameters determing the throughput of air and also of coal. The performance drops along with rising excess air, i.e. in a situation where an increasing proportion of the air throughput is no longer utilized. The other parameters, however, hardly exert any influence. The dependence of the specific heat release rate on the apparatus design, therefore, is negligible and will be -- with an excess of air $\lambda \approx 1.3$ (5 % O_2 in the flue gas) -- approx. 1.2 to 1.5 MW/m^2. This correspondends to the values which in the meantime have been observed also at demonstration plants (3). Most of the arrow constellations revealing a sizeable influence are backed by measuring data plotted on diagrams, a selection of which is given hereunder.

2.1. C-Loss and CO Emissions

The C-loss is a critical factor for the economics of fluidized bed plants, whereas keeping the CO content in the flue gas within admissible limits generally does not pose any problems. As can be taken from figure 2, the two data sets are of a striking parallelity. The reason for this is that the more CO will be generated at reduced temperatures within the local and thermal transition zone between reactor zone and flue gas duct, the more carbon passes through this transitional zone as char carry over. Tars and volatile hydrocarbons were not observed. On being introduced into the hot ash of the fluidized bed, the coal will be dispersed immediately and exposed to the excess air whose oxygen reacts first with the volatile matter.

Diminishing C-loss along with pressure rise is related to an increased O_2 concentration, whereas diminishing C-loss along with rising temperature is attributed to higher reaction velocity. Increasing fluidizing velocities reduce the residence time of the coal in the reactor and, thus, cause higher C-losses. If one found a means of extending this residence time -- be it by appropriate plant design or/and by coal preparation -- the specific heat release rate could be improved proportionately to the fluidizing velocity.

A longer residence time of the coal by means of increased bed height will diminish C-losses, too.

C-loss may be influenced also by coal preparation measures. As shown on figure 3, the C-loss will, when fueling closely sized coal fractions, pass through a maximum as soon as the particle diameter approches the elutriation cut point. Coarse coal grains will remain in the bed up to the moment where they are burnt down to a size allowing their elutriation or preventing them from being recycled by the inertial separators. With sufficiently small fractions (coal dust) the reaction time is apparently shorter than the residence time in the reactor space so that the coal particles are almost completely burnt up. As far as industrial plants are concerned, the logical conclusion from this is to separate coal dust from the coarser fractions and blow the dust pneumatically into the fluidized bed from below, in order to allow a maximum residence time of the dust and avoid erosion in the feed ducts, whereas the coarse fractions, being introduced from above, are allowed sufficient time to spread over the bed while being burnt up. In this case it can be taken from the diagrams, e.g. figure 3, where the preparation cut points for each specific plant are viz. which granular fraction should be separated and/or further comminuted.

Examination of the carbon carry-over by means of screening for its size distribution does not yield accurate results since char aggregations will disintegrate. The results of figure 3 are, however, reconfirmed by this approximative evaluation. Moreover it can be verified from fly ash separation in two subsequent cyclones that the fine dust from the second cyclone is very low in carbon, whereas the "coarse dust" of the first one will always contain the bulk of the unburnt carbon.

Apart from the determinable and adjustable operational parameters, C-loss is also a function of the specific plant parameters. Measuring data can best be reproduced in laboratory equipment. When doing so, one observes other and so far not measurable operational conditions which bear on the results. Among these have to be considered the size distribution of the fluidized bed ash particles which changes during operation, or changing fluidity and cohesive properties of the bed ash when adding various gradations of limestone.

A comparison of the C-loss measured in reactor no. 1 with that of the semi-technical plant V (figure 5) -- the cross-section of the free-board has been enlarged in both units -- shows good coincidence. It should be borne in mind, however, that here varying particle gradations and bed heights compensate each other in a way not clearly identified so far.

As was expected, there are differences also in the C-losses for the different laboratory reactor types since inertial separators are not optimized. This is not disturbing as long as feed materials, viz. types of limestone and coal, are compared by measurements in one reactor only. As soon as it comes to scaling up results, however, one has to know about the reasons and influences of specific operational conditions.

2.2. SO_2 Emission and NO_x Emission

Statements on the pressure-dependences of SO_2 and NO_x emissions (figure 2) are so far based on measurements of two pressure levels (1.1 and 4.5 bar). When moving to the higher pressure SO_2 and NO_x emissions will be diminished by more than 50 %. The qualitative evaluations of early orientation tests on the new pressure apparatus IV where measurements at several pressures between 1 and 10 bar are to be carried out, do reconfirm this improvement.

Figure 10 shows the strong dependence of SO_2 emissions on the size of the limestone (at one fixed Ca/S ratio). It is, however, striking and so far not explainable (figure 5) that varying sizes of one same type of limestone lead to different temperature dependencies. Dolomite shows a similar behaviour (figure 6). When adding coarse material, SO_2 emission will slump with rising temperatures, whereas the opposite happens when material of small grain sizes is added.

Excess air (figure 7) has a weak influence on SO_2 emission, while its effect on NO_x emission is strong since in this case the oxygen concentration is decisive for the conversion of that proportion of fuel-nitrogen which is transformed to NO. (Due to the low temperatures in a fluidized bed plant, 10 to 30 % only of the fuel-nitrogen and no nitrogen from the air is converted to NO.) A lack of O_2 favours rather the competing reaction which yields molecular N_2.

The dependencies of SO_2 and NO_x emissions are mostly active in opposite directions (figure 2). A good insight into the conditions leading to NO formation is possible with the secondary air reactor. When plotting the NO_x emission against different incremental primary air/secondary air ratios, a NO_x minimum is met at a distribution of primary versus secondary air of 50 : 50. This effect was most obvious in reactor no. 1 (4), whereas it was less pronounced in the bigger reactor no. III where, at the same time, the maximum emission values were reduced. The lowest values were observed in the semi-technical reactor (figure 8); they were in the same order of magnitude which prevails also in other larger plants. From this may be concluded that the NO emissions measured in the laboratory reactors are atypically high. The formation of coarse bubbles in big reactors bring about a certain distribution of O_2 as high as into the upper bed zones. Such by-pass effect can be compared with the feed of secondary air. Consequently, the way how oxygen acts on the coal and, possibly, the removal of reducing volatile coal components are main determinants for NO_x emission. Emissions from the semi-technical plant may be considered typical for NO_x emissions from full-scale plants (figure 8), with 1 g NO_2/kWh being approximately equivalent to 200 ppm NO. So, even though the numerical values obtained from laboratory measurements are exaggerated in respect of their absolute value and do not allow any generalization as to NO_x emissions, one may nonetheless derive certain tendencies (e.g. dependence on excess air) which can be scaled-up to bigger plants.

Typical figures for SO_2 emissions cannot be identified since the main influential factor on SO_2 emission will be the amount of limestone added. SO_2 emission, therefore, is only to a small extent typical for a given plant. Figure 9 shows a dependence on the limestone/sulphur mole ratio when feeding different coals high in ash and with varying sulphur contents, but adding one same limestone at pressures of 1.1 and 4.5 bar. It is the spontaneous desulphurization of coals rather than their sulphur content which brings about the difference in SO_2 emissions, -- emissions which on a laboratory scale can be reduced to zero. To find out the limestone with optimum sulphur capturing efficiency (i.e. accomplishing the desired desulphurization with admixture of the possible minimum sorbent amount), some three dozens of limestomes of different geological formations, deposits, and trade marks were tested (5). Geologically young and porous limestones appear to be best suited.

Similar differences as to sulphur capturing properties can be observed also among dolomites. In this case only the $CaCO_3$ proportion acts as a sulphur capturing medium. Optimum desulphurization is a function of the size of limestone particles (6). As can be seen on figure 10, limestone dust $<$ 10 µm is an excellent sulphur capturing medium due to its big surface and thorough distribution in the fluidized bed and this notwithstanding its short residence time. Unlike this, the residence time of coarser fractions with a more reduced total surface is too short as to allow adequate reaction with SO_2. Those particles, however, which are not elutriated and, therefore, accumulate in the fluidized bed on having been fed continuously to it, provide again a very good sulphur capturing efficiency. As soon as particle sizes increase further, however, this beneficial effect is lost again. Such loss of efficiency along with increasing particle size is less pronounced with dolomite due to the fact that here the percentage of magnesium carbonate enlarges the pore volume during combustion and this volume does not get blocked by sulphate formation.

2.3. Halogen Emission

At the temperatures prevailing in a fluidized bed plant, fluorides and chlorides as mineral components of the coal are released as HF and HCl also in the presence of lime. Early results have shown that on condition of low temperatures in the flue gas duct, HF and HCl can be bound by lime-containing fluidized bed flue ash. Trials on an optimization of these bonding conditions have been initiated.

3. Summary

The experiments on a laboratory scale and in the semi-technical plant have releaved a considerable development potential for fluidized bed plants (7) as well as the fact that tests on a smaller scale may sizeable contribute to this end so that results from the different plants are appreciated as being complementary to each other.

References

(1) Münzner, Heinrich: Einfluß von Betriebsparametern auf die Schadstoff-Emissionen einer Wirbelschichtfeuerung im Labormaßstab. VDI-Bericht Nr.266 (1977), S. 79

(2) Schilling, Hans-Dieter, Münzner, Heinrich, Bonn, Bernhard, Wiegand, Detlef: Die Wirbelschichtfeuerung und ihre Bedeutung für den Wärmemarkt. Erdöl und Kohle 9 (1981).

(3) Langhoff, Josef, Kirschke, Hermann, Lemiesz, D., Marnitz, Chr.: Die Wirbelschichtanlage Flingern - Aufbau und erste Betriebserfahrungen. Vortrag VGB-Fachtagung "Kohlefeuerung 1980" Essen, 21.11.1980, und Mannheim, 5.12.1980.

(4) Bonn, Bernhard, Münzner, Heinrich: Schadstoffemissionen bei Wirbelschichtfeuerungen. VDI-Bericht Nr. 322 (1978), S. 103/109

(5) Münzner, Heinrich: Schwefelbindung an Kalk in Wirbelschichtfeuerungen. VDI-Bericht Nr. 345 (1979), S. 319/322

(6) Münzner, Heinrich, Bonn, Bernhard: Sulfur Capturing Effectivity of Limestones and Dolomites in Fluidized Bed Combustion. Vortrag 6th Int'l Conference on Fluidized Bed Combustion, April 1980, Atlanta, USA.

(7) Schilling, Hans-Dieter: Technischer Stand und wirtschaftliche Chancen der Wirbelschichtfeuerung zur Strom- und Wärmeerzeugung aus Kohle. Chem.-Ing.-Techn. 51 (1979), Nr. 3, S. 184/191.

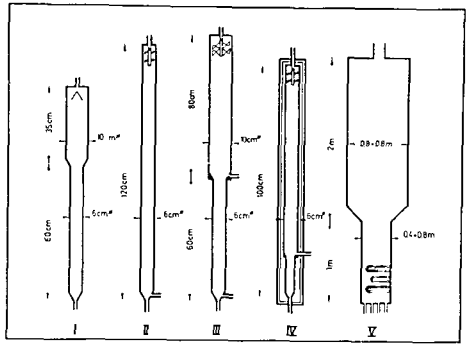

Figure 1: Shapes of the fluidized bed reactors used

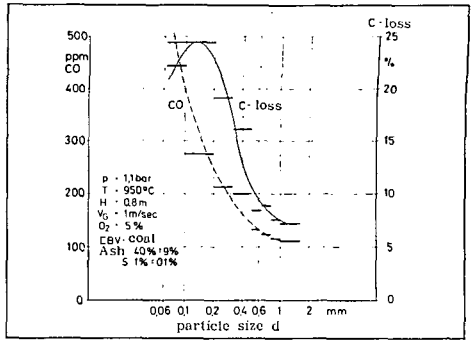

Figure 3: C-loss and CO emission as a function of grain size

Parameter Range (Standard)	MW/m²	%C-Loss	gCO/kWh	gSO_2/kWh	gNO_x/kWh
Pressure 1 - 4,5 bar (1,1 bar)	↗	↘	↘	↘	↘
Temperature 750 - 950°C (850°C)	→	↘	↘	⌣	↗
Excess air in the 0,5 - 12% O_2 flue gas (5%)	↘	↘	→	→	↗
Fluidizing velocity 0,3 - 1,5 m/sec (1m/sec)	↗	↗	→	↗	↘
Bed height (fluidized) 0,2 - 1,2 m (0,8m)	→	↘	↘	↘	→
Secondary air 0 - 66 % (0)	→	⌣	↘	↘	⌣
Ca/S 0 - 3 mol/mol (1)	→	→	→	↘	→
Particle size of coal 0 - 2 mm (0,1-1mm)	→	⌒	↘	→	→
Particle size of limestone 0 - 2 mm (0-0,1mm)	→	→	→	⌒	⌣

Figure 2: Variation of operational parameters in fluidized bed reactors on laboratory scale

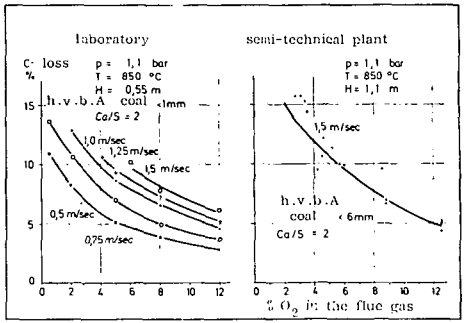

Figure 4: Carbon loss as a function of excess air

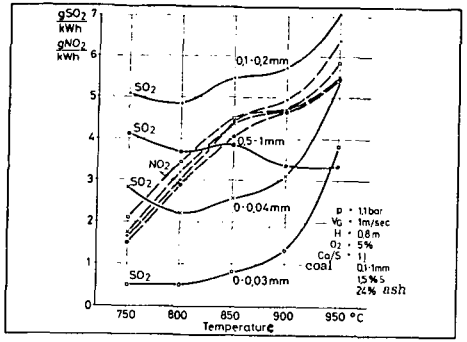

Figure 5: SO_2 and NO_x emissions for different sorbent sizes of cretaceous limestone as a function of temperature

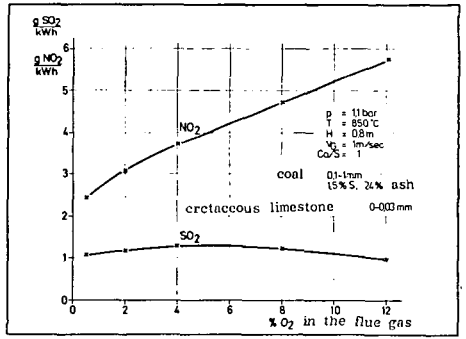

Figure 7: SO_2 and NO_x emissions as a function of excess air

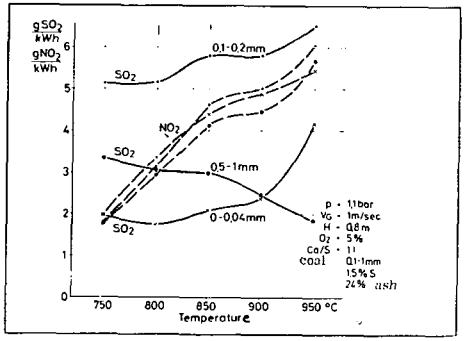

Figure 6: SO_2 and NO_x emissions for various sorbent sizes of dolomite as a function of temperature

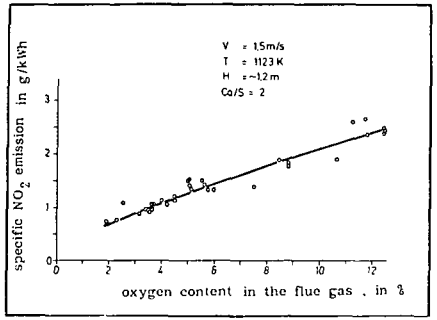

Figure 8: Specific NO_2 emission from the semi-technical fluidized bed plant

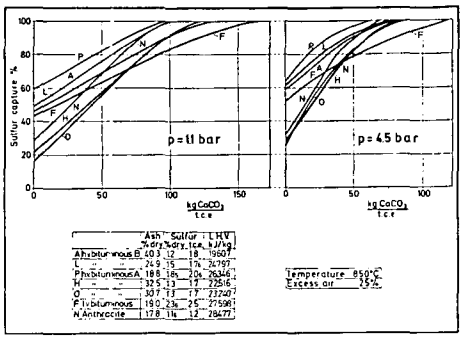

Figure 9: Sulphur capture as a function of the amount of limestone added per t.c.e.

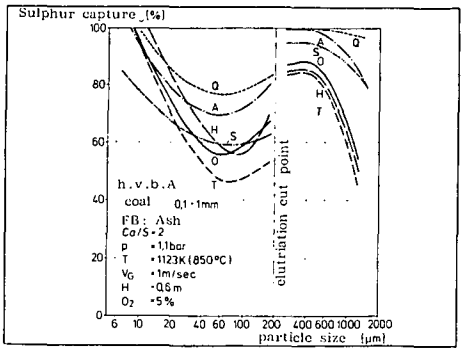

Figure 10: Sulphur capture as a function of limestone particle size

SULFUR CAPTURE AND NITROGEN OXIDE REDUCTION ON THE 6' X 6' ATMOSPHERIC FLUIDIZED BED COMBUSTION TEST FACILITY

T. M. Modrak and J. T. Tang

The Babcock & Wilcox Company
Research and Development Division
Alliance Research Center
Alliance, Ohio 44601

C. J. Aulisio

Electric Power Research Institute
Palo Alto, California 94304

INTRODUCTION

Atmospheric fluidized bed combustion (AFBC) is being developed as a cost-effective, low-polluting method of direct coal utilization for electric power generation. An earlier state-of-the-art assessment (EPRI Final Report FP-308) concluded that the existing AFBC data base was inadequate for the design of utility-scale units -- that is, the available data were limited in scope, and since they had been derived mainly from laboratory-scale equipment, it was doubtful whether they could be applied to the design of utility boilers. The need for a large, well- instrumented facility capable of long-term testing was clearly indicated.

As a result, a 6-foot x 6-foot (6' x 6') AFBC Development Facility was built at The Babcock & Wilcox Research Center in Alliance, Ohio. A complete description of the facility design details are contained in EPRI Final Report CS-1688.

PROJECT RESULTS

Construction of the 6' x 6' facility was completed in October 1977. Following a 5-month startup and debugging phase, the first test series was begun in April 1978. Since then, approximately 2000 hours of testing per year have been logged at the facility. The facility has demonstrated the capability for long-term, steady-state operation, with tests typically lasting from 300 to 500 hours. The AFBC unit is large enough to result in gas-solid residence times for the various zones of the combustor that are typical of those expected for utility-scale units. A wide range of conditions can be tested at the facility. Also, the computerized data acquisition system has been shown to provide accurate, comprehensive documentation of the test results.

SUMMARY OF TESTS

Testing completed as of July 1981, along with a short description of each test series is summarized below:

Test Series	Date	Hours Firing Coal	Comments
1	May 1978	277	Initial characterization
2	June 1978	248	Long duration test to characterize performance
3	August 1978	278	Recycle
4	September 1978	241	Coal size variation, temperature variation
5	November 1978	204	Limestone and coal size variation, temperature variation
6	February 1979	406	New distributor plate, Battelle emission testing - Pittsburgh #8 coal
7	March 1979	171	Single coal feed point - 36 ft^2, bed depth variation, coal and limestone variation
8	May 1979	427	Recycle; underbed single point, temperature variation
9	June 1979	298	Coal size variation, temperature variation
10	July 1979	194	Recycle; overbed and 4-point underbed with coal and limestone
11	August 1979	96	Pulverized coal
12	December 1979	265	New in-bed tube bundle, new baghouse, GCA emission testing - Pittsburgh #8 coal
13	January 1980	318	Recycle; underbed single point, limestone size variation, excess transport air
14	February 1980	277	Recycle; underbed single point and overbed, slumped bed heat transfer study test
15	April 1980	382	Fuller Kinyon pump characterization, baghouse recycle, lignite test
16	May 1980	147	Turndown (slumping) test
17	June 1980	344	Limestone size variation, center recycle
18	July 1980	326	New distributor plate, 4 ft/sec characterization test
19	October 1980	365	4 ft/sec testing, recycle
20	December 1980	344	Feed nozzle design testing, 8 ft/sec
21	January 1981	170	Feed nozzle design testing, 8 ft/sec
22	March 1981	380	NO_x reduction tests
23	June 1981	485	12 ft/sec testing

Significant data were generated in the areas of fly ash recycle, coal particle size, limestone particle size, 5 ft/sec, 8 ft/sec, and 12 ft/sec fluidizing velocity operation, combustion of lignite, and nitrogen oxide reduction. Testing continued to emphasize fly ash recycle as a means of improving combustion efficiency and sulfur capture. In addition to center underbed recycle, overbed recycle with gravity and pneumatic feed as well as baghouse ash recycle configurations were tested. Recycled fly ash testing continued to result in combustion efficiencies on the order of 98%. The highly successful lignite test resulted in combustion efficiencies approaching 99%. The lignite test proved the capability of a fluidized bed combustor (FBC) to combust fuels which can be troublesome. One test was devoted to testing feed nozzles designed to prevent feedline pluggage during slumping. A power outage simulation test was also carried out. The test was designed to determine minimum flow rates through the in-bed tube bundle required to prevent tube overheating during a power outage. Results indicated that tube overheating may be prevented with minimal design considerations.

Tests were also conducted to evaluate bed height reduction as a means of load control in an AFBC facility. These variable bed height tests provided the data needed to design an automatic load control system that will be installed on the 6' x 6' in 1982.

One series of tests was devoted to two-stage combustion, i.e., allowing a portion of the forced draft air to bypass the bed, recombining with the fluidizing gas in the freeboard region. These tests, aimed at NO_x reduction, are discussed later in this paper.

A significant amount of data covering AFBC have been generated on the 6' x 6'. Some of these data have been summarized and discussed in various technical papers

and, therefore, will not be repeated in this paper. Sulfur capture and nitrogen oxide reduction are the two items that will be discussed in the following sections.

SULFUR CAPTURE

No Fly Ash Recycle

Numerous non-recycle tests have been run on the 6' x 6' AFBC at a fluidizing velocity near 8 ft/sec. This large data bank provides information enabling a better understanding of sulfur capture with various operating parameters. A plot of percent sulfur removal versus calcium-to-sulfur ratio showed that sulfur removal is a strong function of the amount of fresh limestone feed (Figure 1). However, the data is quite scattered, indicating that other factors such as particle size, entrainment loss, bed temperature, coal combustion, and sulfur release level may also have a significant influence on sulfur capture efficiency. To more thoroughly investigate these factors, data from a narrow range of Ca/S ratio were subjected to analysis. Sulfur removal was shown to be related to the size of limestone being fed into the unit (Figure 2). The plot indicates that larger limestone feed sizes result in a decreased ability to remove sulfur, a trend which is most pronounced at higher Ca/S values. This suggests that the effect of the fresh limestone feed is predominant since the spent bed lime utilization in these tests range between 23% and 40%. Consequently, the rate of sulfur capture for the bed material is many times smaller than for freshly calcined limestone at all size ranges that exist within the FBC unit. For average limestone feed sizes below 1200 microns (weight-mass average), a significant drop in sulfur retention occurred as a result of high elutriation loss of limestone feed. Further analyses were performed by restricting both the Ca/S ratio and limestone feed size. The data scatter, evident in Figure 2, was found to be related to the effects of bed particle size, extent of bed lime utilization, and bed voidage (Figures 3 and 4). Sulfur removal decreases with:

1. An increase in bed particle size for a narrow range of bed lime utilization (0.30 - 0.33).

2. High bed lime utilization.

3. Higher bed voidage.

Also, spent bed lime utilization is related to both residence time and Ca/S feed ratio, reaching 35% with a residence time of 13 hours at a Ca/S of 2.5 (Figure 5).

Increasing the fluidizing velocity to 12 ft/sec resulted in lower sulfur capture, as shown in Table 1. We believe the causes of this reduction to be: 1) higher elutriation of limestone from the bed, and 2) increased freeboard combustion of coal and its volatile matter. The table shows that carbon and limestone carryover losses were 12% and 55%, respectively. These are about 50% and 34% more than the loss at 8 ft/sec, respectively.

Reducing fluidizing velocity to about 5 ft/sec generally resulted in an improvement in sulfur capture. This was due to smaller limestone feed size and lower elutriation loss (Table 2). In addition, spent bed lime utilization reached 40%.

Table 1

Comparison of Sulfur Capture Efficiency and NO_x Emissions for 8 ft/sec and 12 ft/sec Fluidizing Velocities Under Similar Conditions of: 1) Non-Recycle and 2) Ca/S : 2.4 - 2.8

Item	Fluidizing Velocity 8 ft/sec	Fluidizing Velocity 12 ft/sec
$\%SO_2$ Capture	78.5	46.2
Combustion Efficiency - %	92	88
NO_x - ppm	285	158
CO - ppm	106	1696
Bed Voidage	0.62	0.72
Limestone Feed Size (weight mean average)	2908μ	984μ
Spent Bed Size (weight mean average)	2337μ	1279μ
Spent Bed Lime Utilization - %	31	29
Elutriation of Available Lime Per Limestone Feed	41	55
Elutriation of Carbon Per Carbon Feed From Coal	8	12

Table 2

Comparison of Sulfur Capture Efficiency and NO_x Emissions for 5 ft/sec and 8 ft/sec Fluidizing Velocities Under Similar Conditions of: 1) Non-Recycle and 2) Ca/S : 1.6 - 1.8

Item	Fluidizing Velocity 5 ft/sec	Fluidizing Velocity 8 ft/sec
$\%SO_2$ Capture	58	54
Combustion Efficiency - %	94	92
Spent Bed Lime Utilization - %	40	33
% Carbon in Carryover Per Carbon Feed	7.7	9.6
NO_x - lb/MKb	0.22	0.39
Bed Voidage	0.55	0.66
Limestone Feed Size (weight mean average)	815μ	1200μ
Spent Bed Size (weight mean average)	923μ	824μ
CO in Stack Gas - ppm	173	126

Fly Ash Recycle

Operation of the 6' x 6' since May 1979 has emphasized fly ash recycle operation. Recycle has generally improved sulfur capture as shown on Figure 6. Generally speaking, for a given test condition and a narrow range of limestone to coal feed rate, one expects the total available mole of calcium to each mole of coal sulfur to increase as the recycle ratio (recycle rate/coal rate) increases (Figure 7a). The total available calcium oxide is defined as the combined calcium oxide from the limestone feed and the unreacted calcium oxide in the recycle stream; it is designated as $(CaO)_R + (CaO)_L$. The available calcium oxide can change by varying the limestone feed rate or the recycle ratio.

Figure 7b is a plot of the expected trend of the effect of recycle ratio on sulfur capture for two different Ca/S feed ratios. Ideally, for a given set of conditions, sulfur capture should increase with increasing recycle ratio due to an increase in the total available calcium-to-sulfur ratio. The rate of increase in sulfur capture (slope of the curve) will gradually diminish as the reactivity of the recycled lime decreases due to higher calcium utilization. As the curve begins to level off, a point is reached beyond which any further increase in the recycle rate has little benefit on sulfur capture. The recycle ratio for which this occurs should increase as:

1. The particle size of the recycle stream decreases since the smaller lime size results in better reactivity at higher calcium utilization levels.

2. The limestone feed rate increases (higher Ca/S ratio). High limestone feed rates generally result in greater elutriation of freshly calcined limestone. This helps to increase the reactivity of the recycle stream, thus promoting SO_2 capture.

3. The reactivity of recycled lime improves. The improvement can be achieved through either grinding or partial hydration.

The recycle analysis was conducted by first choosing all tests with and without recycle. The data were compared by restricting the Ca/S feed ratios to narrow ranges. Figure 8 shows that the available calcium-to-sulfur ratio, $[(CaO)_L + (CaO)_R]/S$, increases dramatically as the recycle-to-feed ratio is increased. Figure 9 shows the effect of recycle on sulfur capture at three Ca/S ratios. Figure 10 shows that 90% sulfur capture can be obtained at a recycle-to-coal ratio of about 1.3 with a Ca/S feed ratio of 2.5 - 2.9.

By extrapolation, a recycle ratio of about 4 - 5 will be required at a Ca/S feed ratio of 1.5 - 2.0.

Figure 11 shows sulfur capture as a function of fluidizing velocity for both the non-recycle and recycle operating conditions. Note the significant decrease (approximately 20 percentage points) in sulfur capture for the high fluidizing velocity (12 ft/sec) tests as compared to the 8 ft/sec tests. The major reason for this reduction is attributed to the increased freeboard combustion. This, of course, causes more sulfur release in the freeboard.

NITROGEN OXIDE REDUCTION

Single-Stage Combustion

The mechanism of NO_x formation in an AFBC unit is extremely complicated, involving the formation and destruction of NO_x through various chemical reactions that occur in the bed and in the freeboard. Thus, it depends upon the coal devolatization rate and its volatile content, excess air, bed temperature, CO and SO_2 concentrations in the emulsion phase, and the bed hydrodynamics.

At 8 ft/sec fluidizing velocity, NO_x emissions were generally in the 300 ppm - 400 ppm range. However at 5 ft/sec, the NO_x was found to change with the Ca/S feed ratio as shown on Figure 12. It is believed that this effect is a result of the following mechanisms as noted by Exxon [1]:

$$CaO + SO_2 \longrightarrow CaSO_3$$

$$CaSO_3 + 2NO \longrightarrow CaSO_3\ (NO)_2$$

$$CaSO_3\ (NO)_2 \longrightarrow CaSO_4 + N_2 + 1/2\ O_2$$

As pointed out by Exxon's study, the above mechanisms could only occur in the presence of sulfated lime and with a deficit of oxygen. The rate of NO_x reduction was found to be directly proportional to concentrations of both NO and SO_2 in the gas phase as follows:

$$\frac{1}{W} \quad \frac{d(NO)}{dt} = K\ (NO)^n\ \ (SO_2)^m$$

Where W is the bed weight and n has a value between 0.53 - 0.67 for the temperature range of 1400° - 1600°F. The proposed mechanisms qualitatively appear to provide an explanation to our observation for the low velocity tests. It is generally believed that the relatively smaller spent bed size in these tests resulted in a fast bubbling bed with the relative excess gas velocity $(U - U_{mf})/U_{mf}$, ranging from 8 to 12. Consequently, a majority of oxygen along with air would bypass the emulsion phase via the bubble phase, resulting in a reducing atmosphere in the emulsion phase that enhanced the NO_x reduction through the mechanisms proposed by Exxon.

The NO_x emission data taken from non-recycle tests with Ohio #6 coal and 8 ft/sec fluidizing velocity appeared related to the operating excess air. However, the results were quite scattered, especially at levels below 25% excess air (Figure 13). These scattered NO_x data were found to be associated strongly to the extent of the reducing condition in AFBC where the NO_x level was usually below 200 ppm if the CO concentration in the stack gas exceeded 200 ppm (Figure 14). Further analysis of the data indicated that the high NO_x emissions were associated closely with the bed voidage, where the effect became more pronounced at higher oxidizing conditions (Figure 15).

The effect of carbon loading in the freeboard on NO_x reduction was quite evident at a high fluidizing velocity (12 ft/sec) and a recycle ratio of 1.0 - 1.4. A reduction of NO_x emissions from 0.43 to 0.23 lb/million Btu was observed (Figure 16) as carbon loading increased from 14% to 19%.

Two-Stage Combustion

Staged combustion has been proposed as a means of reducing NO_x from an AFBC unit. Several investigators [2, 3, and 4] have conducted tests to quantify the NO_x reduction with staging. However, these tests were run in small units and only overall effects were measured. To aid in evaluating the effect of staging on NO_x reduction and performance variables, the 6' x 6' AFBC facility was modified to allow air injection at an elevation of 96 inches above the distributor plate. This elevation was chosen based on data from previous tests [2]. Two injection ports -- on opposite walls of the unit -- were installed with valves to control flow and an orifice to measure flow.

Tests were conducted at the conditions listed in Table 3.

Table 3

Summary of Operating Conditions and Measured Performance Variables

Condition/Variable	Test					
	1a	1b	2a	2b	3a	3b
Bed Temp, °F	1564	1546	1544	1547	1512	1553
Bed Height - inches	51.8	52.5	50.0	49.8	47.7	47.8
Superficial Velocity - ft/sec	7.3	8.0	7.1	7.1	6.5	7.0
Coal Feed - lb/hr	1887	2042	2070	2064	2192	2228
Ca/S Ratio	2.7	2.7	2.1	2.5	2.7	2.5
Recycle - lb/hr	2560	2680	2800	2920	2280	2280
In-Bed Air Flow - lb/hr	19500	21500	19400	19400	18300	18900
Overbed Air Flow - lb/hr	0	0	2300	2300	4850	4670
Flue Gas						
O_2 - %	2.9	2.9	2.9	3.1	2.9	2.7
SO_2 - ppm	170	265	562	527	461	458
CO - ppm	208	185	247	203	248	248
NO_x - ppm	416	372	195	175	88	117
Sulfur Capture - %	91.6	86.1	77.1	75.1	74.9	76.1
Combustion Efficiency - %	98.1	97.4	96.8	96.7	96.0	96.1

At each test condition, gas traverses were made at six heights along the centerline of the unit. The gas concentration profiles obtained in-bed (16 inches above the distributor plate) are shown on Figure 17. Note the peak in O_2 and the drop in other gas concentrations near the 36-inch insertion depth. This is probably due to the recycle stream which is being injected with transport air at the 36-inch distance. Profiles above the bed (in the freeboard) were considerably more uniform.

An integrated average of the profile obtained at each elevation was calculated. This average was then plotted versus distance above the distributor plate for CO, SO_2, and NO_x as shown on Figures 18, 19, and 20. There are several points that are readily apparent from these figures.

- With zero overbed air, there is a significant reaction occurring in the freeboard, e.g., reduction of CO and NO_x.
- Two-stage combustion produces the expected trends in reducing NO_x while increasing SO_2 and CO in the bed.

- The addition of air at the 96-inch elevation allows further combustion to occur in the freeboard, thus increasing SO_2 and reducing CO and NO_x.

- Reducing the NO_x level in the bed reduces NO_x throughout the process.

- Gas concentrations measured at the 240-inch elevation, using the freeboard sampling system and analysers, agree remarkably well with the similar, but completely separate, furnace outlet system and analysers.

Figure 21 shows a plot of the furnace outlet NO_x and SO_2 gas concentrations at the three test conditions -- 0%, 10%, and 20% overbed air.

CONCLUDING REMARKS

Twenty-three test series have been completed on the 6' x 6' AFBC Development Facility covering over 7100 hours of operation. Data obtained thus far have clearly shown that fly ash recycle can improve combustion efficiency to the level needed for commercial operation. Recycle also improves sorbent utilization, thus reducing the limestone needed for sulfur capture. Measured NO_x emission levels from the 6' x 6' AFBC unit are well below current EPA limits. However, two-stage combustion tests have shown that NO_x can be reduced to about 0.15 lb/million Btu. Additional work needs to be completed to improve sulfur capture and combustion efficiency with two-stage combustion.

Information obtained thus far has allowed a significant improvement in our understanding of the AFBC process and should prove useful to researchers in this field. Further, design of prototype hardware and other equipment developed and tested on the 6' x 6' should prove useful for commercial design.

REFERENCES

[1] G. A. Hammons and A. Skoop, "NO_x Formation and Control in Fluidized Bed Coal Combustion Processes," presented at the ASME Winter Annual Meeting, Washington, DC; November 28 - December 2, 1971.

[2] J. Tatebayashi, Y. Okada, K. Yano, and S. Ikeda, "Simultaneous NO_x and SO_2 Emission Reduction With Fluidized Bed Combustion", 6th International Conference on Fluidized Bed Combustion, Atlanta, GA; April 1980.

[3] T. Hirama, M. Tomita, T. Adachi, and M. Horio, "An Experimental Study for Low NO_x Fluidized-Bed Combustor Development 2 - Performance of Two Stage Fluidized-Bed Combustion"; EST, Vol. 14, No. 88; pp. 960-965.

[4] T. E. Taylor, "NO_x Control Through Staged Combustion in Fluidized Bed Combustion Systems", 6th International Conference on Fluidized Bed Combustion, Atlanta, GA; April 1980.

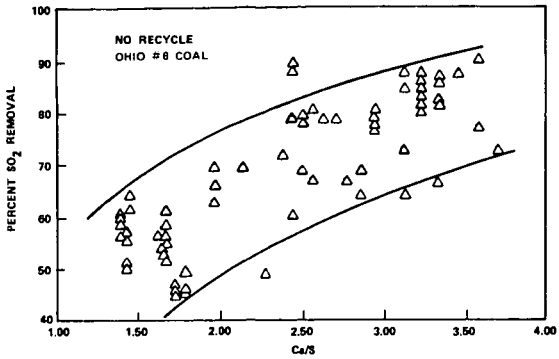

Figure 1 Sulfur Capture as a Function of Calcium/Sulfur (Ca/S) Feed Ratio

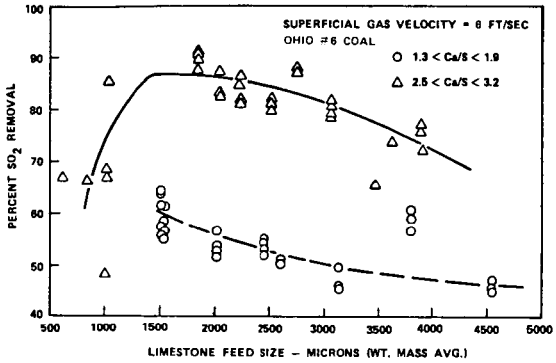

Figure 2 Sulfur Capture as a Function of Limestone Feed Size

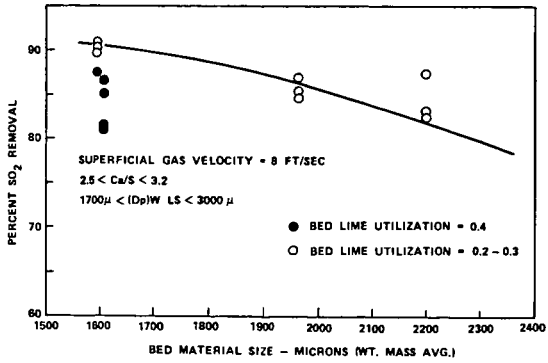

Figure 3 Sulfur Capture as a Function of Bed Particle Size

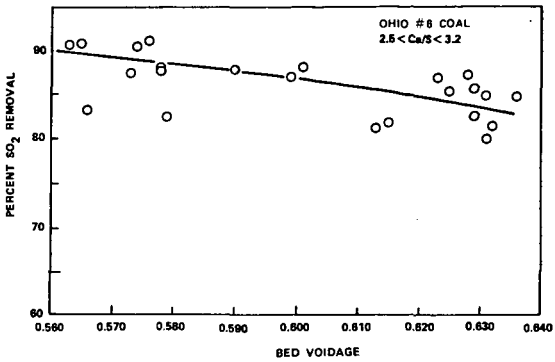

Figure 4 Sulfur Capture as a Function of Bed Voidage

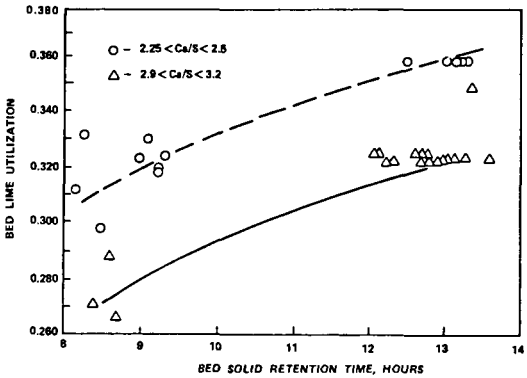

Figure 5 Bed Lime Utilization as a Function of Retention Time

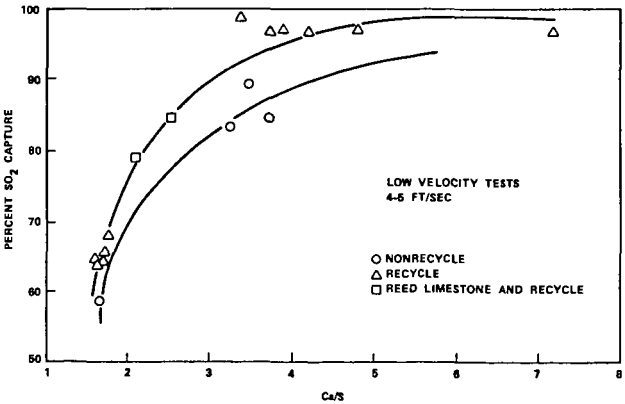

Figure 6 Sulfur Capture as a Function of Calcium to Sulfur Feed Ratio

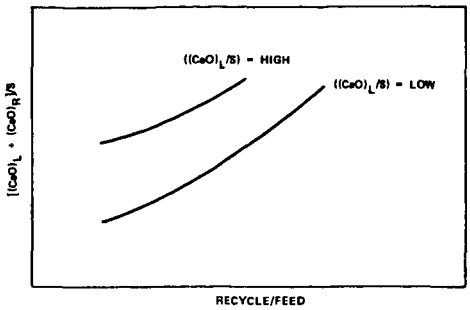

(a) TOTAL AVAILABLE CALCIUM PER SULFUR RATIO VERSUS RECYCLE RATIO

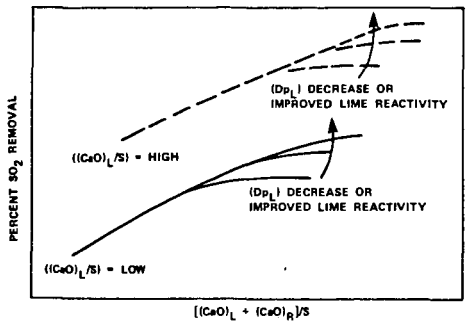

(b) EFFECTS OF THE TOTAL AVAILABLE CALCIUM PER SULFUR RATIO ON PERCENT SO_2 CAPTURED

Figure 7 Effect of Recycle on Sulfur Capture

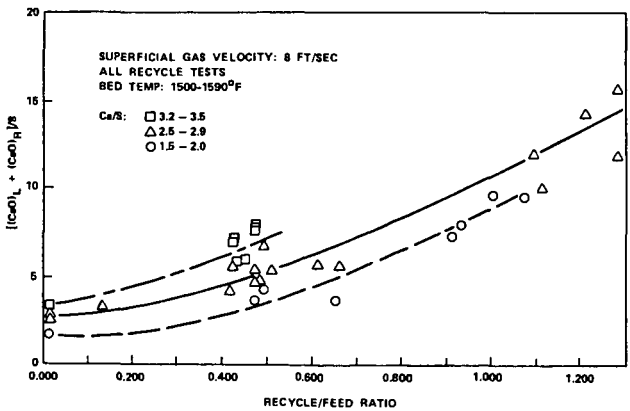

Figure 8 Effect of Recycle on the Available Calcium to Sulfur Ratio

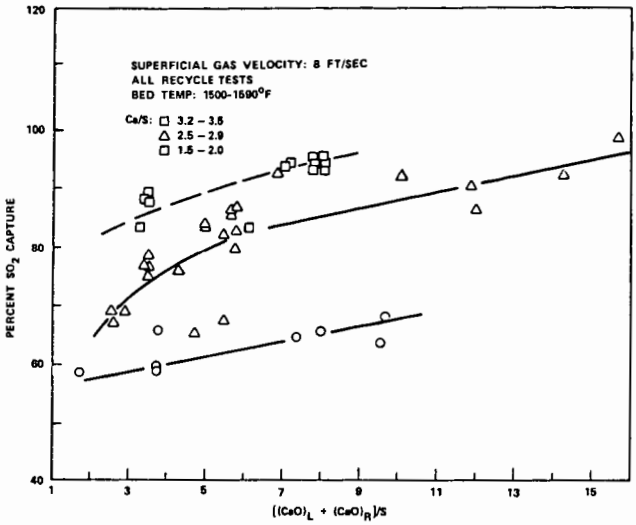

Figure 9 Effect of Available Calcium to Sulfur (Recycle) on Sulfur Capture

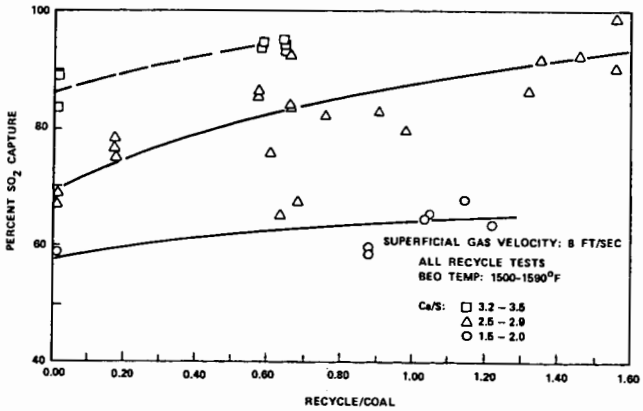

Figure 10 Sulfur Capture as a Function of Recycle Ratio

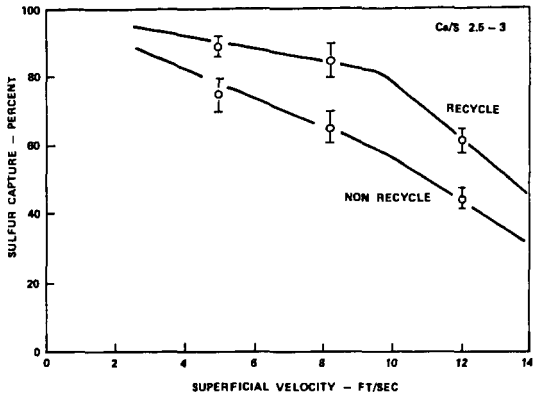

Figure 11 Sulfur Capture as a Function of Fluidizing Velocity

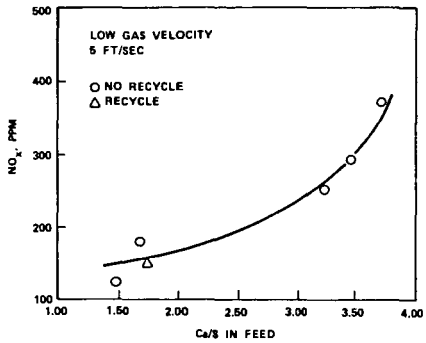

Figure 12 Nitrogen Oxide as a Function of Ca/S Feed Ratio

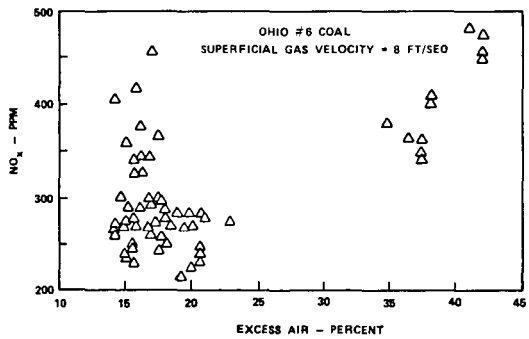

Figure 13 Nitrogen Oxide as a Function of Excess Air

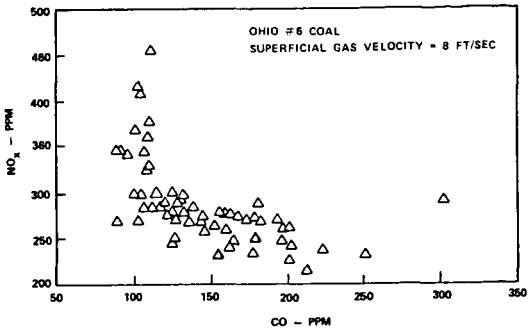

Figure 14 Nitrogen Oxide as a Function of Carbon Monoxide

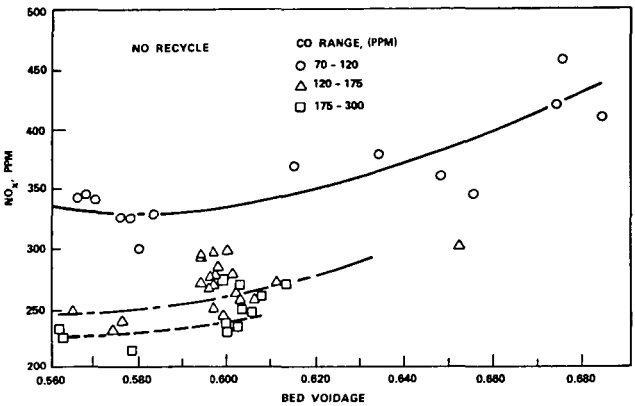

Figure 15 Nitrogen Oxide as a Function of Bed Voidage

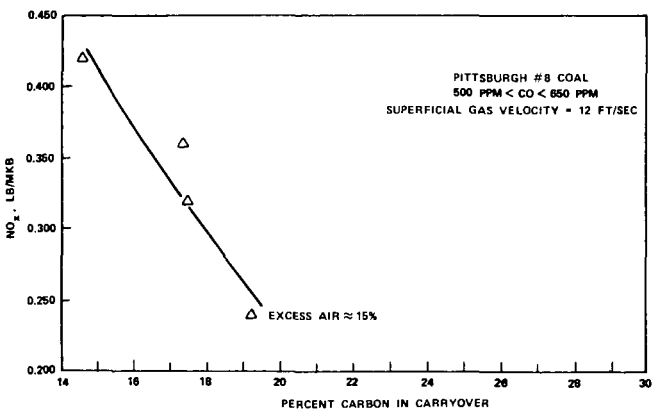

Figure 16 Nitrogen Oxide as a Function of Carbon Loading

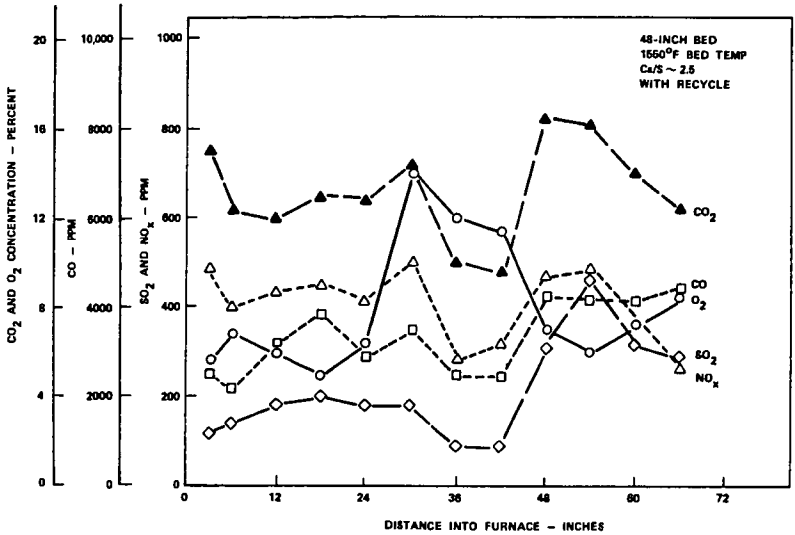

Figure 17 Gas Concentration Profiles – In-Bed (16 Inches Above the Distributor Plate)

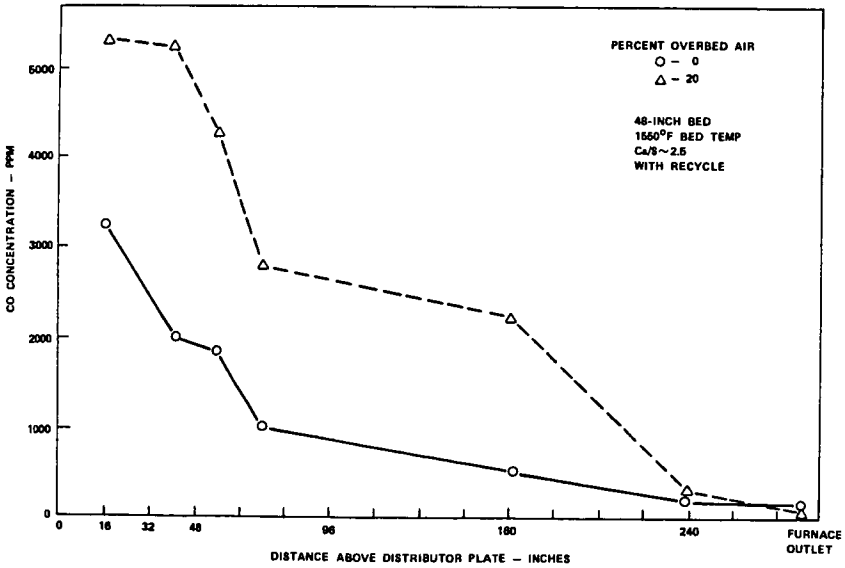

Figure 18 Average Carbon Monoxide Concentration as a Function of Distance Above the Distributor Plate

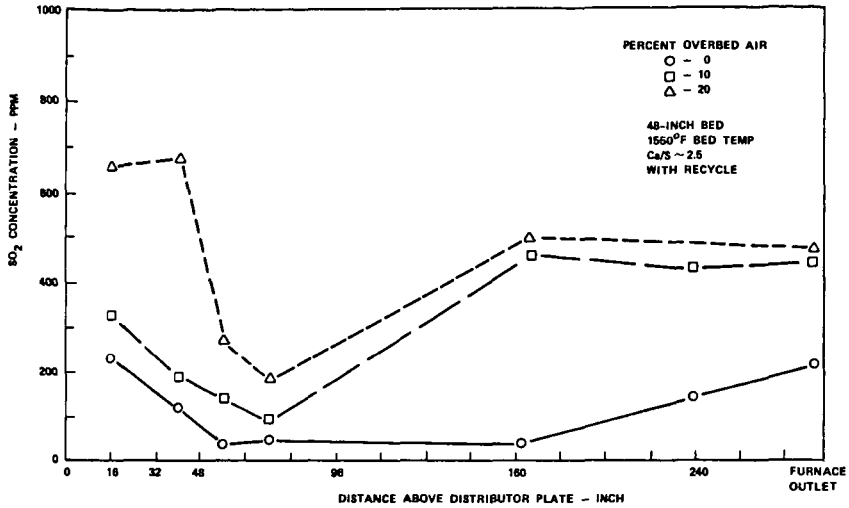

Figure 19 Average Sulfur Dioxide Concentration as a Function of Distance Above the Distributor Plate

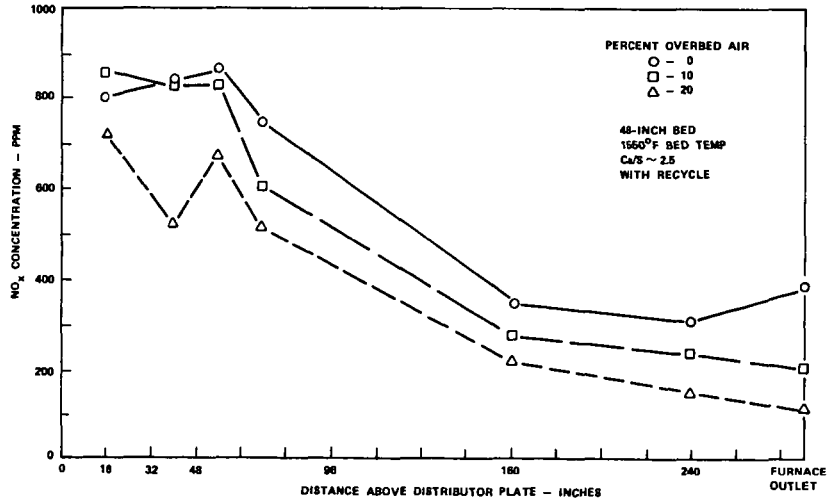

Figure 20 Average Nitrogen Oxide Concentration as a Function of Distance Above the Distributor Plate

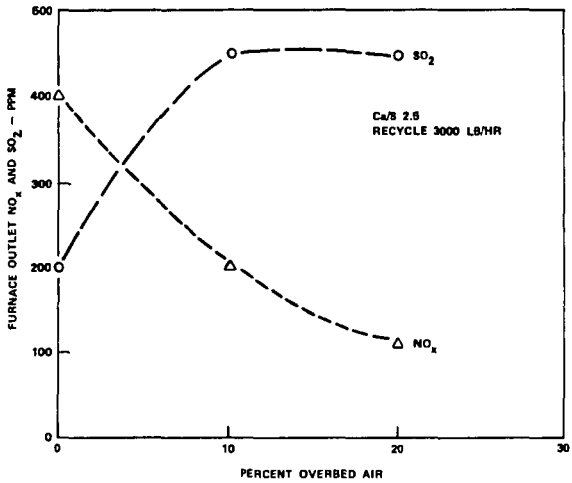

Figure 21 Measured Outlet Gas Concentrations at Various Percent Overbed Air Rates

PARTICLE ENTRAINMENT AND NITRIC OXIDE REDUCTION IN THE FREEBOARD OF A FLUIDIZED COAL COMBUSTOR

P. M. Walsh, T. Z. Chaung, A. Dutta, J. M. Beér, and A. F. Sarofim

The Energy Laboratory and Department of Chemical Engineering
Massachusetts Institute of Technology, Cambridge, MA 02139

1.0 Introduction

Economic design of fluidized bed combustors requires a combination of fluidizing velocities and particle sizes which result in the unavoidable carry over of bed solids, coal char particles and unburned gaseous combustion products into the freeboard. Depending upon the design parameters, the last 5 to 10% of the combustibles will burn, and also significant reduction of SO_2 and NO_x will take place, in the freeboard of the fluidized combustor - between the top of the bed and the first row of the convective tube bank. Despite the importance of the freeboard to the efficient and clean operation of fluidized combustors, until recently little attention was paid to the understanding of the freeboard reactions. Pereira et al (1) and Gibbs et al (2) have determined chemical species concentration variation along the height of a 30 x 30 cm cross section fluidized bed and found that significant reduction of NO_x takes place above the bed surface. Okada et al (3) have shown that the fine sorbent particles entrained into the freeboard will enhance sulfur capture and that the entrained char particles will react with NO_x and reduce its emission.

In earlier designs of fluidized combustors the problem posed by unacceptably high carbon carry over at fluidizing velocities was resolved by the introduction of the fines precipitated from the flue gas into a "carbon burn-up cell," an uncooled fluidized bed operating at lower fluidizing velocity. In recent designs, instead of the carbon burn-up cell the method of fines reinjection into the fluidized bed is adopted. In order to achieve operational simplicity the fines in most practical applications are added to fresh feed and returned into the bed. Fines reinjection significantly increases the fine particle concentration in the bed and in the freeboard with the consequence of further enhancing the rate of the heterogeneous reactions of char oxidation, and SO_2 and NO_x reduction in the freeboard.

Modeling of the freeboard reactions has been hindered by incomplete understanding of the processes which govern the entrainment of bed solid particles into the freeboard and the mixing of these solids with the reactant gas. Entrainment models by George and Grace (4), Wen and Chen (5) and Horio et al (6) have fulfilled an important role in predicting solids concentration in the freeboard, but due to a dearth of experimental information on entrainment rate as a function of the fluidization parameters of the bed, these models could not be rigorously tested and developed to the stage where they can be incorporated into FBC combustion models with sufficient confidence.

The importance of the NO-carbon reaction for the reduction of NO in fluidized combustion of coal was recognized and experimentally demonstrated by Pereira and Beér (7), Gibbs et al (2) and Furusawa et al (8). Kinetic parameters for this reaction were reported by Beér et al (9), Kunii et al (10) and Chan (11). Chan also found that the NO-char reaction can be significantly enhanced in the presence of CO.

The problems of predicting NO_x reduction in the freeboard with sufficient accuracy are not only due to uncertainties about solids entrainment but also about the relative significance that CO, coal volatiles, volatile nitrogen compounds, or hydrocarbons may have on NO reduction (Sarofim and Beér (12), Yamazaki et al (13)). In recent experimental studies at MIT detailed hydrocarbon species concentration measurements by Walsh et al (14) have shown that CO and hydrocarbon concentrations are high in the "splash zone" immediately above the bed so that their effect on NO reduc-

tion in this region may not be neglected.

In the following, model calculations are presented of the reduction of NO along the height of the freeboard of the MIT 0.6 x 0.6m cross section, 4.5m high fluidized bed. In the model a new approach is made to the prediction of solids concentration in the freeboard (Chaung (15)) which is assisted by measurement data on the descending flux of particles. The NO reduction along the height above the bed is then predicted from experimental information on the carbon content of bed solids and the chemical kinetic rate equation on the NO-carbon reaction. The NO reductions so calculated are then compared with measurement data obtained burning bituminous and subbituminous coals in the 0.6 x 0.6m MIT experimental facility.

2.0 Particle Entrainment in the Freeboard

2.1 Theory of Particle Entrainment

A model has been developed for the entrainment of particles from the bed into the freeboard of a fluidized combustor. Its purpose is to provide an estimate of the total surface area of each solid species participating in chemical reactions in this zone. The model is based on the following assumptions:

1. Bursting bubbles eject particles into the freeboard.
2. Particle-particle interactions and wall effects are negligible.
3. The changes in mass and size of a particle due to chemical reaction while in the freeboard are negligible.
4. Interaction of the concentration, temperature, and velocity gradients surrounding each particle are negligible.
5. The initial velocities of particles ejected from the bed are given by a semi-empirical log-normal distribution having a geometric mean value proportional to bubble velocity.
6. Bubble diameters are determined by the heat exchanger tube spacing and the bubble growth model of Mori and Wen (16).

The sequence of steps in the calculation of particle density (mass of particles/volume of gas-particle mixture) is as follows:

1. The initial velocities of the particles leaving the bed are given by the assumed semi-empirical velocity distribution.
2. The initial flux of particles is proportional to the flux of bubbles at the top of the bed. The proportionality factor is determined by equating the kinetic energies of a bursting bubble and the particles which it ejects.
3. The equation of motion is solved for each particle size and initial velocity to determine the particle trajectories.
4. The particle density is determined from the ratios of flux to velocity at each freeboard height. Total density is found by summing the contributions from all sizes and initial velocities.

Because solution of the equations of motion is time-consuming, for the required range of particle sizes and initial velocities, a simplified version of the model was also developed, based on two additional assumptions:

7. Small particles, having $u_t < u_g$, ascend with constant velocity, $v_s = u_g - u_t$.
8. The drag force is negligible on particles having $u_t \geq u_g$.

Chaung (15) showed that the deviation of the particle fluxes predicted by the two models was less than the uncertainty in the results of the more accurate version.

Detailed description of the essential features of the model.

Initial velocity distribution.

A log-normal fit was made to the distribution of ejected particle velocities given by George and Grace (4), which were normalized to the absolute bubble velocities, u_b. The geometric mean particle velocity and standard deviation were 2.44 u_b and 1.43, respectively.

Initial Entrainment

George and Grace (4), defined a parameter, ξ, equal to the ratio of the volumes of entrained particles and bursting bubble. Using this parameter, the entrainment from the bed surface, E_o, can be expressed by

$$E_o = \xi\, Q_b\, \rho_s\, (1 - \varepsilon_{mf})\, A_t \qquad 1)$$

Glicksman et al. (17) give an expression for the visible bubble flow rate, Q_b, valid over the entire range of bubble volume fraction, δ:

$$Q_b = u_g - (1 - \delta)\, [1 - \frac{\pi}{2}\, \ell n\, (1 - \frac{6\delta}{\pi})]\, u_{mf} \qquad 2)$$

The total energy of a bubble before bursting can be equated to the energy of the entrained particles and the energy of the bubble through-flow gas. The total energy of the bubble is given by the following equation from Davidson and Harrison (18):

$$(KE)_b = \frac{1}{2}\, m_{b,eff}\, u_b^2 \qquad 3)$$

where the effective mass of a bubble, $m_{b,eff}$, is

$$m_{b,eff} = \frac{1}{2}\, (\text{mass of fluid displaced by the bubble})$$

$$= \frac{2}{3}\, \pi\, R_b^{\,3}\, \rho_s\, (1 - \varepsilon_{mf}) \qquad 4)$$

Defining the root-mean-square velocity of the entrained particles as $\overline{v}_p$, the total kinetic energy of the particles ejected by the bubble is:

$$(KE)_p = \frac{1}{2}\, [\, \xi\, (\frac{4}{3}\, \pi R_b^{\,3})\, \rho_s\, (1 - \varepsilon_{mf})]\, \overline{v}_p^{\,2} \qquad 5)$$

where

$$\overline{v}_p = [\, \int v_p^{\,2}\, dm_p]^{1/2} \qquad 6)$$

The kinetic energy of bubble through-flow gas is approximately

$$(KE)_g \cong \frac{1}{2}\, [\rho_g\, \pi R_b^{\,2}\, (u_b + 3\, u_{mf})]\, (u_b + 3\, u_{mf})^2 \qquad 7)$$

which is usually negligible compared with $(KE)_b$ or $(KE)_p$. The energy balance, i.e., $(KE)_b \cong (KE)_p$, then yields:

$$\xi = \frac{u_b^2}{2\, \overline{v}_p^{\,2}} \qquad 8)$$

The absolute bubble velocity is given by

$$u_b = u_g - u_{mf} + 0.711\ (gd_b)^{1/2} \qquad 9)$$

The bubble diameter, d_b, at the top of the bed was found by assuming an initial diameter equal to the spacing of the heat exchanger tubes, and growth according the correlation of Mori and Wen (16). This result; with the assumed velocity distribution; Equations 2, 8, and 9; and the appropriate experimental data; provide the information required to calculate the initial entrainment by Equation 1. No assumption has been made regarding the source of the particles, i.e., whether they originate in the wake or the cap of a bubble.

Calculation of Particle Density

The equation of motion of the particles is

$$v_s \frac{dv_s}{dZ} = -\frac{3}{4} \frac{C_d\ \rho_g\ (v_s - u_g)\ |v_s - u_g|}{\rho_s\ d_p} - \frac{(\rho_s - \rho_g)\ g}{\rho_s} \qquad 10)$$

Subject to the initial conditions

$$v_s = v_{si} \text{ at } Z = 0 \qquad 11)$$

The total particle density profile along the freeboard is obtained by summing up all the contributions from ascending and descending particles.

$$\rho\ (Z) = \sum_i \sum_j \left[\frac{E_u\ (d_{pi}, v_{sj})}{v_u\ (d_{pi}, v_{sj})} + \frac{E_d\ (d_{pi}, v_{sj})}{v_d\ (d_{pi}, v_{sj})} \right] \qquad 12)$$

(all particle sizes)

(all initial velocities)

The calculation must be repeated 6000 times if the particle size range is divided into 60 intervals and the initial velocity distribution into 100 intervals.

The Simplified Model

In order to save computer time the model was simplified by neglecting the transient term for small particles and the drag force term for large particles. The equations to be solved are then:

for small particles ($u_t < u_g$), $v_s = u_g - u_t$

for large particles ($u_t \geq u_g$), 13)

$$v_s \frac{d\ v_s}{dZ} = -\frac{(\rho_s - \rho_g)\ g}{\rho_s} \qquad 14)$$

which gives for ascending particles

$$v_s = \sqrt{v_{si}^2 - 2gZ\ \frac{(\rho_s - \rho_g)}{\rho_s}} \qquad 15)$$

The maximum height that a large particle can reach is

$$H_{max} = \frac{\rho_s v_{si}^2}{2(\rho_s - \rho_g)g} \qquad 16)$$

for descending particles

$$v_s = -\sqrt{2g\left(\frac{\rho_s-\rho_g}{\rho_s}\right)(H_{max}-Z)} = -\sqrt{v_{si}^2 - 2gZ\left(\frac{\rho_s-\rho_g}{\rho_s}\right)} \qquad 17)$$

Since the local velocity of each particle is obtained in analytic form, the particle density (Equation 12) yields a closed-form expression:

$$\rho(Z) = \int_{\sqrt{2gZ\,(\rho_s-\rho_g)/\rho_s}}^{\sqrt{2gH_f\,(\rho_s-\rho_g)/\rho_s}} \frac{2(1-y_c)E_o\, f_i dv_{si}}{\sqrt{v_{si}^2-2gZ(\rho_s-\rho_g)/\rho_s}} \quad \text{(Large particles not elutriacted)}$$

$$+ \int_{\sqrt{2gH_f(\rho_s-\rho_g)/\rho_s}}^{v_{si_{max}}} \frac{(1-y_c)E_o f_i dv_{si}}{\sqrt{v_{si}^2-2gZ(\rho_s-\rho_g)/\rho_s}} \quad \text{(Large particles elutriated)}$$

$$+ \int_{y_c^o = \sum_{u_t(d_{p_i}) < u_g} y(d_{p_i})}^{d_{pc}} \frac{y(dp)\cdot E_o \cdot d(dp)}{u_g\, u_t\,(dp)} \quad \text{(Small particles elutriated)} \qquad 18)$$

where y_c^o is the mass fraction of small particles, and $f_i\, d\, v_{si}$ represents the mass fraction of particles with an initial velocity between v_{si} and $v_{si} + dv_{si}$. The validity of the approximations made in simplifying the model was by comparing the particle densities predicted by the two methods (15). The maximum discrepancy was less than 30% of the particle density predicted by the complete model, and the significant features of both density profiles were identical. The results presented here were obtained using the simpler model.

Two Component Bed

When the bed has two components, for example a very small amount of char mixed with stone, the initial entrainment of the char, $E_{o,c}$, is a small fraction of the total initial entrainment. Assuming that the stratification factor is equal to the density ratio,

$$E_{o,c} = E_o \frac{\rho_s}{\rho_{s,c}} Y_c \qquad 19)$$

The initial velocity distribution for the char is the same as for the stone, and the total char density is found by the same procedure as before, with $\rho_{s,c}$ in place of ρ_s.

2.2 Measurement of Particle Flux

All of the experiments described in the present paper were performed using the M.I.T. Fluidized Combustion Research Facility, shown in Figure 1. The combustor has a square cross-section, 0.6m x 0.6m; and the total height, from distributor to exit, of 4.5m. The system has been described in detail elsewhere, (Beér et al. (19)).

The mass fluxes of particles extrained in the freeboard at various superficial gas velocities were measured in cold flow experiments by collecting descending particles at various heights above the surface of the fluidized bed. The particle collecting probe was formed by cutting a 22mm diameter tube in half lengthwise, so that it collects particles falling through a narrow strip on one axis of the combustor cross-section. The bed was a single batch of Ottawa Silica Sand (grade #20). Fine particles were removed from the bed by running for several hours prior to making the flux measurements. During the experiments attrition of bed particles and elutriation of fines were negligible. The bed particle size distribution had a geometric mean diameter of 720 $\pm$ 50μm, determined by sieve analysis. The bed was fluidized by ambient air supplied by forced-draft blowers. Bed temperature (average) and pressure (at the distributor) were 330 $\pm$ 20 K and 111 $\pm$ 2 kPa, respectively. Superficial velocity, calculated for the empty tude at the bed temperature and pressure, was varied from 0.42 to 0.86 m/s. The superficial velocity and void fraction at minimum fluidization were 0.37 $\pm$ 0.02 m/s and 0.50 $\pm$ 0.01, respectively.

For measurement of the particle fluxes, the probes were first oriented upside-down until steady bed conditions were achieved at the desired superficial velocity; the probe was then rotated to face upward and collect the descending particles. After sufficient time had elapsed to approximately half-fill the probe, the blowers were stopped, and the particles removed and weighed. Sampling times varied from 1 minute to 10 hours, depending on height and superficial velocity. The method relies upon the assumption that the paths of particles in the vicinity of the probe, moving either upward or downward, are not significantly affected by the motion of the gas around the probe.

2.3 Comparison of the Measured and Predicted Particle Flow Rates

The complete set of experimental particle flow data were reported by Mayo (20). An exponential decay of the particle flow rate with height was observed, having a characteristic length which increased with increasing gas velocity.

Some representative data points are shown in Figure 2, together with the corresponding flow rates calculated using the entrainment model. The predicted profiles show a small region of approximately constant particles flow rate just above the bed, followed by an approximately exponential decay higher in the freeboard. The model thus displays a property analogous to the "splash zone" observed at the top of bubbling fluidized beds. Agreement between the calculated and experimental profiles is best for the intermediate gas velocities, with the predicted flow rates generally larger than the observed values.

The fluxes of ascending and descending particles, and the particle density for the case with gas velocity equal to 0.53 m/s, are shown in Figure 3. The model predicts a maximum in the density near the bed surface, where most of the large particles change direction and return to the bed. Ascending particle flux and density become constant at a height of about 2 m, where only small particles, moving at constant velocity equal to $u_g - u_t$, continue upward. This point is the so-called "transport disengaging height".

3.0 Nitric Oxide Reduction in the Freeboard

3.1 The Mechanism of Nitric Oxide Reduction

The model for NO reduction in the freeboard has been under development for some time. An earlier version, having a less complete description of particle entrainment, was employed by Beer et al (21) for the prediction of NO profiles. Destruction of NO in the freeboard is assumed to occur by heterogeneous reactions with the coal char entrained from the bed:

$$NO + C = CO + 1/2\ N_2$$

$$2\ NO + C = CO_2 + N_2$$

Plug flow is assumed for the gas phase, and the char particle density is calculated using the model for particle entrainment described in Section 2, above. The rate of change of NO concentration with height is given by:

$$u_g \frac{dC_{NO}}{dZ} = - k\ A\ \rho_c(Z) C_{NO} \qquad 20)$$

where A is the specific surface area of char available for reaction, and ρ_c is the calculated char particle density. Rate coefficients in the temperature range of interest have been reported by Chan (11).

$$k = 5.95\ T \exp(- E_a/R_o T)\ m/s$$

$$E_a = 81.6 \times 10^6\ J/kmol$$

$$T \leq 1016\ K$$

and by Song (22):

$$k = 4.1 \times 10^3\ T \exp(- E_a/R_o T)\ m/s$$

$$E_a = 136.8 \times 10^6\ J/kmol$$

$$T > 1016\ K.$$

The surface area assumed for the subbituminous coal char was based on the CO_2-BET surface areas reported for lignite and brown coal chars by Guerin et al. (23), Smith and Tyler (24), and Ashu et al (25). These workers reported specific surface areas ranging from 5 to 7 x 10^5 m^2/kg for particle sizes from 89 to 2000 μm. A value of 6 x 10^5 m^2/kg was used in the present calculations. The surface area of the bituminous char was taken near the lower limit of the range reported by Smith (26): 1.5 x 10^5 m^2/kg. The char is treated as if all of its internal surface area were exposed to NO at the concentration and temperature found at the exterior of the particles (effectiveness factor of unity).

Nitric oxide profiles are found by integrating Equation 20, starting with the experimentally measured concentration at, or near, the surface of the bed.

3.2 Measurement of Gas Composition and Char Properties

Gas samples were withdrawn from the combustor through stainless steel probes. With the exception of the continuous sampling probe 4.1m above the distributor, all the probes were water cooled. Probes located in the bed were equipped with sintered quartz filters having pore sizes varying from 90 to 150 μm and sample openings 14.3 mm in diameter. Those located in the freeboard had quartz wool filters. The

accuracy of the reported axial positions of the probes is subject to an uncertainty of ± 40 mm; the probe tip locations relative to the centerline of the combustor varied from 50 to 170 mm. The gas sample continuously withdrawn at z = 4.1m passed through a KF 310 Heated Bypass Filter (Permapure Products, Oceanport, N.J.) to a heated line, and was dried by permeation distillation. This sample was analyzed using Beckman Model 865 non-dispersive IR analyzers for CO and CO_2, a thermoelectron Model 10 Chemiluminescent NO_x analyzer, and a Beckman Model 755 Paramagnetic oxygen analyzer. The total sample flow rate was about 10^{-4} m^3/s (NTP). The gas samples from the other probes were dried by permeation distillation, collected in 250 cm^3 bulbs for analysis on a HP 5830 A gas chromatograph. Hydrocarbons C_1 through C_3 were detected using flame ionization, and CO, CO_2, N_2, and O_2 by thermal conductivity. A thermoelectron Model 10 NO_x analyzer, was also used to measure the NO mole fraction in this sample. The flow rate was 2 to 20 x 10^{-6} m^3/s (NTP).

A gas sample withdrawn from the bed and mixed in a bulb is, in a simplified picture, a mixture of gases withdrawn from the emulsion and bubble phases. At typical operating conditions the composition is heavily biased toward the emulsion (Walsh et al (27)). In order to distinguish the NO contents of the emulsion and bubble phases, the length and diameter of the sample line to the NO analyzer were minimized so that a time-dependent NO mole fraction was observed. The measured NO mole fractions are shown in Figures 4-9, with bars indicating the maximum and minimum values recorded. An analysis by Pereira et al (28) concluded that, in the presence of excess air, NO is greater in the emulsion than in bubbles; and that under stoichiometric or sub-stoichiometric conditions the NO concentrations in the two phases are identical. To determine the mixed-mean NO mole fraction at the top of the bed, the average of the relative maxima observed in the time-dependent NO signal was assigned to the emulsion, and the average of the relative minima was assigned to the bubbles. The two averages were then weighted according to the relative flow rates of bubble and emulsion gas:

$$\bar{\bar{X}}_{NO} \simeq \bar{X}_{NO,max} \left[\frac{(1-\delta)u_{mf}}{u_g}\right] + \bar{X}_{NO,min} \left[1 - \frac{(1-\delta)u_{mf}}{u_g}\right] \qquad 21)$$

This weighted value is shown as a data point at the top of the bed in Figures 6-8; it is the initial value used when Equation 20 is integrated starting at Z=0.

Bed solid samples were withdrawn using a probe located 0.66m above the distributor. The probe was stainless steel, water cooled, and had a N_2 quench stream cocurrent with the sample. The outer and inner diameters of the probe were 44mm and 19mm, respectively. The extracted particles were separated from the gas stream in a water cooled cyclone and collected in a cooled vessel. The inert bed material was Ottawa silica sand. The coal char was separated from ash and sand particles collected in Runs C25-28 in order to determine the char particle size distribution. This was done by froth flotation. A representative sample of the bed solids was introduced into a flotation cell which contained a stirred kerosene-water emulsion together with 4-methyl-2-pentanol. The stirrer keeps the solids in suspension, breaks the kerosene into fine droplets, and disperses it uniformly. Nitrogen was introduced through a sintered stainless steel filter at the bottom of a cell, forming bubbles which adhere to the char particles and lift them up forming a froth, while the sand and ash particles were selectively depressed. The froth was collapsed in a filtering funnel and the char particles collected on the filter. The char was air dried for 24 hours and its size distribution determined using a Joyce Leobl "Magiscan" Image Analyzer. The size of each particle was defined as the diameter of the sphere with volume equal to the volume of the spheroid generated by rotation, about the major axis, of the ellipse defined by the length and breadth of the particle. An apparent char density, $\rho_{s,c}$, was determined from the calculated volume of the particles and the total mass of char; the results are given in Table 2. The char size distribution for Run C22 was found by sieving the bed sample and measuring the weight loss on ignition of each size fraction; in Run A14 the distribution was

assumed to be identical to that of the feed coal. The solid densities of the char in Runs A14 and C22 were estimated from published data.

Two coals were used in the present experiments: bituminous coal from the Arkwright mine in the Pittsburgh seam and subbituminous coal from the Colstrip mine in the Rosebud seam in Rosebud County, Montana. The composition of these coals is given in Table 1.

The size distribution of the fuel and bed particles were determined by sieve analysis. All of the size data for fuel, bed, and char particles were fit by log-normal distribution functions. The geometric means (mass basis) and standard deviation are listed in Table 2. The sizes were converted to a specific surface area basis for the computations. The fluidized combustor operating conditions and relevant experimental data are also listed in Table 2. The data from Runs A14 and C22 were first reported by Beer et al (19).

3.3 Comparison of the Measured and Predicted Nitric Oxide Profiles

The NO profiles predicted by the model are shown in Figures 4-9, together with the experimental data. When the calculation is started at the bed surface (solid line in Figures 4 and 5, dotted line in Figures 6-8) the agreement with experiment is good for Runs A14, C22, and C25; but very poor for Runs C26 and C28, in which there is a very rapid decrease in NO just above the bed, and a discrepancy of about 200 mole ppm between the predicted and observed NO mole fractions. There are not enough data to support a correlation of this behavior with operating conditions, however, it can be seen from the data in Table 2 that C26 and C28 have the lowest bed temperatures and lowest gas velocities. When calculation of the NO concentration for these two runs is started at the next higher data point, excellent agreement with experiment is obtained from that point upward (solid lines).

In Run C27 the combustor was operated using two-stage addition of the combustion air, with the secondary air injector located 1.7m from the distributor. The air/fuel ratio in the bed was sub-stoichiometric, giving very low NO near the top of the bed. The increase in NO mole fraction on addition of the secondary air indicates that some fuel nitrogen species, not detected in the NO mode of the NO_x analyzer, are present in the gas leaving the bed. When the calculation of the NO profile is begun after mixing of the secondary air, the mechanism of the char entrainment/NO-char reduction model is still consistent with the experimental data.

The predictions of the combined model for char entrainment and NO reduction are in good agreement with the observed NO profiles at distances above 0.5m from the bed, in the absence of staged air addition; the model is not able to account for the rapid reduction of NO observed in the splash zone under some conditions. There are several phenomena, not incorporated in the model, which might account for a steep gradient in NO concentration in the splash zone. First, the reduction of NO may only be an apparent one due to uncertainty in the determination and weighting of the bubble and emulsion gas compositions. The estimate of the mixed mean gas composition in the bed (Equation 21) depends on the model used to estimate partitioning of the gas between bubble and emulsion. Other factors may contribute to the uncertainty in bed gas composition, for example, variation in the sample flow rate with the concentration of solids at the probe tip; and mixing of the sample in the probe, sample line, and reaction chamber of the NO analyzer. A second set of phenomena which might account for rapid reduction of NO in the splash zone is the alternate reaction pathways for destruction of NO, including reduction by CO, hydrocarbons, and NH_3. Chan (11) has shown that the NO-char reaction is enhanced in the presence of CO, the effect increasing with decreasing temperature. Reaction of NO and CO, catalyzed by coal ash, is also possible. Mori and Ohtake (29) measured an NO decomposition rate of 273 mole ppm/s.m^2 on alumina, in the presence of 1000 mole ppm CO at 1041 K. The rate of reaction was approximately first order in CO and zeroth order in NO, for NO above 300 mole ppm.

Nitric oxide reduction by methane, with reduction of up to 700 mole ppm NO in 0.5 s, was observed in $NO-CH_4-O_2-CO_2-Ar$ mixtures at 1323 K by Yamazaki et al (13). The temperature dependence of the rate is not reported so the possible contribution of this process at 1040-1100 K cannot be determined. Although the reduction of NO was only significant for O_2/CH_4 mole ratios of about 0.5 to 2.0, such conditions might exist locally during mixing of gases in the splash zone of the fluidized bed.

Reactions of NO with NH_3 such as:

$$NO + NH_3 = H_2O + N_2 + 1/2H_2$$

(Duxbury and Pratt (30)) are another possible contribution to the rapid NO disappearance at the top of the bed. Neither ammonia nor NO_x was measured in the present experiments, so the contribution of this reaction cannot be precisely estimated. However, the increase in NO observed in run C27 on addition of secondary air is evidence that N-containing species other than NO may be present in the freeboard at least under sub-stoichiometric conditions. De Soete (31) determined an overall rate expression for the homogeneous reaction between NO and NH_3 giving N_2 from measurements in ethene/oxygen flames over the temperature range 1800 to 2400 K. The reaction is first order with respect to both NO and NH_3. The applicable temperature range is far from fluidized combustor conditions, however, the rate expression predicts an initial NO destruction rate of 140 mole ppm/s at 1040 K in a mixture containing 600 mole ppm each of NO and NH_3. It is possible that this reaction contributes to NO reduction in the splash zone. If it does contribute, the optimum (from the point of view of NO emissions) primary stoichiometric ratio in a configuration with staged air addition, may be one at which some NO is left unreduced at the top of the bed, providing a reactant for direct conversion of NH_3 to N_2 in the splash zone.

4.0 Conclusions

A mechanistic model for particle entrainment into the freeboard has been developed and used in conjunction with a chemical kinetic description of the NO-char reaction for prediction of the reduction of NO along the height of the freeboard in fluidized coal combustion. Bed conditions, including the mass fraction of char in the bed, are input to the model. Predicted NO profiles showed good agreement with experimental data obtained while burning bituminous and subbituminous coals under a variety of operating conditions. The steep reduction in NO observed in the splash zone immediately above the bed in some cases could not be adequately explained by the present model. This result points to the importance of the reactions in the splash zone, where it is thought that NO reducing reactions other than the NO-char reaction will have to be taken into account for satisfactory prediction of the NO profile under all conditions. The model is now in a form in which it can be integrated into system models for predicting NO emissions as a function of operating conditions.

Acknowledgements

The development of the models for particle entrainment and nitric oxide reduction was supported by DOE under Contract No. EX-76-A-01-2295. The experimental work was supported by DOE under Grant No. DE-FG22-80PC30215, Dr. H. A. Webb, Project Manager.

Nomenclature

A	Specific BET surface area of char (m^2/kg)
A_t	Cross sectional area of the bed (m^2)
C_D	Drag coefficient
C_{NO}	NO concentration ($kmole/m^3$)
d_b	Bubble diameter (m)
$\bar{d}_B$, $\bar{d}_c$, $\bar{d}_f$	Geometric mean diameters of bed particles, char particles, and fresh coal particles, respectively (m)
E_a	Activation energy (J/kmol)
E_d, E_u	Mass flow rates of downward and upward moving particles, respectively (kg/s)
E_o, $E_{o,c}$	Initial entrainment rates of stone and char particles from the bed surface, respectively (kg/s)
H_f	Total freeboard height (m)
k	Rate coefficient (units variable)
L_f	Expanded bed height (m)
m_p	Mass of a single particle (kg)
Q_b	Visible bubble volume flow rate (m^3/s)
R_o	Gas constant = 8314 J/kmol · K
R_b	Bubble radius (m)
T	Temperature (K)
T_B	Bed temperature (K)
T_g	Gas temperature (K)
u_b	Absolute bubble velocity (m/s)
u_g	Superficial gas velocity (m/s)
u_{mf}	Minimum fluidization velocity (m/s)
u_t	Particle terminal velocity (m/s)
v_d, v_u	Downward and upward particle velocities, respectively (m/s)
v_s, v_{si}	Particle local velocity and particle initial velocity, respectively (m/s)
$\bar{v}_p$	Root-mean-square particle initial velocity (m/s)

X_k	Mole fraction of species k
Y_c	Mass fraction of char in the bed
z	Distance above the distributor (m)
Z	Distance above the bed surface (m)
ξ	Volume fraction of particles ejected per bursting bubble
ε_{mf}	Bed voidage at minimum fluidization
$\rho(Z)$, $\rho_c(Z)$	Local density of stone and char particles, respectively, at freeboard height Z, (kg/m^3)
ρ_g	Gas density (kg/m^3)
ρ_s, $\rho_{s,c}$	Solid densities of stone and char, respectively (kg/m^3)
δ	Bubble volume fraction
σ_f, σ_B, σ_c	Geometric standard deviations of fresh coal particles, bed particles and char particles, respectively

TABLE 1. ANALYSIS OF COALS

Analysis (wt %)	Bituminous, Arkwright, Pittsburgh Seam	Subbituminous, Colstrip Mine, Rosebud Seam, Rosebud County, MT
Proximate	(as received)	(as received)
moisture	1.6	19.19
ash	8.01	8.29
volatile matter	33.93	28.74
fixed carbon	56.46	43.78
Ultimate	(daf)	(dry)
C	76.36	67.80
H	5.23	4.45
N	1.47	1.00
S	2.61	.59
O	5.26	15.91
ash	-	10.25

TABLE 2. OPERATING CONDITIONS AND EXPERIMENTAL DATA
(pressure = 101 kPa)

Run Number	A14	C22	C25	C26	C27**	C28
Coal Type	Bitum-minous	Subbitu-minous	Subbitu-minous	Subbitu-minous	Subbitu-minous	Subbitu-minous
$\bar{d}_f$ (μm)	674	1000	1750	1750	2100	2100
σ_f	1.87	1.8	1.83	1.83	2.12	2.12
Stoichiometric air/fuel ratio	1.19	1.22	1.21	1.25	1.02	1.07
T_B (K)	1105	1134	1110	1050	1095	1040
T_g(z=4.1 m)	-	-	1002	932	1043	988
u_g(m/s)	0.98	1.46	1.00	0.80	0.94	0.86
X_{O_2}(z=0.9 m) (mole %)	6	8	4.1	-	1.7	2.3
X_{O_2}(z=4.1 m) (mole %)	-	-	3.2	4.0	3.5	1.5
X_{CO}(z=0.9 m) (mole %)	2	0.9	1.5	0.25	2.1	0.9
X_{CO}(z=4.1 m) (mole %)	-	-	<0.005	<0.005	0.11	0.14
X_{HC}(z=0.9 m) (mole %)	0.2	0.02	0.32	0.03	0.78	>0.33
$\bar{d}_B$ (μm)	815	1300	800	800	760	720
σ_B	1.42	1.32	1.44	1.44	1.35	1.37

Table 2 Cont'd

Run Number	A14	C22	C25	C26	C27**	C28
Coal Type	Bitum-minous	Subbitu-minous	Subbitu-minous	Subbitu-minous	Subbitu-minous	Subbitu-minous
$\bar{d}_c$ (μm)	674*	1123	2300	2300	2300	2400
σ_c	1.87*	1.41	1.55	1.54	1.52	1.55
Apparent char solid density $\rho_{s,c}$ (kg/m^3)	1400	1200	915	909	930	920
Estimated bubble fraction, δ	0.2	0.2	0.125	0.128	0.226	0.196
Carbon mass fraction in the bed, Y_c	0.01	0.0012	0.0015	0.0011	0.0056	0.0023
$\overline{\overline{X}}_{NO}$ at bed surface (mole ppm)	380	500	717	561	~ 2	595
BET specific surface of char (m^2/kg)	1.5×10^5	6×10^5	6×10^5	6×10^5	6×10^5	6×10^5

*The char size distribution in the bed for Run No. A14 is assumed to be the same as the feed size distribution.

**Run No. C27 used staged addition of the combustion air.

References

1. F. J. Pereira, J. M. Beér, B. Gibbs, and A. B. Hedley, Fifteenth Symposium (Int'l) on Combustion, The Combustion Institute, Pittsburgh, PA, 1975, p1149.

2. B. M. Gibbs, F. J. Pereira, and J. M. Beér, Inst. Fuel, Symposium Series No. 1, Fluidized Combustion Paper D.6, 1975, pp1-13.

3. Y. Okada, J. Tatebayashi, and R. Yamamura, "Experimental Emission Control on Fluidized Bed Combustion of Coal," presented at AIChE Annual Meeting, San Francisco, CA, 1979.

4. S. E. George and J. R. Grace, AIChE Symposium Series, No. 176, Vol. 74, 1978, p67.

5. C. Y. Wen and L. H. Chen, The Proceedings of the Sixth International Conference on Fluidized Bed Combustion, USDOE, CONF-800428-Vol. 3, p1115.

6. M. Horio, A. Taki, Y. S. Hsieh, and I. Muchi, in Fluidization, Grace and Matsen, eds., Plenum, N.Y., 1980, p509.

7. F. J. Pereira and J. M. Beér, Deuxième Symposium Européen sur la Combustion, Orléans, France, 1975, p339.

8. T. Furusawa, D. Kunii, A. Oguma, and N. Yamada, Proc. Soc. Chem. Eng., Japan, 4 (1978)562.

9. J. M. Beér, A. F. Sarofim, L. K. Chan, and A. M. Sprouse, The Proceedings of the Fifth International Conference on Fluidized Bed Combustion, The MITRE Corporation, Vol. II, McLean, VA, 1978, p577.

10. D. Kunii, T. Furusawa, and K. T. Wu, in Fluidization, Grace and Matsen, eds., Plenum, N.Y., 1980, p175.

11. L. K. Chan, Kinetics of the Nitric Oxide-Carbon Reaction Under Fluidized Bed Combustor Conditions, Dissertation, MIT, Cambridge, MA, 1980.

12. A. F. Sarofim and J. M. Beér, Seventeenth Symposium (Int'l) on Combustion, The Combustion Institute, Pittsburgh, PA, 1979, p189.

13. S. Yamazaki, M. Hiratsuka, and Y. Fujitani, Combustion Science and Technology, 20 (1979)25.

14. P. M. Walsh, M. Nicastro, C. Sundback, J. M. Beér, W. R. Brooks, A. Dutta, C. J. Giallombardo, L. R. Glicksman, and M. C. Zhang, "Experimental Studies for Testing of Models and for Scale-up of Fluidized Bed Combustion," Technical Report for the Period April 14 to August 14, 1981, prepared for the Tennessee Valley Authority under Contract No. TV-55783, August 25, 1981.

15. T. Z. Chaung, "Further Studies on the Mechanistic Freeboard Model: Simulation and Measurements of Solid Flux in the Freeboard," In J. F. Louis and S. E. Tung, "Modeling of Fluidized Bed Combustion of Coal, Quarterly Technical Progress Report No. 20, prepared for DOE/Morgantown under Contract No. EX-76-A-01-2295, 1981.

16. S. Mori and C. Y. Wen, AIChE Journal 21 (1975)109.

17. L. R. Glicksman, J. Valenzuela, and W. Lord, "Fluid Dynamics Component Model," in "Modeling of Fluidized Combustion of Coal," J. F. Louis and S. E. Tung, Quarterly Tech. Progr. Report No. 12, Contract No. E(49-18)-2295, MIT, Aug. 1979.

18. J. F. Davidson and D. Harrison, Fluidised Particles, Cambridge University Press, 1963.

19. J. M. Beér, A. F. Sarofim, S. S. Sandhu, M. Andrei, D. Bachovchin, L. K. Chan, T. Z. Chaung, and A. M. Sprouse, "NO_x Emission from Fluidized Coal Combustion," Final Report prepared for USEPA under Grant No. R804978020, 1981.

20. J. E. Mayo, "Determination of Solids Loading in the Freeboard Section of a Fluidized Bed Coal Combustor," B.S. Thesis, Dept. of Chemical Engineering, MIT, Cambridge, MA, 1980.

21. J. M. Beér, A. F. Sarofim, P. K. Sharma, T. Z. Chaung, and S. S. Sandhu, in Fluidization, Grace and Matsen, eds., Plenum, N.Y., 1980, p185.

22. Y. H. Song, Fate of Fuel Nitrogen During Pulverized Coal Combustion, Dissertation, MIT, Cambridge, MA, 1978.

23. H. Guerin, T. Siemieniewska, Y. Grillet, and M. François, Carbon 8 (1970)727.

24. I. W. Smith and R. J. Tyler, Combustion Science and Technology 9 (1974)87.

25. J. T. Ashu, N. Y. Nsakala, O. P. Mahajan, P. L. Walker, Fuel 57 (1978)250.

26. I. W. Smith, Fuel 57 (1978)409.

27. P. M. Walsh, A. K. Gupta, J. M. Beér, and K. S. Chiu, "Proceedings of the DOE/WVU Conference on Fluidized Bed Combustion System Design and Operation," Morgantown, WV, October 27-29, 1980, p455.

28. F. J. Pereira, J. M. Beér, and B. M. Gibbs, "Nitric Oxide Emissions from Fluidized Coal Combustion," presented at the Central States Section, The Combustion Institute, Spring Meeting, April 5-6, 1976.

29. Y. Mori and K. Ohtake, Combustion Science and Technology 16 (1977)11.

30. J. Duxbury and N. H. Pratt, Fifteenth Symposium (Int'l) on Combustion, The Combustion Institute, Pittsburgh, PA, 1975, p843.

31. G. G. De Soete, Fifteenth Symposium (Int'l) on Combustion, The Combustion Institute, Pittsburgh, PA, 1975, p1093.

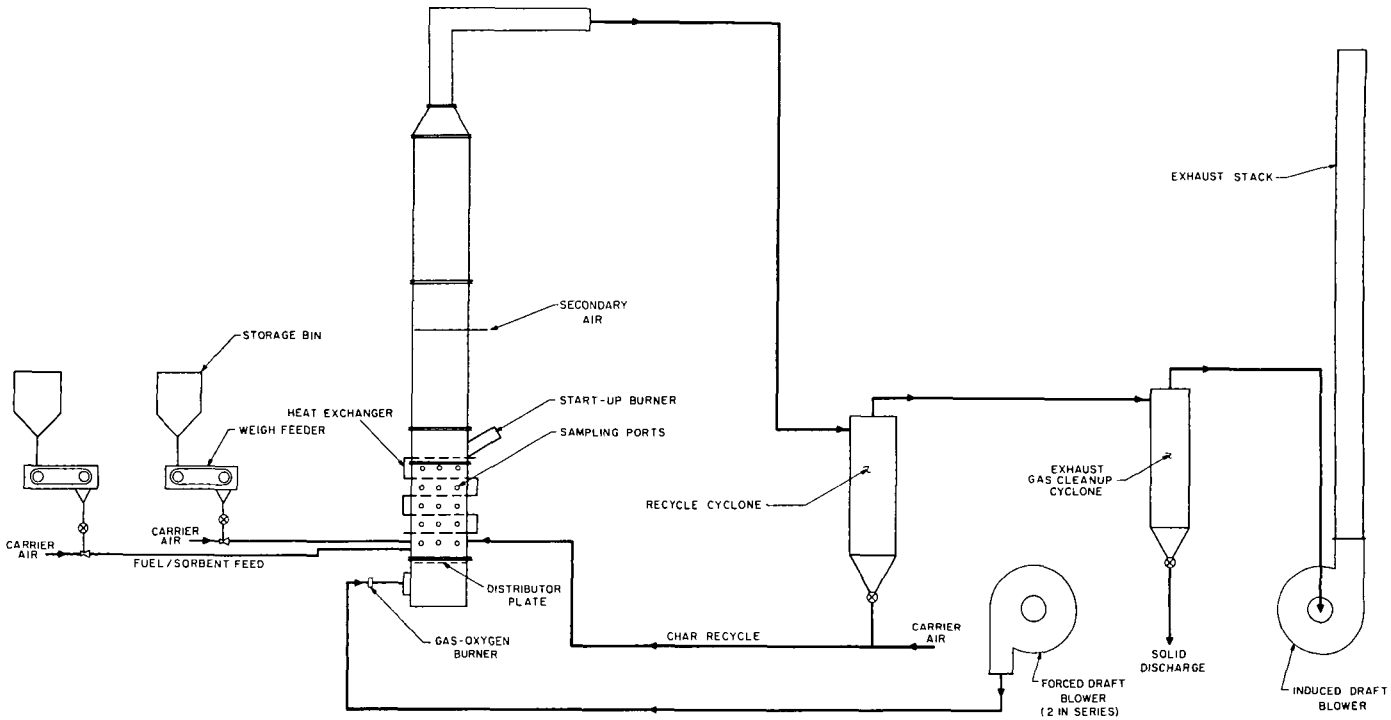

FIGURE 1. M.I.T. 0.6 m x 0.6 m, 500 kW (THERMAL) FLUIDIZED COMBUSTION RESEARCH FACILITY

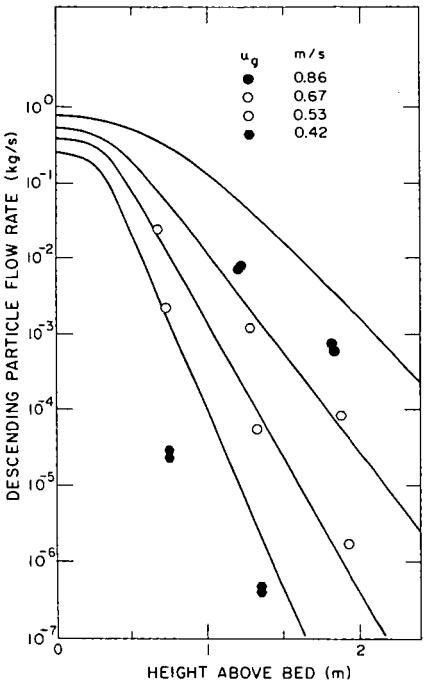

FIGURE 2. DESCENDING PARTICLE FLOW RATE VS. HEIGHT ABOVE THE BED. COMPARISON OF MODEL PREDICTIONS WITH EXPERIMENT.

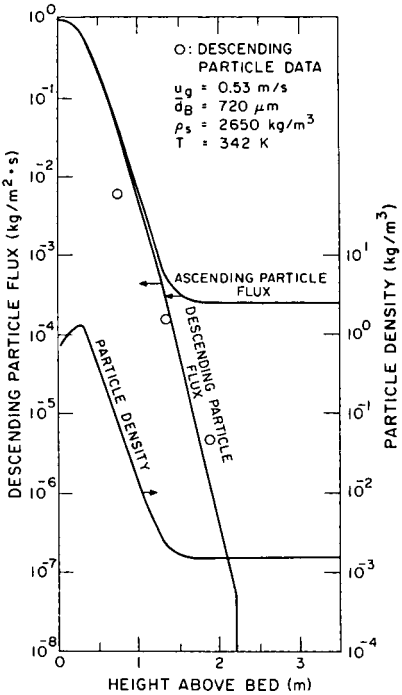

FIGURE 3. PARTICLE DENSITY, ASCENDING FLUX, AND DESCENDING FLUX VS. HEIGHT ABOVE THE BED.

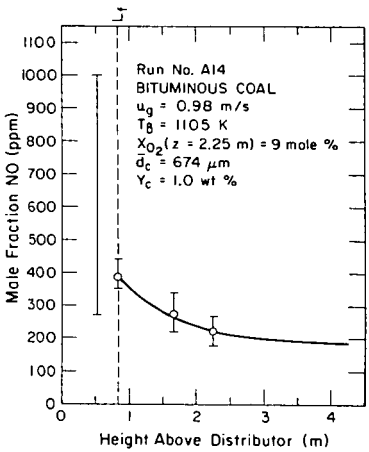

FIGURE 4. MOLE FRACTION NITRIC OXIDE VS. AXIAL POSITION
I MEASURED
— CALCULATED

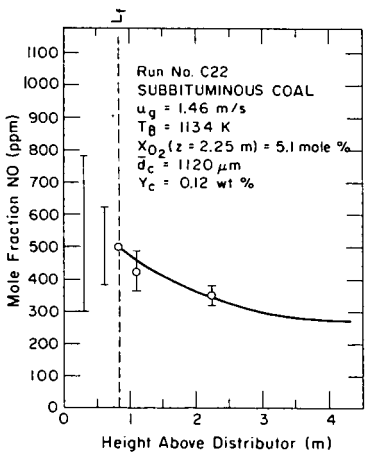

FIGURE 5. MOLE FRACTION NITRIC OXIDE VS. AXIAL POSITION
I MEASURED
— CALCULATED

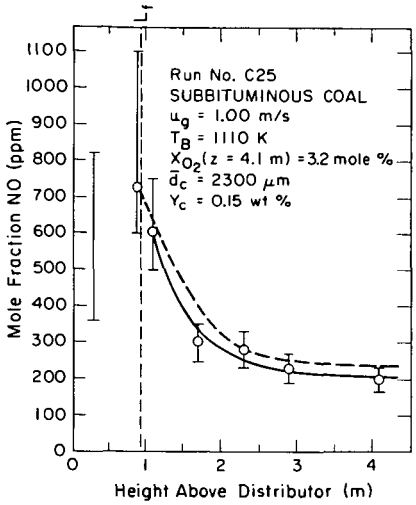

FIGURE 6. MOLE FRACTION NITRIC OXIDE VS. AXIAL POSITION
I MEASURED
=== CALCULATED

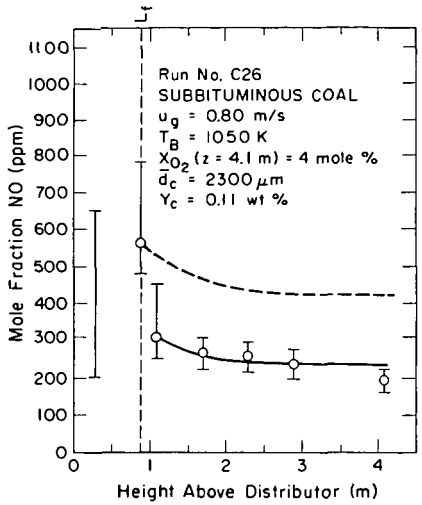

FIGURE 7. MOLE FRACTION NITRIC OXIDE VS. AXIAL POSITION
I MEASURED
=== CALCULATED

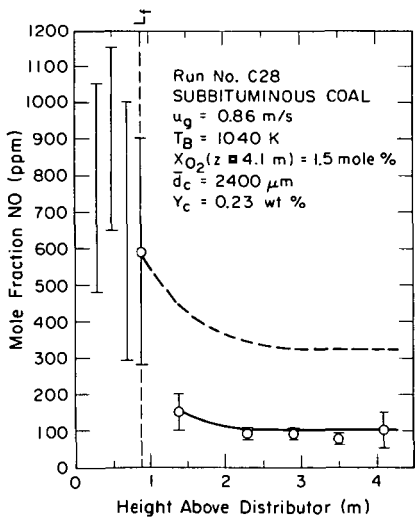

FIGURE 8. MOLE FRACTION NITRIC OXIDE VS. AXIAL POSITION
I MEASURED
=== CALCULATED

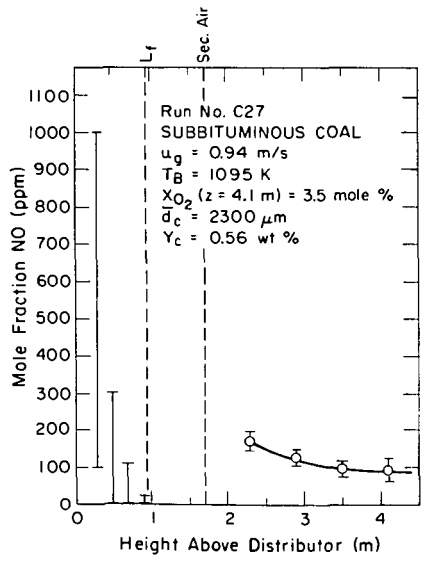

FIGURE 9. MOLE FRACTION NITRIC OXIDE VS. AXIAL POSITION
I MEASURED
— CALCULATED

"NO_x" Formation and Kinetics of "NO_x" Reduction in Fluidized Bed Combustion of Carbonaceous Materials

Takehiko Furusawa, Mikio Tsunoda,
Seiichi Sudo, Shunichi Ishikawa and Daizo Kunii

Department of Chemical Engineering
University of Tokyo
Bunkyo-Ku Tokyo 113 JAPAN

In contrast with the extensive investigations concerning sulfer retention in the United States, the initial stage of development in Japan has focused on the nitric oxide emission control.

The staged air firing is considered to be the most promising method for control. In this operation the fluidized bed is maintained under a deficiency of air and the design factors influencing sulfur retention, formation and destruction of nitric oxide, ammonia and other nitrogeneous compounds, and combustion efficiency are complex interactions. The optimum design of a fluidized bed combustor requires sound qualitative information concerning the behavior of nitric oxide formation and quantitative descriptions of the kinetics of "NO" destruction. The objective of this report is to describe the recent findings concerning "NOx" formation and the kinetics of "NOx" reduction reactions in fluidized bed combustion of carbonaceous materials.

I. NITRIC OXIDE EMISSION FROM FLUIDIZED BED COMBUSTION

Equipment, Procedure and Materials

The combustors are stainless steel vessels, 50mm diam. 580mm long and 76mm diam. 850 mm long. The lower part of the vessel was packed with refactory materials and used for preheating. Fluidizing air or simulated air consisting of oxygen and argon enters the combustor through a multi-orifice plate distributor into a bed of microspherical particles whose chemidal and physical properties are given in Table 1. The multi-orifice plate was designed so that a pressure drop sufficient to achieve homogeneous fluidization could be obtained. In a series of experiments carried out to investigate the influence of air staging, the primary stage of the bed was maintained at substoichiometric conditions, while the balance of the air was introduced through the nozzles into the freeboard.

The static bed height was specified to be 10cm. The fluidized bed combustor was externally heated by an electric furnace. The temperature of the bed was controlled by a conventional PID electronic controller.

Feeding of the carbonaceous materials employed was done by means of a solid feeder developed in our laboratory. Thus continuous feed of a small flow rate of solids (such as 0.2 g/min) could be realized. The solids were sent into the fluidized bed combustor at a point 30~35mm above the distributor.

Ash was removed by elutriation and the elutriated solids were removed from the off-gas by a small cyclone separator. In a certain series of experiments, collected solids were used for chemical analysis to obtain the combustion efficiency.

Upstream from the cyclone separator, (5cm below the top cover of the combustor) the off-gas was continuously diverted to a gas-analysis system. A chemiluminescent NOx analyzer provided continuous measurement for NOx while gas chromatography provided intermittent analysis for H_2 N_2, CO, CO_2, CH_4 and C_2H_4. Known gas mixtures were used to calibrate the gas chromatograph. Kitagawa NH_3 low-range ditector tubes were used to analyze NH_3. the experimantal conditions employed are shown in Table 1, while the carbonaceous materials employed for the present series of experiments are shown in Table 2.

Table 1 Scope of experiment

Inert particles: Microspherical particles
SiO_2:8.93%, Al_2O_3:90.61%, Fe_2O_3: 0.46%
Surface mean particle diameter of the inert particles:
580 microns for coal and char, 613 microns and 322 microns for coke
Bulk density: 0.57 g/cm^3
Temperature of fluidized bed: 700-1000°C
Static height of bed: 10cm
Diameter of coal and char particels: 500-710 microns
Mean diameter of coke particles,
Coke I : 109 microns
Coke II : 191 microns
Coke III: 460 microns
(A) ID 50mm combustor (height 490mm)
Flow rate of fluidizing air and
simulated air: 4.2-8.1 Nℓ/min
Feed rate of fuel particles: 0.5-1.7 g/min
(B) ID 76mm combustor (height 850mm)
Flow rate of fluidizing air and
simulated air: 3.9-10.4 Nℓ/min
Feed rate of fuel particles: 0.37-1.27 g/min

The effects of volatile components on nitric oxide emission[4,6)]

Fundamental investigations concerning the effects of stoichiometric ratio and combustion temperature on "NO" emission were carried out by use of various types of carbonaceous materials indicated in Table 2. Typical results are shown in Fig.1 (a) and (b). Figure 1 (a) indicates that a considerably high level of "NO" emission in the presence of reducing gas (H_2, CO and CH_4) was observed under a substoichiometric combustion of coal while quite a low level of "NO" emission was detected under a starving combustion of char.

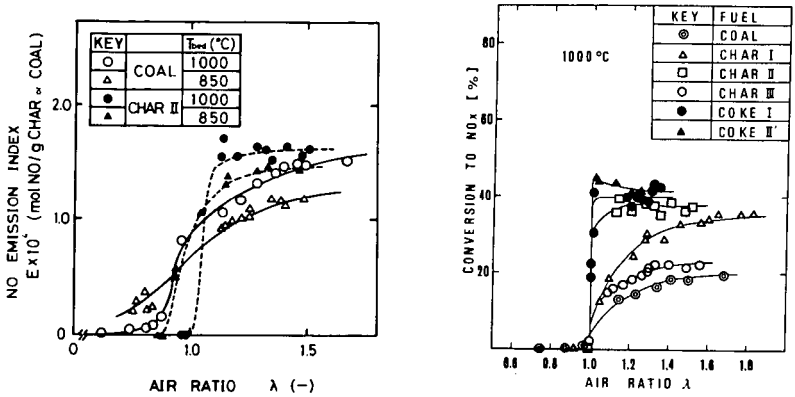

(a) (b)

Fig. 1 Effects of stoichiometric ratio and combustion temperature on "NO" emission

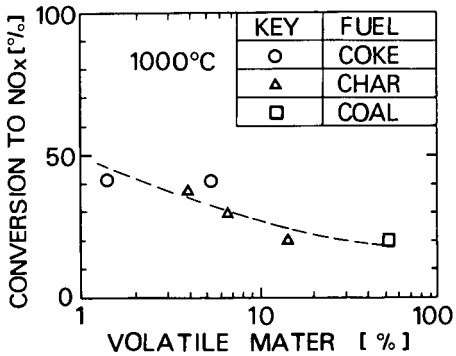

Fig. 2 Conversion of fuel nitrogen to NO with respect to volatile components

Table 2 Proximate and ultimate analyses of carbonaceous materials used

Proximate analysis [wt%]

		Volatile matter	Fixed-carbon	Ash	Moisture
Char I	*1	3.83	54.09	19.8	22.28
Char II	*2	2.74	66.00	24.47	6.69
Char III	*3	10.89	65.04	19.84	4.32
Coal	*4	43.3	39.1	12.7	4.9
Coke I	*5	1.4	96.0	1.4	1.2
Coke II	*5	3.7	92.5	0.2	3.6
Coke II'	*5	5.3	90.9	0.4	3.4
Coke III	*5	10.9	85.7	1.7	1.7
Carbon	*6	5.2	94.7	0.1	(3.2)

Ultimate analysis [dry%]

		C	H	N	S	O	Ash
Char I	*1	96.21	0.59	0.54	0.27	3.91	25.48
Char II	*2	71.66	1.03	0.61	0.01	0.34	26.35
Char III	*3	70.99	2.77	1.27	0.02	4.21	20.74
Coal	*4	66.9	5.4	1.4	0.1	13.2	13.0
Coke I	*5	94.0	1.3	0.7	2.7	-	1.3
Coke II	*5	89.2	2.1	1.5	2.9	4.1	0.2
Coke II'	*5	91.7	2.6	2.4	2.1	0.7	0.5
Coke III	*5	87.1	4.0	2.5	1.4	3.2	1.8
Carbon	*6	97.2	1.4	0.1	0.1	1.1	0.1

*1 Char I: produced from Liddell coal/Australia
*2 Char II: produced from Taiheiyo coal, pyrolysis temperature: 800°C
*3 Char III: produced from Taiheiyo coal, pyrolysis temparature: 600°C
*4 Coal: Taiheiyo coal
*5 Coke: originated from petroleum residue
*6 Carbon: activated carbon from petroleum residue

"NO" emission from char or coke, both of which contained less volatiles than coal is radically reduced as the stoichiometric ratio is reduced. This fact together with the reduced ammonia emission suggests that staged air firing may provide advantageous combustion modification for the control of "NOx" emission. This is discussed in the forth coming sections.

Figure 1(b) demonstrates the conversion ratio of fuel nitrogen to fuel NO of various carbonaceous materials. In this experiment the effect of thermal-NO was elimated by using AR/O_2 mixture instead of air. The level of NO emission under an excess air condition seemed to be considerably dependent on the volatile contents of fuel.

The fraction of fuel bond nitrogen which formed fuel-NO at $\lambda = 1.3$ is illustrated in Fig.2 where volatile contents were calculated on

ash and moisture free basis. This indicates that the conversion rate of fuel bond nitrogen to nitric oxide was reduced with the increased volatile contents.

Jonke et al.[3] reported that "NO" emission under a substoichiometric combustion of coal was increased at decreased temperature. This behavior was observed in Fig.1(a). Thus "NO" emission level from high volatile coal at elevated temperatures, approaches the level of "NO" emission from less volatile fuels at lower temperatures. This fact together with the decreased ammonia formation at elevated temperatures suggests also the efficient combustion modification for the reduction of "NO" emission.

Formation of nitrogenous compounds and staged combustion[4,5,6]

A series of experiments were carried out to investigate the influence of air staging. In this operation, the primary stage, which was a fluidized bed, was maintained at substoichiometric conditions while the balance of air, (the secondary air) was introduced through a nozzle into the freeboard. A significant reduction of "NO" emission by staged air firing can only be realized provided the emission of "NO" as well as other nitrogeneous compounds from the primary stage are significantly reduced. Thus the ammonia emission from coal and char are measured by the detector tube method. Typical results are shown in Fig. 3. Ammonia emission was not detected under an excess air condition. Under a substoichiometric condition, this could be reduced by elevating the combustion temperature, or reducing moisture, or volatile contents. In the case of char combustion, the ammonia emission under starving combustion at 850°C was approximately 1/7 of the "NO" emission under an excess air condition.

These results suggest that a significant reduction of "NO" emission can be achieved by a staged combustion of char. A preliminary experiment was carried out to evaluate the possibilities of staged air firing. Experimental results indicate that an approximately 90% reduction of "NO" emission was attained in the case of staged combustion of char where this was evaluated on the basis of an "NO" emission index obtained for conventional operations. However, the maximum level of "NO" reduction in this operation for coal remained at 33.5%.

Effect of in situ formed carbon on "NO" reduction[1,2,9]

Carbonaceous materials within the bed were reported to be effective in "NO" destruction. The steady state carbon concentration within the bed was measured. After terminating the feed of fuel solids, the amount of carbon dioxide and monoxide originating from the remaining carbon particles was measured by means of the gas bag method. The results obtained are compared with the level of "NO" emission in Fig. 4. These results indicate that "NO" emission was inversely related to the steady state carbon concentration. Furthermore, the steady state carbon concentration within the bed was found to be considerably small.

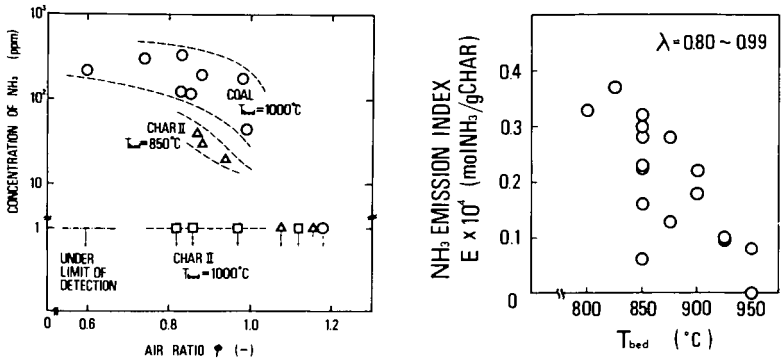

(a) (b)

Fig. 3 Emission of ammonia from combustion of coal and char

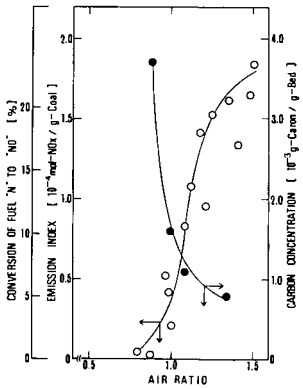

Fig. 4 NO emission decreased with the increase of steady state carbon concentration within the bed

Intrinsic Ratio of Fuel Nitrogen Conversion to Nitric Oxide

The significant magnitude of nitric oxide destruction by char or other reducing gas suggests that the concentration of nitric oxide measured at the top of the bed or freeboard did not reflect the intrinsic evolution level of nitric oxide from the combustion. Thus the measured value depended on the relative importance of the rate of "NO" formation reaction and the rate of "NO" reduction. The experimentally obtained concentration profiles along the height of the bed and freeboard may verify this mechanism. Information concerning the intrinsic evolution level of "NO" from char particles is required to describe the above process quantitatively. The response curve of "NO" formed within the combustor by the puls input char was measured so that the effect of the subsequent "NO" reduction by char or other reducing gas could be minimized. This is shown schematically in Fig.5(a). The response peak of "NO" formed by the combustion with the reduced intensity of the input puls tends to a certain value from which the intrinsic ration of fuel nitrogen conversion to nitric oxide could be evaluated. Typical results are illustrated in Fig. 5(b). This value seems to be a little smaller than the value obtained by continuous combustion in a small experimental facility. This fact suggests that the emission level of nitric oxide is affected by the intensity of combustion, consequently the steady state carbon concentration within the bed. However, these results do not reduce the validity of the experimental results obtained by a small scale combustion facility concerning the behavior of nitric oxide emission.

II. KINETICS OF "NO" DESTRUCTION

Rate of "NO" reduction by char[7)]

An isothermal fixed bed tubular reactor of diluted char particles and activated carbon (char II, carbon in table 2) was used to measure the reaction rate over a temperature range which is of practical importance in fluidized bed combustion. Since the "NO" concentrations employed in the experiment were of the order of several hundred ppm, the amount of carbon could be assumed to be constant. The details were reported elsewhere.

The reduction of "NO" by char and activated carbon was first order with respect to "NO" concentration. Figure 6 represents the Arrhenius plot for char where alpha (α) denotes the ratio of the concentration of oxygen to the concentration of "NO" at the inlet. Thus the line coresponding to $\alpha=0$ indicates this rate.

At lower temperature ranges the activation energy for char was 16.3 kcal/mol and coincided with the data reported previously. Above 680°C the activation energy was 58.6 kcal/mol. The reason for the increase in the activation energy has not been explained. In the lower temperatures the desorption of carbon-oxygen surface complex was considered to control the overall rate. The gaseous reaction product was N_2, CO and CO_2. As the temperature was elevated, the fraction of CO in the reaction product increased.

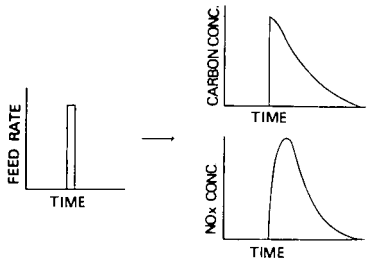

(a)

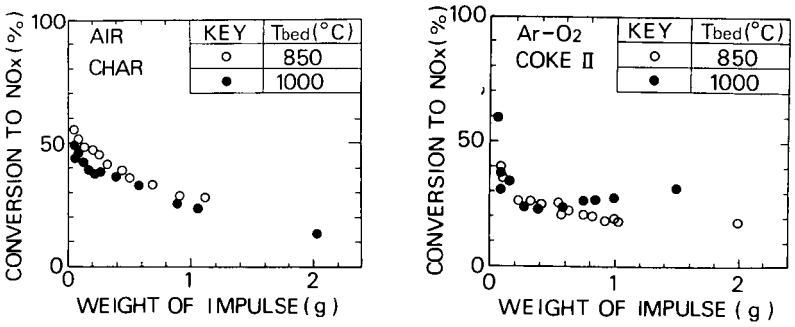

(b)

Fig. 5 Intrinsic conversion ratio of fuel nitrogen to nitric oxide

Rate of "NO" reduction by char under an excess air condition[10,11)]

Kinetic information concerning whether or not "NO" can be reduced by char in the presence of oxygen is required in order to analyze the mechanism of "NO" destruction within the bed and freeboard. The use of a fixed bed of diluted char particles was restricted to a range of lower temperatures and lower oxygen concentrations since the char was consumed by combustion reaction. The rate of char combustion is approximately a hundred times faster than the "NO" reducton.

The "NO" destruction accompanied by oxidation of char was also assumed to be first order with respect to "NO" concentrations. This assumption was verified under low oxygen and "NO" concentrations. The results are shown in Fig. 6. The reaction was significantly accelarated by adding oxygen. An increased rate was also observed for "NO" destruction by activated carbon.

Over a range of higher temperatures the effects of the added oxygen on the rate could not be investigated since the carbon concentration

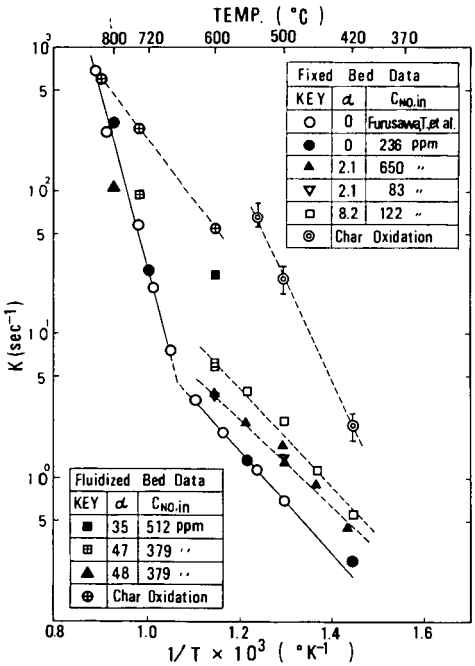

Fig. 6 Rate of NO reduction by char and the effect of oxygen on "NO" reduction

could not be assumed constant. Thus a fluidized bed reactor with a continuous feed and discharge of carbon (150mm height) was used to analyze the rate for higher oxygen concentration; namely, a large value of α and a higher temperature. Furthermore, the reduction of "NO" in a simulated combustion product containing CO_2 was studied. A remarkable result from these experiments is that a significant reduction of "NO" was realized even under an excess air condition in which oxygen remained in the outlet flow.

The simplified bubbling bed model by Kunii and Levenspiel was used to evaluate the reaction rate in the presence of oxygen. First, the effective bubble diameter was calculated as an adjustable parameter by curvefitting the experimental data obtained in the absence of oxygen to the curve calculated theoretically by the above model and the kinetic data shown previously. Then the increased rate in the presence of oxygen was evaluated by changing the rate, but by keeping the other parameter, including the effective bubble diameter, constant.

In this evaluation of the rate, the effect of fuel "NO" formed by the simultaneously occuring combustion of char was compensated for. The details are shown elsewhere. The estimated rate is shown in Fig. 5. An increased rate of "NO" reduction was observed in the presence of oxygen at both 600°C and 750°C. The rate was not significantly reduced by the presence of oxygen at 800°C. At 853°C the rate of "NO" destruction was reduced by coexisting oxygen. The extent of "NO" reduction by both char and activated carbon in both the absence and presence of oxygen was measured over a temperature range of 700∿900°C where the height of the bed was 150mm. The results together with the extent of oxygen consumption is shown in Fig. 7. The increased rate for char was verified up to approximately 750°C and that for the activated carbon up to 950°C.

Reduction of "NO" in the presence of carbon monoxide and hydrogen[8,12)]

The preliminary investigation concerning the reduction of nitric oxide by char in the presence of hydrogen or carbon monoxide was carried out over a temperature range of 700-800°C in a fixed bed reactor mentioned previously. The reaction was first order with respect to nitric oxide. Ammonia was formed in the nitric oxide hydrogen-char system. The presence of hydrogen and carbon monoxide decreased the consumption of carbon to nearly zero, as:

$$NO + CO \rightarrow CO_2 + \tfrac{1}{2} N_2 \quad (1)$$
$$NO + H_2 \rightarrow H_2O + \tfrac{1}{2} N_2 \quad (2)$$
$$NO + \tfrac{5}{2} H_2 \rightarrow NH_3 + H_2O \quad (3)$$

The rates and activation energies obtained for the above catalytic reactions for (1) or (2) + (3) agreed with the rate of noncatalytic reduction of nitric oxide by char within the experimental error. This strongly suggested that the activated adsorption of nitric oxide on the char surface controlled the overall rates. The ratio of ammonia formed by reaction (3) to the consumed nitric oxide which is found to be constant at each temperature is decreased with an increased temperature.

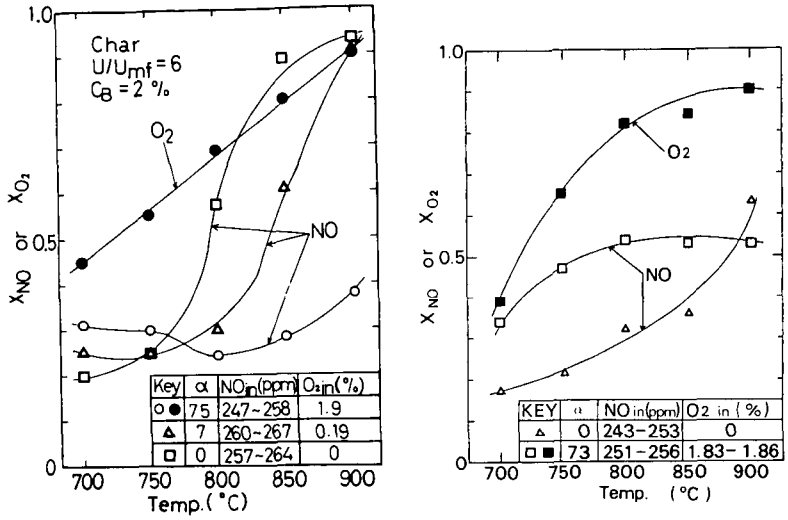

(a) Char (b) Carbon

Fig. 7 Increased extent of "NO" reduction caused by oxygen

Concluding Remarks

This paper descirbed the recent findings concerning the behavior of "NOx" formation in a fluidized bed combustor obtained by use of a variety of carbonaceous materials. The "NO" emission under an excess air condition was decreased with an increase in the volatile contents of fuels. The emission of "NO" and other nitrogeneous contents formed under a substoichiometric combustion was also strongly dependent on the volatile contents. The staged combustion of less volatile char and coke provided a radical reduction of "NO" emission. The steady state carbon concentration was measured and "NO" emission was found to be inversely related to the carbon concentration. The intrinsic conversion ratio of fuel nitrogen to "NO" was measured. The kinetics of "NO" destruction by char in both the absence and presence of oxygen was investigated. The rate for char was increased up to 750°C. "NO" was reduced catalytically by carbon monoxide and hydrogen over a char surface, but the rate was not increased.

Acknowledgement

D. K. whishes to express his thanks to Grant-in-Aid for Energy Research (NO 311604, NO 411003 & NO 505021) of the Ministry of Education. T.F. received Grant-in-Aid for Scientific Research (NO 455363 & NO 555374) from the same body. The experimental assistance by Mr. A. Kato was

greatly acknowledged.

Literature Cited

1) Beér, J.M., A.F. Sarofim, L. Chan & A. Sprouce: Proceedings of the 5th Int. Conference on Fluidized Bed Combustion, p577 - p592 (1977)
2) Beér, J.M., A.F. Sarofim & Y.Y. Lee, Proceedings of the 6th Int. Conference on Fluidized Bed Combustion, p942 - p955 (1980)
3) Jonke, A.A., G.J. Vogel, E.L. Carls et al.: Chem. Eng. Prog. Symp. Series 68, NO 126, 241 (1972)
4) Furusawa, T., T. Honda, J. Takano and D. Kunii: J. of Chem. Eng. Japan 11, 377 (1978)
5) Furusawa, T., N. Yamada, T. Sendo and D. Kunii: J. of Chem. Eng. Japan 12, 71 (1979)
6) Furusawa, T., T. Honda, J. Takano and D. Kunii: Fluidization, Proceedings of 2nd Eng. Found. Conf., Cambridge University Press (1978)
7) Furusawa, T., D. Kunii, N. Yamada and A. Oguma: Int. Chem. Eng. 20, 239 (1980) or Kagaku Kogaku Ronbunshu 4, 562 (1978)
8) Furusawa, T., D. Kunii and T. Tsunoda: under preparation
9) Gibbs, B.M., F.J. Pereira and J.M. Beér: 16th Symposium on Combustion, Cambridge, 461 (1976)
10) Kunii, D., K.T. Wu and T. Furusawa: Chem. Eng. Sci. 35, 170 (1980)
11) Kunii, D., T. Furusawa and K.T. Wu: ed. J.R. Grace and J.M. Matsen, Fluidization, Plenum Publishing Corp. New York, p175 - p183 (1980)
12) Cowley, L.T. and P.T. Roberts: Paper submitted for presentation at the Fluidized Combustion Conference, 28-30th Jan. (1981) held at the Energy Research Institute, University of Cape Town, South Africa

REDUCTION OF NITRIC OXIDE BY CARBONACEOUS SOLIDS IN AN ATMOSPHERIC PRESSURE FLUIDIZED-BED REACTOR

By

Z. Huang,[1] G. T. Chen,[1] and C. Y. Wen[2]
Department of Chemical Engineering
West Virginia University
Morgantown, WV 26506

J. Y. Shang,[3] J. S. Mei,[4] and J. E. Notestein[5]
Technology Development and Engineering Division
U.S. Department of Energy
Morgantown Energy Technology Center
Morgantown, WV 26505

Abstract

The fluidized-bed combustion process, due to its ability to control pollutant emissions and its inherent capability to accommodate a wide variety of fuels, has been the subject of accelerating development for industrial and utility applications. However, fluidized-bed combustion boilers based on the current design and operation may not be able to meet the future stringent standards on nitrogen oxides emissions without additional provisions. In this paper, a preliminary study on the reduction reactions of nitric oxide with three different carbonaceous solids using a 9.6-centimeter diameter, electrically heated, batch fluidized-bed reactor operated at various design and operating conditions is discussed. Results of this investigation indicates that the NO reduction reaction appears to be dependent upon not only the operating variables such as bed temperature, carbonaceous solid loading in the bed, but also on the physical properties of the carbonaceous solids as well. Prediction of NO reduction by one of the carbonaceous solids using a two-phase bubble model shows good agreement with experimental data within the range of experimental conditions.

Introduction

Among the various techniques for direct conversion of the chemical energy in coal to thermal energy, the fluidized-bed combustion (FBC) process appears to be one of the most attractive means due to its inherent features. The higher heat capacity of the solid bed material leads to good combustion stability which, consequently, permits use of essentially all fossil fuels including low-grade fuels high in ash and/or moisture content and low in heating value, such as coal refuses, peat, oil shales, etc. The use of a sulfur-accepting sorbent affords in situ capture of the sulfur dioxide evolving from the burning of sulfur-bearing fuels. Bed temperature is maintained sufficiently low and, thus, results in relatively low emissions of nitrogen oxides and less slagging and fouling problems than in conventional coal-fired boilers. Lastly, the presence of vigorous particle mixing in the fluidized bed provides higher bed-to-surface heat transfer rates which results in less heat exchange surface relative to conventional coal-fired boilers. As a consequence, fluidized-bed combustion boilers fueled by coals and low-grade fuels have been the subject of accelerating developments for industrial and utility applications both in the U.S. and abroad. In recent years a number of fluidized-bed boilers have been

[1]Visiting scholars from People's Republic of China.
[2]Benedum Professor.
[3]Division Deputy Director.
[4]Mechanical Engineer.
[5]Division Director.

constructed and operated to demonstrate a variety of industrial and utility applications and process reliability; for example[1,2,3] the commercial prototype fluidized-bed boiler at Georgetown University, the industrial application of a fluidized-bed boiler at Great Lakes Naval Training Station, and the prototype anthracite culm fluidized-bed combustion boiler at the industrial park in Shamokin, PA. In addition, a 20 MWe fluidized-bed boiler pilot plant is currently under construction by TVA for the utility application[3].

At present, the EPA nitrogen oxides emission standard is 0.6 lb NO_2/million Btu input; most of the fluidized-bed combustion boilers, which are based on the current design and operation principles, can meet the standard without additional efforts. However, it is anticipated that nitrogen oxides emission standard may become more stringent in the future. The fluidized-bed boilers using the current design and operation principles may not be able to meet the stringent standards for NO_x emissions without additional provisions. It is, therefore, the objective of this project to investigate and determine the pertinent design and operational variables which affect NO_x emissions from fluidized-bed combustion boilers. Results of this investigation may enable further insight to be gained into the mechanism of NO_x destruction in the bed and provide design and operational information for the future development of low-NO_x fluidized-bed combustion boilers to meet the anticipated stringent EPA nitrogen oxides emission standards.

Experimental Facility

Experiments on nitrogen oxides reduction were conducted using an electrically heated, laboratory-scale, fluidized-bed reactor, which is shown schematically in Figure 1. This laboratory-scale batch fluidized-bed reactor consists of a 9.6-cm diameter, 47 cm tall, stainless steel cylindrical vessel. The lower section of the vessel is surrounded by a 20-cm tall, 1.36 KW electric heater, such that the bed can be heated to about 1000°C. The stainless steel cylindrical vessel is also heavily insulated with Fiberfrax. The bed is supported on a 6.35 mm thick stainless steel perforated gas distributor with fifty-six (56), 0.8-mm diameter orifices.

Bed temperature was regulated and controlled by a transformer. Reaction temperature was measured by a chromel-alumel thermocouple with a Hastalloy sheath of 3.175 mm diameter. Readings were displayed in degrees on a digital thermometer. The thermocouple was suspended at a point which was 5 cm from the distributor; the axial temperature distribution in the bed and freeboard was measured by moving the thermocouple.

Temperature recordings in the bed above 2.5 cm from the distributor indicated that the bed temperatures were essentially uniform. However, a temperature gradient of approximately 18°C/cm was observed in the freeboard section of the reactor. The bed was fluidized by pure nitrogen gas; carbon monoxide, methane, and nitric oxide could also be introduced into the fluidizing gas stream in controlled amounts. All gas flow rates were measured by rotameters. Exit gas composition was continuously monitored by preset gas analyzers as shown below:

Compound	Principle of Operation	Instrument[1]
NO	Chemiluminescence	Thermo-Electron, Series 10
CO	IR	MSA-LIRA, Model 303
CO_2	IR	MSA-LIRA, Model 303
O_2	Paramagnetic	Leeds and Northrup
Total HC	Flame Ionization	Beckman, Model 400

[1]The use of brand names is for the identification purposes only and does not constitute endorsement by the Department of Energy.

The analyzed flue gas concentrations were registered on a six-channel strip chart recorder.

Materials Used for the Experiments, Chars and Coke

Nitric oxide reduction experiments were conducted using two different chars and a coke. Char 1 was produced from Wyoming sub-bituminous coal by Occidental Research Corporation's (OCR) Flash Pyrolysis process, with BET (Brunauer-Emmett-Teller) surface area of 290 m^2/g, a size range of 30 x 70 mesh, and a density of 2.010 g/cm^3. Its chemical composition is listed in Table 1. Char 2 was made in situ from Pittswick bituminous coal (8 x 12 mesh in size). The Pittswick coal was fed a little at a time into the bed where sand was fluidized and heated to a temperature of 850°C by the preheated nitrogen gas to prevent the coal from clinkering. The coal was then pyrolyzed in a nitrogen atmosphere for half an hour to produce Char 2. The chemical composition of Char 2 and its parent coal are also listed in Table 1. Char 2 had a BET surface area of 2.4683 m^2/g and a density of 2.288 g/cm^3. It is important to note that the analytical data for Char 2 on a weight basis, such as its chemical composition and surface area, are not as precise as desired because the char samples contained a certain amount of sand which could not be completely separated from the char before analysis.

Metallurgic coke, obtained from Mercury Coal and Coke, Inc., near Morgantown, was also used in these tests. It was ground and screened to obtain coke particles of 12 to 20 mesh size. The coke particles were then fluidized with nitrogen in the hot fluidized bed at 900°C for one hour. After the material was cooled, the test feedstock coke was obtained. The BET surface area of this coke was 0.8668 m^2/g and its density was 2.067 g/cm^3. Its chemical composition is listed in Table 1.

Bed Material

Glass sand with a mean particle diameter of 0.286 mm was used as the bed material. The size distribution of the sand is listed in Table 2. The BET surface area was 0.846 m^2/g and its density was 2.664 g/cm^3.

The minimum fluidization velocity of the sand was determined experimentally at elevated temperature. A pressure drop versus gas velocity is plotted in Figure 2. As can be seen, the minimum fluidization velocity is approximately 5.5 cm/sec at a bed temperature of 822°C.

Experimental Procedure

The experimental procedures for NO reduction by Char 1 and by metallurgic coke were precisely the same. First, the reactor containing 1164 g of sand was heated while the sand was simultaneously fluidized with preheated nitrogen. When the desired reaction temperature was reached, the fluidizing gas was turned off and a feed hopper with a long dipleg was inserted rapidly into the reactor through a stopcock in the feedline on top of the reactor. A weighed amount of char (or coke) was then poured into the hopper from which it dropped onto the hot sand. The hopper was then removed, the cock closed, and the nitrogen switch was turned on immediately such that the char was distributed evenly throughout the bed. When the bed temperature had restabilized at the desired level, a measured flow of nitric oxide was admitted. The concentrations of each component in the exit gas were continuously monitored and recorded on a six-channel strip chart recorder.

In order to reach the required steady-state conditions in a short duration of time, the experiments to determine NO reduction capability of Char 1 and coke were conducted in sequence from low temperature (600°C) to high temperature (850°C) at the same carbon loading.

The experimental procedure for the reduction of nitric oxide by Char 2 was similar to the procedure for Char 1 and metallurgic coke as described above, except that the tests were carried out in a temperature sequence from 850°C (highest) to lower temperatures, since Char 2 was produced "in situ" under a nitrogen atmosphere at 850°C which was the highest chosen reaction temperature for an experiment.

Experimental Results and Discussion

Experiments on the reduction of NO by carbonaceous solids were carried out at various operating conditions. Results of these experiments and their corresponding operating conditions are presented in Tables 3, 4, and 5 for Char 1, Char 2, and metallurgic coke respectively. A discussion of these data is presented below.

Effect of Char Surface Area and Porosity on Nitric Oxide Reduction

Experimental results of NO reduction by a batch of carbonaceous solids in the absence of oxygen were plotted in Figure 3 at identical operating conditions. Results shown in Figure 3 indicate that heterogeneous reduction of NO by Char 1 and Char 2 are significantly higher than that achieved with metallurgic coke. The reactivities of the three carbonaceous solids are compared in Table 6. Differences in the reduction of NO by these carbonaceous solids may be attributed to the differences in physical properties, such as specific surface area and porosity. Char 1, which gives the highest NO reduction, poses the highest specific surface area, although its carbon content is less than the metallurgic coke. Scanning Electron Microscope (SEM) porosity measurement also indicates that Char 1 exhibits the highest porosity. As can be seen in Figure 4, micropores with size ranging from 100 μm to 0.3 μm cover nearly 100 percent of its surface. Although the metallurgic coke has the highest carbon content among the three tested carbonaceous solids, its specific surface area is the smallest. The coke also has comparatively smaller pores which range in size from 10 μm to 1.5 μm and cover only about 1 percent of its surface as can be seen in Figure 5. Figure 6 shows the porosity measurement of Char 2, which has pore sizes ranging from 40 μm to 1 μm and covering 45 percent of its surface. A comparison of the data presented in Table 6 and the porosity measurements given by SEM indicates that the low NO conversion rate achieved by metallurgic coke may be attributed to its small BET surface area as well as its low porosity. Interpretation of these data suggests that internal diffusion may also play an important role in determining the overall reaction rate of a large porous solid particle, which has relatively low porosity and small BET surface area, with a reactant gas.

Effect of Bed Temperature in Nitric Oxide Reduction by Chars

The reduction reaction between NO and char was found to be strongly influenced by operating bed temperature. Figures 7 and 8 show the effect of bed temperature on NO reduction by Char 1 and Char 2. As can be seen, nitric oxide concentration in the exit gas decrease with increasing bed temperature of both Char 1 and Char 2. Within the range of operating conditions, NO reductions of 90 percent or better were attainable provided that the bed temperature was maintained at or above 800°C. As the bed temperature was raised, further, NO outlet concentration decreased continuously, but at a decreasing rate. However, thermodynamic calculations indicated that at a temperature or 900°C, equilibrium concentrations of thermal NO may reach 500 ppm for a mixture of 2 percent oxygen and 75 percent nitrogen[4]. In view of the current practice in design and operation of fluidized-bed combustion boilers, the use of excess oxygen at higher bed temperatures may promote the formation of thermal NO. The higher bed temperature is also unfavorable to the sulfation reaction of natural sorbents in the atmospheric pressure fluidized bed. Therefore, an optimum temperature range for NO_x and SO_2 emission control appears to be 800° to 850°C.

Effect of Char Loading on Nitric Oxide Reduction

The effect of char loading in the fluidized bed on NO reduction by char is illustrated in Figure 9. As can be seen, the reduction of NO increases with increase in char loading. At bed temperature of 750°C, the effect of char loading is most important around 1 percent where it results in a NO reduction of 87 percent. At higher char loading, the reduction of NO is generally higher; however, the effect of the char loading becomes less significant. The same trend can also be observed at the temperature range below 750°C, even though the reduction of NO falls below 60 percent due to the strong temperature dependence of the reduction reaction. Higher char loading in the bed may increase the chances of clinker formation which is caused by local temperature excursion as a consequence of the poor solid mixing and the inability to dissipate the heat of combustion. In addition, the loss of unburnt carbon in the drained spent-bed material may become unacceptable if the char loading in the bed becomes too high. However, recent developments in fluidized-bed combustion technology have indicated that two-stage combustion systems with the increased char loading in the first stage enhances the overall reduction of nitric oxide emission significantly[5].

Prediction of NO Reduction by Char 1

Recent experimental studies[6] on the reduction reaction of nitric oxide with char have concluded that the reaction is first order with respect to the NO concentration. This practice is, hence, adopted in the present study. The reaction rate constants of the reaction of NO with Char 1 at the corresponding temperatures and char loadings were calculated based on the experimental data presented at Table 3. The activation energy and the frequency factor within the range of operating conditions are 31.7 kcal/mol and 9.66×10^8 sec^{-1} respectively. The rate constants of NO-char plotted as a function of inverse temperatures for several experimental studies[7] are compared with the present results in Figure 10. As can be seen, the reaction rate constants obtained from the present experiment show good agreement with previous investigations. The NO-char reaction kinetics can be represented by the following correlation and this was employed in the NO emission modeling. In view of the low

$$k = 9.66 \times 10^8 \exp\left(-\frac{31,700}{RT}\right) sec^{-1} ,$$

superficial velocity, the shallow bed, and relatively small bed diameter, a two-phase bubble model[8] with both the bubble and emulsion phases treated as plug flow was employed for the prediction of NO conversion. The NO reduction by Char 1 was calculated using this approach over the range of experimental conditions. The comparison of calculated versus test data values may be observed in Table 3, as well as Figure 7. As can be seen in Figure 7, the calculated values for NO reduction show excellent agreement with experimental data.

Conclusions

Tests to determine the NO reduction capability of two different chars and a metallurgic coke were conducted in an electrically heated, batch, fluidized-bed reactor in the absence of oxygen. Based on the experimental results, the following conclusions can be drawn.

- Reduction of nitric oxide depends strongly on the physical properties of the carbonaceous solids such as specific surface area and pore size distribution; and, to a lesser extent, on the carbon content.

- Reduction reaction between NO and carbonaceous solids was found to be strongly influenced by bed temperature. Within the range of operating conditions, the degree of NO reduction increases with bed temperature. However, the formation of thermal NO and the unfavorable sulfation reaction for natural sorbents in an

atmospheric pressure fluidized bed at higher temperature posts an upper limit on temperature range for NO_x and SO_x emission control. A preferred operating temperature range from this standpoint appears to be 800°-850°C.

- NO reduction by char increases with char loading in the bed. With 1 percent of char loading in the bed, 90 percent or better NO reduction is attainable for both Char 1 and Char 2 provided that bed temperature is maintained at or above 800°C.

- Reaction rate constants based on the present experimental data show good agreement with the previous investigations. The rate constant can be represented by the following correlation:

$$k = 9.66 \times 10^8 \exp\left(-\frac{31,700}{RT}\right) \sec^{-1}$$

- Prediction of nitric oxide reduction by Char 1 using a two-phase bubble model gives good agreement with the experimental data within the range of experimental conditions.

References

1. Proceedings of the Fifth International Conference on Fluidized-Bed Combustion, Washington, DC, December 1977.

2. Proceedings of DOE/WVU Conference on Fluidized-Bed Combustion System Design and Operation, Morgantown, WV, October 1980.

3. The proceedings of the Sixth International Conference on Fluidized-Bed Combustion, Atlanta, Georgia, August 1980.

4. Pereira, F. J. M. A., "Nitric Oxide Emission from Fluidized Coal Combustion," Ph.D. Thesis, University of Sheffield, 1975.

5. Gibbs, B. M., F. J. Pereira, and J. M. Béer, "The Influence of Air Staging on the NO Emission from a Fluidized-Bed Coal Combustor," Paper Presented at 16th Symposium (International) on Combustion, The Combustion Institute, Pittsburgh, PA, 461, 1977.

6. Béer, J. M., A. F. Sarofim, S. S. Sandhu, M. Andrei, D. Bachovchin, L. K. Chan, T. Z. Chang, and A. M. Sprouse, "NO_x Emissions from Fluidized Coal Combustion," EPA Grand No. R804978020 Report, 1979.

7. Furusawa, T., D. Kunii, A. Oguma, and N. Yamada, "Kinetic Study of Nitric Oxide Reduction by Carbonaceous Materials," Kagaku Kogaku Rombunshu, 4 (6), 562 (1978).

8. Davidson, J. F. and D. Harrison, "Fluidized Particles," Cambridge University Press., 1963.

3:sw:515f

TABLE 1

Chemical Analysis of Carbonaceous Solids

	Char 1	Char 2	Pittswick Bituminous Coal	Metallurgic Coke
Ultimate Analysis, Wt %				
Moisture	2.09	0.63	1.35	0.09
Ash	16.79	60.05	14.15	10.07
Sulfur	0.83	1.64	3.85	0.83
Hydrogen	1.35	0.40	5.04	0.53
Nitrogen	0.96	0.66	0.98	0.84
Total Carbon	75.24	37.90	69.10	87.40
Oxygen (by difference)	2.74	1.28	5.53	0.23
Elemental Analysis, Wt %				
Silicon, SiO_2	35.06	84.51	49.16	44.19
Aluminum, Al_2O_3	16.91	7.62	23.66	19.34
Iron, Fe_2O_3	14.84	5.38	17.72	17.76
Calcium, CaO	11.32	0.49	1.55	5.75
Magnesium, MgO	4.48	0.01	0.85	0.98
Sodium, Na_2O	--	--	1.23	2.20
Potassium, K_2O	0.70	0.62	2.59	1.53
Phosphorus, P_2O_5	0.73	0.05	0.05	0.32
Titanium, TiO_2	0.85	0.34	1.21	1.21
Sulfur, SO_3	6.50	1.63	1.72	4.06

TABLE 2

Screen Analysis of Sand

Size Range, mm	Wt %
-0.589 + 0.419	2.2
-0.419 + 0.249	72.7
-0.249 + 0.179	18.9
-0.179 + 0.150	4.2
-0.150	1.0

Mean Diameter, d_p = 0.286 mm

TABLE 3

Experimental Results of NO Reduction by Char 1

Run No.	Char g	Char Wt %	Sand g	T °C	NO_{in} ppm	NO_{out} ppm	N_2 M^3/hr	U_{mf} cm/S	U cm/S	L_{mf} cm	L_f cm	ϵ_{mf}	$\left(\frac{NO_{out}}{NO_{in}}\right)$ exp.	$\left(\frac{NO_{out}}{NO_{in}}\right)$ cal.	k 1/sec
5-28-1	12	0.01031	1164	600	965	745	0.85	5.5	10.6	10	12.065	0.42	0.772	0.837	15.477
5-28-2	12	0.01031	1164	650	965	615	0.85	5.5	11.2	10	12.065	0.42	0.637	0.637	28.622
5-28-3	12	0.01031	1164	700	965	360	0.85	5.5	11.8	10	12.065	0.42	0.373	0.360	67.269
5-28-4	12	0.01031	1164	750	965	125	0.85	5.5	12.4	10	12.065	0.42	0.130	0.128	155.295
5-28-5	12	0.01031	1164	800	965	25	0.85	5.5	13.0	10	12.065	0.42	0.026	0.030	341.263
6-5-1	24	0.02062	1164	600	980	660	0.85	5.5	10.6	10	12.065	0.42	0.673	0.701	11.842
6-5-2	24	0.02062	1164	650	980	390	0.85	5.5	11.2	10	12.065	0.42	0.397	0.409	29.532
6-5-3	24	0.02062	1164	700	980	150	0.85	5.5	11.8	10	12.065	0.42	0.153	0.137	65.746
6-5-4	24	0.02062	1164	750	980	10	0.85	5.5	12.4	10	12.065	0.42	0.010	0.023	199.890
6-8-1	36	0.03093	1164	600	975	580	0.85	5.5	10.6	10	12.065	0.42	0.595	0.588	10.389
6-8-2	36	0.03093	1164	650	975	300	0.85	5.5	11.2	10	12.065	0.42	0.308	0.264	25.311
6-8-3	36	0.03093	1164	700	975	60	0.85	5.5	11.8	10	12.065	0.42	0.062	0.055	67.035
6-9-1	48	0.04124	1164	600	985	475	0.85	5.5	10.6	10	12.065	0.42	0.482	0.494	10.969
6-9-2	48	0.04124	1164	640	985	215	0.85	5.5	--	--	--	--	0.218	--	--

TABLE 4

Experimental Results of NO Reduction by Char 2

Run No.	Char* g	Sand g	T °C	NO_{in} ppm	NO_{out} ppm	N_2 M^3/hr	U cm/S	U_{mf} cm/S	$\frac{NO_{out}}{NO_{in}}$
6-1-7	12.85	1164	850	955	0	0.85	13.6	5.5	0
6-1-8	12.85	1164	800	955	75	0.85	13.0	5.5	0.079
6-1-9	12.85	1164	750	955	250	0.85	12.4	5.5	0.262
6-1-10	12.85	1164	700	955	525	0.85	11.8	5.5	0.550
6-1-11	12.85	1164	650	955	700	0.85	11.2	5.5	0.733
6-1-12	12.85	1164	600	955	790	0.85	10.6	5.5	0.827
6-3-1	25.7	1164	850	940	30	0.85	13.6	5.5	0.032
6-3-2	25.7	1164	800	940	62	0.85	13.0	5.5	0.066
6-3-3	25.7	1164	750	940	165	0.85	12.4	5.5	0.176
6-3-4	25.7	1164	700	940	490	0.85	11.8	5.5	0.521
6-3-5	25.7	1164	650	940	665	0.85	11.2	5.5	0.707
6-3-6	25.7	1164	600	940	760	0.85	10.6	5.5	0.809

*Calculated values based on the assumption that volatiles in the coal escaped during char formation.

TABLE 5

Experimental Results of NO Reduction by Metallurgic Coke

Run No.	Coke g	Sand g	T °C	NO_{in} ppm	NO_{out} ppm	N_2 M^3/hr	U cm/S	U_{mf} cm/S	$\frac{NO_{out}}{NO_{in}}$
6-3-7	24	1164	700	940	900	0.85	11.8	5.5	0.957
6-3-8	24	1164	750	940	855	0.85	12.4	5.5	0.910
6-3-9	24	1164	800	940	770	0.85	13.0	5.5	0.819
6-3-10	24	1164	850	940	620	0.85	13.6	5.5	0.660

TABLE 6

Comparison of Reactivity for Different Carbonaceous Solids

	Size Mesh	BET Surface Area m^2/g	Char g	Bed Material (Sand) g	N_2 M^3/hr	T °C	NO_{in} ppm	NO_{out} ppm	Reactivity $\frac{\text{Mole-of-NO-Reduced}}{\text{g-of-char} \cdot \text{hr}}$
Char 1	30 x 70	290	24	1164	0.85	700	980	150	1.31×10^{-3}
Char 2	8 x 12	2.4683	25.7	1164	0.85	700	940	490	6.64×10^{-4}
Coke	12 x 20	0.9	24	1164	0.85	700	940	900	6.32×10^{-5}

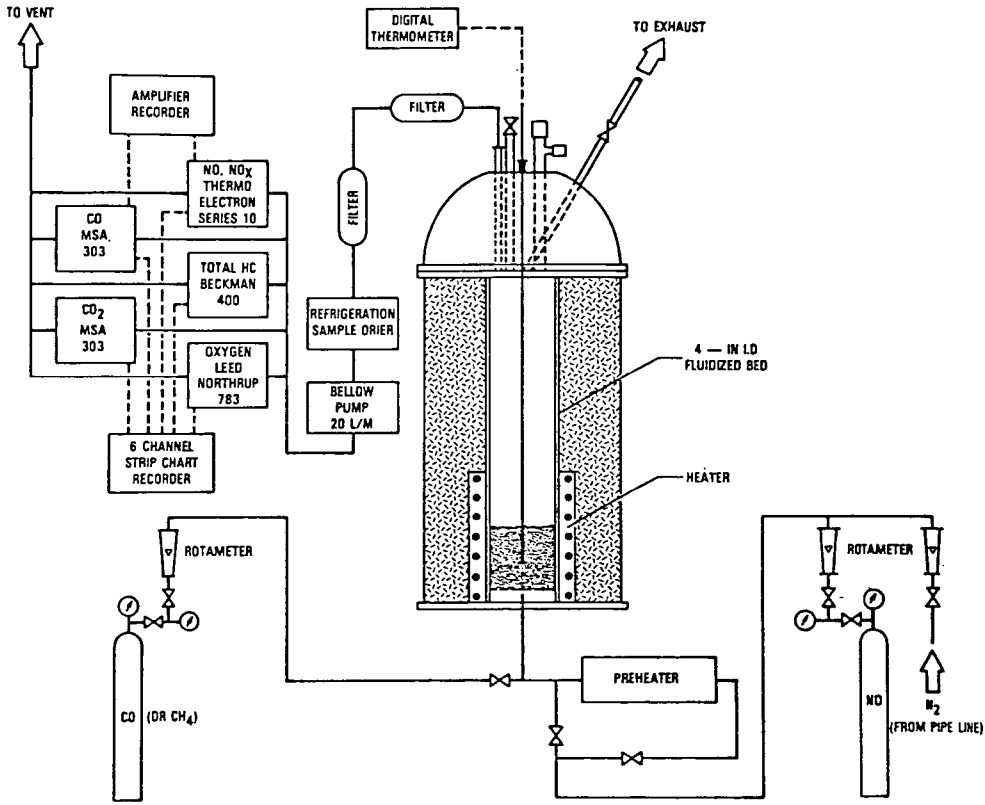

FIGURE 1 — SCHEMATIC DIAGRAM OF EXPERIMENTAL APPARATUS

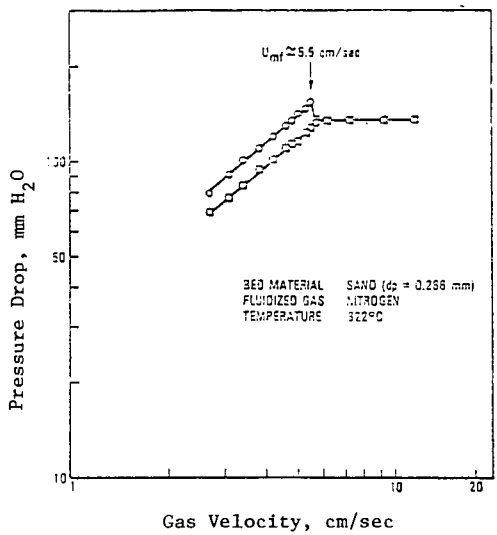

FIGURE 2. Pressure Drop Versus Gas Velocity

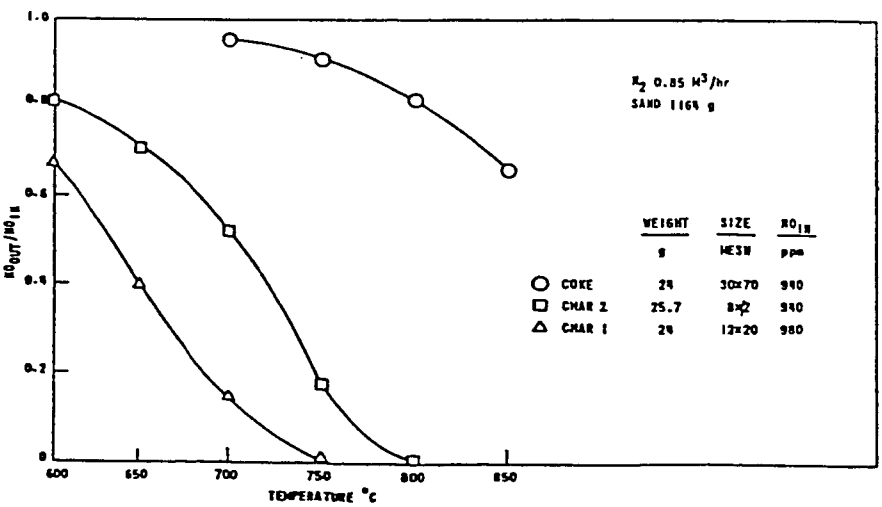

FIGURE 3. Comparison of NO Reduction by Different Carbonaceous Solids

FIGURE 4
IMAGE OF SEM POROSITY MEASUREMENT OF CHAR 1

FIGURE 5
IMAGE OF SEM POROSITY MEASUREMENT OF METALLURGIC COKE

FIGURE 6
IMAGE OF SEM POROSITY MEASUREMENT OF CHAR 2

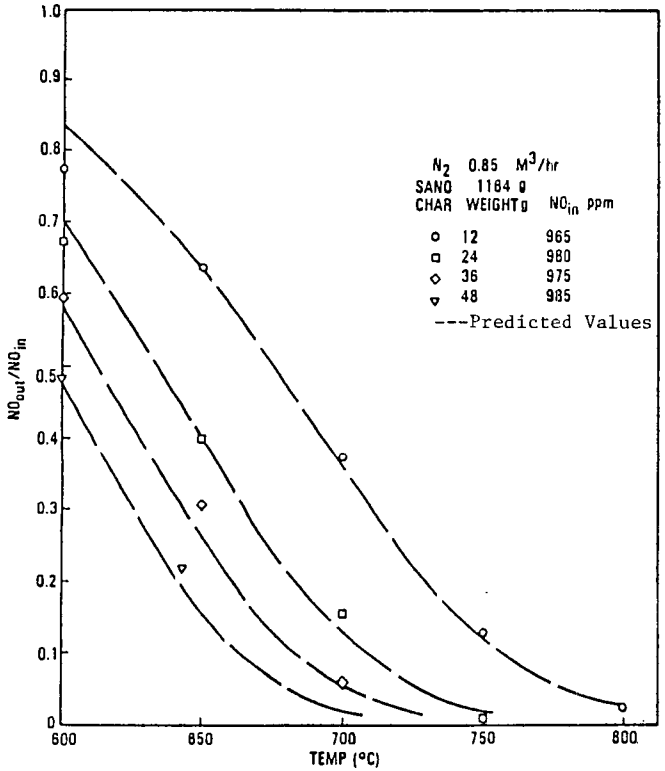

FIGURE 7. Temperature Effect on Reduction of NO by Char 1

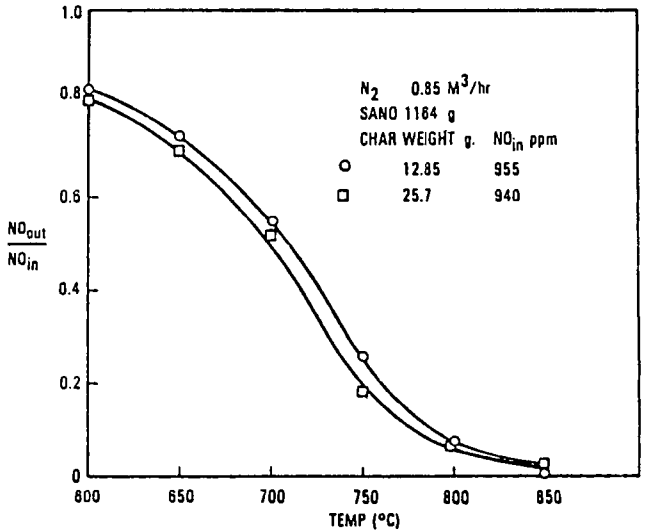

FIGURE 8. Temperature Effect on Reduction of NO by Char 2

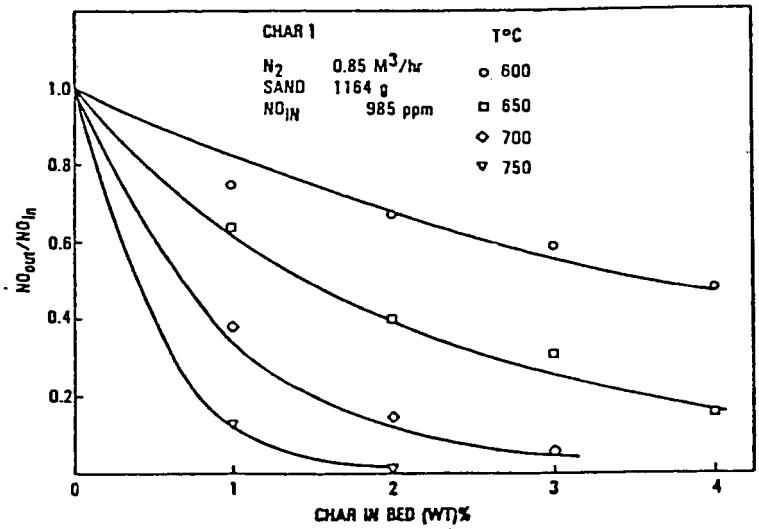

FIGURE 9. Effect of Char Loading on NO Reduction

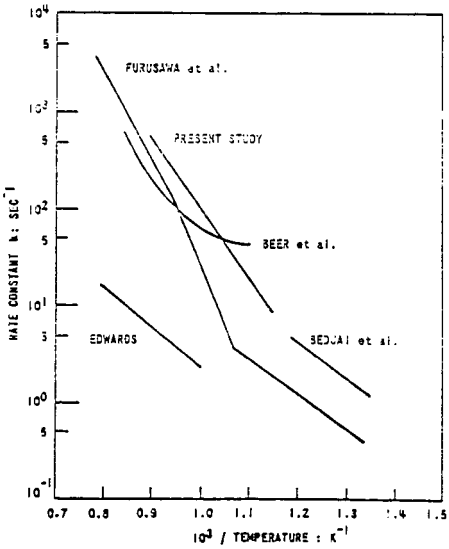

FIGURE 10. Comparison of Rate Constants for NO Reduction by Char

The effect of coal particle size on the performance of a fluidised bed coal combustor

by

M. Brikci-Nigassa, E.S. Garbett and A.B. Hedley

Sheffield Coal Research Unit, Department of Chemical Engineering and Fuel Technology, University of Sheffield
Sheffield S1 3JD, United Kingdom.

Introduction

The technology of fluidised bed coal combustion (FBC) and its advantages over conventional coal burning systems is now well established and is extensively reported in the literature (1,2,3,4). A common way of introducing coal to the bed is via coal feed points in the distributor plate and for this method it is usual to use crushed coal of particles less then 6 mm. Problems associated with this method include the determination of the correct number and spacing of feed points, blockages and the obvious expense in coal preparation. Crushed coal is used because it was thought necessary to keep the coal particle sizes approximately equal to those making up the bulk of bed and so maintain good fluidisation characteristics. However, Highley et al. (5) showed that large coal particles (< 50 mm) could be burnt quite easily in an FBC whilst at the same time overcoming the coal feed problems outlined above by overbed feeding. Also, using uncrushed coal allows the bed and freeboard heights to be reduced (5) making obvious savings in capital and running costs. An increase in the size of coal particle fed to the combustor results in an increase in the bed carbon loading (6) which influence such important phenomena as NO emissions and elutriation (7). However, there is little information on the effect on the performance of an FBC due to a variation of particle size in the coal feed. This paper therefore, reports a study of the combustion of monosized coal fractions fed continuously to the bed via an overbed feeder. Data showing the effect of coal size, excess air and combustion efficiency are presented. Measurements using crushed coal (< 1.5 mm) fed pneumatically to the bed are included for comparison.

2. Experimental procedure

The fluidised bed combustor shown schematically in Fig. 1, was 0.3 m square section and 1.83 m high and constructed from stainless steel, the walls being insulated with kaowool. The bed which was 0.6 m deep, consisted of sand of mean particle size 600 μm. Fluidising air was introduced to the bed through a bubble cap distributor plate. Crushed coal (< 1.5 mm) was fed pneumatically into the bed from a sealed hopper via a calibrated rotary valve feeder (Fig. 1). Large coal (N.C.B. 501) previously sieved to give monosized fractions (6.3, 9.5 and 12.5 mm) was fed by a vibratory feeder from a pressurised hopper to the surface of the bed. A vibratory feeding system was adopted after degradation of the coal feed occurred when a screw feeder was initially used. The large coal passed over two grids which allowed any fines present to fall through. Start up of the bed was achieved using an overbed gas burner which preheated the bed to 725 K before coal was injected. Particulate carry over in the gaseous combustion products was removed by a two-stage cyclone. Solids separated by the cyclones dropped into catchpots (Fig. 1). In order to measure the rate of elutriation of material during steady-state combustion, the carry over from the combustor was diverted into a seperate catchpot. The temperature of the bed was controlled by a cooling coil immersed in the bed. Thermocouples were located in three positions in the bed: top, middle and bottom and also in the freeboard (Fig. 1). All bed and freeboard temperatures and the cooling water temperature were recorded continuously on chart recorders.

During all the experimental runs the fluidising velocity was kept constant ($\sim 0.8\ ms^{-1}$) and changes in stoichiometry were achieved by varying the coal feed rate to the combustor. Gas samples were obtained from the bed, freeboard and exit flue by means of sampling ports located along one wall of the combustor. Water cooled stainless steel probes lined with silica were used for gas sampling. An on-line chemiluninescent analysis (TECO Model 10A) was used to determine the nitric oxide content of the combustion gas.

3. Experimental results

3.1 NO emissions

NO concentrations throughout the bed and freeboard for the crushed coal (< 1.5 mm) are shown in Fig. 2 for bed temperatures ranging between 1043 and 1193 K. A sharp increase in NO concentration is observed from 400 to 1300 ppm for a bed temperature of 1043 K and concentrations rise to 1500 ppm at the top of the bed for T_b = 1193 K. For all the bed temperatures there is a sharp decrease in NO concentration through the freeboard giving exit values of 375 ppm for T_b = 1043 K and 700 ppm for T_b = 1193 K. Similar trends are seen in Fig. 3 for the large coals (6.3, 9.5 and 12.5 mm). The concentrations of NO at the top of the bed are of the order of 1400 ppm and at the exit they have fallen to 500 ppm for a bed temperature of 1143 K. These measurements were repeated for different values of excess air (XSA) and Fig. 4 shows the variation of NO concentration at the exit flue (corrected to 3% O_2) for XSA values of between 6 and 47% for all the large coals at T_b = 1043 and 1093 K. For the 6.3 mm coal at 10% XSA and T_b = 1043 the NO concentration is 360 ppm; the corresponding value at T_b = 1093 K is 475 ppm. After these initial values the NO concentrations at both temperatures show a sharp increase to about XSA = 25% followed by a levelling off for higher values of XSA. These trends are repeated for the 9.5 mm coal but with reduced concentrations throughout. It was expected that the 12.5 mm would show a further overall decrease in NO concentration but as can be seen in Fig. 4 the 12.5 mm curve falls between those of the 6.3 and 9.5 mm coals still, however, showing the same trends as the latter two sizes.

3.2 Elutriation rates

The measured elutriation rates under steady-state conditions are shown in Figs. 5, 6 and 7. Fig. 5 shows the total carry over (i.e. ash and carbon) leaving the combustor for the 9.5 mm coal at different levels of excess air and temperature. A sharp decrease in elutriated material is observed when the level of excess air is increased from 10% to about 20%; this rate of decrease reduces as the excess air is increased beyond 20%. The carbon content of the carry over material for the 9.5 mm coal is plotted against the excess air for the four bed temperatures (Fig. 6). The proportion of carbon in the carry over decreases with increasing temperature and excess air. The same trend is observed for all the coal sizes studied (17).

The effect of coal particle size on the carry over and carbon loss at 20% excess air is indicated in Fig. 7. A sharp decrease in carry over is observed when coal sizes of increasing diameters are used in the fluidised bed combustor. Beyond the 9.5 mm coal size, elutriation rates level off and as the bed temperature increases, show an upturn (Fig. 7). This unexpected behaviour of the carry over due to the 12.5 mm coal is in parallel with the NO results for the same coal as discussed above.

3.3 Combustion efficiency

The quantity of heat lost as carbon elutriated from the combustor is the major factor affecting the efficiency of fluidised bed coal combustors. Combustion effiency has been determined for each coal particle size at about 20% excess air. The results are shown in table 1 in terms of carbon percentage combustion efficiency. Loss of carbon occurred almost entirely by elutriation.

Table 1. Combustion Efficiency as a function of coal size and bed temperature.

Temp (K)	Combustion efficiency @ 20% XSA		
	6.3 mm	9.5 mm	12.5 mm
1043	84%	88%	90%
1093	88	90	91
1143	90	92	92
1193	-	95	93

An increased carbon combustion efficiency is achieved with the increase of air up to about 20-25%, a further increase in excess air beyond this value does not improve the carbon combustion efficiency significantly. The combustion efficiency is observed to increase with bed temperature for the 6.3 and 9.5 mm coals (table 1). The 12.5 mm results show only a slight sensitivity to bed temperature (1043 K - 1193 k, 20% excess air). The highest carbon combustion efficiency of 95% is achieved with the 9.5 mm at a bed temperature of 1193 K (table 1).

4. Discussion

The levels of NO at the exit of an FBC may be expressed as a sum of the rates of formation and reduction, without specifying any mechanisms, as follows

$$\text{Rate of NO emitted at the flue} = \underset{A}{\text{Rate of formation in the bed}} - \underset{B}{\text{Rate of reduction in the bed}} + \underset{C}{\text{Rate of formation in the freeboard}} - \underset{D}{\text{Rate of reduction in the freeboard}} \quad 1)$$

It is clear from Figs. 2 and 3 that A > B and D > C for all the coals used in these experiments. There are many experimental data available which show that NO reduction in an FBC can take place via NO-char reactions (8,9,10) and so the level of NO reduction may be expected to be proportional to the carbon loading in the bed, which in turn is proportional to the diameter of the coal particles in the feed. When large coal is fed to the bed the rate of NO formation will be slower and lower than for crushed coal but the rate of reduction will also be lower even for larger carbon loading because of the low carbon surface area per unit mass.

This could explain why, as shown in Figures 2 and 3, approximately the same levels of NO concentration are observed at the top of the bed for both crushed and large coals. These similar levels of NO also contradict the suggestion (11) that overbed feeding of large coal may increase NO reduction at the top of the bed due to an increased carbon loading in that region. The NO concentrations in the 0.3 m square FBC, therefore, appear to be independent of coal feed position and size of coal fed. The major portion of NO reduction reported here, takes place in the freeboard (Figs. 2 and 3). In particular the highest reduction rate occurs in the region immediately above the bed where the char concentration is high due to splashing. It is in the freeboard then that the effect of carbon loading in the bed on NO reduction is most evident since the level observed for the 9.5 mm coal are lower than for the 6.3 mm and crushed coals. The NO levels in the freeboard are seen to decrease exponentially with height (Figs. 2 and 3) in the same manner as the solids population decreases (12).

Assuming that large coal particles do not break when introduced to the bed then it would be expected that the elutriation rate would be significantly reduced compared to when crushed coal is fed to the bed. Figure 5 shows a reduction in the elutriation rate of carbon as the coal feed particle size increases but the difference is not as great as would be expected bearing in mind that the large coal is a monosized feed and does not include any fines. In particular the carbon elutriation rate for the 12.5 mm coal although initially (T_b = 1043 K) less than that measured for the 9.5 mm subsequently becomes greater for T_b > 1093 K. This may be explained by the fact that this coal (12.5 mm) in particular suffers from breakage due to thermal shock when introduced to the bed. This also explains why the NO concentrations for this coal fall between those measured for the 6.3 and 9.5 mm coals (Fig. 4). Particle attrition may also be significant within the bed (13,14,15) particularly for the larger coals. Merrick and Highley (16) derive an expression for particle size reduction due to attrition based on Rittingers Law of abrasion and showed that the shrinkage rate was proportional to the particle size viz:

$$\frac{d\,d_p}{dt} = \frac{-K}{3}\, f\,(d_p)(U - U_{mf})\, d_p \qquad 2)$$

Thus the elutriation rate for the larger coals could be significantly enhanced due to attrition phenomena. The lowest elutriation rates observed (Fig. 7) are for the 9.5 mm coal at 1193 K and 20% XSA. The effect of increasing the bed temperature and excess air will be to increase the combustion rate with a consequent reduction in the amount of carbon thrown into the freeboard. Thus the elutriation rates will decrease for an increase in both T_b and XSA. This trend can be seen in Figs. 5 and 6.

5. Conclusions

The measurements of nitric oxide concentrations in the bed and freeboard of the 0.3 m square fluidised bed have shown that nitric oxide is produced within the bed and are reduced in the freeboard. Elutriation rates and NO concentrations measured at the exit of the freeboard both decrease with increasing coal particle size up to a size of 9.5 mm for most conditions. The combustion of monosized coal particles in the fluidised bed has highlighted the interdependence of elutriation rate, bed carbon content, carbon concentration in the freeboard and nitric oxide emissions. The results also indicate that an optimum operating condition for this particular fluidised bed combustor may exist for the 9.5 mm coal size at 20% XSA. However, further experimental results are necessary, in particular with respect to the complex phenomena occurring in the freeboard region.

6. Acknowledgements

This work forms part of the activities of the Sheffield Coal Research Unit sponsored by Shell Coal International and the National Coal Board, to whom the authors are grateful for financial assistance. The views expressed here are those of the authors and not necessarily those of the sponsors.

7. Nomenclature

d_p	coal particle dia.
$f(d_p)$	fraction of coal particles in bed smaller than d_p.
H	total bed height.
K	abrasion constant.
U	superficial fluidising velocity.
U_{mf}	minimum fluidising velocity.
y	vertical co-ordinance.
ε	dimensionless height (= y/H).

8. References

1. Skinner, D.G., Fluidised combustion of coal, Mills & Boon, Monograph No. CE/3, 1974.

2. Inst. of Fuel Symp. Ser. No. 1, Fluidised Combustion, 1975, Sessions B, C and D.

3. Gibson, J. and Highley, J., J. Inst. Energy, 1979, 52, 51.

4. Sixth Int. Conf. on Fluidised Bed Combustion, Atlanta, Proceedings, 1980.

5. Highley, J. et al., Inst. of Fuel Symp. Ser., No. 1, Fluidised Combustion, 1975, Paper B3.

6. Donsi, G. et al., 17th Symp. on Combustion (Int.), Leeds, 1978.

7. Sarofim, A.F. and Beer, J.M., 17th Symp. on Combustion (Int.), Leeds, 1978, 189.

8. Beer, J.M. et al., 5th Int. Conf. on Fluidised Bed Combustion, Washington D.C., 1977.

9. Furusawa, T. and Kunii, K., Soc. of Chem. Eng., Japan, 1977.

10. Gulyurtlu, I., Ph.D. Thesis, University of Sheffield, 1980.

11. Bachovchin, D.M., Beer, J.M. and Sarofin, A.F., A.I.Ch.E. Symp. Ser., 1981, 77, No. 205, 76.

12. Lewis, W.K. et al., Chem. Eng. Prog. Symp. Ser., 1962, 58, 38.

13. D'Amore et al., 6th Int. Conf. on Fluidised Bed Combustion, Atlanta, 1980, 2, 675.

14. Beer, J.M. et al., Inst. Energy Symp. Ser., No. 4, London, 1980, Paper IV-5.

15. Cowley, L.T. and Roberts, P.T., Fluidised Comb. Conf., Cape Town, 1981, 2, 443.

16. Merrick, D. and Highley, J., A.I.Ch.E. Symp. Ser., 1974, 70, No. 137, 366.

17. Brikci-Nigassa, M., Ph.D. Thesis, University of Sheffield, 1982.

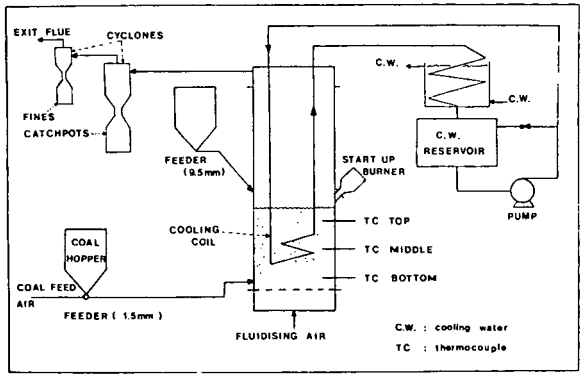

Fig. 1. (top). Fluidised bed combustor.

Fig. 2. (bottom). NO concentration as a function of excess air.

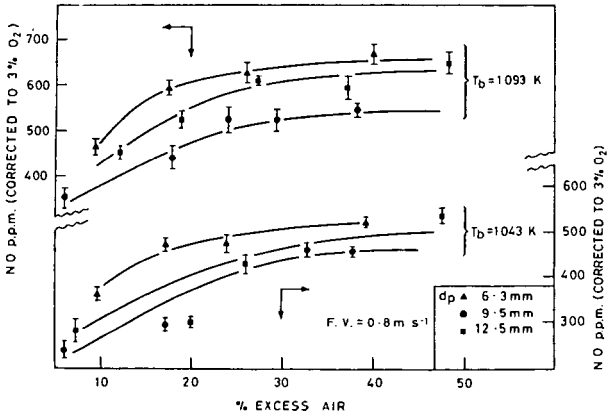

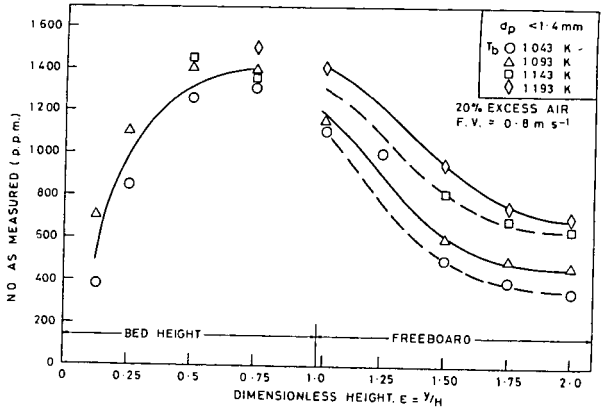

Fig. 3. (top). NO profiles for the crushed (< 1.5 mm) coal.

Fig. 4. (bottom). NO profiles for the large coals.

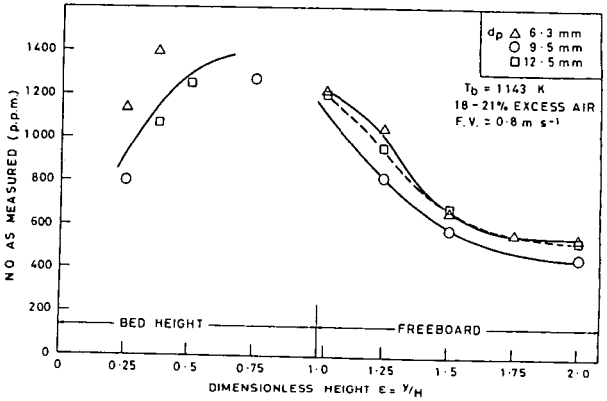

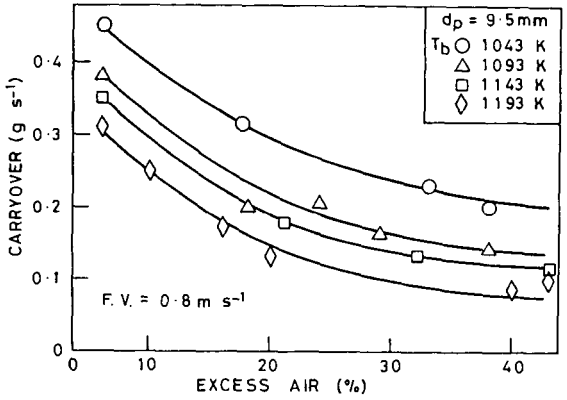

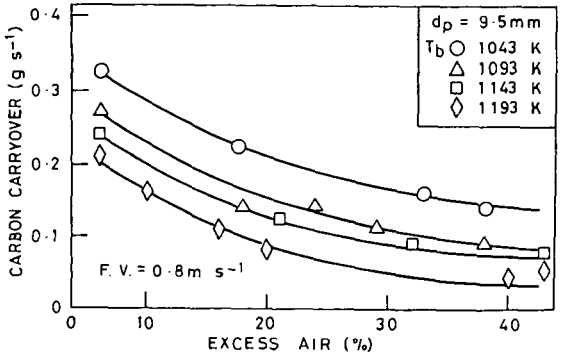

Fig. 5. (top). Carryover (carbon + ash) as a function of excess air (9.5 mm coal).

Fig. 6. (bottom). Carryover (carbon only) as a function of excess air (9.5 mm coal).

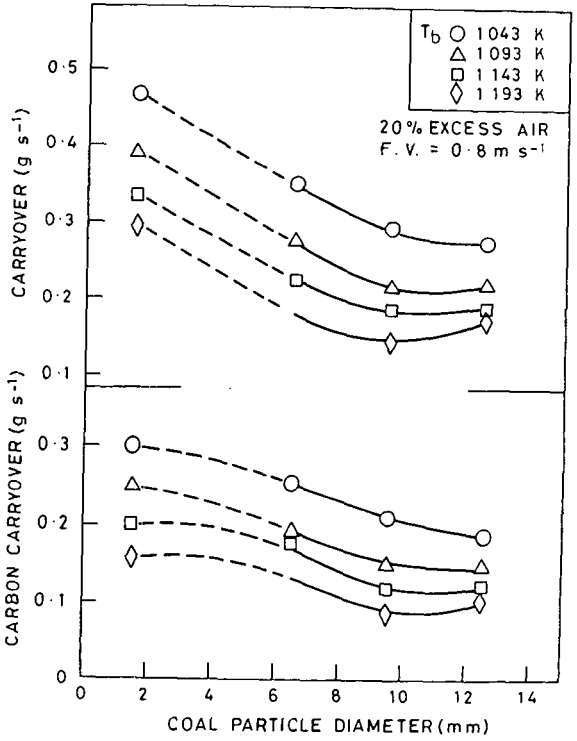

Fig. 7. Carbon and ash carryover (top) and carbon carryover only (bottom) as a function of coal particle diameter.

The influence of particle size distribution on the combustion rates in a batch fed fluidised bed

E.S. Garbett and A.B. Hedley

Sheffield Coal Research Unit, Department of Chemical Engineering and Fuel Technology, University of Sheffield, Sheffield, S1 3JD United Kingdom.

Introduction

The advantages of burning coal in fluidised bed combustors (FBC) have been repeatedly demonstrated over the past few years and commercial units are now being built and supplied to industry (1). The design of such FBC's is based on the practical experience gained from pilot plant studies and also on the predictions of mathematical models. Central to any model of coal combustion in FBC's is the rate at which particles burn in the bed which determines the carbon loading and hence pollutant emissions, heat release rates, coal feed rates and elutriation rates (2). Particle size and temperature usually indicate the controlling mechanism of combustion; large particles and high temperature suggest that diffusion is dominant whereas chemical kinetics became important for small particles and low temperatures (3). In a typical FBC the particle sizes range from that of the maximum of the input feed down to that of particles which are about to be elutriated and particle temperatures can have a value anywhere between the bed temperature T_b and T_b + 200K (4,5,6). It is not unreasonable to assume therefore, that the combustion of particles can be controlled by a combination of diffusional and chemical processes acting simultaneously. Indeed, the data of Avedesian and Davidson (7), where the combustion of char particles in a batch fed fluidised bed was assumed to be diffusion controlled, has recently (6) been shown to be consistent with the alternative situation described above where both processes are acting together. The effect on the carbon loading in an FBC where the combustion is either controlled by diffusion or by a combination process has been investigated by Garbett and Hedley (8) who also showed the importance of particle surface temperatures. The particle size distribution of the coal feed is a parameter which is important in the design of FBC's but whose influence on the combustion rates in the bed has not been studied. It is the purpose of this paper therefore, to develop a theory to predict the burnaway, burnout time and particulate phase oxygen concentration in a batch fed FBC and show their dependence on the input particle size distribution which is accurately known.

The Model

The model of the batch fed FBC employed here is essentially the two-phase bubbling bed model of Avedesian and Davidson (7) where a bed of inert particles at a temperature T_b is fluidised by air at a superficial velocity U_o and a minimum fluidised velocity U_{mf}. The oxygen required for combustion which is controlled by a combination of diffusion and chemical kinetics, is transferred to the char particles in the particulate phase from the bubbles and the reaction is given by $C + O_2 \rightarrow CO_2$. The batch is assumed to comprise solely of char particles so that devolatilisation is neglected. It is also assumed that the particles do not swell or break up when introduced to the bed and so retain their original size distribution.

The Theory

The reaction rate of a single particle of char of mass m_p in a fluidised bed where both diffusional and chemical kinetics are considered simultaneously, can be expressed in terms of diffusional and chemical resistances as follows (3).

$$R = \frac{K_c K_D C_p}{K_c + K_D} \qquad 1)$$

where $K_D = -k_1 x$ 2)

$K_c = -k_2 x^2$ 3)

(See equations 28) and 31) for values of k_1 and k_2)) C_p is the oxygen concentration (moles/m^3) in the particulate phase of the bed and is a function of time.

The rate of consumption of carbon at the particle surface is therefore given by

$$\frac{dm_p}{dt} = \frac{-k_1 k_2 x_p^3 \; M_o \; C_p}{k_1 x_p + k_2 x_p^2} \qquad 4)$$

leading to

$$\frac{dx_p}{dt} = \frac{-2M_o C_p}{\pi\rho} \left[\frac{1}{\frac{x_p}{k_1} + \frac{1}{k_2}} \right] \qquad 5)$$

where x_p is the diameter of a particle of mass m_p and M_o is the molecular weight of oxygen.

For convenience let $F(C) = \frac{2M_o C_p}{\pi\rho}$, $e = \frac{1}{k_2}$ and $f = \frac{1}{k_1}$

If after a time t a particle whose original diameter was x burns to give a diameter x_t, then

$$x_t = \frac{1}{f} \left[(e^2 + 2efx + f^2x^2 - 2f \int_o^t F(C)dt)^{\frac{1}{2}} - e \right] \qquad 6)$$

Let the original size distribution of a batch of carbon delivered to the fluidised bed be given by an equation of the form.

$$W_i = \theta(x) \qquad 7)$$

where W_i is the initial weight of the batch which consists of particles whose diameter is greater than or equal to x. It will be assumed that x must lie in the range $x_1 \leq x \leq x_2$ such that whatever the form of the function θ the conditions $\theta(x_1) = 1$ and $\theta(x_2) = 0$ are satisfied.

The initial mass of the batch which has particles whose diameters lie between x and x +dx is therefore, $m_i \; dW_i$, where m_i is the mass of the original batch. After a time t the mass will reduce to $m_i \; dW_i \; x_t^3/x^3$.

Therefore the mass of carbon in the bed after a time t is

$$m = \int_{x_1}^{x_2} m_i \; \frac{x_t^3}{x^3} \; \psi(x) \; dx \qquad 8)$$

where $\psi(x)\,dx = -dW_i$ and the lower limits of the integral are chosen to indicate

all the initial values of x for which $x_t > o$. Suppose an initial diameter y_o is defined so that all particles with an initial diameter $x < y_o$ would have burned away completely after a time t, then the mass fraction of carbon in the bed at this time t is

$$\frac{m}{m_i} = \int_{x=z}^{x=x_2} \frac{x^3_t}{x^3} \psi(x)\,dx \qquad 9)$$

where $z = x_1$ if $y_o \leq x_1$

and $z = y_o$ if $y_o > x_1$

By substituting y_o in equation 6) we have

$$\int_o^t F(C)\,dt = ey_o + \frac{f}{2} y_o^2 \qquad 10)$$

Combining equations 6), 8) and 10) gives

$$\frac{m}{m_i} = \int_{x=z}^{x=x_2} \frac{\left\{\left[\left(\frac{k_1}{k_2}\right)^2 + 2\left(\frac{k_1}{k_2}\right)(x-y_o)+(x^2-y_o^2)\right]^{\frac{1}{2}} - \frac{k_1}{k_2}\right\}^3 \psi(x)}{x^3}\,dx \qquad 11)$$

Burnout time

To derive an expression for the burn-out time we need to investigate dm/dt or $d(m/m_i)/dt$. From an oxygen balance on the bed (7) we have

$$12(C_o-C_p)A[U_o-U_{mf})(\exp(-B))] = -\frac{dm}{dt} \qquad 12)$$

where C_o is the inlet oxygen concentration (mole/m^3).

Therefore $C_p = C_o + \frac{dm/dt}{F(U_o)}$ 13)

where $F(U_o) = 12A[U_o - (U_o-U_{mf})(\exp(-B))]$

It can therefore be shown that

$$\frac{dm}{dt} = \frac{2C_o}{\left[\frac{\pi\rho}{M_o}\cdot\frac{(e+fy_o)}{dm/dy_o} - \frac{2}{F(U_o)}\right]} \qquad 14)$$

Also, from equation 13)

$$C_p = C_o\left[1 + \frac{1}{\left(\frac{F(U_o)\pi\rho(e+fy_o)}{2M_o\,dm/dy_o}\right)-1}\right] \qquad 15)$$

dm/dy_o can be found using the mathematical identity,

$$\frac{d}{dy_o}\left[\int_a^b g(x,y_o)\,dx\right] = \int_a^b \frac{\partial}{\partial y_o}\left(g(x,y_o)\,dx\right) + g(b,y_o)\frac{db}{dy_o} - g(a,y_o)\frac{da}{dy_o} \qquad 16)$$

Applying this to equation 11) gives

$$\frac{dm}{dy_o} = -3k_1(e+fy_o)m_i \int_{x=z}^{x=x_2} F_1(x,y_o)\ \psi(x)\,dx \qquad 17)$$

where

$$F_1(x,y_o) = \frac{\left\{\left[\left(\frac{k_1}{k_2}\right)^2 + 2\left(\frac{k_1}{k_2}\right)(x-y_o) + (x^2-y_o^2)\right]^{\frac{1}{2}} - \frac{k_1}{k_2}\right\}^2}{x^3\left[\left(\frac{k_1}{k_2}\right)^2 + 2\left(\frac{k_1}{k_2}\right)\cdot(x-y_o) + (x^2-y_o^2)\right]} \qquad 18)$$

Substituting dm/dy_o from equation 17) into equation 14)

re-arranging and integrating the result gives

$$\int_o^t dt = -\frac{1}{F(U_o)C_o}\int_{m_i}^{m} dm - \frac{\pi\rho}{6M_oC_ok_1m_i}\cdot\int_{m_i}^{m}\frac{dm}{\int_z^{x_2} F_1(x,y_o)\psi(x)\,dx} \qquad 19)$$

It can be shown that equation 19) reduces to

$$t = \frac{m_i\ (1-m/m_i)}{F(U_o)C_o} + \frac{\pi\rho\ y_o^2}{128C_ok_1} + \frac{\pi\rho\ y_o}{64C_ok_2} \qquad 20)$$

<u>The form of the initial size distribution</u>

Assume that the original carbon sample before any sieving into limited size range fractions, can be described by a Rosin-Rammler distribution

$$W = \exp\ (-bx^n) \qquad 21)$$

where b and n are constants. If the original material is then sieved into limited size fractions and only particles with diameters in the range $x_1<x<x_2$ are retained then the weight fraction W_i of the sieved material is (9)

$$W_i = \frac{\exp(-bx^n) - \exp(-bx_2^n)}{\exp(-bx_1^n)-\exp(-bx_2^n)}$$

Therefore

$$\psi(x) = \frac{bnx^{n-1}\ \exp(-bx^n)}{\exp(-bx_1^n)-\exp(-bx_2^n)} \qquad 22)$$

and the initial weighted mean particle size $\bar{x}_i$ is (9)

$$\bar{x}_i = \frac{\sqrt{(\frac{1}{n}+1)}}{b^{1/n}} \qquad 23)$$

Defining dimensionless parameters $X = \frac{x}{\bar{x}_i}$ and $Y = \frac{y_o}{\bar{x}_i}$ then from equation 22) we get

$$\psi(\bar{x}_i, x) = \frac{naX^{n-1}\exp(-aX^n)}{\exp(-aX_1{}^n)-\exp(-aX_2{}^n)} \qquad 24)$$

where $a = \left[(\frac{1}{n}+1) \right]^n$

Substitution of $\psi(\bar{x}_i, x)$ from equation 24) into equation 11) and making other appropriate terms dimensionless gives

$$\frac{m}{m_i} = \frac{1}{N}\int_Z^{X_2} \left\{ F_2(\bar{x}_i, X, Y) - \left(\frac{k_1}{k_2\bar{x}_i}\right)\right\}^3 an\, X^{n-4}\, e^{-ax^n}\, dx \qquad 25)$$

where

$$F_2(\bar{x}_i, X, Y) = \left[\left(\frac{k_1}{k_2\bar{x}_i}\right)^2 + \left(\frac{2k_1}{k_2\,\bar{x}_i}\right)(X-Y) + (X^2-Y^2)\right]^{\frac{1}{2}}$$

$$N = \exp(-aX_1{}^n) - \exp(-aX_2{}^n) \quad \text{and} \quad Z = \frac{z}{\bar{x}_i}$$

The lower limit of integration in equation 25) is given by

$Z = X_1$ if $Y \leqslant X_1$

and

$Z = Y$ if $Y > X_1$

Similarly equation 20) for the burn-out time, becomes

$$t = \frac{m_i\,(1-{}^m/m_i)}{F(U_o)C_o} + \frac{\pi\rho(\bar{x}_i{}^2Y^2)}{128C_o k_1} + \frac{\pi\rho(\bar{x}_i Y)}{64C_o\, k_2} \qquad 26)$$

and equation 15), the particulate phase oxygen concentration, becomes

$$C_p = C_o\left[1 - \frac{1}{\left(\frac{F(U_o)\,\pi\rho}{192k_1 m_i \int_Z^{X_2} F_3(\bar{x}_i, X, Y)\,d}\right) + 1}\right] \qquad 27)$$

where

$$\int_Z^{X_2} F_3(\bar{x}, X, Y)\,dX = \frac{na}{N\bar{x}_i{}^{3/2}} \int_Z^{X_2} \left[F_2(\bar{x}_i, X, Y)\left(\frac{k_1}{k_2\bar{x}_i}\right)\right]^2 X^{n-4}\, e^{-aX^n}\, dX$$

Numerical Calculations

The diffusion constant k_1 from equation 2) can be expressed as follows (7)

$$k_1 = 2\pi k D_E \qquad 28)$$

where k is a constant relating the mass of carbon consumed to the mass of O_2 transported to the particle surface. It is assumed here that the carbon-oxygen reaction can be represented by $C + O_2 \rightarrow CO_2$ so that k = 12/32

D_E is the effective diffusion coefficient and can be represented by (7)

$$D_E = \frac{D_G \, Sh}{2} \qquad 29)$$

where Sh is the local particle Sherwood Number and D_G is the diffusion coefficient calculated from (3)

$$D_G = D_i \frac{(P_i)}{P} \left(\frac{T}{T_i}\right)^{1.75} \qquad 30)$$

The chemical constant k_2 can be represented by (10,11)

$$k_2 = k' \, T_b^{\frac{1}{2}} \exp(-E/R_g T_p) \qquad 31)$$

The above data is summarised in Table 1. The bed data used in the calculations are that of Avedesian and Davidson (7).

Table 1

Data used in calculations

Symbol	Value	Reference
k	0.375	
T_i	1000 K	(3)
D_i	1.61	(3)
T_b	1173 K	(7)
T_p	1173 K	(7)
k´	1034	(11,12)
Sh	1.8	(8)
E	15 K cal/mole K	
P/P_i	1	

The three distributions used in the calculations are summarised in Table 2. In all the results presented here the top and bottom size of each distribution were constant at 3 and 0.3mm respectively.

Table 2

Particle size data

	b=11.12	b=625	b=10000
n	1.5	4	4
$\bar{x}_i$	0.1813	0.1813mm	0.0906mm
Γ	0.9033	0.9064	0.9064
x_1	0.3mm	0.3mm	0.3mm
x_2	3mm	3mm	3mm
m_i	5gm	5gm	5gm

Results and Discussion

Evaluation of m/m_i

To demonstrate the type of results to be expected from the theory equation 25) was numerically integrated to give values of m/m_i for increasing values of Y using the values of k_1 and k_2 indicated in Table 1 and the distributions in Table 2. For comparison the values of m/m_i for the pure diffusional and chemical cases were calculated using a method similar to that described by Leesley and Siddall (9) for pulverised fuel. Figures 1, 2 and 3 show the variation of m/m_i, the unburnt fraction of carbon remaining, with the dimensionless particle diameter Y for the three original distributions. In every case the combined curve m_{C+D}/m_i falls inside the envelope of the two extreme conditions of pure diffusional (m_D/m_i) and of pure chemical (m_C/m_i). The curves represented in these figures (1,2, and 3) are not burnaway rates but indicate the changing particle size distribution as the batch disappears. For example, in figure 1, when 50% of the batch has burnt away (i.e. $m/m_i = 0.5$) the combined case requires that all particles of a size below 18% of the maximum particle size in the original batch must have disappeared. Corresponding values for the pure diffusion case and pure chemical case are 34% and 12% respectively. Thus for a given carbon loading the carbon particle size distribution in the bed will be different for different combustion mechanisms and this will obviously influence important phenomena such as elutriation, and NO reduction by char. To combine Figures 1 to 3 for comparison purposes the data have been represented in Figure 4 as a ratio of unburnt fraction for the combined case (m_{C+D}) to that for the diffusion case (m_D) as a function of the particle diameter Y. It is clearly seen that as the original size distribution moves from a wide one (n=1.5, b=11.12) to a fine one (n=4.0, b=10,000) the difference between m_{C+D} and m_D increases

Evaluation of t

The burnaway rates of the batch for each original size distribution and for a combustion mechanism where both diffsuion and chemical kinetics are acting simoultaneously were calculated from equation 26) and are shown in Figure 5. The burnaway rate is higher for the distribution represented by n=4.0, b=10,000 than for the other two distributions as would be expected. What is not evident

from Figure 5, due to the scale, is that the time for total burnaway is the same for each distribution since they all have the same maximum particle size of 3mm.

Evaluation of C_p

Equation 27) was numericatly integrated to give the particulate oxygen concentration C_p for the three distributions. The results are shown in Figure 6. An interesting feature of these results is the value of C_p at t=o. According to Avedesian and Davidson (7) the value of C_p should be almost zero for the batch fed system but it is clear from Figure 6 that this is not the case.

Equations 25), 26) and 27) are valid only for constant temperature and pressure. These conditions are usually met in FBC's except that the particle temperature T_p can vary during burnaway and can be appreciably higher than the bed temperature (4,5,6). The effect of increasing T_p would be to increase the value of k_2 relative to k_1 and the controlling mechanism would tend towards that of diffusion. Increasing the pressure of the system would only have a significant effect if the combustion rate was initially dominated by chemical kinetics.

Conclusions

A theoretical model has been developed which predicts the change in size distribution during burnaway, burn-out times and particulate phase oxygen concentrations as a function of original particle size distribution in a batch fed fluidised bed. If the original size distribution is accurately known a batch fed experiment could be devised to determine the role of chemical kinetics for a given type of coal and would thus be an aid to modelling of fluidised bed combustion.

Acknowledgements

The work described here form part of the activities of the Sheffield Coal Research Unit sponsored by Shell Coal International and the N.C.B.. The authors are grateful for the financial assistance of the Sponsors and wish to point out that the views expressed here are those of the authors and not necessarily those of the Sponsors. We are also grateful to Dr. R.G. Siddall and Dr. P.J. Foster for many illuminating discussions.

Nomenclature

a	Constant defined by equation 24)
A	Area of fluidised bed (m^2)
b	Rosin-Rammler constant - equation 21)
B	Oxygen exchange parameter - equation 12)
C_o	Oxygen concentration of fluidising air ($mole/m^3$)
C_p	Particulate phase oxygen concentration ($mole/m^3$)
D_G	Gas diffusion coefficient (m^2/s)
e	constant ($= 1/k_2$)
f	constant ($= 1/k_1$)
$F(U_o)$	Defined by equation 12)
F(C)	Function of Oxygen concentration ($= 2M_oC_p/\pi\rho$)

k_1	Constant defined by equation 2)	
k_2	Constant defined by equation 3)	
k'	Constant defined by equation 31)	
K_c	Chemical rate constant	
K_D	Diffusional rate constant	
m	Mass of char in bed at time t	(kg)
m_i	Initial mass of batch	(kg)
m_p	Mass of single char particle	(kg)
N	Function of particle size - equation 25)	
P	Pressure	(atm)
R	Reaction rate of single particle	(kg/s)
R_g	Gas constant	
t	Burnaway time	(s)
T	Temperature	(K)
T_b	Bed temperature	(K)
T_i	Reference temperature - equation 30)	(K)
T_p	Particle surface temperature	(K)
U_{mf}	Minimum fluidising velocity	(m/s)
U_o	Superficial fluidising velocity	(m/s)
W	Weight fraction of coal	(kg)
x	Particle diameter	(mm)
$\bar{x}_i$	Initial weighted mean particle size	(mm)
x_p	Particle diameter	(mm)
x_t	Particle diameter	(mm)
X	Dimensionless particle diameter	$(= x/\bar{x}_i)$
y_o	Particle diameter	(mm)
Y	Dimensionless particle diameter	$(= y_o/\bar{x}_i)$
z	Particle diameter (lower limit of integration)	mm
Z	Dimensionless particle diameter	$(= z/\bar{x}_i)$

Greek Symbols

ρ	Char density
θ	Size distribution function equation 7)
ψ	Size distribution function equation 8)
Γ	Gamma function

References

1. Gibson, J. and Highley, J., J. Inst. E., 1979, 52, 51.

2. Sarofim, A.F. and Beer, J.H. Combustion Inst. Conf. No. 17, 1978, 189.

3. Field, M.A. Gill, D.W., Morgan, B.B. and Hawksley, P.G.W., Combustion of Pulverised Coal, 1967, BCURA.

4. Basu, P., Fuel, 1977, 56, 390.

5. Yates, J.R. Witkowski, A.R. and Harrison, D., Trans. I. Chem. E. 1980, 58, 69.

6. Garbett, E.S. and Hedley, A.B. Power Ind. Research, 1981, 1, 91.

7. Avedesian, M.M. and Davidson, J.F., Trans. I. Chem. E.

8. Garbett, E.S. and Hedley, A.B., Inst. Energy Symp. Series No. 4, 1980, paper IV-6.

9. Leesley, M.E. and Siddall, R.G., J. Inst. F., 1972, 45, 169.

10. Marsden, C., Ph.D. Thesis, University of Sheffield, 1964.

11. Beer, J.M., Ph.D. Thesis, University of Sheffield, 1959.

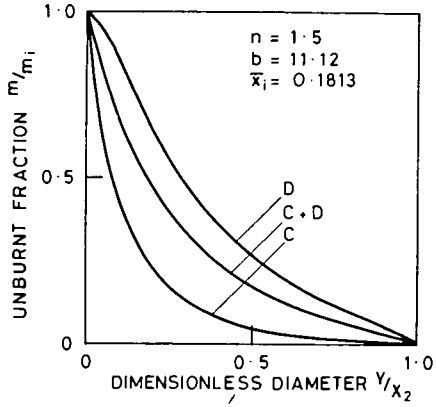

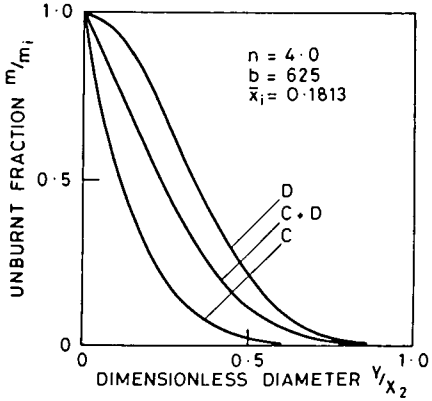

Fig. 1. (top) and Fig. 2. (bottom). Unburnt mass fraction (m/m_i) of the batch during burnaway.

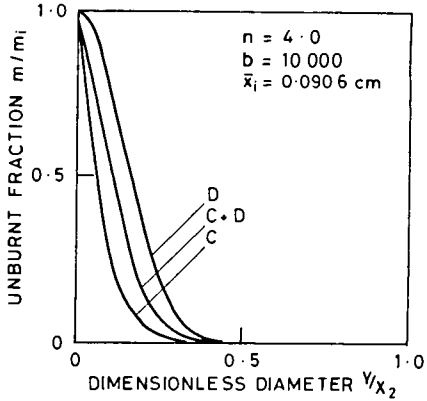

Fig. 3. (top). Unburnt mass fraction (m/m_i) of the batch during burnaway.

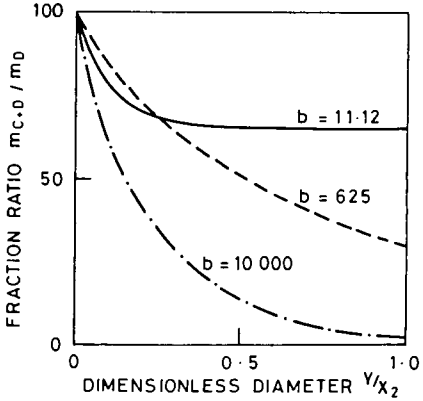

Fig. 4. (bottom). Unburnt mass fraction ratio (m_{C+D}/m_D) during burnaway for the three distributions.

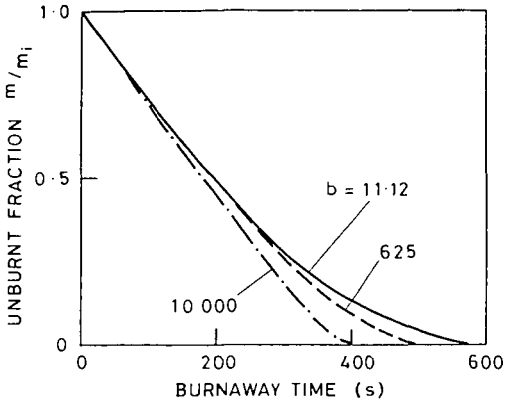

Fig. 5. (top). Burnaway rate of the batch for the three distributions.

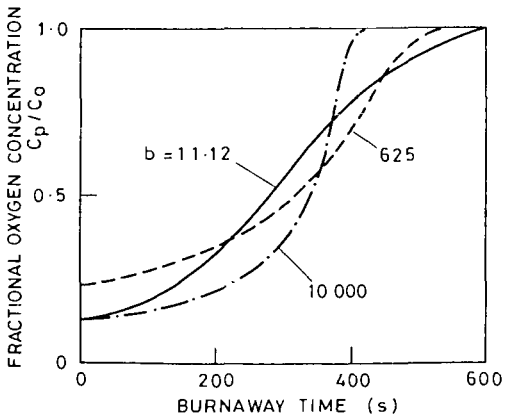

Fig. 6. (bottom). Particulate phase oxygen concentration (C_p) during burnaway for the three distributions.